Dynamic analysis and design strategies for mistuned bladed disks

Sang-Ho Lim

To cite this version:

Sang-Ho Lim. Dynamic analysis and design strategies for mistuned bladed disks. Mechanics [physics.med-ph]. University of Michigan-Ann Arbor, 2005. English. NNT : . tel-00375423

HAL Id: tel-00375423
https://theses.hal.science/tel-00375423

Submitted on 14 Apr 2009

DYNAMIC ANALYSIS AND DESIGN STRATEGIES FOR MISTUNED BLADED DISKS

by

Sang-Ho Lim

A dissertation submitted in partial fulfillment
of the requirements for the degree of
Doctor of Philosophy
(Mechanical Engineering)
in The University of Michigan
2005

Doctoral Committee:

Professor Christophe Pierre, Co-Chair
Associate Research Scientist Matthew P. Castanier, Co-Chair
Associate Professor Nickolas Vlahopoulos
Assistant Professor Bogdan I. Epureanu

To my mother, wife, and sons

ACKNOWLEDGEMENTS

First, I wish to express my utmost gratitude to my advisors and co-chairs of my doctoral committee, Professor Christophe Pierre and Dr. Matthew P. Castanier, for their inspiring and encouraging guidance during the past years. Without their supervision and supports, I would never have been able to finish this work.

I am also grateful to my colleagues sharing the office for their friendship, help, and providing a good working atmosphere. It has been a very nice time and a good memory for me.

I also wish to thank my wife, Sung-Min, for her patience, sacrifice, and continuous loving supports. In addition, I would like to extend my sincere gratitude to my mother and all my other family members for their love and encouragements.

There are many other people who also gave warm help and valuable advice to me during my stay in Ann Arbor. I would like to give many thanks with apologies to all those not mentioned.

TABLE OF CONTENTS

CHAPTER

LIST OF FIGURES

Figure

LIST OF TABLES

Table

CHAPTER I

Introduction

1.1 Dissertation Objectives

Bladed disks are used in various important engineering applications, such as fans, impeller pumps, windmills, propellers, turbine generators, and jet engines. In a nominal design, a bladed disk is a structure of cyclic symmetry, where all the disk-blade sectors are identical and arranged around the central axis. In practice, however, there are always small variations in structural properties along the sectors, resulting from manufacturing tolerances, material deviations, and uneven operational wear. Due to these small irregularities, which are referred to as mistuning, the cyclic symmetry of the bladed disk is destroyed.

Since a nominal bladed-disk design features cyclic symmetry, only a single sector model is required for the vibration analysis of the whole assembly, and the modes appear in the form of circumferential harmonic waves. Therefore, the vibration energy is evenly distributed to every sector in a perfectly tuned bladed disk when an engine order excitation, which is harmonic in time and differs by a constant phase angle from blade to blade, is applied. The free response of a bladed disk features groups of system modes dominated by blade motion, whose natural frequencies are located in narrow frequency bands around the blade-alone natural frequencies. Because of this high modal density, the modes are significantly altered by small mistuning (especially, blade mistuning) so that the mode shapes are not spatially harmonic any more. Consequently, the dynamic behavior of a bladed disk with mistuning may be qualitatively different from that of the tuned configuration. The vibration energy can become concentrated in a few blades, and those blades experience higher levels of stress than would be predicted from a nominal design. In addition, cyclic symmetry cannot be used for the analysis of a mistuned bladed disk, and the model of the whole mistuned assembly is required, which is costly.

In order to understand the basic mechanisms of the mistuning effects on bladed disk dynamics, lumped parameter models have been often studied. Using these models, many mistuning phenomena—such as mode pair splitting, mode localization, and forced vibration response magnification—have been explained, and the maximum forced response magnification that can be reached due to mistuning has been estimated. Also, reduced-order models (ROMs) have been developed based on the parent finite element models (FEMs) in order to provide an accurate prediction of the vibratory response of bladed disks, and some ROMs have been used to identify the mistuning in actual bladed disks. Still, there is a need for smaller and more accurate ROMs, because Monte Carlo simulations of randomly mistuned bladed disks are commonly performed for design evaluation. Furthermore, most ROMs have been developed by assuming that mistuning is small, which is not necessarily the case.

Recently, it has been reported that, when mistuning is intentionally introduced to nominal designs, the maximum blade forced response level can be decreased. That is, a nominally mistuned design can be robust with respect to unavoidable random mistuning. However, it is not known which patterns of intentional mistuning are optimal. In addition, optimization procedures can be prohibitively expensive due to the huge design space of intentional mistuning patterns, even for lumped parameter models.

The primary objectives of this research are as follows:

- To develop an efficient and accurate reduced-order modeling method for the vibration of bladed disks with small mistuning.
- To apply the reduced-order modeling methods to the identification of mistuning.
- To investigate the underlying mechanism of intentional mistuning so that some strategies to reduce the design space for intentional mistuning patterns can be extracted.
- To develop a reduced-order modeling technique that can handle the cases in which mistuning is so large that ROMs for small mistuning cannot be used.

1.2 Background

The effect of mistuning on turbomachinery rotors has long been studied by experiments and by analytical and numerical models. In 1957, Tobias and Arnold [1] reported that inevitable imperfections in rotating disks cause mode pairs with identical natural frequencies to separate into two distinct modes. Since then, there has been a significant amount of research on understanding and predicting the vibration of mistuned bladed disks. Many of these studies have employed lumped parameter models using analytical, numerical, statistical, and perturbation methods (Whitehead [2], Wagner [3], Dye and Henry [4], Ewins [5, 6], El-Bayoumy and Srinivasan [7], Griffin and Hoosac [8], Lin and Mignolet [9], Wei and Pierre [10, 11], and Óttarsson and Pierre [12], etc.). In particular, Wei and Pierre [10, 11] demonstrated that bladed disk systems with low damping, high modal density, and moderately weak interblade coupling are most susceptible to mode localization and resonant amplitude magnification. Although a lumped parameter model can provide basic understanding of the underlying mechanisms of mistuning phenomena, it cannot be used for accurate predictions of the dynamic response of an actual bladed disk.

Therefore, FEMs have been employed to yield ROMs by using component mode synthesis (Irretier [13], Zheng and Wang [14], Castanier *et al.* [15], Kruse and Pierre [16, 17], Bladh *et al.* [18–20], Moyroud *et al.* [21]), a receptance technique (Yang and Griffin [22]), and classical modal analysis with mistuning projection (Yang and Griffin [23]). Castanier *et al.* [15] introduced a component-based ROM in which mistuning is implemented by varying blade modal stiffness. Bladh *et al.* [18] extended this modeling method by introducing the projection of mistuning to cantilevered-blade normal modes so that mistuning is implemented in the modal domain. Mistuning implementation in the modal domain has a great advantage in that a small number of modal mistuning values are sufficient to describe complex parameter variations in a blade. Yang and Grffin's method [23] is also notable due to the compact size of the resulting ROM, which is achieved by recognizing that, when a tuned system has a set of normal modes that are closely spaced in a frequency range, a slightly mistuned system also has normal modes closely spaced in the same frequency range and the mistuned normal modes can be captured using only that set of tuned normal modes. In Yang and Griffin's method [23], tuned-system normal modes are used directly to construct a ROM without substructuring a bladed disk. Therefore, no additional errors are introduced in a ROM of tuned systems. However, since mistuning is directly projected to tuned-system modes in this method, the knowledge of mass or stiffness mistuning matrices in physical coordinates is required for the implementation of mistuning into a ROM, which is cumbersome.

Once a ROM of a bladed disk is obtained, the next concern is to assess the safety of a given design using the model. Typically, blade forced-response level is represented by an amplification factor that is the ratio of the largest blade response in a mistuned system to that in the tuned counterpart. Therefore, the assessment is usually performed by identifying the maximum amplification factor. Some researchers [2, 24–28] have derived analytical forms for the maximum amplification factor. Most famously, Whitehead [2, 24, 25] reported an amplification factor of $(1 + \sqrt{N_b})/2$, where N_b is the number of blades. In Kenyon *et al.*'s work [27], only mode distortion was considered to find the maximum amplification factor. Therefore, their maximum factor could not reach Whitehead's factor. Rivas-Guerra and Mignolet [28] argued that Whitehead's factor is recovered only when the engine order of excitation is equal to 0 or $N_b/2$ for N_b even. Despite all these research efforts, the obtained maximum amplification factors are based on lumped parameter models, and thus may not be applicable to actual bladed disks. Therefore, statistical analyses have often been used to determine confidence limits (e.g., the 99th percentile value) for the amplification factor, which requires a large number of Monte Carlo simulations on mistuned bladed disks. Hence, the development of a small, accurate ROM has been an important issue, even though a method to reduce the number of simulations required for the accurate estimation of the response statistics has been developed [29].

Another use of a ROM is to identify mistuning in actual bladed disks. Mistuning identification is important as a means of monitoring the quality of the manufacturing process, and also in the maintenance checks of operational rotors. Judge *et al.* [30, 31] first reported a mistuning identification method using a ROM. Subsequently, Feiner and Griffin [32, 33] developed another method using a simpler model. These methods are based on the assumption that the dynamic behavior of an actual bladed disk is exactly represented by a FEM. The sensitivity of the identification results to the possible modeling errors, which might be critical, has not been examined.

Although a nominal design of a bladed disk usually means a tuned configuration, there have been many studies showing that a nominally mistuned design can reduce blade forced response level. Ewins [34] reported that deliberate, significant detuning has the possibility to reduce blade vibration levels for specific engine orders of excitation. Griffin and Hoosac [8] observed that the level of the maximum blade forced response is reduced by constructing an alternate mistuning configuration with two blade populations, where each population has different mean natural frequencies. Recently, the beneficial effect of intentionally incorporating mistuning into a nominal design has been studied more systematically (Castanier and Pierre [29, 35, 36], Brewer *et al.* [37]). In these studies, it has been shown that using two or more blade designs with nominally different natural frequencies can make a bladed disk system more robust with respect to random mistuning. The performance of intentionally mistuned designs is dependent on the pattern of intentional mistuning. Therefore, one recent study [38] was focused on finding an optimal intentional mistuning pattern using an optimization algorithm. However, only limited information was used to evaluate each iteration of the intentionally mistuned design, without identifying the maximum blade response, because of cost.

1.3 Dissertation Outline

The remaining chapters of this dissertation are compiled from a collection of six manuscripts (five technical papers and one technical note) that have been prepared for submission to scientific journals. Because of this, some of the background material is repeated in various chapters. The remaining chapters are summarized as follows.

In chapter II, a component-based modeling framework for mistuned bladed disks is developed, in which a mistuned bladed disk is substructured into a tuned bladed disk and virtual mistuning components. From this framework, a compact ROM is derived for the case of small mistuning. The obtained ROM uses a small set of tuned-system normal modes as a basis, and mistuning is projected to cantilevered-blade component modes, and then to tuned-system modes via the modal participation factors of cantilevered-blade modes for tuned-system modes.

In chapter III, a new technique for mistuning identification based on the modeling technique developed in chapter II is presented. A sensitivity study is performed for both modeling errors and data noise, and in order to compensate for these modeling errors, the concept of “cyclic modeling error” is introduced.

In chapter IV, two methods to calculate the upper bound of the amplification of the blade forced response are presented. First, using lumped parameter models, the maximum amount of vibration energy that can be concentrated in a single blade is calculated, and the response of the blade is obtained. In another method, the worst combination of closely spaced tuned-system traveling wave modes is found to yield the largest blade response. Also, some indicators to approximate the largest stress level in a blade are studied.

In chapter V, the basic mechanism of intentional mistuning is investigated using lumped parameter models, and three guidelines to reduce the design space for intentional mistuning patterns are proposed. They are validated by testing all the patterns available for 12-blade systems when two blade types are used, and their effectiveness is also examined using a ROM for an industrial rotor.

In chapter VI, a new reduced-order modeling technique is developed for bladed disks with large, geometric deviations from a nominal design. By accounting for the effects of the deviations as though they were produced by external forces, a set of basis vectors are established using a combination of tuned-system normal modes compensated by static modes. The developed method shows fast convergence, and produces ROMs as compact as those for small mistuning.

Finally, in chapter VII, the contributions of this research are summarized, and ideas for future work are proposed.

CHAPTER II

A Compact, Generalized Component Mode Mistuning Representation for Modeling Bladed Disk Vibration

New techniques are presented for generating reduced-order models of the vibration of mistuned bladed disks from parent finite element models. A novel component-based modeling framework is developed, by partitioning the system into a tuned bladed disk component and virtual mistuning components. The mistuning components are defined by the differences between the mistuned and tuned mass and stiffness matrices. The mistuned system model is assembled with a component mode synthesis technique, using a basis of tuned-system normal modes and attachment modes. The formulation developed is general and can be applied to any mistuned bladed disk, including those with large, geometric mistuning (e.g., severe blade damage). In the case of small (i.e., blade frequency) mistuning, a compact reduced-order model is derived by neglecting the attachment modes. For this component mode mistuning model, the blade mistuning is projected first onto the component modes of a tuned, cantilevered blade, and then projected again onto the tuned-system normal modes via modal participation factors. In this manner, the measured modal characteristics of mistuned blades can be used to capture systematically the effects of the complex physical sources of mistuning. A numerical validation of the methods developed is performed for both large and small mistuning cases using a finite element model of an industrial rotor.

2.1 Introduction

A bladed disk consists of a set of disk-blade sectors that are typically assumed to be identical. In practice, however, there are always small variations in the structural properties of individual blades, resulting from manufacturing tolerances, material deviations, and operational wear. These variations are referred to as blade mistuning. Due to mistuning, the vibratory response of an industrial bladed disk may be considerably different from that of its nominal, tuned design. Over the past 40 years much research has been done on the dynamic behavior of mistuned bladed disks, and many of these studies have been based on lumped parameter models [3–11]. While such simple models do provide a basic understanding of the effects of mistuning, they cannot be used to predict accurately the vibratory response of industrial bladed disks. Therefore, various techniques have been developed to construct reduced-order models (ROMs) of bladed disks systematically from their finite element representations. These include component mode synthesis [13, 15, 18–21, 39], a receptance technique [22], and classical modal analysis with a mistuning projection [23]. The major differences between these reduced-order modeling techniques are the substructuring approach and the mistuning implementation. Another method to obtain the response of mistuned systems without building an attendant reduced-order model has been proposed by Petrov *et al.* [40]. In this approach, the response of a mistuned system is calculated using response levels for the tuned assembly, together with a modification matrix constructed from the frequency response function matrix of the tuned system and a matrix describing the mistuning.

In general, reduced-order models are obtained by substructuring a bladed disk into disk and blade components, as this allows for easy implementation of blade mistuning.

However, one approach [23] has recently been proposed by Yang and Griffin, in which the tuned-system normal modes are used without substructuring to generate a reduced-order model. One advantage of avoiding substructuring is that there is no additional error introduced in the tuned system model. Another advantage is that, since the number of tuned-system normal modes required is on the order of the number of blades, the size of Yang and Griffin's reduced-order model is smaller than that of any other.

The way in which blade mistuning is implemented into a reduced-order model is a key issue, because mistuned reduced-order models should be able to replicate the behavior of actual mistuned systems. Castanier *et al.* [15] included mistuning in a component-based reduced-order model by varying the blade modal stiffnesses that appear explicitly in a synthesized stiffness matrix. Bladh *et al.* [18] extended this method by projecting mistuning onto the normal modes of a tuned cantilevered blade fixed at the disk-blade interface. Since a small number of modal stiffness variations are directly employed in the reduced-order model, the implementation of mistuning is quite efficient. Also, since different mistuning patterns can be used for the various individual blade modes, multi-blade-mode bladed disks can be modeled realistically. Therefore, this mistuning projection method has great potential for general implementation in reduced-order models. Yang and Griffin [23] used a similar mistuning projection, but in theory their method requires the knowledge of the mistuned mass and stiffness matrices in physical coordinates, since the mistuning expressed in physical coordinates is directly projected to the tuned system modes. Therefore, they only considered the case of a mistuned blade stiffness matrix proportional to the nominal matrix. The method proposed by Petrov *et al.* [40] also uses a mistuning matrix in physical coordinates. Therefore, for the practical implementation of mistuning, it is clear that the mistuning projection method of Bladh *et al.* [18] is useful, with the caveat that the component mode shapes of mistuned and tuned blades are assumed to be the same and that only stiffness mistuning is present.

In this paper, a general reduced-order model for mistuned bladed disks is developed. In this approach, the mistuned system is represented by the full tuned system and by virtual mistuning components, and a hybrid-interface method is used to combine them. The mistuning components consist only of mass and stiffness deviations from the tuned configuration, and all the degrees of freedom (DOF) in the mistuning components are considered to be interface degrees of freedom. Since no assumption is made about mistuning in this formulation, the resulting reduced-order model can be constructed for arbitrary mistuning, regardless of whether it is small or large.

Most previous research on mistuning has been based on the assumption that mistuning is small (i.e., small blade-frequency mistuning), which is not necessarily the case. If there is large mistuning, such as a fractured blade tip, or significant variations in blade geometry due to damage, then it is necessary to include a very large number of tuned-system modes or tuned-component (disk and blade) modes in the reduced-order models. This is due to the fact that mistuning may change the mass or stiffness matrices significantly, and the mode shapes of a mistuned blade may be completely different from those of a tuned blade. Because of this difficulty, reduced-order models developed to date have not been able to capture such large mistuning. In the general formulation proposed herein, the attachment modes of the tuned system are used to generate an accurate reduced-order model with a reasonable size for the case of large mistuning. This allows for the efficient prediction of the response of bladed disks with large, mode shape mistuning. Furthermore, intentional mistuning [36], which may be not small in local areas of the blades, can be efficiently studied with this method.

In this paper, a reduced-order model for the special case of small mistuning is also derived from the above general formulation. This model uses the same tuned mode basis, and thus it features the same small number of DOF as that of Yang and Griffin's method [23]. Blade mistuning is implemented using the mistuning projection approach originally developed by Bladh *et al.* [18], which is extended here to handle the generalized blade mistuning cases considered. By using only a few modes of a mistuned cantilevered blade, any type of small structural mistuning can be accurately accounted for. This new approach to small-mistuned bladed disks is referred to as the component mode mistuning (CMM) method. In preceding studies [18–20], a bladed disk was substructured into disk and blade components in order to project mistuning to the normal modes of a tuned cantilevered blade. With the CMM method, modal participation factors of the cantilevered-blade normal modes are used to describe the blade motion in terms of the tuned-system normal modes, and thus, mistuning is projected to cantilevered-blade normal modes without requiring a component-based representation of the full system. Furthermore, by examining modal participation factors, just a few dominant cantilevered-blade normal modes can be used for the mistuning projection.

A major advantage of this method is that, even when mistuning is present in only part of the blade such that the modal mistuning patterns for the various blade modes are different, the influence of mistuning may still be estimated accurately. That is, arbitrary patterns of mistuning in the physical mass and stiffness matrices can be efficiently and accurately implemented in a compact reduced-order model using modal mistuning values for a few cantilevered-blade modes. This feature is especially useful when two groups of blade-dominated modes of the tuned system are closely spaced.

The primary contribution of this paper is a new method for systematically formulating a general reduced-order model of mistuned bladed disks, regardless of whether mistuning is small or large. In particular, the new ROM handles the effects of large structural and geometric variations, such as fractured and damaged blades. Another contribution is the development of a compact modeling framework for a bladed disk with generalized small blade mistuning and aerodynamic coupling. In particular, the CMM model allows one to handle the cases of local blade mistuning and different mistuning patterns for the different blade modes.

The paper is organized as follows. The general formulation of a reduced-order model for a bladed disk with arbitrary mistuning is presented in section 2.2. The CMM representation for the case of small blade mistuning is derived in section 2.3. In section 2.4, the general approach is validated by comparing the results of the finite element model (FEM) and the ROM for an industrial rotor with a rogue blade, which causes large mistuning. In section 2.5, the CMM approach is validated for the same industrial rotor but with small mistuning. The test cases include mistuning that leads to a proportional change in the blade stiffness matrix as well as non-proportional mistuning. The conclusions are given in section 2.6.

2.2 General Reduced-Order Model Formulation for a Mistuned System

A general, component-based framework is considered, whereby a mistuned bladed disk is partitioned into a *tuned bladed disk* component and a set of virtual components that represent the *blade mistuning*, as shown in Fig. 2.1. Each virtual substructure, or mistuning component, is defined as having mass and stiffness matrices equal to the difference between the mistuned and tuned matrices of a single blade. Since the response of a typical bladed disk is much more sensitive to mistuning in the blades than in the disk, only blade mistuning is considered in this study. However, the proposed substructuring approach can be applied to any mistuned system.

In order to combine the tuned system and mistuning components, a hybrid-interface component mode synthesis (CMS) [41] approach is employed. The tuned system is treated as a free-interface component, while the mistuning components are treated as fixed-interface components. For the CMS of the tuned system component, normal modes and attachment modes [41] are needed, where the attachment modes are obtained by applying a unit force to each interface DOF, successively. For the CMS of a mistuning component, normal modes and constraint modes [41] are needed, where the constraint modes are obtained by enforcing a unit displacement at each interface DOF, successively. Note that since all the DOF in the mistuning components are interface DOF, they do not have component normal modes. Therefore, the constraint modes, which in this case are represented by the identity matrix, are sufficient to describe the motion of the mistuning components.

The reduced mass and stiffness matrices in modal coordinates for the free-interface component (the tuned system), $\boldsymbol{\mu}^S$ and $\boldsymbol{\kappa}^S$, can be written using its truncated set of normal modes, $\mathbf{\Phi}^S$, and complete set of attachment modes, ψ^S, as follows:

$$\boldsymbol{\mu}^S = \begin{bmatrix} \mathbf{I} & \mathbf{\Phi}^{S^T}\mathbf{M}^S\mathbf{\Psi}^S \\ \mathbf{\Psi}^{S^T}\mathbf{M}^S\mathbf{\Phi}^S & \mathbf{\Psi}^{S^T}\mathbf{M}^S\mathbf{\Psi}^S \end{bmatrix} \tag{2.1a}$$

$$\boldsymbol{\kappa}^S = \begin{bmatrix} \mathbf{\Lambda}^S & \mathbf{\Phi}^{S^T}\mathbf{K}^S\mathbf{\Psi}^S \\ \mathbf{\Psi}^{S^T}\mathbf{K}^S\mathbf{\Phi}^S & \mathbf{\Psi}^S_{\mathit{\Gamma}} \end{bmatrix} \tag{2.1b}$$

$$\mathbf{x}^S = \begin{Bmatrix} \mathbf{x}^S_{\mathit{\Delta}} \\ \mathbf{x}^S_{\mathit{\Gamma}} \end{Bmatrix} = \begin{bmatrix} \mathbf{\Phi}^S_{\mathit{\Delta}} & \mathbf{\Psi}^S_{\mathit{\Delta}} \\ \mathbf{\Phi}^S_{\mathit{\Gamma}} & \mathbf{\Psi}^S_{\mathit{\Gamma}} \end{bmatrix} \begin{Bmatrix} \mathbf{p}^S_{\mathit{\Phi}} \\ \mathbf{p}^S_{\mathit{\Psi}} \end{Bmatrix}, \tag{2.1c}$$

where $\mathbf{\Lambda}$ is a diagonal matrix of the eigenvalues of the retained normal modes, $\mathbf{x}$ is a vector of physical coodinates, and $\mathbf{p}$ is a vector of modal coordinates. The superscript S denotes a tuned system, and the subscripts $\mathit{\Delta}$ and $\mathit{\Gamma}$ denote the DOF of the disk and the blades, respectively. The subsrcripts $\mathit{\Phi}$ and $\mathit{\Psi}$ denote the generalized coordinates for the retained component normal and interface modes, respectively.

For the mistuning components, the reduced mass and stiffness matrices in modal coordinates, $\boldsymbol{\mu}^\delta$ and $\boldsymbol{\kappa}^\delta$, are the same as those in physical coordinates.

$$\boldsymbol{\mu}^\delta = \mathbf{I}^T \mathbf{M}^\delta \mathbf{I} = \mathbf{M}^\delta \tag{2.2a}$$

$$\boldsymbol{\kappa}^\delta = \mathbf{I}^T \mathbf{K}^\delta \mathbf{I} = \mathbf{K}^\delta \tag{2.2b}$$

$$\mathbf{x}^\delta = \mathbf{I}\,\mathbf{p}^\delta_{\mathit{\Psi}} = \mathbf{p}^\delta_{\mathit{\Psi}}, \tag{2.2c}$$

where

$$\mathbf{M}^\delta = \underset{n=1,\ldots,N}{\mathbf{Bdiag}}\left[\mathbf{M}^\delta_n\right], \quad \mathbf{K}^\delta = \underset{n=1,\ldots,N}{\mathbf{Bdiag}}\left[\mathbf{K}^\delta_n\right],$$

the superscript δ denotes the mistuning components, $\underset{n=1,\ldots,N}{\mathbf{Bdiag}}[\cdot]$ denotes a block-diagonal matrix with the nth block corresponding to the nth blade, and N is the number of blades. Now, the assembly of the components is achieved by satisfying displacement compatibility at the component interface (i.e., $\mathbf{x}^S_{\mathit{\Gamma}} = \mathbf{x}^\delta$). This yields, from Eq. (2.1c) and (2.2c):

$$\boldsymbol{\Phi}^S_{\mathit{\Gamma}}\mathbf{p}^S_{\mathit{\Phi}} + \boldsymbol{\Psi}^S_{\mathit{\Gamma}}\mathbf{p}^S_{\mathit{\Psi}} = \mathbf{p}^\delta_{\mathit{\Psi}}. \tag{2.3}$$

This constraint equation leads to the synthesized representation of a mistuned system:

$$\left[-\omega^2\boldsymbol{\mu}^{syn} + (1+j\gamma)\boldsymbol{\kappa}^{syn}\right]\mathbf{p}^{syn} = \left[\boldsymbol{\Phi}^S\boldsymbol{\Psi}^S\right]^T\mathbf{f}, \tag{2.4}$$

where

$$\boldsymbol{\mu}^{syn} = \boldsymbol{\mu}^S + \begin{bmatrix} \boldsymbol{\Phi}^{S\,T}_{\mathit{\Gamma}}\mathbf{M}^\delta\boldsymbol{\Phi}^S_{\mathit{\Gamma}} & \boldsymbol{\Phi}^{S\,T}_{\mathit{\Gamma}}\mathbf{M}^\delta\boldsymbol{\Psi}^S_{\mathit{\Gamma}} \\ \boldsymbol{\Psi}^{S\,T}_{\mathit{\Gamma}}\mathbf{M}^\delta\boldsymbol{\Phi}^S_{\mathit{\Gamma}} & \boldsymbol{\Psi}^{S\,T}_{\mathit{\Gamma}}\mathbf{M}^\delta\boldsymbol{\Psi}^S_{\mathit{\Gamma}} \end{bmatrix} \tag{2.5a}$$

$$\boldsymbol{\kappa}^{syn} = \boldsymbol{\kappa}^S + \begin{bmatrix} \boldsymbol{\Phi}^{S\,T}_{\mathit{\Gamma}}\mathbf{K}^\delta\boldsymbol{\Phi}^S_{\mathit{\Gamma}} & \boldsymbol{\Phi}^{S\,T}_{\mathit{\Gamma}}\mathbf{K}^\delta\boldsymbol{\Psi}^S_{\mathit{\Gamma}} \\ \boldsymbol{\Psi}^{S\,T}_{\mathit{\Gamma}}\mathbf{K}^\delta\boldsymbol{\Phi}^S_{\mathit{\Gamma}} & \boldsymbol{\Psi}^{S\,T}_{\mathit{\Gamma}}\mathbf{K}^\delta\boldsymbol{\Psi}^S_{\mathit{\Gamma}} \end{bmatrix} \tag{2.5b}$$

$$\mathbf{p}^{syn} = \begin{Bmatrix} \mathbf{p}^S_{\mathit{\Phi}} \\ \mathbf{p}^S_{\mathit{\Psi}} \end{Bmatrix}. \tag{2.5c}$$

As indicated in Eq. (2.5), the mistuned system is described only with the normal modes and the attachment modes of the corresponding tuned system. Since no assumption has been made about mistuning in deriving this reduced-order model, the formulation is entirely general and applicable to any kind of mistuned system. The only restriction is that the number of DOF in a mistuned part must be the same as that in the corresponding part of the tuned system. The number of attachment modes required is the same as the number of DOF of the mistuning components. Although the number of attachment modes may be large (i.e., the number of blade DOF), the attachment modes can be calculated easily and they improve the convergence rate of the natural frequencies and mode shapes of the ROM as the number of tuned-system normal modes increases, as will be discussed in section 2.4. Therefore, an accurate ROM of a reasonable size can be achieved in a systematic manner for arbitrary mistuning by using this general formulation.

2.3 Small Mistuning Case: Component Mode Mistuning Method

In this section, the general ROM developed above is simplified by assuming that blade mistuning is small compared to nominal properties in the modal domain, i.e., $|(\kappa_{ij}^{syn} - \kappa_{ij}^{S})/\kappa_{ij}^{S}| \ll 1$. Because the simplified ROM employs mistuning in component modal coordinates of a tuned cantilevered blade, this new method for small mistuning is called Component Mode Mistuning (CMM).

2.3.1 Approximation for Small Mistuning

Recently, Yang and Griffin reported on modal interaction [42] and applied the results to the modeling of mistuned bladed disks [23]. The main idea for their method is that, when a tuned bladed disk has normal modes closely spaced in a frequency range, a slightly mistuned bladed disk also features closely spaced modes in the same range, and thus the mistuned normal modes can be expressed using a subset of the tuned normal modes. This means that the tuned normal modes outside of the frequency range of interest, or any static modes, can be ignored in modeling a mistuned system with small mistuning.

Using this approach, if $\mathbf{\Psi}^S$ and the corresponding modal coordinates, $\mathbf{p}^S_{\mathit{\Psi}}$, are ignored in Eq. (2.5), then the synthesized representation becomes

$$\boldsymbol{\mu}^{syn} = \left[\mathbf{I} + {\mathbf{\Phi}^S_{\mathit{\Gamma}}}^T \mathbf{M}^\delta \mathbf{\Phi}^S_{\mathit{\Gamma}}\right] \tag{2.6a}$$

$$\boldsymbol{\kappa}^{syn} = \left[\mathbf{\Lambda}^S + {\mathbf{\Phi}^S_{\mathit{\Gamma}}}^T \mathbf{K}^\delta \mathbf{\Phi}^S_{\mathit{\Gamma}}\right] \tag{2.6b}$$

$$\mathbf{p}^{syn} = \left\{\mathbf{p}^S_{\mathit{\Phi}}\right\}. \tag{2.6c}$$

In general, a bladed disk features sets of blade-dominated modes grouped into narrow frequency bands, and the number of normal modes in each band is on the order of the number of blades. Therefore, Eq. (2.6) provides an accurate representation of a small-mistuned bladed disk in a frequency range of interest with matrices of order N.

It can be observed in Eq. (2.6) that the mass and stiffness deviation matrices in physical coordinates are projected to the blade portion of the tuned-system normal modes (in this study, mistuning is limited to the blades). Hence, the reduced mass and stiffness matrices can be obtained only if $\mathbf{M}^\delta$ and $\mathbf{K}^\delta$ are either known or at least estimated so that they match the mass and stiffness characteristics of the actual blades in a certain frequency range. However, such estimation becomes impractical when $\mathbf{M}^\delta$ and $\mathbf{K}^\delta$ are not proportional to the corresponding tuned matrices, which is the case when each blade mode family features a different mistuning pattern.

2.3.2 Component Mode Mistuning Projection

Bladh *et al.* [18] introduced a mistuning projection method, where the stiffness mistuning matrices in physical coordinates are projected to the normal modes of a tuned blade cantilevered at its root. The projection gives the diagonal matrix of modal stiffness deviations with the assumption that the tuned and mistuned blade-alone mode shapes are the same. With this approach, non-proportional blade mistuning can be implemented efficiently using the modal stiffness deviations, without requiring the estimation of $\mathbf{K}^\delta$. However, since the ROM was generated by substructuring a rotor into a disk and blades, the model size was larger than that of Yang and Griffin's model [23], which is on the order of the number of blades.

In this section, the blade portion of the tuned-system normal modes in Eq. (2.6) is represented by the modal participation factors of the component modes of a tuned cantilevered blade, and the mistuning projection method of Bladh *et al.*'s is employed without substructuring. Furthermore, it is shown that, even when the mistuning projection matrices are not diagonal, using only the diagonal terms is a good approximation as long as the motion of a blade in a mistuned system is dominated by one mode of a tuned cantilevered blade.

To carry out this projection, the modal participation factors first need to be obtained to represent the blade motion in tuned-system modes. If only cantilevered-blade normal modes are used to describe the blade motion, then the displacements at the boundaries (e.g., blade-disk boundary, shroud-to-shroud boundary) cannot be captured. Therefore, additional modes are required to describe motion at the boundary. However, since it is not feasible to measure these additional boundary modes, the proposed approach is to determine them by minimizing their contribution to the mistuning projection, which is eventually ignored for small boundary displacements.

Here, the additional mode set is introduced in the following form:

$$\begin{bmatrix} \boldsymbol{\Psi}_o^B \\ \mathbf{I} \end{bmatrix},$$

where $\boldsymbol{\Psi}_o^B$, which is not yet determined, corresponds to the interior DOF of a cantilevered blade, and $\mathbf{I}$ corresponds to the boundary DOF that are fixed in the cantilevered blade. The number of modes in this set is the number of boundary DOF so that any boundary motion can be described. Since mistuning may be random, the nominal mass and stiffness matrices of a blade, $\mathbf{M}_o^B$, $\mathbf{K}_o^B$, are used in minimizing the contribution of the boundary modes. Then, the mass and stiffness projections to the boundary modes become

$$\boldsymbol{\mu}_{\psi\psi}^B = \begin{bmatrix} \boldsymbol{\Psi}_o^B \\ \mathbf{I} \end{bmatrix}^T \begin{bmatrix} \mathbf{M}_{ii,o}^B & \mathbf{M}_{ib,o}^B \\ \mathbf{M}_{ib,o}^{B\ T} & \mathbf{M}_{bb,o}^B \end{bmatrix} \begin{bmatrix} \boldsymbol{\Psi}_o^B \\ \mathbf{I} \end{bmatrix} \tag{2.7a}$$

$$\boldsymbol{\kappa}_{\psi\psi}^B = \begin{bmatrix} \boldsymbol{\Psi}_o^B \\ \mathbf{I} \end{bmatrix}^T \begin{bmatrix} \mathbf{K}_{ii,o}^B & \mathbf{K}_{ib,o}^B \\ \mathbf{K}_{ib,o}^{B\ T} & \mathbf{K}_{bb,o}^B \end{bmatrix} \begin{bmatrix} \boldsymbol{\Psi}_o^B \\ \mathbf{I} \end{bmatrix}, \tag{2.7b}$$

where the subscripts b and i denote the boundary and interior DOF of a cantilevered-blade, respectively.

Now, by taking the first variation of $\boldsymbol{\mu}_{\psi\psi}^B$ and $\boldsymbol{\kappa}_{\psi\psi}^B$ in $\boldsymbol{\Psi}_o^B$, the boundary mode contributions to the mass and stiffness projections are minimized, and $\boldsymbol{\Psi}_o^{B,m}$ and $\boldsymbol{\Psi}_o^{B,k}$ corresponding to the mass and stiffness projection can be obtained from the following equations:

$$\mathbf{M}_{ii,o}^B \boldsymbol{\Psi}_o^{B,m} + \mathbf{M}_{ib,o}^B = 0 \tag{2.8a}$$

$$\mathbf{K}_{ii,o}^B \boldsymbol{\Psi}_o^{B,k} + \mathbf{K}_{ib,o}^B = 0. \tag{2.8b}$$

Here, it should be noted that $\boldsymbol{\Psi}_o^{B,k}$ is the set of Craig-Bampton constraint modes of a cantilevered blade [41].

Now, the motion of the nth blade in the tuned-system modes is described by cantilevered-blade normal modes and boundary modes as follows:

$$\boldsymbol{\Phi}_{\Gamma,n}^S = \begin{cases} \begin{bmatrix} \boldsymbol{\Phi}_o^B & \boldsymbol{\Psi}_o^{B,m} \\ \mathbf{0} & \mathbf{I} \end{bmatrix} \begin{bmatrix} \mathbf{q}_{\phi,n}^m \\ \mathbf{q}_{\psi,n} \end{bmatrix} & \text{for mass mistuning,} \\ \text{or} & \\ \begin{bmatrix} \boldsymbol{\Phi}_o^B & \boldsymbol{\Psi}_o^{B,k} \\ \mathbf{0} & \mathbf{I} \end{bmatrix} \begin{bmatrix} \mathbf{q}_{\phi,n}^k \\ \mathbf{q}_{\psi,n} \end{bmatrix} & \text{for stiffness mistuning.} \end{cases} \tag{2.9}$$

Therefore, the blade portion of the tuned-system modes can be expressed as:

$$\mathbf{\Phi}_{\Gamma}^{S} = \begin{cases} \left(\mathbf{I} \otimes \mathbf{U}^{m}\right) \mathbf{q}^{m}, \\ \\ \quad \text{or} \\ \\ \left(\mathbf{I} \otimes \mathbf{U}^{k}\right) \mathbf{q}^{k}, \end{cases} \tag{2.10}$$

where

$$\mathbf{U}^{m} = \begin{bmatrix} \mathbf{\Phi}_{o}^{B} & \mathbf{\Psi}_{o}^{B,m} \\ \\ \mathbf{0} & \mathbf{I} \end{bmatrix} \quad \mathbf{U}^{k} = \begin{bmatrix} \mathbf{\Phi}_{o}^{B} & \mathbf{\Psi}_{o}^{B,k} \\ \\ \mathbf{0} & \mathbf{I} \end{bmatrix}$$

$$\mathbf{q}^{m} = \begin{bmatrix} \vdots \\ \\ \mathbf{q}_{\phi,n}^{m} \\ \\ \mathbf{q}_{\psi,n} \\ \vdots \end{bmatrix} \qquad \mathbf{q}^{k} = \begin{bmatrix} \vdots \\ \\ \mathbf{q}_{\phi,n}^{k} \\ \\ \mathbf{q}_{\psi,n} \\ \vdots \end{bmatrix},$$

and $\otimes$ denotes the Kronecker product. Note that since $\mathbf{\Psi}_{o}^{B,m}$ and $\mathbf{\Psi}_{o}^{B,k}$ are different, $\mathbf{q}_{\phi,n}^{m}$ and $\mathbf{q}_{\phi,n}^{k}$ are also different. The modal participation factors can be easily calculated because a tuned system is a structure with cyclic symmetry (see Appendix A). In most cases, only a few normal mode participation factors per blade (usually, just one for unshrouded rotors) are dominant, because the blade motion in a tuned-system normal mode tends to be well correlated to that of a cantilevered-blade normal mode (this will be discussed further in section 2.5). Therefore, a few dominant modes are sufficient for the normal mode set, $\mathbf{\Phi}_{o}^{B}$.

Inserting Eq. (2.10) into Eq. (2.6), the reduced mass and stiffness matrices become

$$\begin{aligned}
\boldsymbol{\mu}^{syn} &= \mathbf{I} + \mathbf{q}^{mT}\left(\mathbf{I}\otimes\mathbf{U}^{mT}\right)\mathbf{M}^{\delta}\left(\mathbf{I}\otimes\mathbf{U}^{m}\right)\mathbf{q}^{m} \\
&= \mathbf{I} + \sum_{n=1}^{N}\mathbf{q}_n^{mT}\mathbf{U}^{mT}\mathbf{M}_n^{\delta}\mathbf{U}^{m}\mathbf{q}_n^{m} \\
&= \mathbf{I} + \sum_{n=1}^{N}\mathbf{q}_n^{mT}\begin{bmatrix}\boldsymbol{\mu}^{\delta}_{\phi\phi,n} & \boldsymbol{\mu}^{\delta}_{\phi\psi,n}\\ \boldsymbol{\mu}^{\delta}_{\phi\psi,n}{}^{T} & \boldsymbol{\mu}^{\delta}_{\psi\psi,n}\end{bmatrix}\mathbf{q}_n^{m}
\end{aligned} \tag{2.11a}$$

$$\begin{aligned}
\boldsymbol{\kappa}^{syn} &= \boldsymbol{\Lambda}^{S} + \mathbf{q}^{kT}\left(\mathbf{I}\otimes\mathbf{U}^{kT}\right)\mathbf{K}^{\delta}\left(\mathbf{I}\otimes\mathbf{U}^{k}\right)\mathbf{q}^{k} \\
&= \boldsymbol{\Lambda}^{S} + \sum_{n=1}^{N}\mathbf{q}_n^{kT}\mathbf{U}^{kT}\mathbf{K}_n^{\delta}\mathbf{U}^{k}\mathbf{q}^{k} \\
&= \boldsymbol{\Lambda}^{S} + \sum_{n=1}^{N}\mathbf{q}_n^{kT}\begin{bmatrix}\boldsymbol{\kappa}^{\delta}_{\phi\phi,n} & \boldsymbol{\kappa}^{\delta}_{\phi\psi,n}\\ \boldsymbol{\kappa}^{\delta}_{\phi\psi,n}{}^{T} & \boldsymbol{\kappa}^{\delta}_{\psi\psi,n}\end{bmatrix}\mathbf{q}^{k},
\end{aligned} \tag{2.11b}$$

where

$$\begin{aligned}
\boldsymbol{\mu}^{\delta}_{\phi\phi,n} &= \boldsymbol{\Phi}_o^{B^T}\mathbf{M}^{\delta}_{ii,n}\boldsymbol{\Phi}_o^{B} \\
\boldsymbol{\mu}^{\delta}_{\phi\psi,n} &= \boldsymbol{\Phi}_o^{B^T}\left[\mathbf{M}^{\delta}_{ii,n}\boldsymbol{\Psi}_o^{B,m} + \mathbf{M}^{\delta}_{ib,n}\right] \\
\boldsymbol{\mu}^{\delta}_{\psi\psi,n} &= \boldsymbol{\Psi}_o^{B,m^T}\left[\mathbf{M}^{\delta}_{ii,n}\boldsymbol{\Psi}_o^{B,m} + \mathbf{M}^{\delta}_{ib,n}\right] + \mathbf{M}^{\delta}_{ib,n}{}^{T}\boldsymbol{\Psi}_o^{B,m} + \mathbf{M}^{\delta}_{bb,n} \\
\boldsymbol{\kappa}^{\delta}_{\phi\phi,n} &= \boldsymbol{\Phi}_o^{B^T}\mathbf{K}^{\delta}_{ii,n}\boldsymbol{\Phi}_o^{B} \\
\boldsymbol{\kappa}^{\delta}_{\phi\psi,n} &= \boldsymbol{\Phi}_o^{B^T}\left[\mathbf{K}^{\delta}_{ii,n}\boldsymbol{\Psi}_o^{B,k} + \mathbf{K}^{\delta}_{ib,n}\right] \\
\boldsymbol{\kappa}^{\delta}_{\psi\psi,n} &= \boldsymbol{\Psi}_o^{B,k^T}\left[\mathbf{K}^{\delta}_{ii,n}\boldsymbol{\Psi}_o^{B,k} + \mathbf{K}^{\delta}_{ib,n}\right] + \mathbf{K}^{\delta}_{ib,n}{}^{T}\boldsymbol{\Psi}_o^{B,k} + \mathbf{K}^{\delta}_{bb,n}.
\end{aligned}$$

Since $\mathbf{M}_n^{\delta}$ and $\mathbf{K}_n^{\delta}$ are not necessarily proportional to the nominal matrices, $\mathbf{U}^{mT}\mathbf{M}_n^{\delta}\mathbf{U}^{m}$ and $\mathbf{U}^{k^T}\mathbf{K}_n^{\delta}\mathbf{U}^{k}$ are full matrices, as shown in Eq. (2.11).

Equation (2.11) can be used for any small-mistuned bladed disk, but it still requires to know the mistuning values for the boundary modes. These cannot be readily measured, but they can be computed in the few cases the mistuning distribution within the blades is known (e.g., if one assumes proportional mistuning). Now, suppose that the displacements at the blade structural boundaries in the tuned-system normal modes are very small, so that the contribution of the boundary modes to the mistuning projection is negligible. This is the usual case for unshrouded rotors. Then, the dominant cantilevered-blade normal modes are sufficient to project mistuning without losing accuracy. In this case, the partitions pertaining to the boundary modes can be ignored and the reduced mass and stiffness matrices can be approximated as:

$$\boldsymbol{\mu}^{syn} \approx \mathbf{I} + \sum_{n=1}^{N} \mathbf{q}_{\phi,n}^{m\ T} \boldsymbol{\mu}_{\phi\phi,n}^{\delta} \mathbf{q}_{\phi,n}^{m} \tag{2.12a}$$

$$\boldsymbol{\kappa}^{syn} \approx \boldsymbol{\Lambda}^{S} + \sum_{n=1}^{N} \mathbf{q}_{\phi,n}^{k\ T} \boldsymbol{\kappa}_{\phi\phi,n}^{\delta} \mathbf{q}_{\phi,n}^{k}. \tag{2.12b}$$

Note that $\boldsymbol{\mu}_{\phi\phi,n}^{\delta}$ and $\boldsymbol{\kappa}_{\phi\phi,n}^{\delta}$ still have off-diagonal terms if the mistuned mass and stiffness matrices are not proportional to the nominal matrices. However, each column of $\mathbf{q}_{\phi,n}^{m}$ and $\mathbf{q}_{\phi,n}^{k}$ is usually dominated by one modal participation factor, and the motion of each blade in a system with small mistuning is usually dominated by one mode of a tuned cantilevered blade. In this case, the off-diagonal terms of $\boldsymbol{\mu}_{\phi\phi,n}^{\delta}$ and $\boldsymbol{\kappa}_{\phi\phi,n}^{\delta}$, which represent the coupling between cantilevered-blade modes due to mistuning, can be neglected. Therefore, Eq. (2.12) can be even more simplified as follows:

$$\boldsymbol{\mu}^{syn} \approx \mathbf{I} + \sum_{n=1}^{N} \mathbf{q}_{\phi,n}^{m\ T} \underset{r \in \boldsymbol{R}}{\mathbf{diag}} \left(\mu_{\phi\phi,n,r}^{\delta} \right) \mathbf{q}_{\phi,n}^{m} \tag{2.13a}$$

$$\boldsymbol{\kappa}^{syn} \approx \boldsymbol{\Lambda}^{S} + \sum_{n=1}^{N} \mathbf{q}_{\phi,n}^{k\ T} \underset{r \in \boldsymbol{R}}{\mathbf{diag}} \left(\kappa_{\phi\phi,n,r}^{\delta} \right) \mathbf{q}_{\phi,n}^{k}, \tag{2.13b}$$

where

$$\mu_{\phi\phi,n,r}^{\delta} = \boldsymbol{\Phi}_{r,o}^{B\ T} \mathbf{M}_{ii,n}^{\delta} \boldsymbol{\Phi}_{r,o}^{B}$$

$$\kappa_{\phi\phi,n,r}^{\delta} = \boldsymbol{\Phi}_{r,o}^{B\ T} \mathbf{K}_{ii,n}^{\delta} \boldsymbol{\Phi}_{r,o}^{B},$$

and R is a set of retained cantilevered-blade normal mode numbers. In this equation, the required number of the modal mistuning values per blade is the number of the retained cantilevered-blade normal modes.

Next, the calculation of the modal mistuning matrices, $\boldsymbol{\mu}^{\delta}_{\phi\phi,n}$ and $\boldsymbol{\kappa}^{\delta}_{\phi\phi,n}$, and their diagonal terms are discussed. Assuming that the mode shapes of the actual (i.e., mistuned) nth cantilevered blade have been measured or computed, the tuned-cantilevered-blade normal modes can be expressed as linear combinations of the mistuned-cantilevered-blade normal modes as follows:

$$\mathbf{\Phi}^{B}_{o} = \mathbf{\Phi}^{B}_{n}\mathbf{v}_{n}, \tag{2.14}$$

where $\mathbf{v}_n$ is a matrix consisting of the modal participation factors.

The mode orthogonality with respect to the mass and stiffness matrices for the mistuned cantilevered blade is written as follows:

$$\mathbf{I} = \mathbf{\Phi}^{B^T}_{n}\left(\mathrm{M}^{B}_{ii,o} + \mathrm{M}^{\delta}_{ii,n}\right)\mathbf{\Phi}^{B}_{n} \tag{2.15a}$$

$$\mathbf{\Lambda}^{B}_{n} = \mathbf{\Phi}^{B^T}_{n}\left(\mathbf{K}^{B}_{ii,o} + \mathbf{K}^{\delta}_{ii,n}\right)\mathbf{\Phi}^{B}_{n}. \tag{2.15b}$$

Pre-multiplying by ${\mathbf{v}_n}^T$, post-multiplying by $\mathbf{v}_n$, and using Eq. (2.14),

$${\mathbf{v}_n}^T\mathbf{v}_n = \mathbf{\Phi}^{B^T}_{o}\left(\mathrm{M}^{B}_{ii,o} + \mathrm{M}^{\delta}_{ii,n}\right)\mathbf{\Phi}^{B}_{o} = \mathbf{I} + \boldsymbol{\mu}^{\delta}_{\phi\phi,n} \tag{2.16a}$$

$${\mathbf{v}_n}^T\mathbf{\Lambda}^{B}_{n}\mathbf{v}_n = \mathbf{\Phi}^{B^T}_{o}\left(\mathbf{K}^{B}_{ii,o} + \mathbf{K}^{\delta}_{ii,n}\right)\mathbf{\Phi}^{B}_{o} = \mathbf{\Lambda}^{B}_{o} + \boldsymbol{\kappa}^{\delta}_{\phi\phi,n}. \tag{2.16b}$$

Therefore,

$$\boldsymbol{\mu}^{\delta}_{\phi\phi,n} = {\mathbf{v}_n}^T\mathbf{v}_n - \mathbf{I} \tag{2.17a}$$

$$\boldsymbol{\kappa}^{\delta}_{\phi\phi,n} = {\mathbf{v}_n}^T\mathbf{\Lambda}^{B}_{n}\mathbf{v}_n - \mathbf{\Lambda}^{B}_{o}. \tag{2.17b}$$

The rth diagonal terms of the above mistuning matrices are

$$\boldsymbol{\mu}^{\delta}_{\phi\phi,n,r} = {\mathbf{v}_{r,n}}^T\mathbf{v}_{r,n} - 1 \tag{2.18a}$$

$$\boldsymbol{\kappa}^{\delta}_{\phi\phi,n,r} = {\mathbf{v}_{r,n}}^T\mathbf{\Lambda}^{B}_{n}\mathbf{v}_{r,n} - \lambda^{B}_{r,o}, \tag{2.18b}$$

where $\mathbf{v}_{r,n}$ is the rth column of $\mathbf{v}_n$, and $\lambda_{r,o}$ is the rth element of $\boldsymbol{\Lambda}_o^B$. Since $\mathbf{v}_{r,n}$ is dominated by the factor of the rth mistuned mode, $v_{rr,n}$, for small mistuning cases, the diagonal terms can be approximated as:

$$\boldsymbol{\mu}^{\delta}_{\phi\phi,n,r} \approx v^2_{rr,n} - 1 \tag{2.19a}$$

$$\boldsymbol{\kappa}^{\delta}_{\phi\phi,n,r} \approx \lambda^B_{r,n} v^2_{rr,n} - \lambda^B_{r,o}. \tag{2.19b}$$

If only the eigenvalues (or natural frequencies) of the mistuned cantilevered blades are known, then the mass and stiffness mistuning cannot be obtained from the above equation. However, if only stiffness mistuning is assumed, an equivalent stiffness mistuning value, $\boldsymbol{\kappa}^{\delta}_{\phi\phi,n,r}$, can be computed. Since no mass mistuning is assumed, $\boldsymbol{\mu}^{\delta}_{\phi\phi,n,r} = 0$, and $v^2_{rr,n} \approx 1$. Then, the equivalent stiffness mistuning value becomes

$$\boldsymbol{\kappa}^{\delta}_{\phi\phi,n,r} \approx \lambda^B_{r,n} - \lambda^B_{r,o}. \tag{2.20}$$

Note that this eigenvalue mistuning was employed in the study by Bladh *et al.* [18].

Typically, unsteady aerodynamic coefficients are obtained using aerodynamic codes based on a set of cantilevered-blade normal modes in a cyclic assembly (i.e., a cascade) using a complex cyclic coordinate transformation [43]. Therefore, using the cantilevered-blade mode participation factors computed for the mistuning projection in the CMM method, aerodynamic coefficients can also be projected to the normal modes of the tuned system.

Eventually, the equation of motion for a small-mistuned system with aerodynamic coupling can be expressed as

$$\left[-\omega^2 \left(\boldsymbol{\mu}^{syn} + \boldsymbol{\mu}^a\right) + j\omega\mathbf{c}^a + (1 + j\gamma)\,\boldsymbol{\kappa}^{syn} + \boldsymbol{\kappa}^a\right]\mathbf{p}^S_{\Phi} = \boldsymbol{\Phi}^{S^T}\mathbf{f}, \tag{2.21}$$

where $\boldsymbol{\mu}^a$, $\boldsymbol{\kappa}^a$, and $\mathbf{c}^a$ are the aerodynamic coupling mass, stiffness, and damping matrices in modal coordinates of tuned-system normal modes.

2.4 Large Mistuning Case Study: Rogue Blade

The industrial bladed disk depicted in Fig. 2.1 is used in this study. This integral bladed disk (blisk) has 29 blades, and forms the second stage of a four-drum compressor used in an advanced gas turbine application. The rotor model is clamped at the ribs located at the outer edges of the disk, which is a rough approximation of boundary conditions due to neighboring stages. The finite element model is constructed with standard linear brick elements (eight-noded solids), and it has 126,846 DOF.

Figure 2.2 displays the free vibration natural frequencies of the tuned bladed disk versus the number of nodal diameters. The natural frequencies and mode shapes were obtained via cyclic symmetry using a finite element model of a single sector. The blade-dominated mode families are characterized on the right-hand side of the horizontal lines in Fig. 2.2, where F denotes a flexural bending mode, T a torsion mode, S a stripe mode, and R denotes elongation in the radial direction. The frequencies frequently mentioned in this paper are marked by dotted horizontal lines with the corresponding frequency on the right side.

In this large mistuning case study, a single “rogue blade” is considered to have large mistuning, with all other blades being tuned. Mistuning is introduced by changing the rogue blade geometry significantly, as depicted in Fig. 2.3. It is assumed that the mass density and Young’s modulus are not changed. Therefore, $\mathbf{M}^{\delta}$ and $\mathbf{K}^{\delta}$, which are needed to build the large mistuning ROM, can be obtained from the rogue blade geometry. The ROM can be constructed using a single-sector finite element model, since the attachment modes corresponding to all the rogue blade DOF are obtained from a cyclic symmetry analysis of a single sector.

The size of the resulting reduced-order model is determined by the number of tuned-system normal modes in a truncated set plus the number of attachment modes. In this case study, a ROM is constructed in the frequency range 32–36 kHz (which includes 3T and 2S modes), and the results are compared with those of the finite element model of the complete mistuned bladed disk. At the least, the tuned-system normal modes in the frequency range of interest must be retained, and the attachment modes for all the nodes in the rogue blade are also included. Therefore, the reduced-order model has at least 66 (tuned normal modes in 32–36 kHz) + 2,496 (attachment modes) DOF. Although this size is much greater than that of a ROM for small mistuning, it is still much smaller than that of the 126,846-DOF parent FEM. Furthermore, once a modal analysis is performed for the reduced-order model, 66 normal modes of the mistuned bladed disk may be sufficient to compute the forced response in the range 32–36 kHz.

To validate the ROM, the convergence of the ROM natural frequencies toward the FEM results is tested by increasing the number of tuned-system normal modes. Also, the forced response calculated with the ROM is compared to the FEM results. Figure 2.4 shows the average natural frequency error versus the number of tuned-system normal modes. The tested frequency ranges for the tuned-system normal mode basis are 32–36 kHz, 26–43 kHz, and 22–45 kHz, and the 66 estimated mistuned natural frequencies that exist between 32 and 36 kHz are chosen for comparison with the FEM results. As can be seen in Fig. 2.4, the estimated natural frequencies converge toward the FEM results as the number of tuned-system normal modes increases. Also, note the very small average error, less than 0.02 %, even when the smallest ROM is considered.

Next, the forced response is investigated. From Fig. 2.4, it is clear that 136 tuned normal modes in the range 26–43 kHz and the attachment modes are sufficient to describe the behavior of the mistuned system in the range 32–36 kHz, and this ROM is used to compute the forced response. The structural damping coefficient of 0.006 is used. A unit force normal to the blade surface is applied to one of the nodes at the tip of each blade (see Fig. 2.3), and engine order 1 and 5 excitations are considered. Euclidean displacement norms for each blade are computed, and the maximum response amplitude of any blade is found at each sampled excitation frequency, so as to provide an envelope of the blade amplitudes. The ROM results are shown and compared with FEM results in Fig. 2.5. As can be seen, excellent agreement is obtained, thus providing further validation of the ROM's accuracy.

In Fig. 2.5, note that an additional resonance appears around 34.3 kHz in the response of the mistuned system with the rogue blade, and that this peak is larger than the two resonant peaks for the tuned bladed disk. Hence the presence of a single rogue blade can significantly alter the forced response, and this effect is accurately captured by the ROM. The other two resonant frequencies of the rogue blade system are almost the same as those of the tuned system, and the peak amplitudes are similar. In the case of engine order 1 excitation, the first main peak corresponds to the 30th mode of the 66 mistuned modes in the 32–36 kHz range, the second peak corresponds to the 36th mode, and the third peak corresponds to the 66th mode. In the case of engine order 5 excitation, the three largest peaks correspond to the 4th, 36th, and 41st modes. These mistuned modes are depicted in Fig. 2.6 (the displacement of a node at the tip of each blade is shown). The 30th and 66th modes are nearly sinusoidal waves of harmonic 1 in terms of the blade number, and the 4th and 41st modes are nearly sinusoidal waves of harmonic 5. However, the 36th mode is highly localized to blade 1, which is the rogue blade. Obviously, the largest forced response peak around 34.3 kHz for the rogue blade system is caused by this localization.

2.5 Small Mistuning Case Study

The CMM technique is validated using again the industrial bladed disk in Fig. 2.1. To build a CMM-based reduced-order model, two tuned finite element models are required, as depicted in Fig. 2.7:

1. A single-sector model from which the normal modes of the tuned system are obtained via cyclic symmetry analysis (Commercial FEA software packages, such as MSC/NASTRAN, have cyclic symmetry routines). There are 4,374 DOF per sector in the finite element model.

2. A blade-alone model from which the cantilevered-blade normal modes and the static boundary modes are obtained. This model has a total of 2,496 DOF, and there are 96 DOF at the interface between the blade and the disk.

The tuned-system normal modes were obtained from the single-sector model. Figure 2.2 shows the occurrence of numerous natural frequency veering regions. Earlier studies[16, 39] have shown that large increases in the mistuned forced response, relative to the tuned response, are likely to occur in veering regions. Therefore, the ability of CMM models to capture the mistuned response in veering regions was tested, and two such regions were investigated: region 1 is located at three nodal diameters, around 28 kHz, and region 2 is located at five nodal diameters, around 34 kHz, as labeled in Fig. 2.2.

For the rotor studied, displacements at the blade root are very small compared to those at the blade's interior, such that the contribution to the mistuning projection of the boundary modes defined at the blade-disk boundary can be neglected. Hence the normal mode mistuning projection used in Eq. (2.12) or (2.13) is sufficient to construct a mistuned ROM. Although the CMM method can handle many types of small blade mistuning, here for simplicity mistuning is introduced as slight variations in the Young's modulus of the blades.

That is, only stiffness mistuning is considered, and two cases are investigated: a case of a proportional change in the blade stiffness, and a case of a non-proportional change.

2.5.1 Proportional Mistuning

The mistuned Young's modulus for blade n, E_n, is

$$E_n = E_o(1 + \delta_n^E),$$

where E_o is the nominal Young's modulus value. δ_n^E is a non-dimensional mistuning value for the Young's modulus of the nth blade, and uniform within a blade for the proportional mistuning case. Hence the natural frequencies of all the cantilevered-blade normal modes are mistuned by the same percentage and the mode shapes remain unchanged.

In this case, there are no off-diagonal terms in $\boldsymbol{\kappa}_{\phi\phi,n}^{\delta}$, and only the eigenvalues of the cantilevered blades are mistuned. Hence, Eq.(2.13) is appropriate for implementing mistuning and $\boldsymbol{\kappa}_{\phi\phi,n}^{\delta}$ becomes exactly $\delta_n^E \boldsymbol{\Lambda}_o^B$. A dimensionless eigenvalue mistuning parameter, $\delta_{r,n}^e$, is introduced as

$$\delta_{r,n}^e = \frac{{\omega_{r,n}}^2 - {\omega_{r,o}}^2}{{\omega_{r,o}}^2},$$

where $\omega_{r,n}$ is the rth natural frequency of the nth blade and $\omega_{r,o}$ is the rth natural frequency of a tuned blade. For proportional stiffness mistuning, $\delta_{r,n}^e$ is equal to δ_n^E for any mode r, and the eigenvalue mistuning pattern is the same for all blade modes. The specific pattern used to obtain the FEM and CMM results is shown in Table 2.1.

The CMM model is constructed by selecting a set of tuned-system normal modes to capture mistuned-system normal modes, and a set of cantilevered-blade normal modes to describe the blade motion in the tuned-system normal modes. Since the modal density is high in the investigated veering regions in Fig. 2.2, a narrow frequency band can be selected for the tuned-system mode basis. For example, 26–29 kHz can be chosen for veering region 1. The selection of cantilevered-blade modes depends on the tuned-system modes chosen for a basis. Namely, modal participation factors for the tuned-system modes in cyclic coordinates need to be calculated using a sufficient number of cantilevered-blade modes (see Eq. 2.10 and Appendix), and the dominant cantilevered-blade modes can be determined from inspection of these factors.

Here $\kappa^{\delta}_{\phi\phi,n,r} = \delta^{e}_{r,n}{\omega_{r,o}}^2$, and it is pre- and post-multiplied by the corresponding modal participation factors in the mistuning projection. Hence if the levels of random mistuning are on the same order for any mode r, the modal participation factors weighted by the corresponding cantilevered-blade natural frequencies are meaningful in determining what are the dominant cantilevered-blade modes. Figure 2.8 shows the weighted average modal participation factors, which are defined as

$$\bar{q}^{k}_{\phi,r} = \frac{\omega_{r,o} \sum\limits_{h=0}^{H} \sum\limits_{l=1}^{N_h} |\tilde{q}^{k}_{\phi,h,r,l}|}{\sum\limits_{h=0}^{H} N_h}, \tag{2.22}$$

where N_h is the number of the retained tuned-system normal modes corresponding to harmonic h, when the lowest 30 cantilevered-blade modes are used to describe the blade motion in the tuned modes in the ranges 26–29 kHz and 32–36 kHz.

It should be noted that the number of cantilevered-blade modes and corresponding mistuning patterns does not affect the size of the ROM, but it can affect its accuracy. Nevertheless, it is desirable to retain a small number of mistuning values, and the dominant cantilevered-blade modes required for accurate mistuning representation can be determined from Fig. 2.8. For instance, only the 7th cantilevered-blade mode is dominant for the range of 26–29 kHz, because the corresponding weighted-average modal participation factor is much greater than the others. For the same reason, the 8th and 9th modes are dominant for the frequency band of 32–36 kHz. This means that the eigenvalue mistuning patterns for the 7th mode and for the 8th and 9th modes are sufficient to predict the behavior of the mistuned system in the veering region 1 and 2, respectively.

Once a basis of tuned-system modes is selected and the dominant cantilevered-blade modes are identified for the mistuning projection, a ROM can be built using the CMM technique for the mistuning values in Table 2.1. Next, the results from the ROM are compared with the FEM ones.

The convergence of mistuned natural frequencies and mode assurance criterion (MAC) ratios are presented in Figs. 2.9 and 2.10 for two frequency bands: 26–29 kHz for region 1, and 32–36 kHz for region 2. Figure 2.9 shows the average error of the mistuned system natural frequencies estimated by the CMM model relative to the FEM natural frequencies, versus the number of retained cantilevered-blade modes. Figure 2.10 shows the average MAC ratio between the CMM and the FEM mistuned modes versus the number of retained cantilevered-blade modes. Since most tuned system normal modes in the range 26–29 kHz are dominated by the 7th cantilevered-blade mode, the frequency error and MAC ratio are significantly improved when the 7th mode is retained in the CMM model. Similarly, the frequency error and MAC ratio in the range 32–36 kHz show great improvement when the 8th and 9th cantilevered-blade modes are retained. These convergence trends could be predicted from Fig. 2.8.

The forced response to engine order excitation is considered in the two veering regions indicated in Fig. 2.2: engine order 3 excitation is applied in region 1, and engine order 5 and 24 excitations are applied in region 2. In both cases, the loads and the structural damping coefficient are the same as for the large mistuning study in section 2.4. The effect of aerodynamic coupling is not considered.

Figures 2.11 and 2.12 depict the tuned and mistuned forced responses in veering region 1. In Fig. 2.11, 34 tuned system modes (in the range 26–29 kHz) are used, while Fig. 2.12 is for 106 tuned system modes (in the range 22–34 kHz). In the case of 34 tuned modes, only the 7th cantilevered-blade mode is employed to project mistuning to the tuned system modes. In the case of 106 modes, the 6th, 7th, and 8th cantilevered-blade modes are used because these three modes are dominant in the range 22–34 kHz. Note that the largest resonant blade amplitude of the mistuned system is 2.24 times larger than that of the tuned system. In Fig. 2.11, there are slight differences between the FEM and CMM results for both the tuned and mistuned responses, although for this ROM the average natural frequency error is only 0.0075 % and the average MAC ratio is 99.8958 %. This difference can be explained by noting that the mistuned system modes obtained from the CMM model are in the range 26–29 kHz. Hence, the effects of modes outside this frequency range are not included, and the CMM and FEM results differ even for the tuned response, especially near the edges of the frequency band. As can be seen in Fig. 2.12, when a wider frequency band is chosen, the discrepancy between FEM and CMM results decreases. But, if one considers the peak amplitudes at resonant frequencies, the 34-DOF CMM model results match the FEM ones very closely.

Veering region 2 is more complicated because two close blade-dominated mode families are present in its frequency range. A set of 66 tuned system modes (32–36 kHz) is used for the CMM modeling, and the 8th (3T) and 9th (2S) cantilevered-blade modes are used for the mistuning projection. Figures 2.13 and 2.14 depict forced response results for engine order 5 and 24 excitations, respectively. Note the excellent matches between CMM and FEM results, indicating that the effects of modes outside the 32–36 kHz range are negligible. Also, since the only difference between engine order 5 and engine order 24 excitations for the 29-blade system is the sign of the phase angle of the forcing vector, the tuned forced response is the same in both cases. However, the mistuned forced responses differ for engine orders 5 and 24, and the amplification factors of the largest resonant amplitude are 1.51 and 1.34, respectively.

2.5.2 Non-proportional Mistuning

Here, non-proportional mistuning is considered, and $\boldsymbol{\kappa}^{\delta}_{\phi\phi,n}$ is a full matrix. However, as discussed in section 2.3, it is a good approximation to use only the diagonal terms of $\boldsymbol{\kappa}^{\delta}_{\phi\phi,n}$, which are approximately the eigenvalue mistuning values. Note that the mistuned blades feature different eigenvalue mistuning patterns for different cantilevered-blade modes. Therefore, the number of mistuning patterns required equals the number of cantilevered-blade modes used in the mistuning projection. Although the mode shapes of cantilevered blades are changed by this type of mistuning, Eq. (2.13) with only the diagonal mistuning values is employed again, as in the proportional mistuning case. The results are compared with those obtained using Eq. (2.12) with full mistuning matrices.

The non-proportional mistuning is introduced by using two different sets of Young's moduli for the FEM of the cantilevered blades. One ($\delta^{E}_{n,1}$) is for the lower left and upper right parts of blades and the other ($\delta^{E}_{n,2}$) is for the lower right and upper left parts of blades. The Young's modulus mistuning parameters are listed in Table 2.2, and Fig. 2.15 shows the resulting eigenvalue mistuning patterns for several cantilevered-blade modes.

As can be seen in Fig. 2.15, the eigenvalue mistuning patterns are slightly different from each other. Thus, inaccurate results might be obtained by choosing only one of these patterns, because the dynamic characteristics of a bladed disk can be very sensitive to mistuning. The solution is to utilize all the mistuning patterns that are available. If there is only one blade-dominated mode family in the frequency band selected for the tuned-system mode basis, as in the case of veering region 1, then a single mistuning pattern may be sufficient. However, if multiple blade-dominated mode families are close and they are included in a reduced-order model, as in the case of veering region 2, then every dominant cantilevered-blade mode should have its own mistuning pattern.

These observations are substantiated by investigating the forced response for excitations corresponding to veering regions 1 and 2. In region 1, a single eigenvalue mistuning pattern corresponding to the 7th cantilevered-blade mode has a dominant effect, as in the proportional mistuning case. For the CMM reduced-order model, 106 tuned-system normal modes (22–34 kHz) are retained. Figure 2.16 shows the forced response in veering region 1 by the FEM and the CMM model. In the CMM model, the eigenvalue mistuning patterns for the 1st through the 15th cantilevered-blade modes are set to be the same as that of the 7th mode, although they are actually different. As can be seen, the CMM results are in very good agreement with the FEM ones. This is because the mistuning pattern for the dominant cantilevered-blade mode is correct.

Figures 2.17 and 2.18 show forced response results in the 32–36 kHz range, obtained by four different ROMs and by the FEM. As mentioned earlier, there are two blade-dominated mode groups in this range. In all four cases, 136 tuned system normal modes (26–43 kHz) are used as a basis, but mistuning projections are performed differently. In Fig. 2.17 (a), the single mistuning pattern of the 8th cantilevered-blade mode is used, while in Fig. 2.17 (b), the single mistuning pattern of the 9th cantilevered-blade mode is used. For these single mistuning pattern cases, mistuning is projected to the lowest 15 cantilevered-blade modes. In Fig. 2.18 (a), the two mistuning patterns of the 8th and 9th cantilevered-blade mode are used to project the mistuning values to the corresponding cantilevered-blade modes, respectively. In Fig. 2.18 (b), the six mistuning patterns of the 6th to 11th cantilevered-blade modes are used in the mistuning projection.

Results show clearly that the ROMs with two and six eigenvalue mistuning patterns predict the mistuned system response considerably better than those with the single mistuning patterns. In fact, using a single pattern is seen to lead to poor results, including for the resonant response amplitudes. This demonstrates that when multiple blade-dominated mode groups are so close that they interact in the response of a mistuned system, all the eigenvalue mistuning patterns corresponding to the dominant cantilevered-blade modes are required in the reduced-order model. For a bladed disk with several different eigenvalue mistuning patterns, it can be difficult or impractical to obtain $\mathbf{K}^{\delta}$ in physical coordinates, especially if changes in the individual mistuned mode shapes need to be considered. Nevertheless, the CMM technique only requires the eigenvalue mistuning patterns, which can be measured, thus enabling the projection of non-proportional mistuning to tuned-system modes.

Figure 2.19 shows forced response results for the same frequency range as in Fig. 2.18. The difference is that the changes in the blade mode shapes due to mistuning are considered, and Eq. (2.12) is employed. The eigenvalues and mode shapes of the 1st to 15th cantilevered-blade modes are used, and the full matrices of $\boldsymbol{\mu}^{\delta}_{\phi\phi,n}$ and $\boldsymbol{\kappa}^{\delta}_{\phi\phi,n}$ corresponding to the 1st through 15th cantilevered-blade modes are obtained. Note that the eigenvalues and mode shapes are obtained from the finite element models of the mistuned blades. In Fig. 2.19 (a), only the mistuning values corresponding to the 8th and the 9th cantilevered-blade modes are used in the ROM, while in Fig. 2.19 (b), the mistuning values for the 6th through the 11th cantilevered-blade modes are used. These results are seen to be more accurate than those in Fig. 2.18, because now mode shape mistuning is considered. Also, the results in Fig. 2.19 (b) are slightly better than those in Fig. 2.19 (a). However, note that the accuracy of the results in Fig. 2.18, which only considers eigenvalue mistuning, is still acceptable.

Finally note that the reduced-order modeling framework presented in this paper can be readily applied to shrouded rotors. The interested reader is referred to a previous study by the authors [44].

2.6 Conclusions

A general reduced-order model framework for mistuned bladed disks was developed by dividing a mistuned system into a tuned system and virtual mistuning components. This approach handles the case of large blade mistuning, such as geometric and mode shape mistuning. The method employs tuned-system normal modes and attachment modes to represent mistuned-system normal modes. A compact ROM for the important case of small blade mistuning was also derived from the general formulation, using a component mode mistuning method in which a mistuning projection is performed using the modal participation factors of cantilevered-blade component modes.

In the CMM method, the finite element models of a tuned sector and a tuned cantilevered blade are required. Cantilevered-blade normal modes and boundary modes are employed to describe the blade motion of the tuned-system normal modes that are obtained from the single-sector model. Thereby, mistuning values in the modal domain of the cantilevered-blade component modes are projected onto the tuned-system normal modes. Since the boundary modes are defined by minimizing their contribution in the mistuning projection, they can be neglected when the the tuned-system modes feature displacements at the boundaries that are much smaller than those at the interior of a blade. Therefore, in many cases, modal mistuning values corresponding to dominant cantilevered-blade modes are sufficient to predict the response of a mistuned system. The modal mistuning values corresponding to cantilevered-blade modes can be computed easily from the natural frequencies and mode shapes of mistuned blades. This means that actual arbitrary mistuning in the physical domain can be efficiently implemented in a ROM with a small number of mistuning values in the modal domain.

The general ROM was validated for a large mistuning case, using an industrial turbomachinery rotor with a rogue blade with significantly different geometry. It was observed that the estimated natural frequencies of the mistuned rotor converge rapidly as the selected number of tuned-system modes is increased. Also, the forced response results from the ROM showed excellent agreement with the FEM results.

The CMM method for small blade mistuning was validated for both proportional and non-proportional stiffness mistuning cases. By inspecting the modal participation factors, it was found that there are dominant cantilevered-blade modes that are sufficient for representing mistuning. For proportional stiffness mistuning, a single eigenvalue mistuning pattern was sufficient for mistuning implementation. For non-proportional mistuning, the mistuning values corresponding to individual dominant cantilevered-blade modes were required when two blade-dominated mode groups were close. Selecting just one eigenvalue mistuning pattern produced poor results.

2.7 Figures and Tables

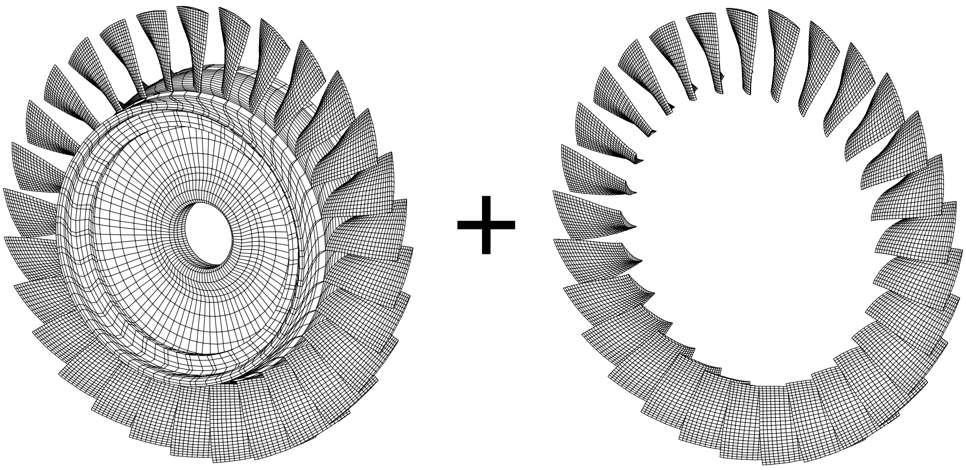

Tuned bladed disk component (M^S, K^S)

Blade mistuning components (M^{δ}, K^{δ})

Figure 2.1: Substructuring of a mistuned bladed disk.

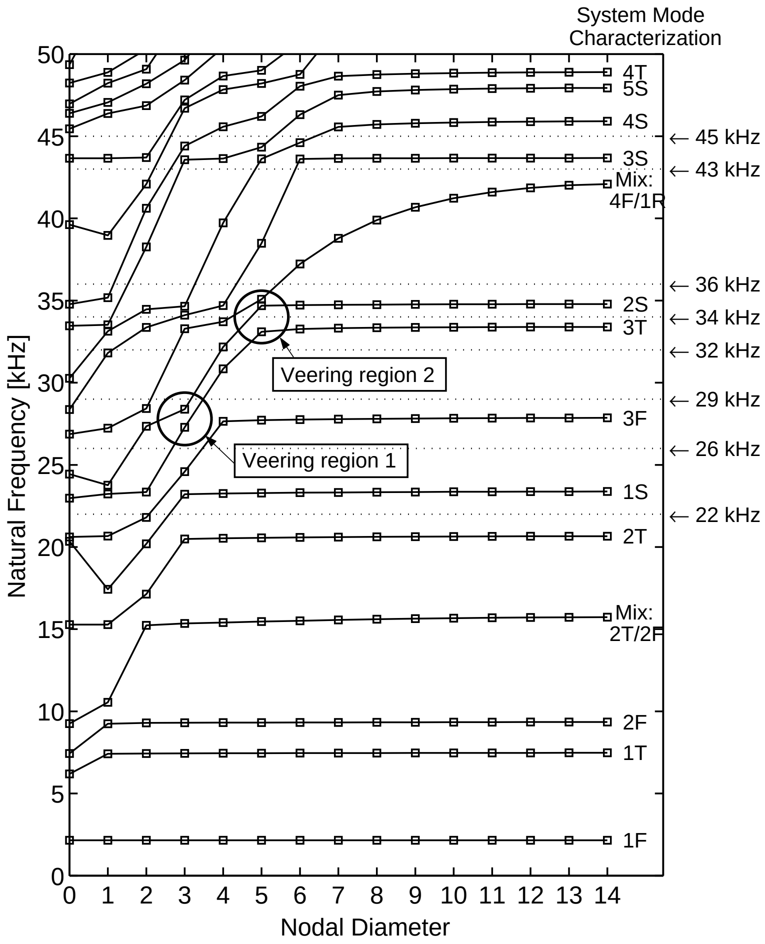

Figure 2.2: Natural frequencies versus number of nodal diameters for the tuned rotor FEM.

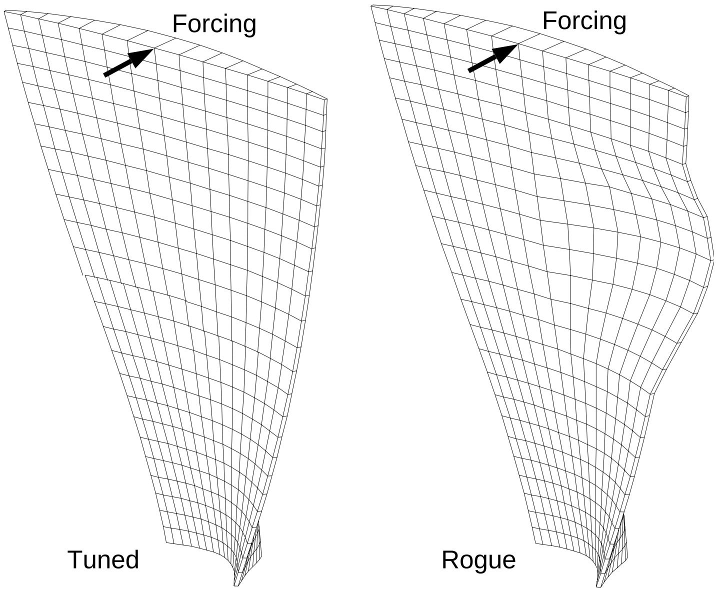

Figure 2.3: Rogue blade geometry.

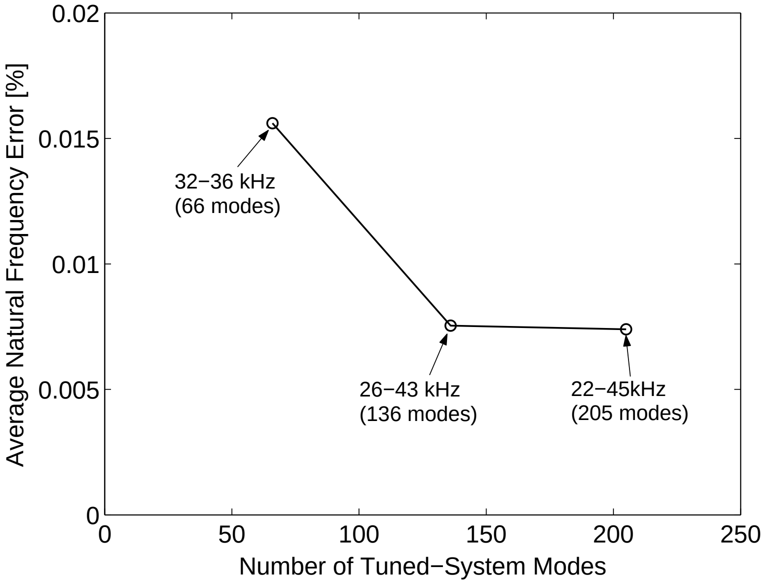

Figure 2.4: Convergence of average natural frequency error for the large mistuning case.

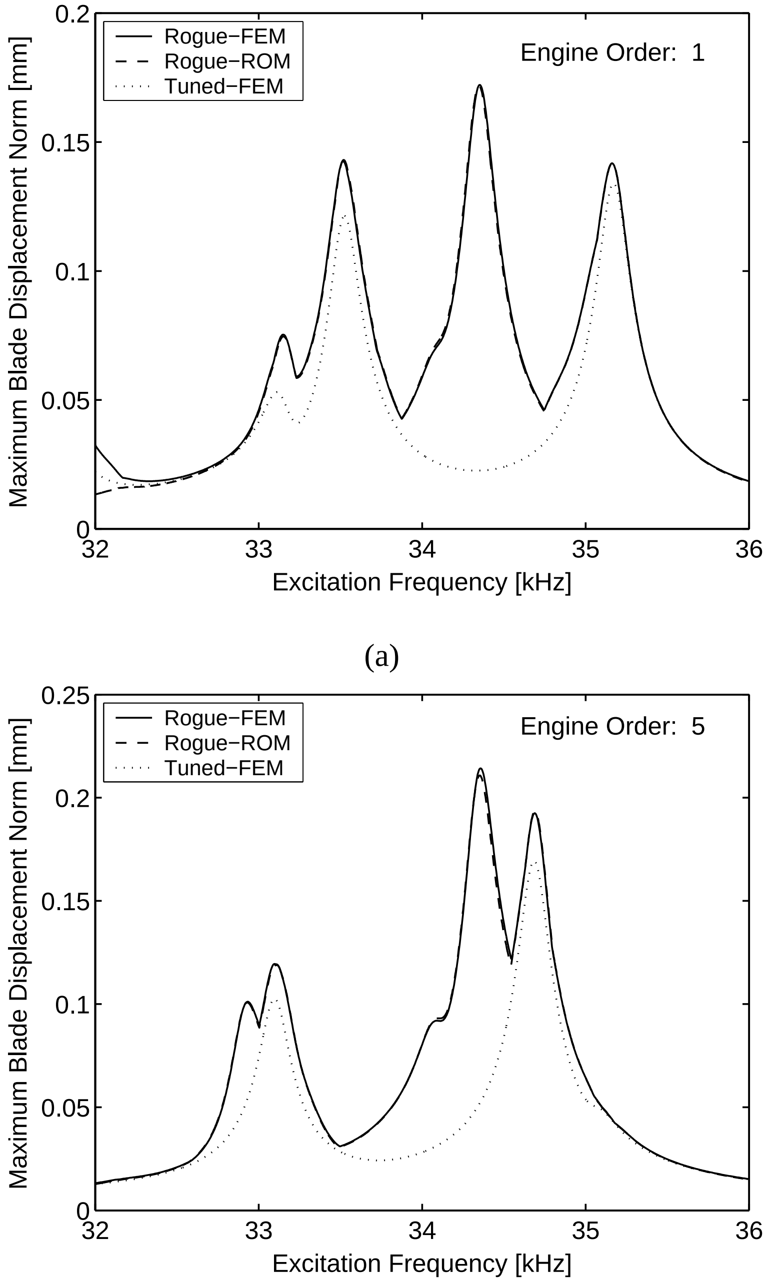

(a)

(b)

Figure 2.5: Forced response results from the FEM (126,846 DOF) and a ROM (2,632 DOF) for two cases of engine order excitation.

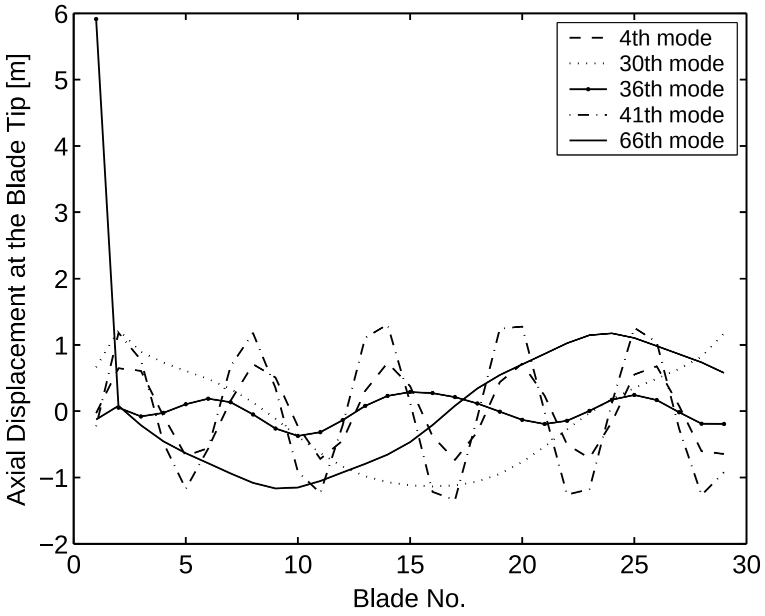

Figure 2.6: Five of the 66 mistuned modes in the 32–36 kHz range.

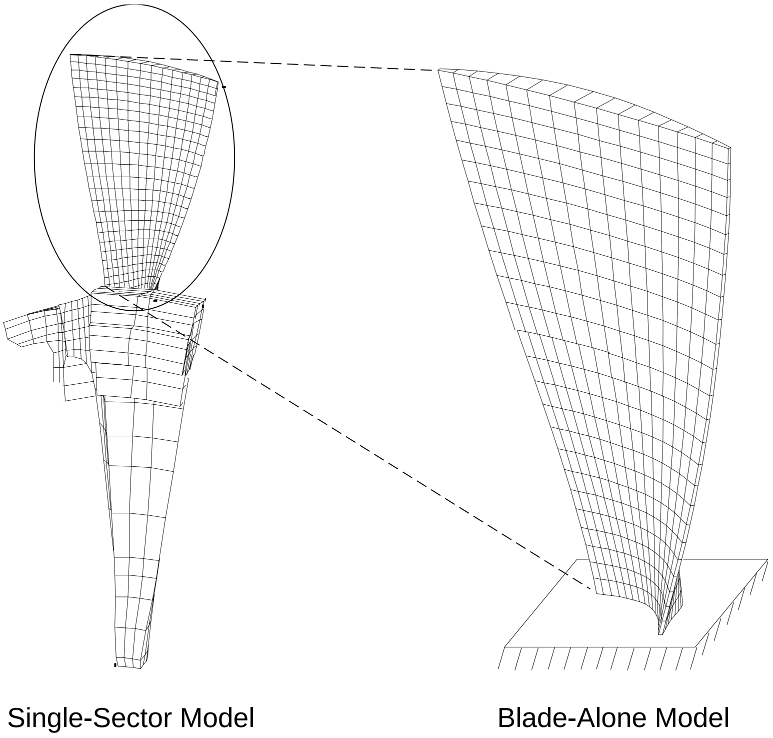

Figure 2.7: Single-sector and blade-alone models of an industrial rotor.

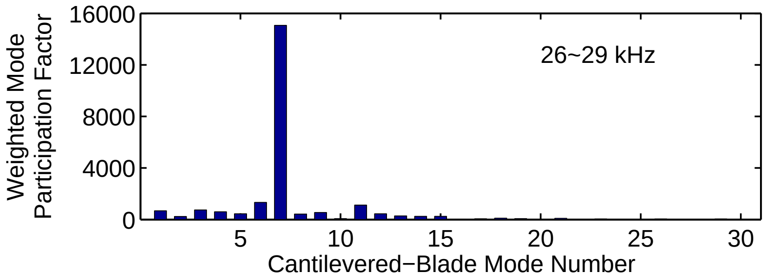

(a)

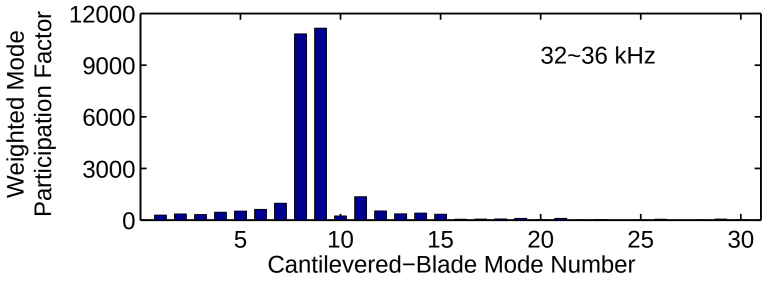

(b)

Figure 2.8: Weighted-average cantilevered-blade mode participation factors for the blade motion in the tuned-system normal modes, (a) in veering region 1 and (b) in region 2.

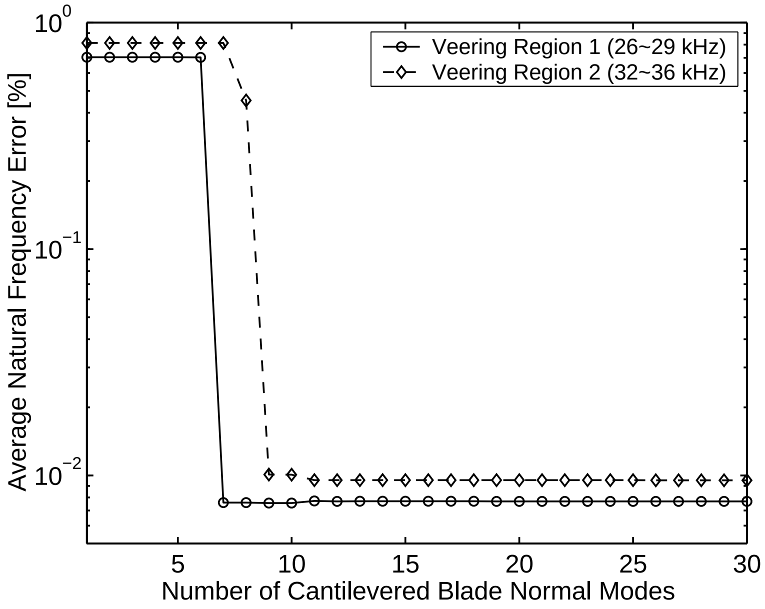

Figure 2.9: Convergence of average natural frequency error.

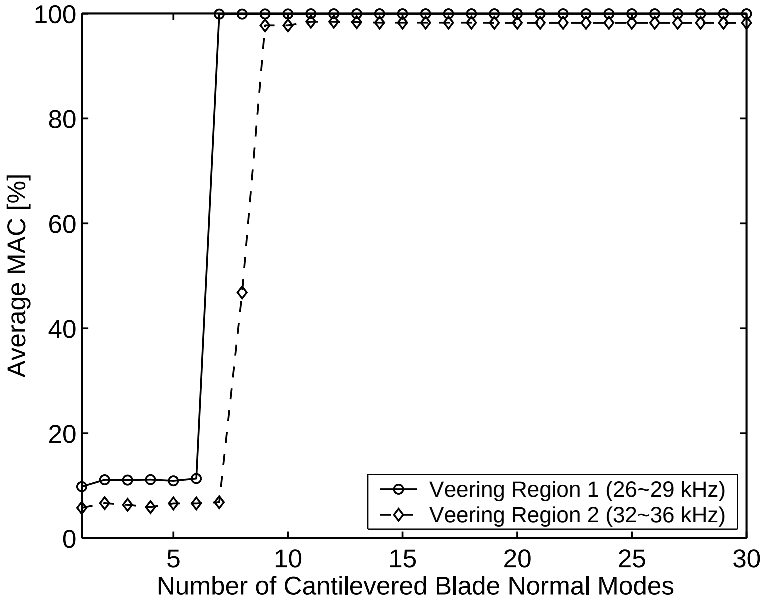

Figure 2.10: Convergence of average MAC ratio.

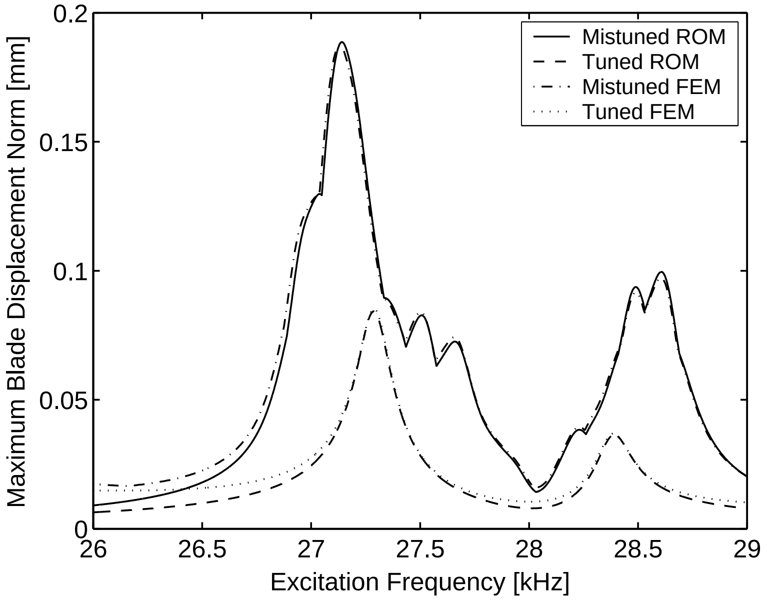

Figure 2.11: Frequency response for engine order 3 excitation, obtained by the FEM and a 34-DOF CMM model.

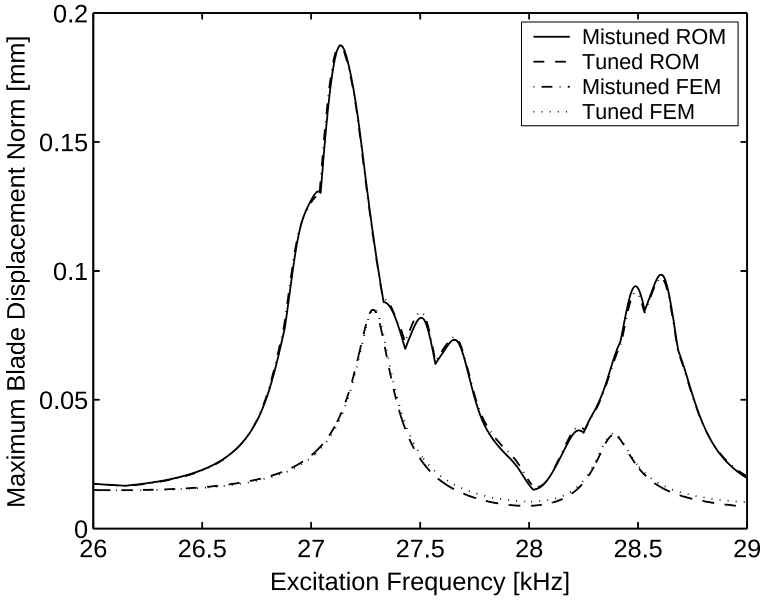

Figure 2.12: Frequency response for engine order 3 excitation, obtained by the FEM and a 106-DOF CMM model.

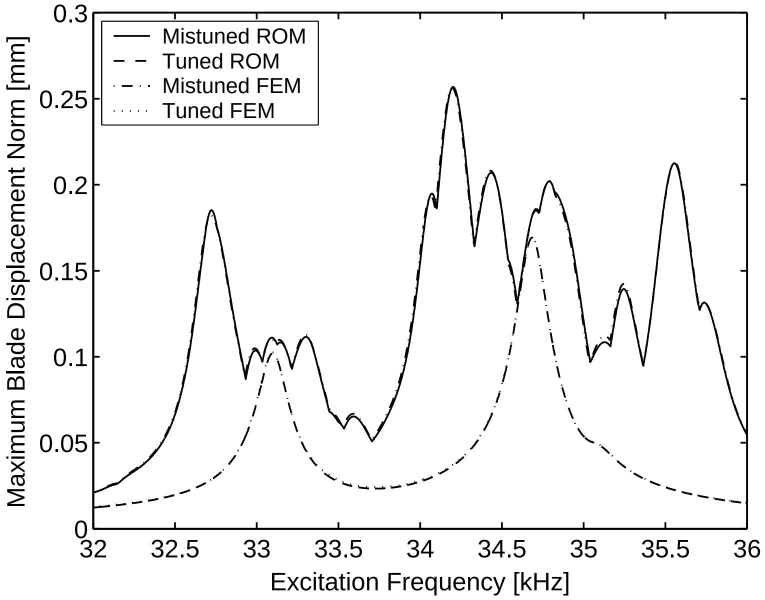

Figure 2.13: Frequency response for engine order 5 excitation, obtained by the FEM and a 66-DOF CMM model.

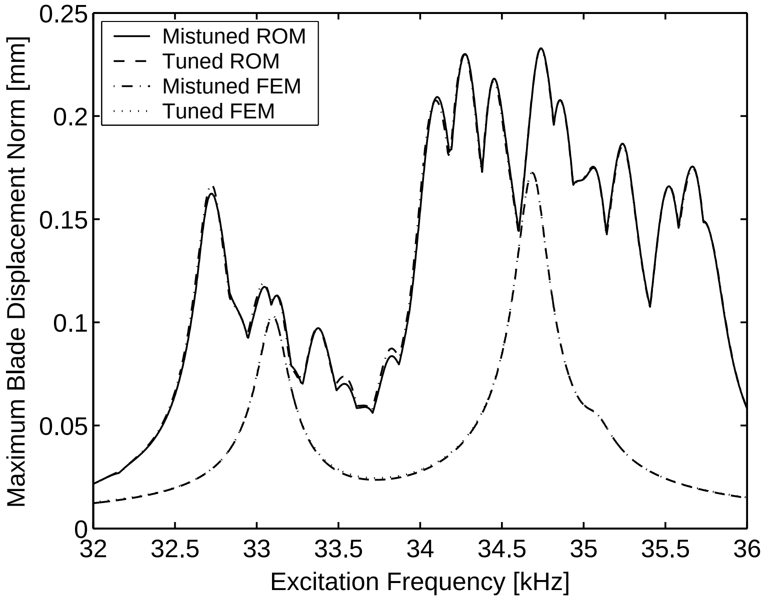

Figure 2.14: Frequency response for engine order 24 excitation, obtained by the FEM and a 66-DOF CMM model.

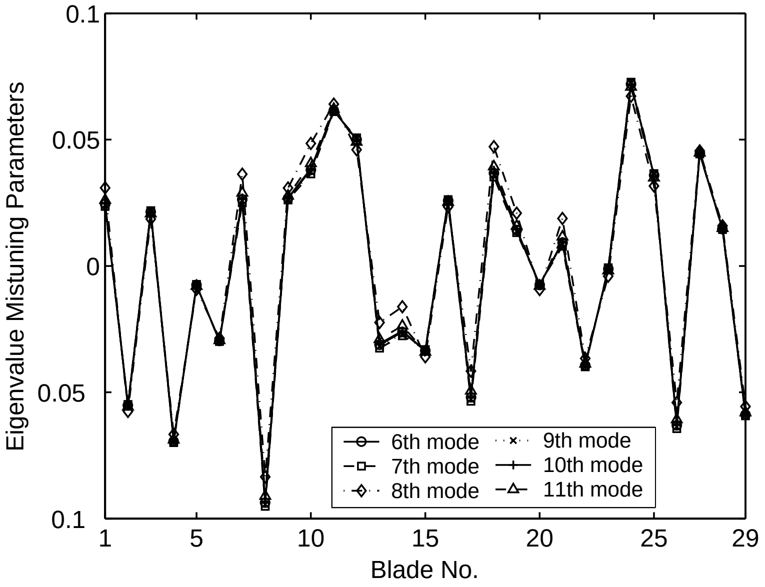

Figure 2.15: Mistuning patterns of cantilevered-blade eigenvalues corresponding to mode 6–11 for the case study rotor with non-proportional mistuning.

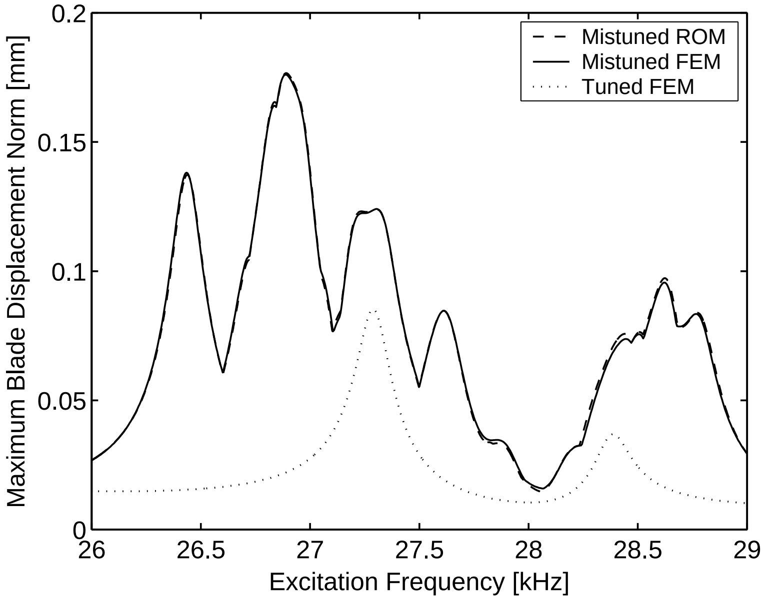

Figure 2.16: Frequency response for engine order 3 excitation, obtained by the FEM and the 106-DOF CMM model with the single eigenvalue mistuning pattern of the 7th cantilevered-blade mode applied to the 1st through 15th cantilevered-blade modes.

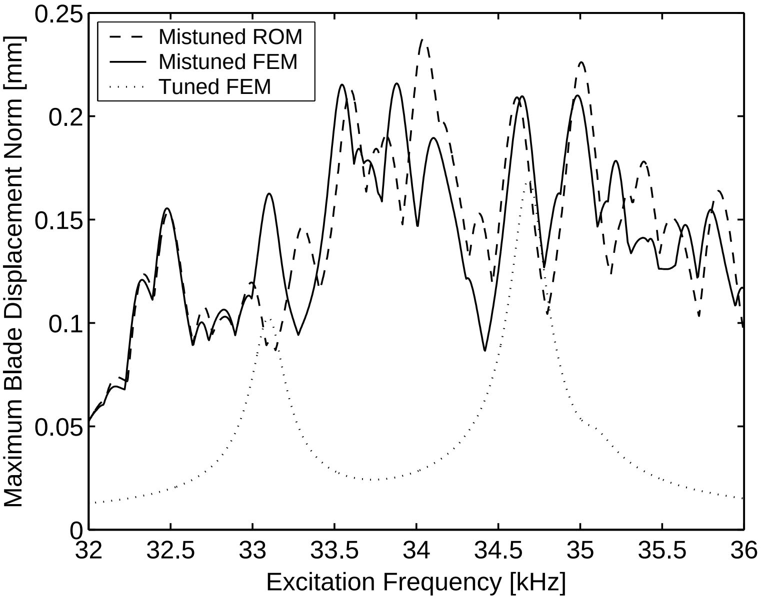

(a)

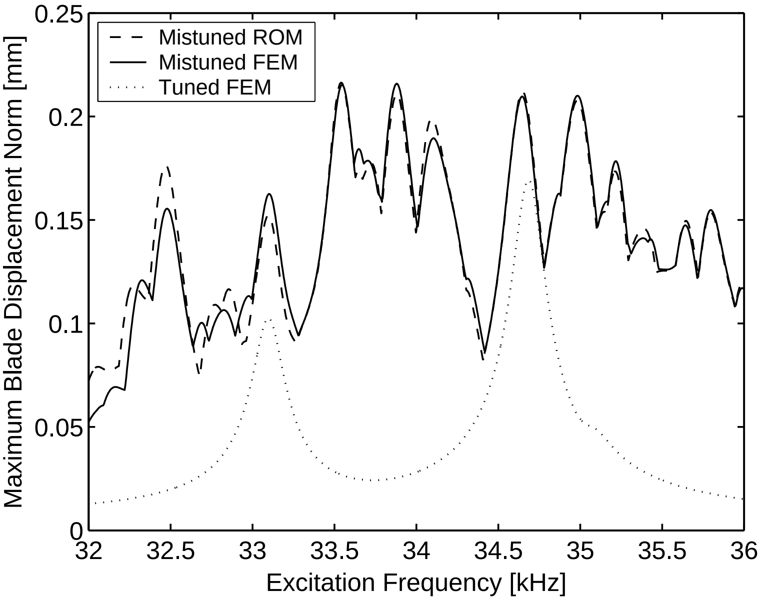

(b)

Figure 2.17: Frequency response for engine order 5 excitation, as obtained by the FEM and 136-DOF CMM models with a single eigenvalue mistuning pattern of (a) the 8th and (b) the 9th cantilevered-blade mode applied to the lowest 15 cantilevered-blade modes.

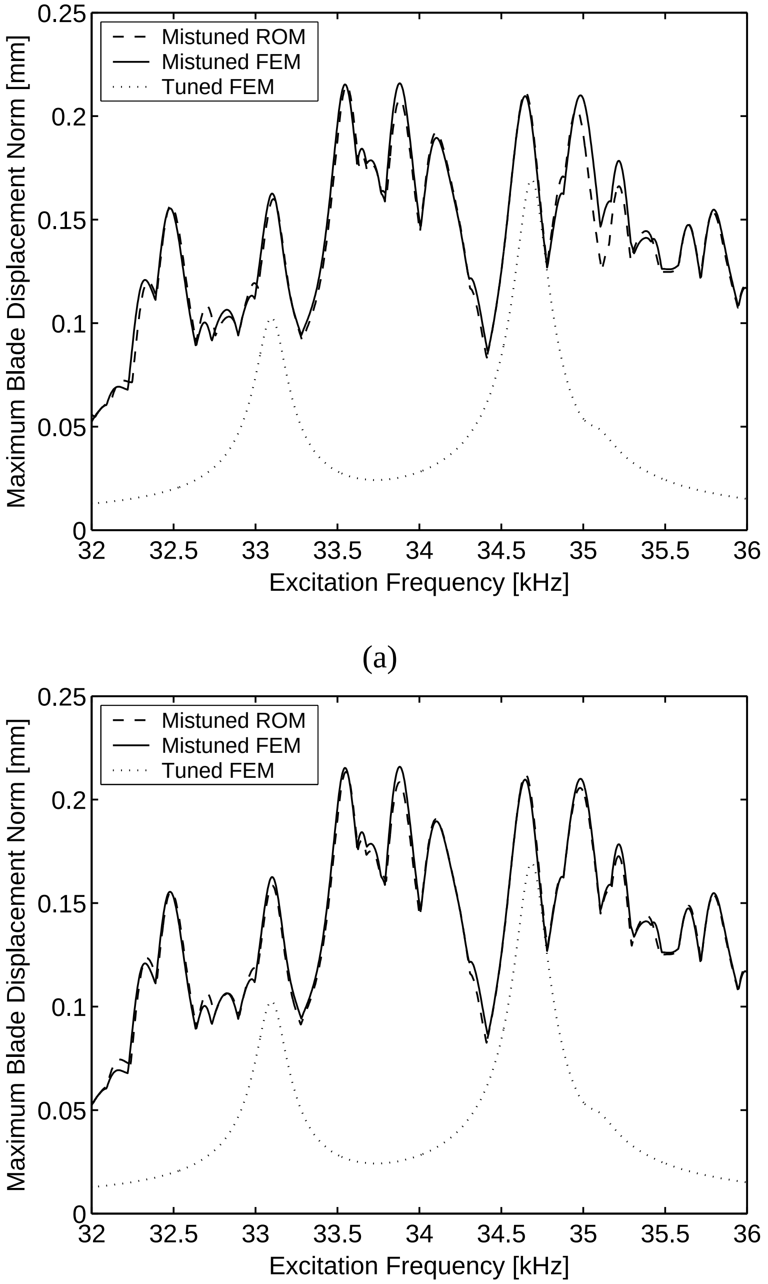

(a)

(b)

Figure 2.18: Frequency response for engine order 5 excitation, as obtained by the FEM and 136-DOF CMM models with eigenvalue mistuning patterns of (a) the 8th and 9th, and (b) the 6th to 11th cantilevered-blade modes applied to the corresponding cantilevered-blade modes.

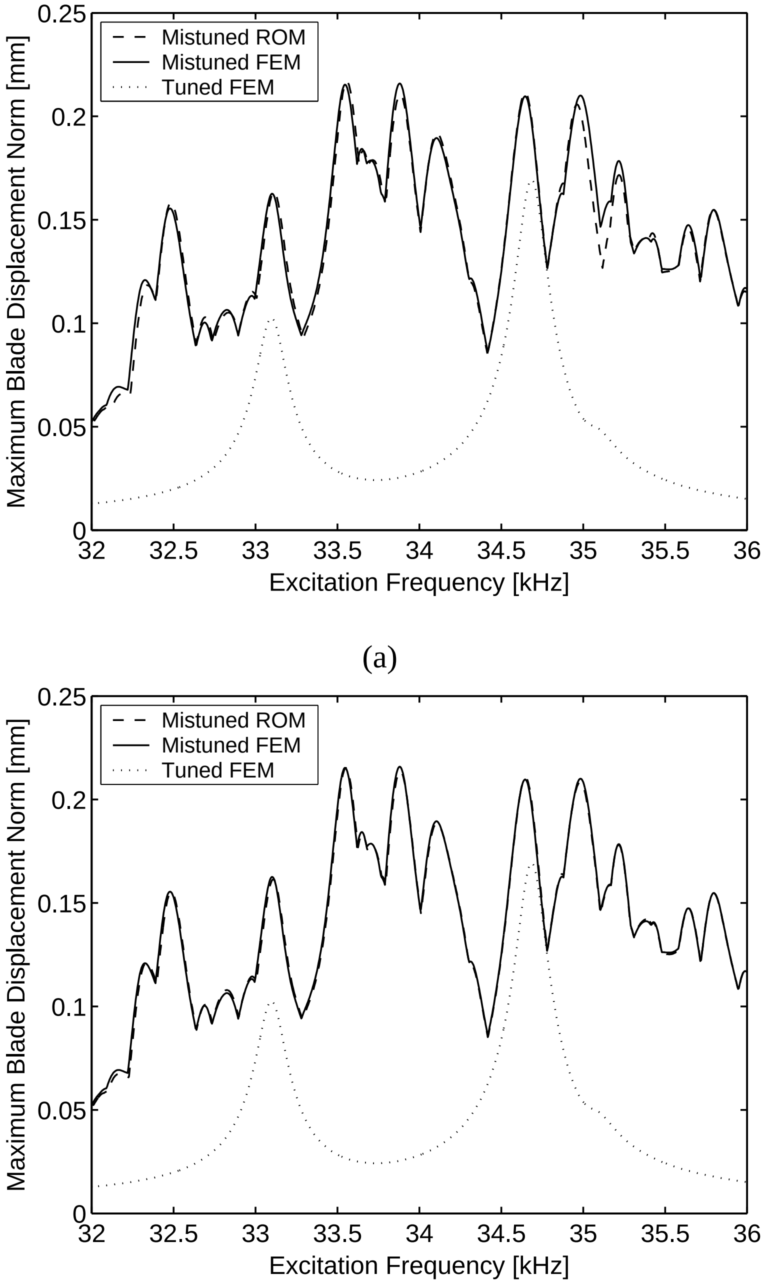

(a)

(b)

Figure 2.19: Frequency response for engine order 5 excitation, as obtained by the FEM and 136-DOF CMM models with mistuning values obtained using eigenvalues and mode shapes corresponding to (a) the 8th and 9th, and (b) the 6th to 11th cantilevered-blade normal modes.

Table 2.1: Eigenvalue mistuning pattern for the case study rotor with proportional mistuning.

Blade	δ_n^e $(= \delta_n^E)$	Blade	δ_n^e $(= \delta_n^E)$
1	0.05704	16	0.04934
2	0.01207	17	0.04479
3	0.04670	18	0.03030
4	-0.01502	19	0.00242
5	0.05969	20	0.01734
6	-0.03324	21	0.02919
7	-0.00078	22	-0.00328
8	-0.01688	23	0.00086
9	0.00242	24	-0.03654
10	-0.02747	25	-0.03631
11	-0.03631	26	-0.01665
12	-0.03570	27	0.00783
13	-0.03631	28	-0.01169
14	-0.03631	29	-0.01332
15	0.00242		

Table 2.2: Young's modulus mistuning parameters for the case study rotor with non-proportional mistuning.

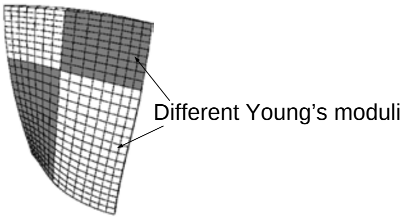

Blade	$\delta^E_{n,1}$	$\delta^E_{n,2}$	Blade	$\delta^E_{n,1}$	$\delta^E_{n,2}$
1	0.04080	0.01030	16	0.01990	0.03120
2	-0.06110	-0.04990	17	-0.02490	-0.07530
3	0.01430	0.02780	18	0.06380	0.01350
4	-0.06230	-0.07580	19	0.03140	-0.00080
5	-0.01170	-0.00390	20	-0.01220	-0.00320
6	-0.02700	-0.03210	21	0.03390	-0.01210
7	0.05190	0.00450	22	-0.03220	-0.04590
8	-0.06720	-0.11630	23	-0.00830	0.00530
9	0.03710	0.01770	24	0.06010	0.08270
10	0.06520	0.01460	25	0.02540	0.04540
11	0.06790	0.05580	26	-0.03980	-0.08310
12	0.04000	0.05910	27	0.04700	0.04230
13	-0.00850	-0.05080	28	0.01780	0.01180
14	-0.00020	-0.04850	29	-0.05070	-0.06600
15	-0.03960	-0.02800			

CHAPTER III

Identification of Mistuning in Bladed Disks and Reduced-Order Model Updating Based on a Component Mode Mistuning Model

A new method for the identification of blade mistuning in bladed disks is presented. The approach is based on the recently developed component mode mistuning reduced-order modeling technique. The equations of motion of the bladed disk reduced-order model are transformed to yield a set of linear equations, and the blade mistuning values are identified using a least-squares procedure that reduces the influence of measurement errors. A sensitivity study is performed, which considers not only data noise but also modeling errors, and it is found that errors in the free vibration eigenvalues of the tuned bladed disk are most critical. In order to compensate for these errors, the identification formulation is modified, so that both tuned-system eigenvalues and blade mistuning values are identified. Thereby, the accuracy of the identification results is considerably improved. Furthermore, the reduced-order model is updated using the identified tuned-system eigenvalues. The new method is validated numerically using the forced responses of the finite element model of an integrally bladed disk.

3.1 Introduction

Small variations in the structural properties of blades in a bladed disk assembly, which are referred to as mistuning, can qualitatively alter its dynamic behavior compared to that expected from the ideally tuned system. In particular, blade forced response amplitudes can be significantly amplified due to mistuning, possibly causing high-cycle fatigue problems. Many researchers have studied the phenomena induced by blade mistuning, and various reduced-order models (ROMs) have been developed to predict efficiently the dynamic behavior of large-scale finite elements models of mistuned bladed disks [15, 19, 20, 23, 44, 45].

The ROM equations of motion are simulated based on the premise that mistuning is known. Since bladed disk response can be highly sensitive to mistuning, precise information on mistuning is required for the accurate prediction of the forced response of a specific bladed disk. Knowing blade mistuning values is also important as a means of monitoring the quality of the manufacturing process, and potentially in the maintenance checks of operational rotors. Mistuning is usually represented by the deviations of the blade-alone natural frequencies from the nominal values, and it can be determined by measuring blade-alone natural frequencies through broach block tests before inserting blades in the disk. Also, methods have been developed to estimate the variations of the structural parameters of blades from measured blade-alone natural frequencies [46, 47]. However, additional mistuning can be generated during both the assembly and the operational life of bladed disks. Furthermore, blades in integrally bladed disks cannot be removed for testing. Therefore, there is a need to identify mistuning without separating the blades from the disk, based on bladed disks system measurements.

In recent years, several methods have been developed to identify mistuning from vibration measurements of bladed disk assemblies. Mignolet and Lin [48] proposed a technique to identify the structural parameters of blades in a lumped parameter model of mistuned bladed disks. Pichot *et al.* [49] tested several global model updating methods using modal data for mistuning identification, also based on a lumped parameter model. However, while a lumped parameter model may capture the basic mechanisms of bladed disk vibration, it cannot be used to represent accurately the dynamic behavior of actual bladed disks. In 2001, Judge *et al.* [30] were first to develop a technique for mistuning identification based a ROM obtained from a parent finite element model (FEM), and they subsequently improved their method [31]. In 2002, Feiner and Griffin [45] proposed a simpler ROM, called the fundamental mistuning model, based on which they later proposed a mistuning identification method [32, 33, 50]. However, their identification procedure is applicable only when one isolated blade-dominated mode family is present in a frequency range of interest.

Recently, the authors have reported a new reduced-order modeling technique for mistuned bladed disks, namely component mode mistuning (CMM) [44]. The construction of a ROM by the CMM technique is also simple, although not so simple as for Feiner and Griffin's model, and a CMM model represents its parent FEM very accurately regardless of the number of mode families present in the frequency range of interest. In this paper, the CMM modeling technique is extended to the problem of mistuning identification.

In many studies on mistuning identification [30, 31, 48, 49, 51], the sensitivity of the identification results to noise in the measured data was examined in order to test the robustness of the identification procedure. However, the sensitivity to modeling errors was not studied, although it could significantly affect the accuracy of the results. These modeling errors can be present in both the parent FEM and the ROM. While the errors generated by an accurate reduced-order modeling process (such as CMM) are negligible, the FEM represents only an approximation of the manufactured bladed disks. As such it may contains errors that should not be neglected, for example in the boundary conditions. Therefore, in this paper the sensitivity to both modeling errors and data noise is studied, and it is found that the identification results are most sensitive to errors in the free vibration eigenvalues of the tuned bladed disk.

Similarly to other ROMs for bladed disks, a CMM model is constructed based on a tuned FEM. As mentioned above, the parent tuned FEM can be slightly different from an actual tuned bladed disk. Since these differences feature cyclic symmetry, in this paper they are referred to as the “cyclic modeling error”. It is shown that the cyclic modeling error appears in the form of an exactly or approximately diagonal matrix in the equations of motion for a CMM model, and that these diagonal terms can be considered as the deviations of the tuned-FEM eigenvalues from those of the actual tuned bladed disk. Therefore, it is proposed in this study to identify both blade mistuning and tuned-system eigenvalues at the same time, in order to compensate for the cyclic modeling error that is shown to be critical to the accuracy of mistuning identification.

The primary contribution of this paper is the development of a simple mistuning identification method that is robust with respect to modeling errors. In particular, a ROM built using the CMM technique is updated using the identified cyclic modeling error present in the parent FEM, so that the forced response of an actual bladed disk can be predicted accurately by the updated ROM.

This paper is organized as follows. In section 3.2, the basic formulation for the mistuning identification method based on a CMM model is derived, and it is numerically validated. The sensitivity of the method to modeling errors and data noise is examined in section 3.3. In section 3.4, the concept of cyclic modeling error is introduced, and a modified method to identify both the blade mistuning values and the cyclic modeling error is proposed. Finally, the conclusions are given in section 3.5.

3.2 Identification of Blade Mistuning

3.2.1 Theory

Component mode mistuning (CMM) is a vibration modeling method for mistuned bladed disks developed by the authors [44]. In this approach, a ROM is constructed using the free response characteristics of the parent FEMs of a tuned bladed disk and of a tuned, cantilevered blade that is fixed at its root. Note that in the real world all bladed disks feature mistuned blades. Therefore in this section, the ”virtual” tuned bladed disk that can be associated with an actual bladed disk is assumed to be represented exactly by its tuned FEM.

In this study, only blade stiffness mistuning is considered, by assuming that mass mistuning can be represented by equivalent stiffness mistuning. In the derivation of the CMM formulation [44], the mistuning in physical coordinates is first projected to the retained cantilevered-blade normal and constraint modes, and then it is projected again to the retained tuned-system modes via the modal participation factors of the cantilevered-blade modes for the blade motion in the tuned-system normal modes.

Therefore, from the CMM formulation the equations of steady-state forced response can be written as follows:

$$\left[-\omega^2\mathbf{I} + (1 + j\gamma)(\mathbf{\Lambda}^S + \mathbf{Q}^T\boldsymbol{\kappa}^\delta\mathbf{Q})\right]\mathbf{p}^S = \mathbf{f}^S, \tag{3.1}$$

where ω is an excitation frequency, $\mathbf{\Lambda}^S$, $\mathbf{p}^S$, and $\mathbf{f}^S$ are the modal stiffnesses (free vibration eigenvalues), coordinates, and forces, respectively, for a truncated set of tuned-system normal modes, and $\boldsymbol{\kappa}^\delta$ is a mistuning projection matrix, which contains the projection of blade stiffness mistuning to a truncated set of cantilevered-blade modes. $\mathbf{Q}$ is the matrix of participation factors of the cantilevered-blade modes for the blade motion in the tuned-system modes. And γ is a structural damping ratio. Aerodynamic coupling effects are neglected in this study, by assuming that measurements are performed on stationary bladed disks [30, 52, 53].

Usually, blade mistuning is represented by the deviations of cantilevered-blade eigenvalues (or natural frequencies) from the nominal values. These deviations are obtained by projecting the blade stiffness mistuning to the cantilevered-blade normal modes. Here, it is assumed that the displacements at the blade root are so small that the mistuning projection to cantilevered-blade constraint modes is neglected, and that the motion of a blade in a bladed disk is dominated by a single cantilevered-blade normal mode, so that the off-diagonal coupling term of the mistuning projection matrix, $\boldsymbol{\kappa}^{\delta}$, can be neglected. That is, $\mathbf{Q}^T\boldsymbol{\kappa}^{\delta}\mathbf{Q}\mathbf{p}^S$ can be approximated by $\mathbf{Q}^T\boldsymbol{\Lambda}^{\delta,cb}\mathbf{Q}\mathbf{p}^S$, where $\boldsymbol{\Lambda}^{\delta,cb}$ is the diagonal matrix of the eigenvalue deviations of the retained cantilevered-bladed normal modes, and now $\mathbf{Q}$ contains only the factors corresponding to the cantilevered-blade normal modes. Hence, in this study, the mistuning values that are sought in the identification procedure are the diagonal terms of $\boldsymbol{\Lambda}^{\delta,cb}$. The number of such diagonal terms is $N_{cb} \cdot N_b$, where N_{cb} is the number of the retained cantilevered-blade normal modes and N_b is the number of blades in the bladed disk.

When the CMM equations of motion are simulated, the eigenvalue mistuning patterns and external forcing are given as input data, and $\mathbf{p}^S$ is the only unknown to be determined for given excitation frequencies. Of course, $\mathbf{Q}$ and $\boldsymbol{\Lambda}^S$ are obtained from the tuned FEMs. However, in the mistuning identification problem, ω, $\mathbf{p}^S$, and $\mathbf{f}^S$ are obtained from experimental measurements. Then, the only unknown becomes the mistuning, $\boldsymbol{\Lambda}^{\delta,cb}$.

The modal coordinates, $\mathbf{p}^S$, can be calculated from the measured displacements using the following relation:

$$\mathbf{x}_{meas} = \mathbf{U}_{meas}\mathbf{p}^S, \tag{3.2}$$

where $\mathbf{x}_{meas}$ is the vector of the displacements at measured degrees of freedom (DOF), and $\mathbf{U}_{meas}$ is the matrix containing the displacements at the measured DOF in the tuned-system modes. If the row and column sizes of $\mathbf{U}_{meas}$ are different, then a least-squares problem needs to be solved by pre-multiplying $\mathbf{x}_{meas}$ by the pseudo-inverse of $\mathbf{U}_{meas}$. The modal external forces, $\mathbf{f}^S$, can also be calculated from the forces measured in physical coordinates, but measuring the forces may be impractical if non-contacting means of excitation, such as acoustic or electromagnetic [30, 31, 52, 53], are used. In this case, $\mathbf{f}^S$ can be neglected if the displacements are measured at resonant frequencies and damping is small.

Finally, the equation of motion (3.1) is transformed to yield the following set of linear equations in the unknown eigenvalue deviations when m sets of experimental data are collected:

$$\begin{bmatrix} \mathbf{Q}_1^T\mathbf{Q}_1\mathbf{p}_1^S & \mathbf{Q}_2^T\mathbf{Q}_2\mathbf{p}_1^S & \cdots & \mathbf{Q}_n^T\mathbf{Q}_n\mathbf{p}_1^S \\ \mathbf{Q}_1^T\mathbf{Q}_1\mathbf{p}_2^S & \mathbf{Q}_2^T\mathbf{Q}_2\mathbf{p}_2^S & \cdots & \mathbf{Q}_n^T\mathbf{Q}_n\mathbf{p}_2^S \\ \vdots & \vdots & \ddots & \vdots \\ \mathbf{Q}_1^T\mathbf{Q}_1\mathbf{p}_m^S & \mathbf{Q}_2^T\mathbf{Q}_2\mathbf{p}_m^S & \cdots & \mathbf{Q}_n^T\mathbf{Q}_n\mathbf{p}_m^S \end{bmatrix} \begin{Bmatrix} \lambda_1^{\delta,cb} \\ \lambda_2^{\delta,cb} \\ \vdots \\ \lambda_n^{\delta,cb} \end{Bmatrix} = \frac{1}{1+j\gamma} \begin{Bmatrix} \mathbf{f}_1^S + \omega_1^2\mathbf{p}_1^S - (1+j\gamma)\mathbf{\Lambda}^S\mathbf{p}_1^S \\ \mathbf{f}_2^S + \omega_2^2\mathbf{p}_1^S - (1+j\gamma)\mathbf{\Lambda}^S p_2^S \\ \vdots \\ \mathbf{f}_m^S + \omega_m^2\mathbf{p}_m^S - (1+j\gamma)\mathbf{\Lambda}^S\mathbf{p}_m^S \end{Bmatrix}, \tag{3.3}$$

where $\mathbf{Q}_i$ is the ith row of $\mathbf{Q}$, n equals $N_{cb} \cdot N_b$, $\lambda_i^{\delta,cb}$ is the eigenvalue deviation of the corresponding cantilevered-blade mode for the corresponding blade, and $\mathbf{p}_k^S$, $\mathbf{f}_k^S$, and ω_k^2 are the tuned-system modal coordinates, modal forces, and excitation frequency corresponding to the kth measured data set, respectively. The above set of complex equations can be divided into two sets of real equations for the real and imaginary parts. Then, the eigenvalue deviations, which are real valued, can be obtained by solving the two sets of real linear equations together using a least-squares method. Note that Eq. (3.3) can also be used for free response data by setting γ and $\mathbf{f}^S$ to be zero.

3.2.2 Numerical Validation

The above mistuning identification method is validated using the tuned FEM of a 24-blade validation bladed disk that was used by Judge *et al.* [30, 31]. The finite element mesh of the bladed disk is shown in Fig. 3.1. Note that since the tuned FEM features cyclic symmetry, the modes can be obtained from the FEM of a single sector. Figure 3.2 displays the natural frequencies of the tuned FEM versus the number of nodal diameters (or the harmonic number).

Usually, bladed-disk system modes that are dominated by blade motion are present in narrow frequency bands so that the lines connecting the natural frequencies are nearly horizontal on a natural frequency plot, and these mode shapes are greatly altered by slight changes in the structural properties of blades. As can be seen in Fig 3.2, the bladed disk model used in this study also features blade-dominated modes that are characterized by close natural frequencies at the higher harmonics. Here 1F denotes the first flexural bending mode of a cantilevered blade, and 1T denotes the first torsion mode. In this study, the eigenvalue mistuning of the 1F mode was investigated. Therefore, 17 tuned-system modes marked with filled circles between the two dotted lines in Fig. 3.2 were selected to construct a 17-DOF ROM using the CMM modeling technique. The matrix of modal participation factors, $\mathbf{Q}$, was composed of only the factors corresponding to the 1F mode.

In lieu of measured data, forced response results obtained for a mistuned FEM were used. Blade mistuning was introduced into the tuned FEM by varying Young's modulus for each blade, such that the mean of the individual blade mistuning values was zero. Engine order 7 excitation was considered by applying a load to one of the nodes at each blade tip, and the amplitude of the axial displacement at a node near each blade tip was recorded at each excitation frequency. The resulting forced responses of the 24 blades are depicted in Fig. 3.3. In order to simulate a case where the resonant peaks overlap so that individual natural frequencies and mode shapes cannot be measured clearly, in this numerical study the structural damping ratio of the FEM was set to be 0.0015, although the structural damping ratio of the actual bladed disk specimen is 0.00015 [30]. As can be seen, the resonant peaks are not clearly separated, except for the first peak around 1.99 kHz. In fact, there are two modes that overlap around 1.99 kHz. The 13 resonant frequencies marked with dotted vertical lines in Fig. 3.3 were selected for the response data to be used in the identification process, and external forces were considered as if they were not measurable. Therefore, when mistuning was identified using Eq. (3.3), the modal forces were neglected.

The number of mistuning values to be determined, which is 24, is greater than the number of modal coordinates in the ROM, which is 17. Therefore, mistuning cannot be identified with a single data set obtained at one frequency. At least two data sets at different frequencies are required, and it can be expected that the identification results become more reliable as more data sets are used when data noise is present. For this test case, 13 data sets were used as mentioned above. The identified mistuning pattern is depicted in Fig. 3.4, and it is compared with the exact (and known) mistuning pattern of the FEM. The mistuning values displayed are the deviations of the 1F-cantilevered mode eigenvalues normalized with the nominal eigenvalue. The discrepancies between the identified and the exact mistuning values are due to the difference between the ROM and the FEM, because in this case there were no “measurement” errors. Since the identified mistuning values are very close to the exact ones, it can be said that the CMM-based ROM represents the FEM very accurately.

Using the identified mistuning, the natural frequencies and mode shapes of the mistuned bladed disk were obtained from the 17-DOF ROM, and typical results are depicted in Fig. 3.5. As can be seen, the results from the ROM with the identified mistuning match very well those from the mistuned FEM, which indicates that the identification of mistuning was successful.

3.3 Sensitivity to Modeling and Measurement Errors

In the previous section, no errors in the response data were considered. Also, since the data were obtained from a mistuned FEM rather than measured from a physical specimen, the parent tuned FEM of the CMM model was exactly the tuned equivalent of the mistuned FEM rather than that of the physical blisk, which means no modeling errors were considered in the parent tuned FEM. In this section, the sensitivity of the identification results to errors in both FEMs and measurements is investigated.

The modeling parameters required for the CMM-based mistuning identification are the tuned-FEM natural frequencies ($\mathbf{\Lambda}^S$), the displacements at measured DOF in the tuned-FEM mode shapes ($\mathbf{U}_{meas}$), and the cantilevered-blade mode participation factors for the blade motion in the tuned-FEM mode shapes ($\mathbf{Q}$). Of course, the cantilevered-blade modes are obtained from the FEM of a tuned, cantilevered-blade model. Excitation frequencies (ω) and physical displacements ($\mathbf{x}_{meas}$) are obtained from measurements, and the damping ratio (γ) can also be determined experimentally. All these modeling parameters and measured data can have errors in them, but the errors in ω are neglected in this study by assuming that excitation frequencies are correctly realized by a signal generator.

The sensitivity to small errors in parameters and data can be assessed by differentiating Eq. (3.3). First, Eq. (3.3) is differentiated with respect to Q_{ir}, which is the element at the ith row and rth column of $\mathbf{Q}$, and multiplied by Q_{ir} in order to obtain the sensitivity to the ratio of the error to the exact value. Here, for simplicity it is assumed that a single data set is measured. The following equation is obtained:

$$\begin{bmatrix}\mathbf{Q}_1^T\mathbf{Q}_1\mathbf{p}^S & \mathbf{Q}_2^T\mathbf{Q}_2\mathbf{p}^S & \cdots & \mathbf{Q}_n^T\mathbf{Q}_n\mathbf{p}^S\end{bmatrix}\frac{\partial\boldsymbol{\lambda}^{\delta,cb}}{\partial Q_{ir}}Q_{ir} = -Q_{ir}\lambda_i^{\delta,cb}(\mathbf{Q}_{i,r}+\mathbf{Q}_{i,r}^T)\mathbf{p}^S, \quad (3.4)$$

where $\boldsymbol{\lambda}^{\delta,cb}$ is the column vector of the deviations of the eigenvalues of cantilevered-blade normal modes, and $\mathbf{Q}_{i,r}$ is a square matrix whose rth row is $\mathbf{Q}_i$ and all the other rows are zero.

Next, consider the sensitivity to errors in $\boldsymbol{\Lambda}^S$. Differentiating Eq. (3.3) with respect to λ_i^S, the ith tuned-system eigenvalue, and subsequently multiplying by λ_i^S, one obtains:

$$\begin{bmatrix}\mathbf{Q}_1^T\mathbf{Q}_1\mathbf{p}^S & \mathbf{Q}_2^T\mathbf{Q}_2\mathbf{p}^S & \cdots & \mathbf{Q}_n^T\mathbf{Q}_n\mathbf{p}^S\end{bmatrix}\frac{\partial\boldsymbol{\lambda}^{\delta,cb}}{\partial\lambda_i^S}\lambda_i^S = -\lambda_i^S\begin{Bmatrix}0 & \cdots & 0 & p_i^S & 0 & \cdots & 0\end{Bmatrix}^T, \quad (3.5)$$

where p_i^S is the ith element of $\mathbf{p}^S$.

And, differentiating Eq. (3.3) with respect to γ and multiplying by γ yields:

$$\begin{bmatrix}\mathbf{Q}_1^T\mathbf{Q}_1\mathbf{p}^S & \mathbf{Q}_2^T\mathbf{Q}_2\mathbf{p}^S & \cdots & \mathbf{Q}_n^T\mathbf{Q}_n\mathbf{p}^S\end{bmatrix}\frac{\partial\boldsymbol{\lambda}^{\delta,cb}}{\partial\gamma}\gamma = \frac{-\gamma}{(1+j\gamma)^2}(\mathbf{f}^S+\omega^2\mathbf{p}^S). \quad (3.6)$$

The modal coordinates, $\mathbf{p}^S$, are calculated from Eq. (3.2). That is, $\mathbf{p}^S$ is a function of $\mathbf{U}_{meas}$ and $\mathbf{x}_{meas}$. Therefore, the differentiation of $\boldsymbol{\lambda}^{\delta,cb}$ with respect to $\mathbf{p}^S$ can indicate the sensitivity to errors in $\mathbf{U}_{meas}$ and $\mathbf{x}_{meas}$. Differentiating Eq. (3.3) with respect to p_i^S, and multiplying by p_i^S, the resulting equation is

$$\begin{aligned}&\begin{bmatrix}\mathbf{Q}_1^T\mathbf{Q}_1\mathbf{p}^S & \mathbf{Q}_2^T\mathbf{Q}_2\mathbf{p}^S & \cdots & \mathbf{Q}_n^T\mathbf{Q}_n\mathbf{p}^S\end{bmatrix}\frac{\partial\boldsymbol{\lambda}^{\delta,cb}}{\partial p_i^S}p_i^S\\ &\qquad = -p_i^S\begin{bmatrix}Q_{1i}\mathbf{Q}_1^T & Q_{2i}\mathbf{Q}_2^T & \cdots & Q_{ni}\mathbf{Q}_n^T\end{bmatrix}\delta\boldsymbol{\lambda}^{cb} \qquad (3.7)\\ &\qquad\quad + \frac{p_i^S}{1+j\gamma}\begin{Bmatrix}0 & \cdots & 0 & \omega^2-(1+j\gamma)\lambda_i^S & 0 & \cdots & 0\end{Bmatrix}^T.\end{aligned}$$

Since the matrices that pre-multiply the partial derivatives in Eqs. (3.4), (3.5), (3.6) and (3.7) are the same, the comparison of the right-hand side terms of these equations can determine which parameter or data error the identification results are most sensitive to. The cantilevered-blade mode participation factors for the tuned-system modes in cyclic coordinates are usually less than 1. Hence, the factors for the tuned system modes in physical coordinates, $\mathbf{Q}$, are smaller than $2/\sqrt{N}$ if the tuned-system modes are obtained using a real-form cyclic analysis [54]. The structural damping ratio is usually very small; note that γ for the validation bladed disk is 0.00015. Furthermore, $\lambda_i^{\delta,cb}$ is a small percentage of the cantilevered-blade eigenvalue; and $\omega^2 - (1 + j\gamma)\lambda_i^S$ is also on the order of $\lambda_i^{\delta,cb}$, because the values of ω^2 and λ_i^S are on the order of the cantilevered-blade eigenvalue and close to each other. These observations indicate that the order of the right-hand side term in Eq. (3.5) is much greater than those in Eqs. (3.4), (3.6) and (3.7). Therefore, it can be expected that the identification results are most sensitive to errors in the tuned-system eigenvalues.

In order to confirm the above sensitivity analysis, mistuning identification was performed for the FEM of the validation bladed disk in Fig. 3.1, using 100 sets of model parameters or measured data with random errors. The same forced response data as in the previous section were used. Note that, since 13 response data sets were selected from the FEM forced response, a total of 1,300 response data sets were used in each case. Six cases were studied: 5% random errors in $\mathbf{Q}$ only; 5% random errors in $\mathbf{\Lambda}^S$ only; 5% random errors in γ only; 5% random errors in $\mathbf{U}_{meas}$ only; random noise in $\mathbf{x}_{meas}$, whose level was 1% of the maximum displacement amplitude in the response data; and all of these errors and noise combined together. For each case, 100 mistuning patterns were identified using Eq. (3.3), and 100 sets of mistuned-system natural frequencies were calculated from the 17-DOF ROM using the identified mistuning patterns. Then, the largest and smallest mistuning values for each of the 24 blades were found, and also, the highest and lowest natural frequencies for each of the 17 bladed-disk system modes were found. The results are depicted in Fig. 3.6. As can be expected, the identification results are not much affected by the errors in $\mathbf{Q}$, γ, $\mathbf{U}_{meas}$, and $\mathbf{x}_{meas}$. And, as can be seen in Fig. 3.6(b), the identification results are highly sensitive to the errors in the tuned-system eigenvalues. Also note that the results in Fig. 3.6(b) and in Fig. 3.6(f) are very similar. This means that the tuned-system eigenvalue errors can be the primary cause of failure of the mistuning identification procedure.

3.4 Identification of the Cyclic Modeling Error

The errors in the modeling parameters for a CMM model are caused primarily by the discrepancy between the parent tuned FEM and the virtual tuned system that can be associated with the physical bladed disk. Here, this difference is referred to as the “cyclic modeling error”, because the deviation of the parent tuned FEM from the virtual tuned system features cyclic symmetry. In this section, the CMM equation of motion, Eq. (3.1), is modified to include a cyclic modeling error term so that, in addition to the blade mistuning values, the modeling errors can be identified. Thereby, the CMM model can be updated, and the accuracy of mistuning identified is significantly improved.

3.4.1 Cyclic Modeling Error

Suppose that there is an ideal tuned FEM that represents exactly the dynamic behavior of the virtual tuned system, and that it has the same number of DOF as the “real” tuned FEM. Also, assume that the difference between the ideal and the real FEMs (i.e., the cyclic modeling error) is small enough that the motion of the ideal FEM can be represented with the mode shapes of the real FEM. Note that it has been recently reported by Yang and Griffin [42] that when a system features a group of modes closely spaced in a narrow frequency range, the motion of a system slightly changed from the original system can be represented with the modes of the original system.

Then, the reduced stiffness matrix of a CMM model for the ideal FEM with mistuning can be written as $\mathbf{\Lambda}^S + \mathbf{\Phi}^{S^T}\mathbf{K}^\delta\mathbf{\Phi}^S + \mathbf{Q}^T\mathbf{\Lambda}^{\delta,cb}\mathbf{Q}$, where $\mathbf{\Phi}^S$ is a matrix containing the modes of the real tuned FEM in physical coordinates, and $\mathbf{K}^\delta$ is the difference between the stiffness matrices of the ideal and the real tuned FEMs. Here again, only a stiffness error is considered, by assuming that the mass modeling error can be represented by an equivalent stiffness modeling error. The projection of the cyclic modeling error onto $\mathbf{\Phi}^S$ can be re-written using the modes in real cyclic coordinates, as follows (for more detail about real-form cyclic analysis, see [54]):

$$\begin{aligned}\mathbf{\Phi}^{S^T}\mathbf{K}^\delta\mathbf{\Phi}^S &= \underset{h=0,\ldots,H}{\tilde{\mathbf{B}}\mathbf{diag}}\left[\tilde{\mathbf{\Phi}}_h^{S^T}\right](\mathbf{F}^T\otimes\mathbf{I})(\mathbf{I}\otimes\mathbf{K}_{sec}^\delta)(\mathbf{F}\otimes\mathbf{I})\underset{h=0,\ldots,H}{\tilde{\mathbf{B}}\mathbf{diag}}\left[\tilde{\mathbf{\Phi}}_h^S\right] \\ &= \underset{h=0,\ldots,H}{\tilde{\mathbf{B}}\mathbf{diag}}\left[\tilde{\mathbf{\Phi}}_h^{S^T}\right](\mathbf{I}\otimes\mathbf{K}_{sec}^\delta)\underset{h=0,\ldots,H}{\tilde{\mathbf{B}}\mathbf{diag}}\left[\tilde{\mathbf{\Phi}}_h^S\right] = \underset{h=0,\ldots,H}{\tilde{\mathbf{B}}\mathbf{diag}}\left[\tilde{\mathbf{\Phi}}_h^{S^T}\tilde{\mathbf{K}}_h^\delta\tilde{\mathbf{\Phi}}_h^S\right],\end{aligned} \tag{3.8}$$

where $\tilde{\mathbf{B}}\mathbf{diag}\,[\bullet]$ denotes a pseudo-block-diagonal matrix, whose block sizes can be different, H equals $(N_b-1)/2$ for N_b odd and $N_b/2$ for N_b even, and $\tilde{\mathbf{\Phi}}_h^S$ is a set of cyclic modes corresponding to harmonic h, which can be obtained from a single-sector FEM. For a single-harmonic mode, the row size of $\tilde{\mathbf{\Phi}}_h^S$ is the number of DOF in a sector, while for a double-harmonic mode it is twice that. The column size of $\tilde{\mathbf{\Phi}}_h^S$ is the number of retained modes for the corresponding harmonic. Here $\mathbf{F}$ is a real-valued Fourier matrix, $\otimes$ denotes the Kronecker product, $\mathbf{K}_{sec}^\delta$ is the deviation of the stiffness matrix of the real single-sector FEM from the ideal one, and $\tilde{\mathbf{K}}_h^\delta$ is defined as

$$\tilde{\mathbf{K}}_h^\delta = \begin{cases}\mathbf{K}_{sec}^\delta & \text{for } h=0\text{, and } h=N_b/2 \text{ if } N_b \text{ is even} \\ \begin{bmatrix}\mathbf{K}_{sec}^\delta & \mathbf{0} \\ \mathbf{0} & \mathbf{K}_{sec}^\delta\end{bmatrix} & \text{for } h\neq 0\text{, and } h\neq N_b/2.\end{cases} \tag{3.9}$$

As can be seen in Eq. (3.8), the projection of the cyclic modeling error appears in the form of a pseudo-block-diagonal matrix.

Now, consider a case in which only one mode (or one mode pair) per harmonic is retained in the CMM model. Then, a single-harmonic block becomes just a scalar, and a double-harmonic block becomes a 2×2 matrix. A mode pair for a double harmonic can be written as follows [54]:

$$\begin{bmatrix} \phi_1^{h,c} & \phi_2^{h,c} \\ \phi_1^{h,s} & \phi_2^{h,s} \end{bmatrix}, \tag{3.10}$$

where $\phi_1^{h,c}$ and $\phi_1^{h,s}$ are the cosine and sine parts for one of the modes in the pair, and $\phi_2^{h,c}$ and $\phi_2^{h,s}$ are for the other mode. This mode pair obeys the following relation:

$$\begin{cases} \phi_1^{h,s} = \pm\phi_2^{h,c} \\ \phi_2^{h,s} = \mp\phi_1^{h,c} \end{cases}. \tag{3.11}$$

Hence,

$$\begin{bmatrix} \phi_1^{h,c} & \phi_2^{h,c} \\ \phi_1^{h,s} & \phi_2^{h,s} \end{bmatrix}^T \begin{bmatrix} \mathbf{K}_{sec}^{\delta} & \mathbf{0} \\ \mathbf{0} & \mathbf{K}_{sec}^{\delta} \end{bmatrix} \begin{bmatrix} \phi_1^{h,c} & \phi_2^{h,c} \\ \phi_1^{h,s} & \phi_2^{h,s} \end{bmatrix} = \begin{bmatrix} A & \mathbf{0} \\ \mathbf{0} & A \end{bmatrix}, \tag{3.12}$$

where

$$A = \phi_1^{h,c^T} \mathbf{K}_{sec}^{\delta} \phi_1^{h,c} + \phi_2^{h,c^T} \mathbf{K}_{sec}^{\delta} \phi_2^{h,c}.$$

Therefore, if a single mode (or a single mode pair) per harmonic is retained, the projection matrix becomes a diagonal matrix. Note that, even if two or more modes (or mode pairs) are retained per harmonic, then the off-diagonal terms may be neglected as long as each mode of the ideal FEM is dominated by only one mode of the real FEM.

3.4.2 Mistuning Identification with ROM Updating

Since the projection of the cyclic modeling error onto the modes of a real FEM is, exactly or approximately, a diagonal matrix, it can be interpreted as the deviations of the real-FEM eigenvalues from the ideal-FEM ones. That is, the equations of motion for a

CMM model of the ideal FEM can be written as

$$\left[-\omega^2\mathbf{I} + (1+j\gamma)(\mathbf{\Lambda}^S + \mathbf{\Lambda}^{\delta,S} + \mathbf{Q}^T\mathbf{\Lambda}^{\delta,cb}\mathbf{Q})\right]\mathbf{p}^S = \mathbf{f}^S, \tag{3.13}$$

where $\mathbf{\Lambda}^{\delta,S}$ is a diagonal matrix of the deviations of the real-FEM eigenvalues, which accounts for the cyclic modeling error. It should be noted that the mean of the blade mistuning values now becomes zero. This is because any offset of the mean value can be eliminated by adjusting $\mathbf{\Lambda}^{\delta,S}$.

In Eq. (3.13), $\mathbf{\Lambda}^S + \mathbf{\Lambda}^{\delta,S}$ is the diagonal matrix of the correct tuned-system eigenvalues of an actual bladed disk. However, since $\mathbf{\Lambda}^{\delta,S}$ is unknown, the correct tuned-system eigenvalues are also unknown. Therefore, both tuned-system eigenvalues and blade mistuning must be identified at the same time. Here the same measured data and modeling parameters as in section 3.2 are assumed to be given, but the tuned-system eigenvalues are also treated as unknowns. Also, the restriction that the mean of mistuning values is zero is imposed by setting

$$\lambda_1^{\delta,cb} = -(\lambda_2^{\delta,cb} + \cdots + \lambda_n^{\delta,cb}). \tag{3.14}$$

Then, the following set of linear equations can be obtained by transforming Eq. (3.1):

$$\begin{bmatrix} \mathbf{B}_2\mathbf{p}_1^S & \mathbf{B}_3\mathbf{p}_1^S & \cdots & \mathbf{B}_n\mathbf{p}_1^S & \underset{r\in\boldsymbol{R}}{\mathbf{diag}}\left(p_{1i}^S\right) \\ \mathbf{B}_2\mathbf{p}_2^S & \mathbf{B}_3\mathbf{p}_2^S & \cdots & \mathbf{B}_n\mathbf{p}_2^S & \underset{r\in\boldsymbol{R}}{\mathbf{diag}}\left(p_{2i}^S\right) \\ \vdots & \vdots & \ddots & \vdots & \vdots \\ \mathbf{B}_2\mathbf{p}_m^S & \mathbf{B}_3\mathbf{p}_m^S & \cdots & \mathbf{B}_n\mathbf{p}_m^S & \underset{r\in\boldsymbol{R}}{\mathbf{diag}}\left(p_{mi}^S\right) \end{bmatrix} \begin{Bmatrix} \lambda_2^{\delta,cb} \\ \vdots \\ \lambda_n^{\delta,cb} \\ \lambda_1^S \\ \vdots \\ \lambda_l^S \end{Bmatrix} = \frac{1}{1+j\gamma} \begin{Bmatrix} \mathbf{f}_1^S + \omega_1^2\mathbf{p}_1^S \\ \mathbf{f}_2^S + \omega_2^2\mathbf{p}_2^S \\ \vdots \\ \mathbf{f}_m^S + \omega_m^2\mathbf{p}_m^S \end{Bmatrix}, \tag{3.15}$$

where

$$\mathbf{B}_i = \mathbf{Q}_i^T\mathbf{Q}_i - \mathbf{Q}_1^T\mathbf{Q}_1,$$

$\mathbf{diag}\,(\bullet)$ denotes a diagonal matrix, l is the number of retained tuned-system modes, and p^S_{ki} is the ith element of $\mathbf{p^S_k}$. By solving these linear equations, both tuned-system eigenvalues and blade mistuning values can be obtained. Then, a CMM model can be updated by replacing $\mathbf{\Lambda^S}$ in Eq. (3.1) with the identified tuned-system eigenvalues.

In order to assess the effectiveness of ROM updating, the identification was performed in the same way as in section 3.3, but Eq. (3.15) was applied. Again, 100 sets of modeling parameters and measured data ($\mathbf{Q}$, $\mathbf{U}_{meas}$, and $\mathbf{x}_{meas}$) with random errors and noise were used, and the identification results are depicted in Fig. 3.7. Note that there was no need to simulate the errors in $\mathbf{\Lambda}^S$, because the new updating technique provides for its identification (thus effectively removing the primary factor of high sensitivity in the identification process). Observe that the accuracy of the identified mistuning and mistuned-system natural frequencies is significantly improved compared with that in Fig. 3.6(f). Also, the updated tuned-system natural frequencies match well with the exact values overall. This means that the ROM has been successfully updated. Still, the updated tuned-system frequency at 4 nodal diameters, as well as the mistuned-system frequencies of the 1st and 2nd modes, are not in good agreement with the exact values. This is because the resonant peak around 1.99 kHz is very small relative to the other peaks. In fact, the two mode shapes around 1.99 kHz are nearly the same as the tuned-system modes with 4 nodal diameters, and thus they are not significantly excited by an engine order 7 excitation.

Therefore, the forced response was computed again, by applying engine 4 excitation to the mistuned FEM of the validation bladed disk, in order to obtain large resonant peaks around 1.99 kHz. The results are plotted in Fig. 3.8, where the dotted line marks the same resonant frequency around 1.99 kHz as in Fig. 3.3. Then, the response data at 1.99 kHz obtained by applying engine order 7 excitation were replaced with the new response data obtained with engine order 4 excitation, and the identification was performed in the same way as above. The results are displayed in Fig. 3.9. As can be seen in Fig. 3.9(a) and 3.9(c), the highest and the lowest values of all the updated tuned-system frequencies and mistuned-system frequencies are very close to the exact values. Therefore, it can be concluded that tuned-system frequencies and blade mistuning can be identified accurately using the developed method, as long as response data are measured at large resonant peaks.

As another validation test for ROM updating, the forced response generated from the updated CMM model was compared with that of the mistuned FEM. First, only blade mistuning was identified using a set of modeling parameters and measured data with errors. Of course the resulting tuned-system natural frequencies are a bit in error, and they are shown in Fig. 3.10. Using the identified mistuning pattern, the forced response was obtained from the CMM model with these slightly incorrect tuned-system natural frequencies, by applying engine order 7 excitation. The CMM results are compared with the FEM results in Fig. 3.11(a), where at every excitation frequency only the largest blade amplitude is plotted so as to provide the response envelope. As can be seen, the non-updated CMM results are poor. Next, both blade mistuning and tuned-system natural frequencies were identified, and the CMM model was updated. Figure 3.11(b) shows the forced response results obtained by the updated CMM model and by the FEM. It can be observed that both results match extremely well.

3.5 Conclusions

A method for the identification of blade mistuning in bladed disks has been developed. In this approach, the equation of motion for a reduced-order model built by a component mode mistuning technique [44] is transformed to obtain a set of linear equations. Thereby, blade mistuning is determined by solving a least-squares problem. This identification method was numerically validated using the FEM of a validation bladed disk. The response data by the FEM were treated as measured data. Also, a sensitivity study was performed analytically, and numerically by adding errors and noise intentionally to modeling parameters and FEM response data. It was found that the accuracy of the identification results is very sensitive to the errors in the tuned-system eigenvalues.

The concept of “cyclic modeling error” has been introduced, which is the difference between a tuned FEM on which a CMM model is based and the virtual tuned system of an actual bladed disk. It was shown that the cyclic modeling error appears as a matrix that is exactly or approximately diagonal in the CMM formulation, so that the modeling errors can be interpreted as the errors in tuned-FEM eigenvalues, which are critical to the accuracy of the mistuning identification results.

The original identification method has been modified by considering tuned-system eigenvalues as well as blade mistuning as the unknowns. Using the identified tuned-system eigenvalues, a CMM model is updated such that the cyclic modeling error is compensated for. As a result, the accuracy of the identified mistuning values is significantly improved. The modified method was numerically validated using the same bladed-disk FEM. Also, it has been demonstrated that the forced response results generated by an updated CMM model are in very good agreement with the FEM results, even if errors are present in modeling parameters and response data. Therefore, it can be concluded that the new method developed is robust with respect to the errors in the parent FEM and measurements, and that a CMM model updated in this way can provide accurate predictions of the forced response of actual mistuned bladed disks.

3.6 Figures

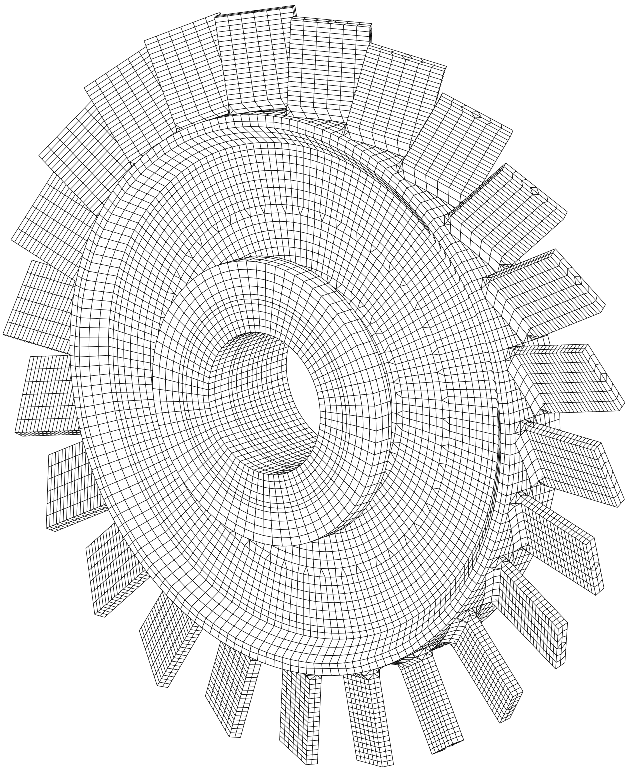

Figure 3.1: Finite element mesh of a 24-blade validation bladed disk.

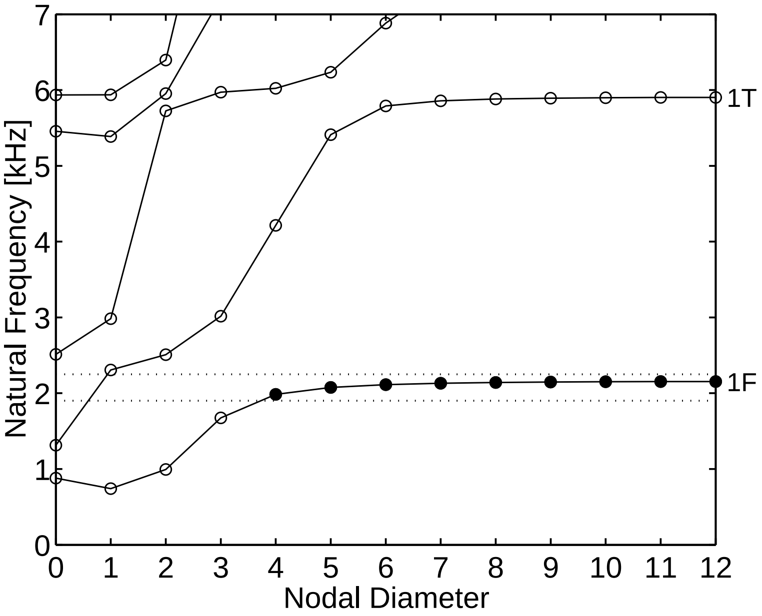

Figure 3.2: Natural frequencies of the validation bladed disk.

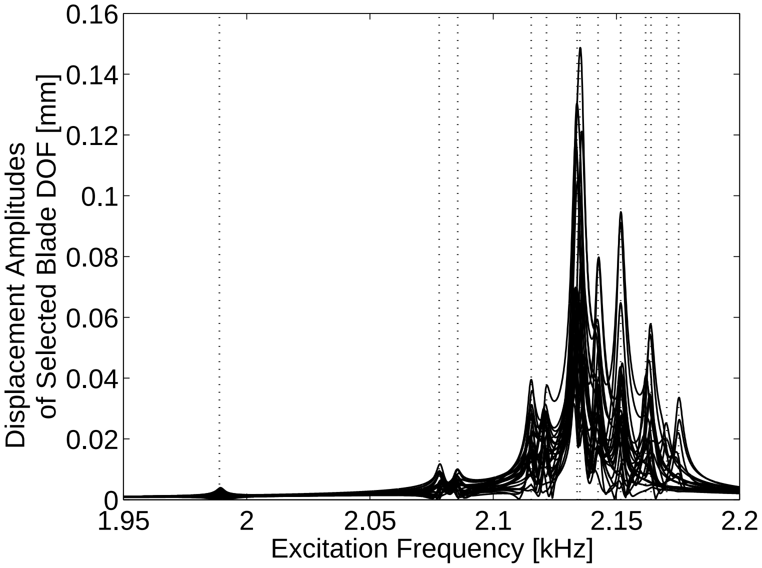

Figure 3.3: Forced response of blades subject to engine order 7 excitation.

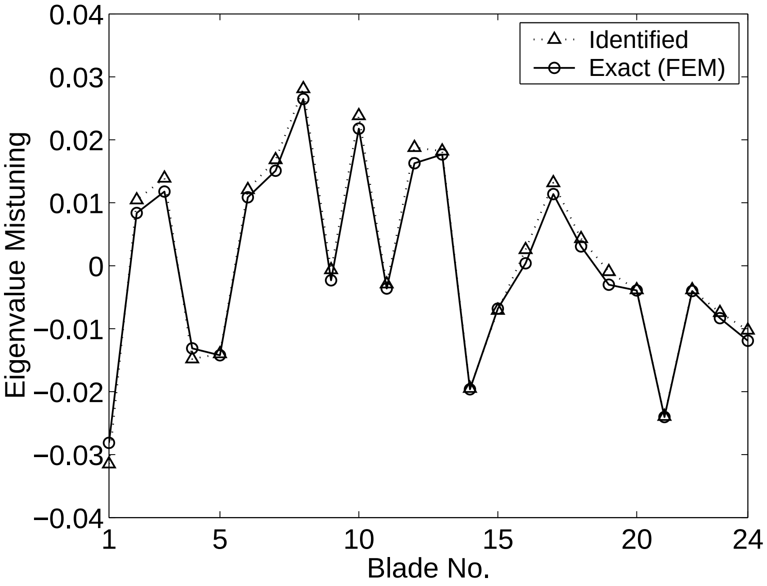

Figure 3.4: Identified eigenvalue mistuning.

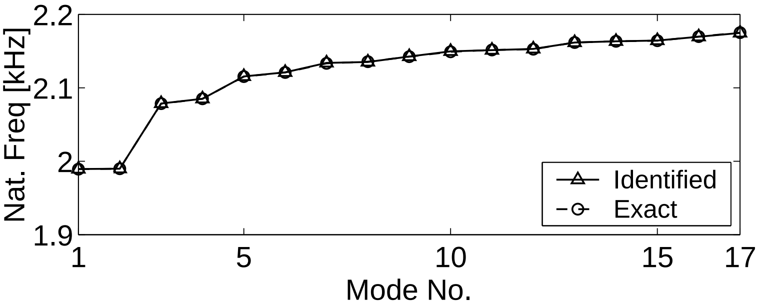

(a) Mistuned-system natural frequencies

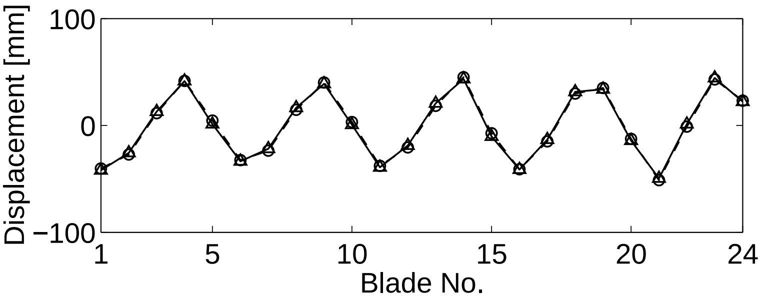

(b) 3rd mode shape at 2.079 kHz

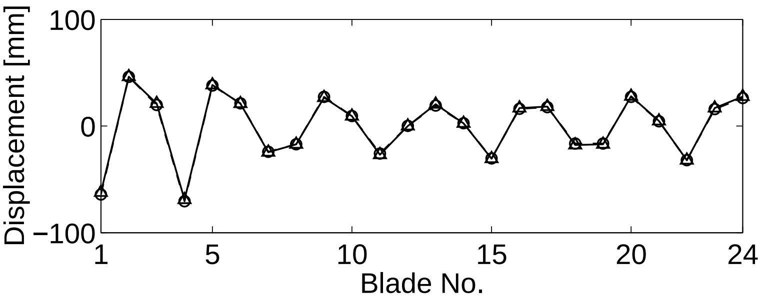

(c) 8th mode shape at 2.136 kHz

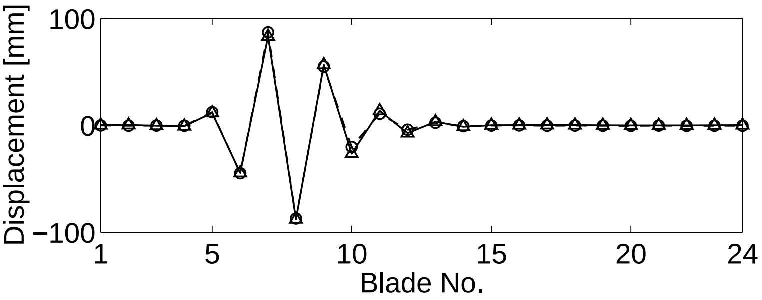

(d) 17 mode shape at 2.175 kHz

Figure 3.5: Free response results from a 17-DOF CMM model with the identified mistuning.

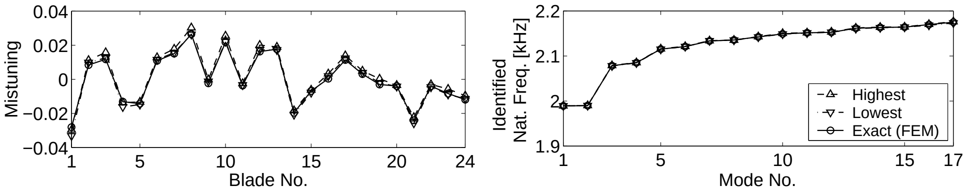

(a) With 5% random errors in $\mathbf{Q}$

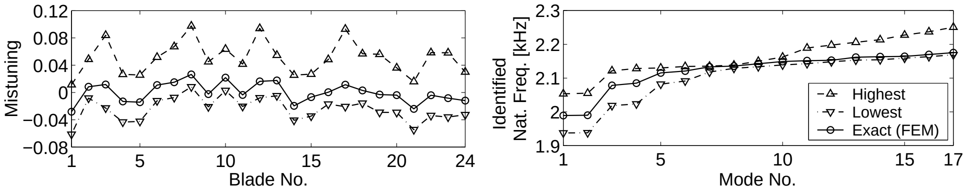

(b) With 5% random errors in $\mathbf{\Lambda}^S$

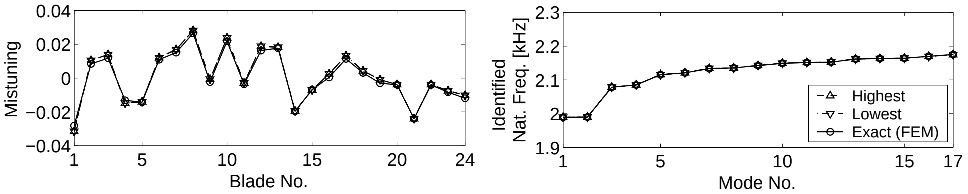

(c) With 5% random errors in γ

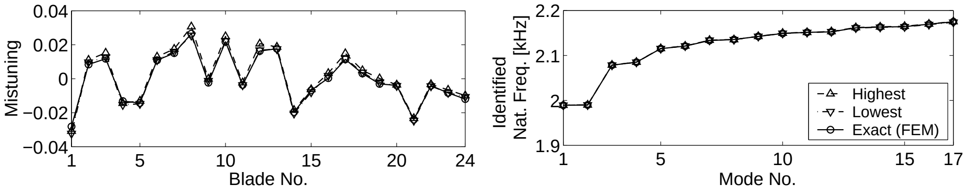

(d) With 5% random errors in $\mathbf{U}_{meas}$

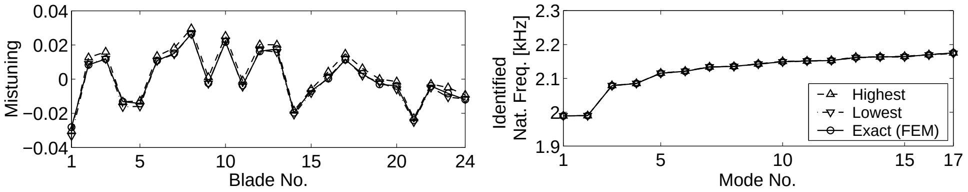

(e) With 1% random noise in $\mathbf{x}_{meas}$

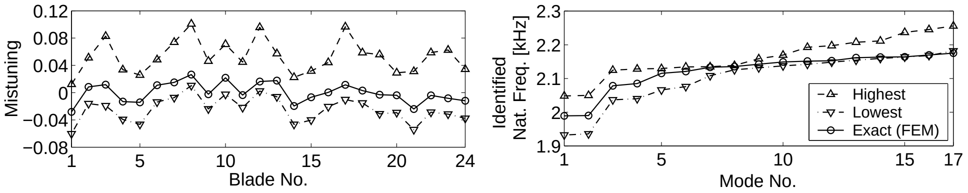

(f) With all the above errors and noise

Figure 3.6: Sensitivity of identification results to errors in model parameters and measured data.

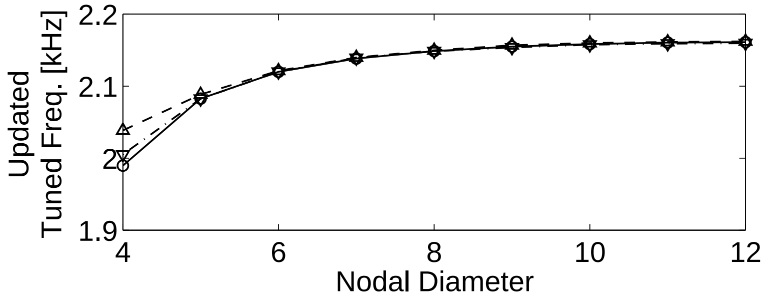

(a) Updated tuned-system natural frequencies

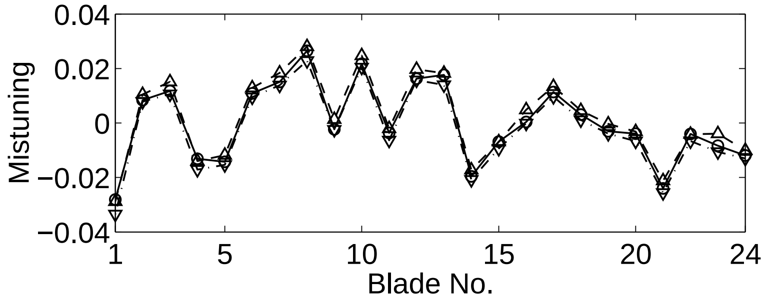

(b) Identified eigenvalue mistuning

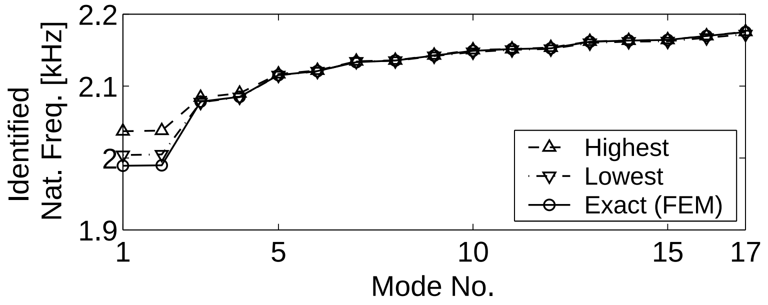

(c) Resulting mistuned-system natural frequencies

Figure 3.7: Identification results with ROM updating in the presence of random errors in all the modeling parameters and the measured data.

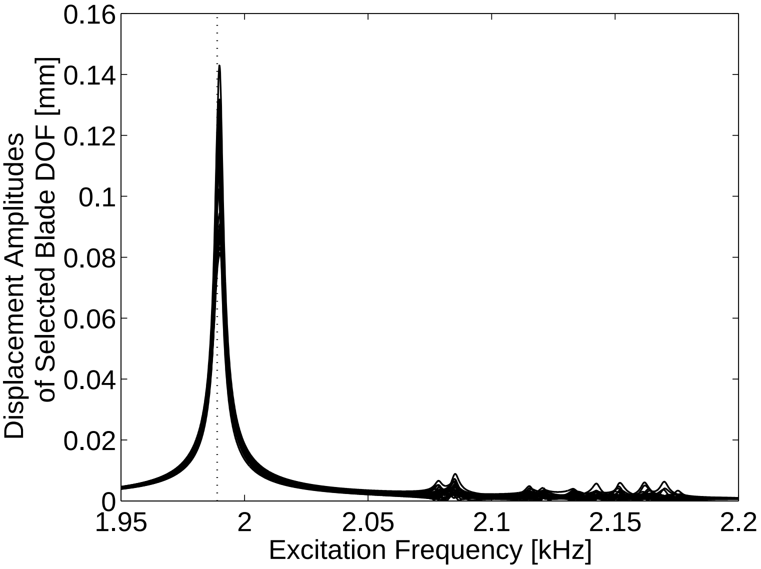

Figure 3.8: Forced response of blades subject to engine order 4 excitation.

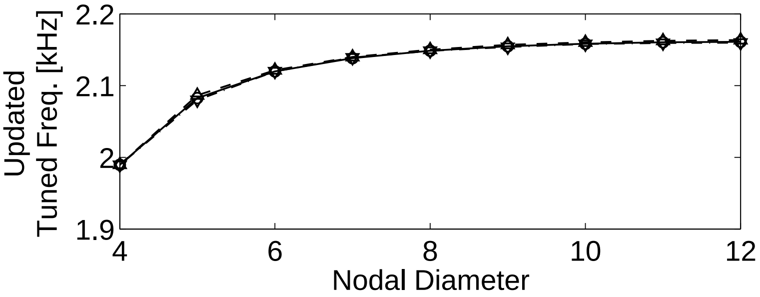

(a) Updated tuned-system natural frequencies

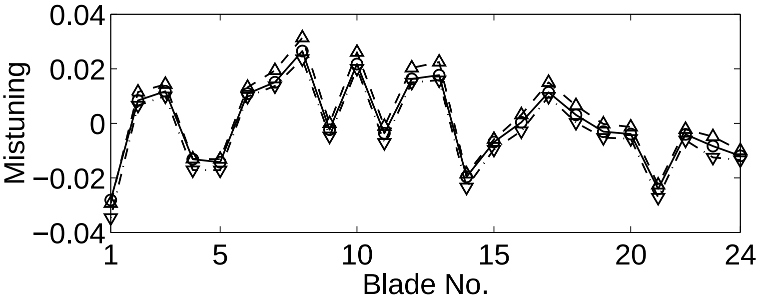

(b) Identified eigenvalue mistuning

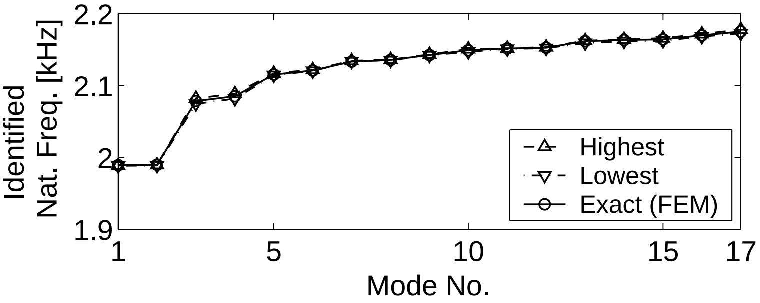

(c) Resulting mistuned-system natural frequencies

Figure 3.9: Identification results with ROM updating when all the data are measured at large resonant peaks.

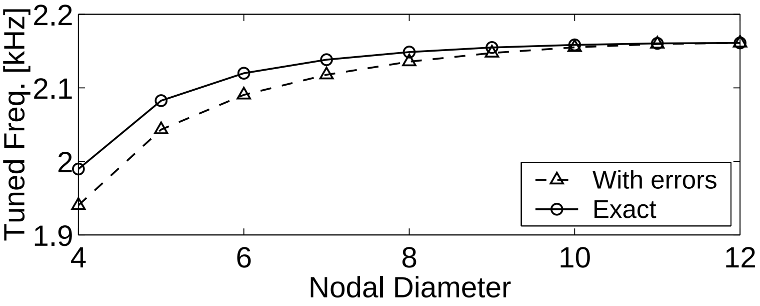

Figure 3.10: Tuned-system natural frequencies with errors.

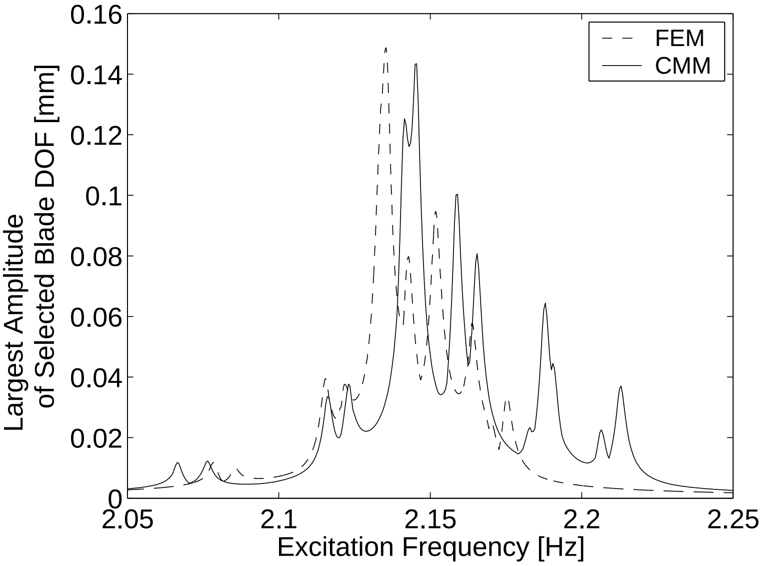

(a) Without ROM updating

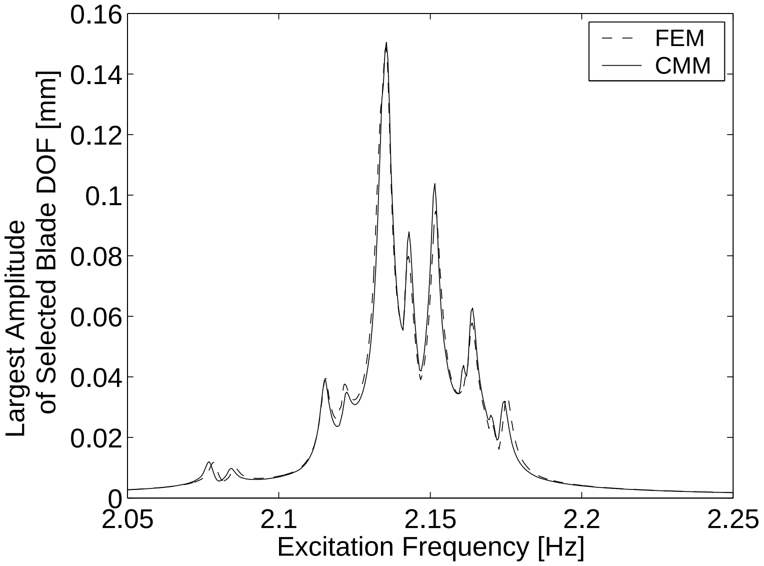

(b) With ROM updating

Figure 3.11: Forced response generated from a CMM model subject to engine order 7 excitation using identification results.

CHAPTER IV

Upper Bounds for Bladed-Disk Forced-Response Amplification Due to Mistuning

Two methods for calculating the upper bound of the mistuning-induced forced-response amplification for blades in bladed disks are presented. In the first method, the upper bounds of blade displacement, velocity, and stress are derived from the maximum vibration energy that can be concentrated into a single blade in lumped parameter models with a single or two degrees of freedom (DOF) per sector, and the obtained upper bound does not depend on the engine order of excitation. It is seen that, if mistuning is small, the blade response normalized by the resonant response of a cantilevered blade is bounded around $(1+\sqrt{N_b})/2$, where N_b is the number of blades in a bladed disk. In another method, the upper bound is obtained by superposing a set of traveling wave modes with closely spaced natural frequencies of a tuned bladed disk. This method is applicable to any bladed disk model. The amplitudes of the traveling waves for a multi-DOF-per sector model are usually different from each other when they are normalized with respect to the mass matrix. Therefore, the latter method yields different upper bounds according to the engine order of excitation. Furthermore, since only closely spaced modes are involved in the calculation, upper bounds lower than those by the first method can be obtained. The latter method is demonstrated using a 2-DOF-per-sector model and a finite element model of an advanced bladed disk.

4.1 Introduction

A nominal design of a bladed disk consists of identical blade-disk sectors. However, there are always slight differences among the blades in a real bladed disk which are called mistuning. Due to mistuning, vibration energy in a bladed disk can be concentrated into a few blades, and the forced-response level of those blades is significantly increased causing high-cycle fatigue problems. Therefore, there has been a large amount of research work about the effect of mistuning. Especially, many efforts have been made to find the maximum blade forced-response level that can be reached due to mistuning, because it is important information in view of design safety.

Typically, blade forced-response level is represented by the amplification factor that is the ratio of the largest blade response in a mistuned system to that in the tuned system. Some researchers [2, 24–28, 55] have derived analytical forms for the maximum amplification factor that is the upper bound of blade-response amplification. Whitehead [2, 24, 25] obtained the famous maximum amplification factor of $(1+\sqrt{N_b})/2$, where N_b is the number of blades in a bladed disk, using a model with a single degree of freedom (DOF) per sector. MacBain and Whaley [55] also derived a closed form expression for the maximum resonant response using a pair of modes with the same number of nodal diameters but different frequencies. However, MacBain and Whaley did not consider the distortion of mode shapes that is also caused by mistuning. In contrast, Kenyon *et al.* [27] reported another study on the maximum forced-response amplification in view of mode shape distortion using a simple 1-DOF-per-sector lumped parameter model. In their work, it was shown that the Whitehead's maximum factor cannot be reached for the simple model with structural mistuning, unless the excitation engine order (EO) is equal to 0 or $N_b/2$ for N_b even, but it was also mentioned that the Whitehead's maximum can be approximated by combining the effects of mode distortion and frequency splitting. Rivas-Guerra and Mignolet [28] also obtained similar results that Whitehead's maximum factor is exactly (for EO$= 0$ or $N_b/2$ if N_b is even) or approximately (for other engine orders) recovered. They also used a 1-DOF-per-sector model.

However, a 1-DOF-per-sector lumped parameter model may not represent an actual bladed-disk design appropriately. Therefore, some studies have been focused on finding the maximum amplification using optimization algorithms [28, 56–59]. Although an optimization process may be applied to any bladed-disk model, it can be expensive when the number of blades is large. Furthermore, blade response is so sensitive to mistuning that the solution may converge to a local maximum not the global maximum. There has been another type of research for determining the statistics of the amplification factors analytically [60, 61] or via accelerated Monte Carlo simulations [29, 39], but the statistics does not provide the maximum amplification. Actually, the maximum amplification factor is required for the accelerated Monte Carlo simulations.

As mentioned above, the amplification factor is a measure relative to a tuned-system resonant response. The amplitudes of tuned-system resonant response of 1-DOF-per-sector models used in the literature are exactly or almost the same for the entire engine orders of excitation. Therefore, the amplification factor could represent the absolute response level. However, for more complicated models where blade DOF and disk DOF exist separately, one can observe the loci of tuned-system natural frequency veer (see for example Fig. 4.5). The tuned modes in a veering region usually have smaller blade displacements than the others so that the tuned system shows smaller resonant blade response when subject to the engine order excitation corresponding to the veering region. In this case, the traditional amplification factor does not measure the absolute level of response, and also the amplification factor can be unbounded as mentioned in Kenyon and Griffin's work [62]

This study is focused on finding closed form expressions of the upper bound of blade response. First, the upper bound of the response of a 1-DOF-per-sector model is revisited by investigating the relation between the amplitude of blade response and the vibration energy input through coupling. When Whitehead [25] derived the maximum amplification factor of $(1+\sqrt{N_b})/2$, hysteretic damping was used. In this study, viscous and structural damping cases as well as hysteretic damping case are examined, and it is shown that Whitehead's maximum factor can be exceeded even in case of a 1-DOF-per-sector model when viscous or structural damping is used. Furthermore, this approach is extended to a 2-DOF-per-sector model, and it is found that, if blade response is normalized by the resonant response of a tuned, cantilevered blade, the ratio is bounded around $(1+\sqrt{N_b})/2$. Since cantilevered-blade response is irrelevant to the engine order of excitation, the ratio can represent the absolute level of blade response.

Also, Whitehead's approach, which is to superpose all the traveling wave modes, is extended to multi-DOF-per-sector models. Recently, Yang and Griffin [42] reported that, when a system has a group of modes closely spaced in a narrow frequency range, the motion of a system slightly mistuned from the system can be approximately described with the closely spaced modes of the original system. And, some reduced-order models for bladed disks have been developed according to this concept [23, 44]. In this study, this concept is used to select a small set of traveling wave modes of multi-DOF-per-sector models to be superposed. Finally, a generalized expression for the upper bound of blade response is obtained, which gives different values for different systems and for different engine orders of excitation. Although the upper bound obtained this way may be unreachable as Whitehead's maximum factor, it is still believed to approximate the real limit of the maximum blade response with negligible cost. And, it is demonstrated that this approach allows lower upper bounds for a 2-DOF-per-sector model than that obtained using the approach mentioned in the previous paragraph.

The stress levels may be computed by post-processing the reduced-order model results with finite element analysis, but this is cumbersome and expensive. In this work, three indicators that can be calculated directly from reduced-order models are also proposed as a way to estimate blade stress levels in a straightforward, systematic, and inexpensive manner. It is shown that these indicators can be used to predict stress values with good accuracy relative to finite element results, even for a case in which the displacement and stress levels show different frequency response trends.

One of the contributions of this paper is that the increase of blade response is bounded around Whitehead's maximum factor, if the reference is the resonant response of a tuned, cantilevered blade, not that of a blade in a tuned bladed disk. Another contribution is the generalization of Whitehead's approach for multi-DOF-per-sector models.

This paper is organized as follows. The relation between the amplitude of blade response and the vibration energy input through coupling is investigated to find the upper bound in section 4.2. In section 4.3, the generalized form of upper bound is derived by extending Whitehead's approach, and applied to a 2-DOF-per-sector model and a finite element model of an advanced bladed disk. In section 4.4, three indicators for predicting blade stress levels directly from reduced-order models of bladed disks are proposed and validated. Finally, conclusions are summarized in section 4.5.

4.2 Energy Concentration through Coupling

The upper bound of blade response in a bladed disk is investigated using the possible maximum amount of vibration energy concentration into a single blade or sector. To do this, the response of a blade is related with the energy input to the blade through coupling using lumped parameter models shown in Fig. 4.1. Each sub-figure shows a single sector of the tuned models. The model in Fig. 4.1(a) has only one blade DOF in each sector, with tuned mass m_b and tuned stiffness k_b. Each blade DOF is directly coupled to other blades. The other one in Fig. 4.1(b) has a blade DOF and a disk DOF in each sector, with disk mass m_d and disk stiffness k_d. For this model, each disk DOF is coupled to other disk DOF. Thus, for the 1-DOF-per-sector model, energy flow among sectors depends on blade displacements, but for the 2-DOF-per-sector model, it depends on disk displacements.

In this study, every mass and stiffness are normalized by the blade mass m_b and stiffness k_b. Displacements, velocities, stresses, and frequencies are also normalized by the largest responses and natural frequency of a tuned, cantilevered blade. Thereby, in this section, all the results are obtained in non-dimensionalized forms. For the forced response, engine order excitations are applied, and only steady-state responses are considered. Mistuned models are generated by adding stiffness variations to the tuned blade stiffnesses. The ith mistuned stiffness is expressed as

$$k_{b,i} = k_b(1 + \delta_i), \tag{4.1}$$

where δ_i is the ith mistuning value.

4.2.1 1-DOF-per-sector model

There are two energy input source for a sector. One is from external forcing, and the other is from other sectors via coupling. These energy sources are balanced with the energy dissipation by damping. In this study, three cases of different damping representations are investigated: hysteretic, viscous, and structural damping. Here, hysteretic damping force is assumed to be proportional to displacement, as in Whitehead's work [25], while structural damping force is proportional to stiffness as well as displacement. Therefore, if stiffness is mistuned, the damping force by structural damping will be different from that by hysteretic damping for the same displacement. For viscous damping, the damping force is proportional to velocity.

First, hysteretic damping is considered. The damping force is written as follows:

$$f_i^d = -jc_h x_i, \tag{4.2}$$

where j is $\sqrt{-1}$, c_h is the damping coefficient, and x_i is the displacement of blade i. Therefore, the average energy dissipated in blade i over a period of oscillation is

$$E_i^d = \frac{1}{2}\mathrm{Re}\left(-jc_h x_i v_i^*\right) = \frac{1}{2}c_h \omega |x_i|^2, \tag{4.3}$$

where v_i^* is the complex conjugate of the velocity of blade i. And, the average energy input to blade i by external forcing is

$$E_i^f = \frac{1}{2}\mathrm{Re}\left(f_i^e v_i^*\right) = \frac{1}{2}\omega F^e |x_i| \sin(\Delta\theta), \tag{4.4}$$

where f_i^e is the external force applied to the ith blade, F^e is the amplitude of the external force, and $\Delta\theta$ is the phase of f_i^e subtracted by the phase of x_i. Because engine order excitations are assumed, the forces applied to the blades have the same amplitude, but different phases.

Therefore, the average energy input to blade i through coupling can be written using Eqs. (4.3) and (4.4) as follows:

$$E_i^c = E_i^d - E_i^f = \frac{\omega}{2}\left(c_h |x_i|^2 - F^e |x_i| \sin(\Delta\theta)\right). \tag{4.5}$$

Now, a displacement amplification factor, which is the ratio of $|x_i|$ to the resonant response of a tuned, cantilevered blade, $|x_{cb}|$, is introduced as follows:

$$q_i = |x_i|/|x_{cb}|, \tag{4.6}$$

where $|x_{cb}|$ is obtained by applying the force of the same amplitude as that of the engine order excitation. Since the resonant frequency is the natural frequency for a 1-DOF system with the hysteretic damping, the resonant response is

$$|x_{cb}| = \frac{F^e}{c_h}, \quad \text{or} \quad F^e = c_h|x_{cb}|. \tag{4.7}$$

Inserting Eqs. (4.6) and (4.7) into Eq. (4.5), and normalizing E_i^c with $(c_h\omega|x_{cb}|^2)/2$, the following equation is obtained:

$$\bar{E}_i^c = q_i^2 - q_i \sin(\Delta\theta), \tag{4.8}$$

where $\bar{E}_i^c$ is the normalized energy input to blade i through coupling. Hence, $\bar{E}_i^c$ is bounded as follows:

$$q_i^2 - q_i \leq \bar{E}_i^c \leq q_i^2 + q_i. \tag{4.9}$$

The derived relation in Eq. (4.9) shows that the normalized energy is limited by the displacement amplification relative to the cantilevered-blade resonant response, and vice versa.

To verify this relation, 1,000 mistuned systems with 12 blades were simulated. For simplicity, each blade DOF was coupled to only two adjacent blades by springs of stiffness k_c. In the tuned system, k_c/k_b was set to be 0.01, which is the value that was used for a weakly coupled system by Wei and Pierre [10], and c_h/k_b was set to be 0.002. Mistuning values were generated by a random number generator in MATLAB, and the used standard deviation of random mistuning was 0.012, because the systems show large increase in blade forced response for this mistuning level. For external forcing, engine order 3 excitation was used.

From each mistuned system, an excitation frequency at which the largest blade response is found was identified using a golden section search method. At that frequency, the response results for all 12 blades were collected. Thus, these simulations yielded 12,000 blade response results, and they are depicted in Fig. 4.2. As can be seen, all the simulation results appear between the two theoretical limit curves, $q_i^2 - q_i$ and $q_i^2 + q_i$. Note that a negative value of normalized energy input indicates a net energy drain to other blades, and that the maximum normalized energy drain is $1/4$ from Eq. (4.9).

Now, consider the worst case in which all the energy drain flows into a single blade. In this case, the maximum amount of the normalized energy input through coupling that the blade can receive is $(N_b - 1)/4$. Therefore, the possible maximum value of q_i is obtained from the following equation:

$$q_i^2 - q_i = (N_b - 1)/4, \tag{4.10}$$

and the value is $(1 + \sqrt{N_b})/2$, which is the factor that Whitehead found $[2, 25]$. Note that Whitehead used the ratio of the largest blade response in a mistuned bladed disk to that in the tuned bladed disk as the amplification factor. Since the largest blade response in a tuned bladed disk with hysteretic damping is the same as the cantilevered-blade resonant response for a 1-DOF-per-sector lumped parameter model, it is no surprise that the obtained maximum factor here is the same as Whitehead's maximum factor.

The next case is for viscous damping. The damping force can be written as:

$$f_i^d = -c_v v_i, \tag{4.11}$$

where c_v is the viscous damping coefficient. Therefore, the average energy dissipation is

$$E_i^d = \frac{1}{2} c_v |v_i|^2, \tag{4.12}$$

and the average energy input to blade i through coupling can be written as follows:

$$E_i^c = \frac{1}{2} \left(c_v |v_i|^2 - F^e |v_i| \cos(\Delta\theta) \right) . \tag{4.13}$$

This equation is similar to Eq. (4.5), but it is written with v_i ,not with x_i. Therefore, a velocity amplification factor is introduced in a similar way:

$$r_i = |v_i|/|v_{cb}|, \tag{4.14}$$

where v_{cb} is the largest velocity of a tuned, cantilevered blade, which occurs at the natural frequency, not the resonant frequency of displacement. And, the value is

$$|v_{cb}| = \frac{F^e}{c_v}, \quad \text{or} \quad F^e = c_v|v_{cb}|. \tag{4.15}$$

Inserting Eqs. (4.14) and (4.15) into Eq. (4.13), and normalizing E_i^c with $(c_v|v_{cb}|^2)/2$, which is the average dissipated energy in a tuned, cantilevered blade at the natural frequency, the following equation is obtained:

$$\bar{E}_i^c = r_i^2 - r_i \cos(\Delta\theta). \tag{4.16}$$

And, $\bar{E}_i^c$ is limited by the velocity amplification as follows:

$$r_i^2 - r_i \leq \bar{E}_i^c \leq r_i^2 + r_i. \tag{4.17}$$

The same mistuned systems as previously used for hysteretic damping were simulated to verify the relation in Eq. (4.17), but viscous damping was used with $c_v/\sqrt{m_b k_b}$ being 0.002. Also, the same engine order excitation was applied. The results are shown in Fig. 4.3, and they are all between the two theoretical limit curves, $r_i^2 - r_i$ and $r_i^2 + r_i$. In the same way as for hysteretic damping, $(1 + \sqrt{N_b})/2$ is obtained again for the possible maximum value of r_i.

Now, the case of structural damping is investigated. The damping force on blade i is written as follows:

$$f_i^d = -jc_s k_b(1 + \delta_i)x_i, \tag{4.18}$$

where c_s is structural damping ratio which is non-dimensional. Therefore, the average energy dissipation is

$$E_i^d = \frac{1}{2} c_s k_b (1+\delta_i)\omega |x_i|^2. \tag{4.19}$$

Hence, the average energy input to blade i through coupling is

$$E_i^c = \frac{\omega}{2} \left(c_s k_b (1+\delta_i)|x_i|^2 - F^e |x_i| \sin(\Delta\theta) \right). \tag{4.20}$$

The stress level in the lumped parameter models can be represented by $k_b(1+\delta_i)|x_i|$. Thus, a stress amplification factor can be defined as follows:

$$p_i = \frac{k_b(1+\delta_i)|x_i|}{k_b|x_{cb}|} = (1+\delta_i)|x_i|/|x_{cb}|, \tag{4.21}$$

where x_{cb} is the resonant response of a tuned, cantilevered blade at its natural frequency. That is,

$$|x_{cb}| = \frac{F^e}{c_s k_b}, \quad \text{or} \quad F^e = c_s k_b |x_{cb}|. \tag{4.22}$$

Again, by inserting Eqs. (4.21) and (4.22) into Eq. (4.20), and normalizing with $(c_s k_b \omega |x_{cb}|^2)/2$, the following relation is obtained:

$$p_i^2 - p_i \leq (1+\delta_i)\bar{E}_i^c \leq p_i^2 + p_i. \tag{4.23}$$

Note that $1+\delta_i$ term still appears the above relation. Simulations for the previous 1,000 mistuned systems were performed with structural damping ratio (c_s) of 0.002, and the results in Fig. 4.4 verify the relation in Eq. (4.23).

Since the maximum normalized energy drain from blade n is $1/4(1+\delta_n)$, the possible maximum value of p_i is obtained from the following equation:

$$p_i^2 - p_i = (1+\delta_i) \sum_{\substack{n=1 \\ n\neq i}}^{N_b} \frac{1}{4(1+\delta_n)}. \tag{4.24}$$

Therefore, the maximum stress amplification depends on mistuning. However, it can be said that, for small mistuning, the maximum stress amplification is approximately $(1 + \sqrt{N_b})/2$.

So far, the amplification of displacement, velocity, and stress has been investigated for the lumped parameter models with hysteretic, viscous, and structural damping, respectively. From the possible maximum vibration energy concentration into a single blade, the upper bounds of the amplification were obtained. When hysteretic damping is used, the upper bound of displacement amplification is the same as Whitehead's maximum amplification factor, $(1 + \sqrt{N_b})/2$. However, a displacement amplification factor larger than $(1 + \sqrt{N_b})/2$ is possible when viscous or structural damping is used, even for a 1-DOF-per-sector model. Similarly, velocity amplification for a bladed disk with hysteretic or structural damping can exceed $(1+\sqrt{N_b})/2$. As a test case, 1-DOF-per-sector models with 3 blades were investigated to find the mistuning patterns that give blade displacement amplification larger than Whitehead's maximum factor (1.3660 for a 3-blade system), when viscous and structural damping is used. For this, a function in the optimization toolbox of MATLAB was used with a constraint that all the blade mistuning values are between $-0.03\sqrt{3}$ and $0.03\sqrt{3}$ that are the limits of a uniform distribution with the standard deviation of 0.03. The same model parameters as previously used were used again, but engine order 0 excitation was applied. Table 4.1 shows examples of the found mistuning values and displacement amplification values.

However, displacement, velocity, and stress amplification factors are almost the same for small mistuning. Note that the locations of the data points in Figs. 4.2, 4.3, and 4.4 are almost the same. This means that Whitehead's maximum amplification factor can be used as an approximate upper bound of any amplification for 1-DOF-per-sector models.

4.2.2 2-DOF-per-sector model

Now, the energy concentration in 2-DOF-per-sector models described in Fig. 4.1(b) is discussed. Here, only the hysteretic damping case is investigated, because the upper bounds of velocity and stress amplification for viscous and structural damping can be obtained in similar ways and will be almost the same as that of displacement amplification for hysteretic damping if mistuning is small. And, not only blade DOF but also disk DOF are subject to hysteretic damping. For external forcing, engine order excitations are used again, but only on blade DOF.

If hysteretic damping is used for both blades and disk, the expression for the damping force on blade i will be the same as Eq. (4.2) for a 1-DOF-per-sector model, and the damping force on disk sector i can be written as follows:

$$f^d_{i,disk} = -j\alpha_h c_h x_{i,disk}, \tag{4.25}$$

where α_h is the ratio of the disk damping coefficient to the blade damping coefficient (c_h), and $x_{i,disk}$ is the displacement of the disk DOF. Hence, the average dissipation energy in sector i is

$$E^d_i = \frac{1}{2}c_h\omega|x_{i,blade}|^2 + \frac{1}{2}\alpha_h c_h\omega|x_{i,disk}|^2, \tag{4.26}$$

where $x_{i,blade}$ is the displacement of the blade DOF. Thus, the average energy input to sector i through coupling becomes

$$E^c_i = \frac{\omega}{2}\left(c_h|x_{i,blade}|^2 + \alpha_h c_h|x_{i,disk}|^2 - F^e|x_{i,blade}|\sin(\Delta\theta)\right). \tag{4.27}$$

Normalizing with $(c_h\omega|x_{cb}|^2)/2$ again, the above equation can be re-written in a non-dimensionalized form as follows:

$$\bar{E}^c_i = q^2_{i,blade} + \alpha_h q^2_{i,disk} - q_{i,blade}\sin(\Delta\theta), \tag{4.28}$$

where $q_{i,blade} = |x_{i,blade}|/|x_{cb}|$, and $q_{i,disk} = |x_{i,disk}|/|x_{cb}|$. From this equation, it can be seen that the maximum energy drain from a single sector is 1/4, if $\alpha_h q_{i,disk}^2$ is small enough to be neglected. In that case, the maximum normalized energy concentration to sector i through coupling becomes $(N_b - 1)/4$, and the maximum value of $q_{i,blade}$ is obtained as $(1 + \sqrt{N_b})/2$ from the following equation:

$$q_{i,blade}^2 + \alpha_h q_{i,disk}^2 - q_{i,blade} = (N_b - 1)/4. \tag{4.29}$$

However, blade stress level may be represented by the blade displacement relative to the corresponding disk displacement. That is, $|x_{i,blade} - x_{i,disk}|$ is more meaningful than $|x_{i,blade}|$, and so is the upper bound of $|x_{i,blade} - x_{i,disk}|/|x_{cb}|$. Since

$$|x_{i,blade} - x_{i,disk}|/|x_{cb}| \leq |x_{i,blade}|/|x_{cb}| + |x_{i,disk}|/|x_{cb}| = q_{i,blade} + q_{i,disk},$$

the maximum value of $q_{i,blade} + q_{i,disk}$ can be used as the upper bound for $|x_{i,blade} - x_{i,disk}|/|x_{cb}|$.

The derivative of $q_{i,blade} + q_{i,disk}$ is zero at its maximum. That is,

$$\frac{\mathrm{d}(q_{i,blade} + q_{i,disk})}{\mathrm{d}q_{i,blade}} = 1 + \frac{\mathrm{d}q_{i,disk}}{\mathrm{d}q_{i,blade}} = 0. \tag{4.30}$$

Also, differentiating Eq. (4.29) with respect to $q_{i,blade}$, the following equation is also obtained:

$$2q_{i,blade} + 2\alpha_h q_{i,disk} \frac{\mathrm{d}q_{i,disk}}{\mathrm{d}q_{i,blade}} - 1 = 0. \tag{4.31}$$

Finally, from Eqs. (4.29), (4.30), and (4.31),

$$(q_{i,blade} + q_{i,disk})_{\max} = \frac{1}{2}\left(1 + \sqrt{\frac{\alpha_h + 1}{\alpha_h} N_b}\right). \tag{4.32}$$

That is, the upper bound of $|x_{i,blade} - x_{i,disk}|$ is larger than that of $|x_{i,blade}|$. However, if the disk DOF displacement is so small that $\alpha_h q_{i,disk}^2$ is negligible, which is the usual case for bladed disks, the upper bound of the relative displacement will be also around $(1+\sqrt{N_b})/2$.

Note that blade response amplification was defined in this section based on the response of a tuned, cantilevered blade, although the amplification factor is traditionally based on the blade response in a tuned bladed disk. The traditional amplification factor for the tuned bladed disk is always equal to 1, even if tuned-bladed-disk response varies with the engine order of excitation. Also, the traditional amplification factor is unbounded, because tuned-bladed-disk response may be very small for a certain engine order as reported by Kenyon and Griffin [62]. However, when blade response is normalized with the response of a tuned, cantilevered blade, the amplification factor for tuned-bladed-disk response may not be 1, but the upper bound of the amplification factor is around Whitehead's maximum factor.

4.3 Superposition of Closely Spaced Modes

As reported in Yang and Griffin's work [42], when a tuned bladed disk has modes with closely spaced natural frequencies, which is the usual case, slightly mistuned systems also have closely spaced modes in the same range, and the motion of mistuned systems can be approximated with the linear combination of the closely spaced tuned-system modes. Thus, here an alternative way to calculate the upper bounds of blade response is investigated using the idea that mistuned-system motion is the superposition of closely spaced tuned-system modes. The only constraint is that the dissipated energy in a system is equal to the energy input by external forcing.

In fact, Whitehead [2, 25] also used this approach for a 1-DOF-per-sector lumped parameter model. In his work, all the modes (traveling waves with the same amplitude) were used to calculate the maximum amplification with the above mentioned constraint, and all the modal masses were equal to 1. However, the traveling wave modes for a 2- or a multi-DOF-per-sector system can have amplitudes different from each other when normalized such that all the modal masses are equal. Furthermore, multiple modes with different natural frequencies but with the same interblade-phase angle can be present in a narrow frequency range where frequency veering is present, while a 1-DOF-per-sector model has only a single natural frequency for each interblade-phase angle. Therefore, the purpose of the investigation in this section is to generalize Whitehead's approach.

4.3.1 Derivation

It is assumed that a mistuned bladed disk is described using a small set of closely spaced tuned-system traveling-wave modes whose damping coefficients are not necessarily equal, and that only structural stiffness is mistuned. Then, the equation of motion can be written as follows:

$$\left[-\omega^2\mathbf{I} + j\mathbf{C} + \mathbf{\Lambda}_t + \Delta\boldsymbol{\kappa}\right]\mathbf{z} = \mathbf{g}, \tag{4.33}$$

where $\mathbf{C}$ is a diagonal matrix in which the ith diagonal term (c_i) is the damping coefficient corresponding to the ith tuned-system mode, $\mathbf{\Lambda}_t$ is a diagonal matrix of real tuned-system eigenvalues, $\Delta\boldsymbol{\kappa}$ is a Hermitian matrix containing the projection of structural stiffness mistuning onto tuned-system modes, $\mathbf{z}$ is a vector of the modal coordinates, and $\mathbf{g}$ is the vector of modal forces. Here, a pure engine order excitation is considered for external forcing so that $\mathbf{g}$ has non-zero, real terms only for the traveling wave modes corresponding to the engine order.

Premultiplying Eq. (4.33) by $\mathbf{z}^*$, the complex conjugate transpose of $\mathbf{z}$, and taking the imaginary part gives

$$\mathbf{z}^*\mathbf{C}\mathbf{z} = \sum_{i\in E}\mathrm{Im}(z_i^* g_i), \tag{4.34}$$

where E is a set of mode numbers corresponding to the engine order of excitation. Note that, since $\mathbf{z}^*\Delta\boldsymbol{\kappa}\mathbf{z}$ is Hermitian and scalar, $\mathbf{z}^*\Delta\boldsymbol{\kappa}\mathbf{z}$ is real. This equation indicates that the energy dissipation in the system is equal to the energy input by external forcing. Suppose an extreme case in which the phase of g_i leads the phase of z_i by $90\,^\circ$ so that the energy input is maximized. For this case, the above equation becomes

$$\sum_{i=1}^{N_m} c_i|z_i|^2 = \sum_{i\in E} |z_i||g_i|, \tag{4.35}$$

where N_m is the number of the retained traveling-wave modes, and this equation is used as the constraint.

Now, a quantity to be maximized needs to be determined. The quantity can be the absolute or relative displacement of blade DOF, or can be the modal displacement of a cantilevered-blade mode, if multiple DOF are used for a blade, such as the one in a finite element model. Note that the modal displacement of a cantilevered-blade mode can be considered similar to the relative displacement in a model with a single DOF for a blade. Since the worst case occurs when all the traveling wave modes are in phase at one blade, the quantity (physical or modal displacement) at the blade in such a situation is maximized. That is, the objective function is

$$\max\left(\sum_{i=1}^{N_m} a_i|z_i|\right),$$

where a_i is the amplitude of the displacement in the ith traveling wave mode. The derivative of the objective function is zero at its maximum. Therefore, $N_m - 1$ equations can be obtained as follows:

$$\frac{\partial|z_1|}{\partial|z_i|} = -\frac{a_i}{a_1} \quad \text{for } i = 2,\ldots,N_m. \tag{4.36}$$

Since there is one constraint equation, one modal coordinate need to be chosen as a dependent variable. Here, z_1 is chosen as the one, and it can be assumed that mode 1 is not in the set E without loss of generality.

Therefore, differentiating Eq. (4.35), and inserting Eq. (4.36), the relation between $|z_i|$ and $|z_1|$ is obtained as follows:

$$|z_i| = \begin{cases} \dfrac{c_1 a_i}{c_i a_1}|z_1| & \text{for } i \notin E, \text{ and } i \neq 1, \\ \dfrac{c_1 a_i}{c_i a_1}|z_1| + \dfrac{|g_i|}{2c_i} & \text{for } i \in E. \end{cases} \tag{4.37}$$

Now, inserting Eq. (4.37) into the constraint in Eq. (4.35), $|z_1|$ is obtained as follows:

$$|z_1| = \frac{a_1}{c_1}\sqrt{\frac{\sum\limits_{i\in E}|g_i|^2/4c_i}{\sum\limits_{i=1}^{N_m} a_i^2/c_i}}. \tag{4.38}$$

Then, $|z_i|$ is obtained by inserting the above equation into Eq. (4.37), and the maximum value of the objective function becomes

$$\left(\sum_{i=1}^{N_m} a_i|z_i|\right)_{\max} = \frac{1}{2}\left(\sqrt{\sum_{i=1}^{N_m}\frac{a_i^2}{c_i}\sum_{i\in E}\frac{|g_i|^2}{c_i}} + \sum_{i\in E}\frac{a_i|g_i|}{c_i}\right). \tag{4.39}$$

Since this maximum value has been derived using only the mode shapes without considering natural frequencies and mistuning level as in Whitehead's approach, this maximum value may not be reached. However, this expression still provides more specific upper bounds for multi-DOF-per-sector models than Whitehead's factor that was derived from a 1-DOF-per-sector model.

4.3.2 Examples

A 2-DOF-per-sector model and a finite element model were considered for the application of the above upper bound calculation.

For a 2-DOF-per-sector model, the model illustrated in Fig. 4.1(b) was used. Each disk DOF was connected to two adjacent disk DOF by springs of stiffness k_c. Also, all the tuned-system modes were assumed to be equally damped, and a cantilevered-blade was also set to have the same damping as that of the tuned-system modes. Hence, the damping coefficient is eliminated when the upper bound of blade response is normalized by the cantilevered-blade response. The used values for the model parameters are $m_d/m_b = 100$, $k_c/k_b = 300$, and $k_d/k_b = 40$. Figure 4.5 shows the plot of the natural frequencies versus nodal diameters for the tuned model with 17 blades. The curves connecting the points at integer nodal diameters were obtained by treating interblade-phase angle as a continuous variable [39]. Since the nodal diameters 1 to 7 corresponds to double modes, the plot shows the frequencies of all the 34 modes.

To calculate the upper bounds, first of all the tuned-system modes that can describe the motion of mistuned systems should be selected. Here, two cases are shown. One is for closely spaced 17 modes marked by filled circles between two dotted lines in Fig. 4.5, and the other is for all the 34 modes. The upper bounds of $|x_b - x_d|$ were obtained for various engine orders of excitation using Eq. (4.39) and normalized by the amplitude of a tuned, cantilevered blade at its resonance with external forcing of the same magnitude as the engine order excitations, and are shown in Fig. 4.6. The dotted lines in Fig. 4.6 represent the upper bound obtained using Eq. (4.32) for a 2-DOF-per-sector model, which is 2.5718 because α_h is equal to m_d/m_b when all the modes are equally damped. It can be seen that, when 17 modes are used, the upper bound values obtained using Eq. (4.39) are smaller than that obtained using Eq. (4.32). Also, the calculated upper bound varies according to the engine orders, and is smallest at engine order 1. However, when all the modes are used, all the calculated upper bounds are the same as 2.5718. Here, it should be noted that the results in Fig. 4.6(a) are more realistic than those in Fig. 4.6(b) because only the 17 modes can mainly interact in mistuned systems when mistuning is small. This indicates that Eq. (4.39) can provide more realistic and lower upper bounds than Eq. (4.32).

The largest amplitudes of $x_b - x_d$ in the tuned 2-DOF-per-sector model were obtained for various engine orders of excitation. And, they are normalized again by the cantilevered-blade response. Figure 4.7(a) shows the normalized tuned responses when the 17 modes are used. As can be seen, all the tuned-system responses are smaller than the cantilevered-blade response. This is because vibration energy flows from blades to disk so that the energy level of blades in a tuned bladed disk becomes smaller than that of a tuned, cantilevered blade. It can be also observed that the variation of the tuned response level along the engine orders in Fig. 4.7(a) is similar to that of the upper bound level in Fig. 4.6(a). This trend can be expected from Eq. (4.39). That is, if a_i for $i \in E$ are small, the corresponding upper bound as well as the tuned response will be small, too. In Fig. 4.7(b), the ratios of the upper bounds to the tuned responses, which are the upper bounds of traditional amplification factor, are depicted. Since the tuned response at engine order 1 is much smaller than others, the ratio at engine order 1 is much higher than others, and exceeds Whitehead's maximum amplification factor (2.5616 for a 17-blade system).

Equation (4.39) was also applied to an advanced rotor design that can replace multiple rotor stages. The finite element model shown in Fig. 4.8 was constructed with 10-noded pyramid elements, and it has 1,299,792 DOF. The natural frequencies of this finite element model are shown in Fig. 4.9. The lowest five blade-dominated mode families are displayed, and the corresponding dominant cantilevered-blade mode is shown on the right-hand side of each mode family. 1F and 2F denote the first and second flexural bending modes, 1T denotes the first torsion mode, and 1S and 2S denote the first and second stripe modes.

For this study, the 1T mode family was chosen, and 28 modes marked by filled circles between two dotted lines in Fig. 4.9 was selected for the description of the bladed disk motion around 1.5 kHz. It was assumed that tuned-system modes and cantilevered-blade modes were equally damped as in the case of the previous lumped parameter model. A unit force normal to the surface was applied on a node at the front edge of each blade tip so that the torsion mode could be well excited, and its phase was adjusted according to the engine order of excitation. Although the forcing was unrealistic, and the upper bound calculation depends on the modal forces, the results can be meaningful as long as the 1T blade mode is dominant in the motion of the bladed disk and the cantilevered blade.

First, calculated were the 1T modal participation factors in the blade motion of the selected tuned-system modes. Then, the upper bounds, tuned-system responses, and resonant cantilevered-blade response of the 1T mode were obtained based on the modal participation factors. The results are shown in Fig. 4.10. As can be seen, the tuned-system response at engine order 1 is smaller than others while the upper bounds are almost the same along the engine orders. Therefore, the ratio of the upper bound to the tuned-system response at engine order 1 is much higher than others, even than Whitehead's maximum factor (3.0495 for a 26-blade system), although the ratios at other engine orders are much lower than 3.0495.

4.4 Predicting Blade Stress Levels Directly from Reduced-Order Vibration Models of Mistuned Bladed Disks

It is well known that the forced vibration amplitudes of bladed disks can increase dramatically due to small, random discrepancies among the blades, which are referred to as mistuning. As a result, blade mistuning can lead to significant durability and reliability problems in turbine engines. In order to analyze bladed disk designs and assess the effects of mistuning, finite element models (FEMs) are typically employed. From a finite element vibration analysis, the displacement and the stress state can be obtained at all degrees of freedom (DOF) and finite elements. However, industrial bladed disk FEMs usually feature very large numbers of DOF, and thus traditional finite element analysis (FEA) can be prohibitively expensive. To address this issue, a variety of techniques [15, 22, 23, 40, 44] have been developed for constructing reduced-order models (ROMs) from FEMs.

Although such ROMs can be used to solve the vibration response quickly and accurately relative to FEA, they are typically formulated in terms of modal and physical displacement variables for the bladed disk, whereas the primary variable of interest for durability and reliability studies is stress. To calculate blade and/or disk stress levels, the displacements predicted by the ROM analysis can be projected back to finite element coordinates and then post-processed via FEA [39]. However, it may be cumbersome and expensive to translate the ROM output to the FEM input format and then calculate the stress field with FEA, especially if this process needs to be repeated many times for a Monte Carlo simulation. In order to take full advantage of a highly efficient reduced-order modeling technique, it would be better to be able to predict the increase in stress levels due to mistuning directly from the ROM.

In structural dynamic problems, changes in vibratory stress levels can usually be approximated based on changes in the corresponding displacement levels, as long as the shape of the vibration response does not change significantly over a frequency range of interest. However, bladed disk structures feature frequency regions of high modal density, and in these regions blade mistuning can greatly alter the system mode shapes, from an extended pattern for a tuned system to a localized pattern for a mistuned system. Nevertheless, for the resonant response of both tuned and mistuned bladed disks, the displacement shape of each blade often resembles that of a tuned cantilevered-blade mode (the mode of a single blade cantilevered at its interface with the disk). Indeed, if the blade motion is dominated by a single cantilevered-blade mode throughout the frequency range of interest, then blade displacements may be used to describe stress levels. However, if there is more than one dominant cantilevered-blade mode, which occurs when blade modes have close natural frequencies, then blade stress trends may not match blade displacement trends. Also, blade mistuning is usually modeled as a variation of blade stiffness. Therefore, even if two blades have the same displacements, they may experience different levels of stress. In general, some care must be taken to relate blade displacement results to stress levels.

In this work, three indicators are proposed as ROM-based measures of the level of blade stress in a mistuned bladed disk. These indicators are defined using (1) the Euclidean norm of blade displacements, (2) the modal amplitude of a cantilevered blade, and (3) the strain energy in a blade. All three indicators can be calculated directly from the ROM results, without requiring an expensive finite element stress analysis for the mistuned bladed disk. In the following sections, these indicators are formulated, and then their accuracy is examined and validated by comparing their stress predictions to the largest Von Mises stresses in the blades calculated from a much more costly finite element analysis.

4.4.1 Stress Indicators

If a tuned blade is modeled as a single-DOF lumped parameter model with a mass (m_b) and a spring (k_b), the stress level is proportional to $k_b|x|$, where $|x|$ is the amplitude of the spring deformation. Then, the ratio of the stress level of a mistuned blade to that of a tuned, cantilevered blade at its resonance becomes $(1+\delta)|x|/|x_{cb}|$, where δ is a non-dimensional blade-stiffness mistuning value, and $|x_{cb}|$ is the amplitude of the resonant response of a tuned, cantilevered blade. That is, the stress ratio is the product of $1+\delta$ and the displacement ratio, $|x|/|x_{cb}|$. If this stress ratio and the stress level of a cantilevered blade are known, then the stress level of any blade can be calculated.

However, when using a finite element model, the elastic deformation induced by the motion of the disk is included in the blade motion, and thus the stress state for a blade in a bladed disk assembly can be different from that for a cantilevered blade. Still, if the blade vibration is dominated by motion corresponding to a single mode of a tuned cantilevered blade, then the level of the largest stress in a blade—which is perhaps most meaningful in terms of design safety—can be approximated by assuming that the disk-induced motion is negligible, which is often the case for blade-dominated system modes. In this work, based upon this assumption, three indicators are proposed that represent the largest stress in a blade when normalized by the largest stress in a cantilevered blade at the resonance condition corresponding to the dominant cantilevered-blade mode. Therefore, each indicator is referred to as a normalized stress indicator (NSI). Each NSI is defined such that it can be calculated directly from the displacements obtained from a ROM analysis.

The first normalized stress indicator is formulated in terms of the Euclidean norm of the physical blade displacement vector:

$$(1+\delta)u_m/u_{cb}, \tag{4.40}$$

where u_m is the Euclidean displacement norm for a blade in the mistuned bladed disk, and u_{cb} is the Euclidean displacement norm for the resonant response of a tuned cantilevered blade. Here, δ is the modal stiffness mistuning value for the dominant cantilevered-blade mode.

The second normalized stress indicator is formulated in terms of modal amplitudes:

$$(1+\delta)a_m/a_{cb}, \tag{4.41}$$

where a_m is the dominant modal amplitude of a mistuned blade when the vibration response is described in tuned cantilevered-blade modal coordinates, and a_{cb} is the modal amplitude for the resonant response of a tuned cantilevered blade. Note that a_m and a_{cb} correspond to the same cantilevered-blade mode. However, this formulation does not require that cantilevered-blade modes be used as basis vectors in the ROM, because the system motion can be projected onto these modes to retrieve a_m. Furthermore, a coordinate transformation between ROM modal coordinates and cantilevered-blade modal coordinates can be calculated *a priori* to make this an extremely inexpensive indicator to compute.

The third normalized stress indicator is formulated in terms of blade strain energy. For a single-DOF lumped parameter model, the ratio of the strain energy in a mistuned blade to that in a tuned, cantilevered blade at its resonance beomes $(1+\delta)(|x|/|x_{cb}|)^2$. Therefore, using the strain energy in a blade, an analogous indicator is proposed:

$$\sqrt{(1+\delta)E_m/E_{cb}}, \tag{4.42}$$

where E_m is the peak strain energy of a blade in the bladed disk during one period of oscillation, and E_{cb} is the peak strain energy during one period of oscillation for the resonant response of a tuned cantilevered blade.

Although disk-induced motion is usually small, the physical displacements of blades are determined by the disk-induced rigid body and elastic motion as well as by the cantilevered-blade motion. Only the disk-induced elastic motion and the cantilevered-blade motion affect the blade stress level. However, the NSI proposed in Eq. (4.40) is affected by the rigid body motion. Nevertheless, this does not imply that this NSI is less accurate than the other two, because none of the proposed NSIs accounts for the disk-induced elastic motion appropriately. Also note that, even if the disk-induced elastic motion may affect considerably the stress level locally near the blade root, the change in total blade strain energy due to this motion may be very small.

In order to test the three proposed indicators, the FEM of an industrial rotor with 29 blades shown in Fig. 4.11 was used. (This rotor model was also studied in previous work by the authors [44], in which its vibration characteristics, including the plot of natural frequencies versus number of nodal diameters, can be found.) Blade mistuning was implemented by varying Young's modulus in the finite elements of the blades, and 50 randomly mistuned systems were obtained. Each mistuned system was tested in two excitation frequency regions: 9–11 kHz and 26–29 kHz. The second flexural bending (2F) mode of a cantilevered blade is the dominant blade motion in 9–11 kHz, and the third flexural bending (3F) mode is dominant in 26–29 kHz. For external forcing, engine order excitations were considered by applying a unit force normal to the blade surface on one of the nodes at each blade tip. Engine order 1 and 3 were used for 9–11 kHz and 26–29 kHz, respectively. For each mistuned system and frequency region, a resonant frequency at which the largest Euclidean blade displacement norm occurs was identified. At that frequency, the response data for the 29 blades obtained from the FEA were collected. Thus, for each frequency region, 1450 sets of blade response data were obtained, and the Euclidean blade displacement norm, the amplitude of the 2F or 3F cantilevered-blade mode, and the peak blade strain energy during a period of oscillation were calculated for each data set. Also, the largest peak Von Mises stress in each blade during a period of oscillation was calculated using the complex stress state for the finite element centers obtained from the FEA. The results for the 2F and 3F regions are shown in Figs. 4.12 and 4.13, respectively.

In these figures, the “normalized largest stress” is defined as the ratio of the largest Von Mises stress of a blade in a mistuned system to that of a tuned, cantilevered blade. If the NSIs were to measure the normalized largest stress exactly, then all the data points should appear on the lines of unit slope in Figs. 4.12 and 4.13. However, as mentioned above, the disk-induced component of blade motion is not accounted for by the NSIs. Therefore, not all the data points fall on the lines, although they are located close to them. In Fig. 4.12, although all indicators underestimate the stress level, the NSI based on the Euclidean norm is seen to be a better stress approximation than the other two indicators. This is because disk-induced elastic motion increases the stress level for the 2F mode region, and the rigid body motion also increases the level of the NSI using the Euclidean norm. The data points in Fig. 4.13 are considerably more scattered than in Fig. 4.12, especially for small NSI values, but the general trend is that the NSIs overestimate the blade stress level slightly.

This means that disk-induced elastic motion generally tends to decrease the stress level in the 3F region. Hence, it can be seen that the results of the NSI based on the Euclidean norm are worse. Finally, Figs. 4.12 and 4.13 show that the NSIs based on modal displacement and on blade strain energy produce almost the same results, which means that the blade strain energy is determined mostly by the dominant cantilevered-blade mode.

All three of the proposed indicators show good agreement with the normalized largest Von Mises stress. However, it should be noted that the NSIs of Eqs. (4.40) and (4.42) require the recovery of all the physical blade displacements in finite element coordinates. In contrast, the NSI of Eq. (4.41) is based on modal displacements, and therefore it is the least expensive to obtain.

4.4.2 Estimation of Blade Stress Level

Now, suppose that the NSI value of a blade can be calculated and that the largest stress for the cantilevered-blade response is known. Then, the largest stress in the blade can be approximated as the product of the NSI value and the cantilevered-blade stress. In this section, two cases of blade stress estimation are studied using the same model as in the previous section. The mistuning values are those given in Table 2 in the authors' previous work [44] that was obtained by a random number generator. In the first case considered, a single cantilevered-blade mode is dominant over the frequency range of interest. In the second case, two blade-dominated mode families are so close that the dominant cantilevered-blade mode for each blade can be different and change throughout the investigated frequency region.

In order to calculate the NSI value, the dominant cantilevered-blade mode needs to be known. Usually, within a given blade-dominated mode family, blade motion is governed by a single cantilevered-blade mode. However, if more than one blade-dominated mode family is present in the motion of a mistuned system, the modal displacements of the corresponding cantilevered-blade modes need to be calculated for each blade at every frequency, in order to determine which mode is dominant. That is, even if the stress measures defined in Eq. (4.40) or (4.42) are used, the modal displacements still need to be calculated. This encourages again the use of Eq. (4.41) as a stress indicator. Therefore, the estimation of blade stress in this study was performed using only the cantilevered-blade modal amplitude stress indicator, Eq. (4.41).

The first case considered concerns the frequency range 26–29 kHz, in which, as mentioned earlier, the 3F blade mode is dominant. From the FEA, stresses and displacements were obtained by applying engine order 3 excitation. Since the FEA stress calculation is computationally expensive, it was performed only at the natural frequencies of the mistuned bladed disk, and the NSI values were calculated from Eq. (4.41) based on these FEA results. In addition, a 34-DOF ROM was built using the component mode mistuning method [44] and NSI values were again calculated, but this time based on the ROM results and at all excitation frequencies in the 26–29 kHz range. At each frequency, the largest Von Mises stresses for the 29 blades were calculated from the FEA results or estimated from the NSI values, and the largest value among all blades was taken, thus providing the maximum stress envelope in terms of frequency. Figure 4.14 compares the results from the FEA and those by the NSIs. It can be seen that the results obtained with the FEM-based NSI and by the ROM-based NSI match very well, and that they are in good agreement with the direct FEA stress calculation across the frequency range.

The second case features two close blade-dominated mode families in the 32–36 kHz range, dominated by the third torsion (3T) and the second stripe (2S) cantilevered-blade modes. For this frequency region, a larger ROM with 66 DOF was constructed, which included modes from both families. Engine order 5 excitation was applied. At every frequency, a dominant cantilevered-blade mode was determined for each blade, and then the NSI value and the estimated stress were obtained according to this dominant mode. In addition, the Euclidean blade displacement norm was calculated for each blade via FEA or ROM, and the maximum norm among all blades was selected. The results obtained for the tuned bladed disk are shown in Fig. 4.15: the Euclidean blade displacement norm is depicted in Fig. 4.15(a) and the maximum stress in Fig. 4.15(b), in terms of the excitation frequency. Observe the three resonant peaks in the investigated frequency region, as shown in Fig. 4.15(b), although the smallest peak barely appears in Fig. 4.15(a). The motion of the bladed-disk assembly is dominated by the 3T blade mode at the first peak around 33.1 kHz, and by the 2S blade mode at the second peak around 34.7 kHz. However, at the third peak around 35.1 kHz, the motion is dominated by disk rather than blade motion, contrary to the other two peaks. Therefore, the third peak in Fig. 4.15(a) is small. Also, it is seen that the stress results obtained with the NSI do not approximate well the FEA stress calculation around the third peak, as shown in Fig. 4.15(b). This is because at the third peak the blade stress level is affected greatly by the disk-induced elastic motion. Also, comparing Figs. 4.15(a) and 4.15(b), observe that the trend of the displacement results is qualitatively different from that of the stress results. That is, although the 3T blade mode gives smaller maximum displacements than the 2S mode, the maximum stress for the 3T mode is higher than for the 2S mode.

Results were also obtained for the mistuned system, and they are depicted in Fig. 4.16. Note again that the trend of the displacement results is considerably different from that of the stress results. It can also be seen in Fig. 4.16(b) that the NSI results are in very good agreement with the FEA results, except around 35.1 kHz which corresponds to the third peak in Fig. 4.15(b). Since the tuned-system mode corresponding to the third peak features small blade motion, this mode is not altered as much by blade mistuning as the other blade-dominated modes. Therefore, even for the mistuned system, the motion corresponding to this mode occurs around 35.1 kHz.

4.5 Conclusions

Using the relation between blade response and vibration energy input through coupling, the maximum energy concentration in a single blade has been derived for 1-DOF-per-sector models with different damping representations. Therefore, the upper bounds of the amplification of the blade displacement and velocity, which turned out to be the same as Whitehead's maximum amplification factor, were found for hysteretic and viscous damping, respectively. Also, the upper bound of blade stress was found to be around the Whitehead's factor for structural damping. It was also demonstrated that the amplification of blade displacement can exceed $(1+\sqrt{N_b})/2$ if viscous or structural damping is used although it is still bounded around $(1+\sqrt{N_b})/2$ if mistuning is small.

The upper bound for a 2-DOF-per-sector model was also found from the maximum energy concentration. Although the traditional amplification factor is the ratio of the largest blade response in a mistuned system to that in the tuned system, the upper bound was normalized by the resonant response of a tuned, cantilevered blade so that the absolute blade responses could be measured and compared. It was found that the upper bound is larger than that for a 1-DOF-per-sector model, and that it is still around $(1+\sqrt{N_b})/2$ if disk displacements are negligible.

Whitehead [25] obtained the upper bound of blade response by superposing all the traveling wave modes for a 1-DOF-per-sector model. This approach was extended to general bladed-disk models with multiple DOF per sector. The generalized expression gives specific upper bounds for different systems and for different engine orders of excitation. The expression has been applied to a 2-DOF-per-sector model and a finite element model.

From the results for the 2-DOF-per-sector model, it was seen that the generalized expression allows lower upper bounds than that obtained from the maximum vibration energy concentration, when only closely spaced traveling wave modes are used.

Three normalized stress indicators were proposed as approximate measures of the largest blade stress level in a mistuned bladed disk. These stress measures were defined using the Euclidean blade displacement norm, the amplitude of a dominant cantilevered-blade mode, and the strain energy in a blade. All three can be calculated efficiently from results obtained with a reduced-order model, without having to resort to expensive finite element stress calculations for the mistuned bladed disk. The three NSIs were tested using the finite element model of an industrial rotor. All three indicators showed good accuracy relative to finite element results. However, the computational cost of the NSI based on the amplitude of a dominant cantilevered-blade mode is significantly lower than the other two, especially when more than one dominant blade mode is present in a frequency range.

It was demonstrated with a case study that, when more than one blade-dominated mode family is present in the frequency region of interest, blade displacement amplitudes can feature trends that are qualitatively different from those of stress levels. This suggests that using raw displacement results from reduced-order models can lead to erroneous predictions for stress. Instead, stress indicators, such as those proposed in this work, should be calculated to assess bladed disk designs.

4.6 Figures and Tables

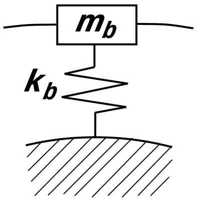

(a) 1-DOF-per-sector model

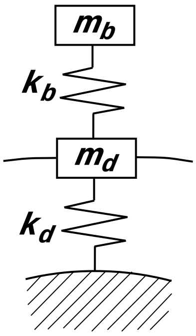

(b) 2-DOF-per-sector model

Figure 4.1: Lumped parameter models of bladed disks.

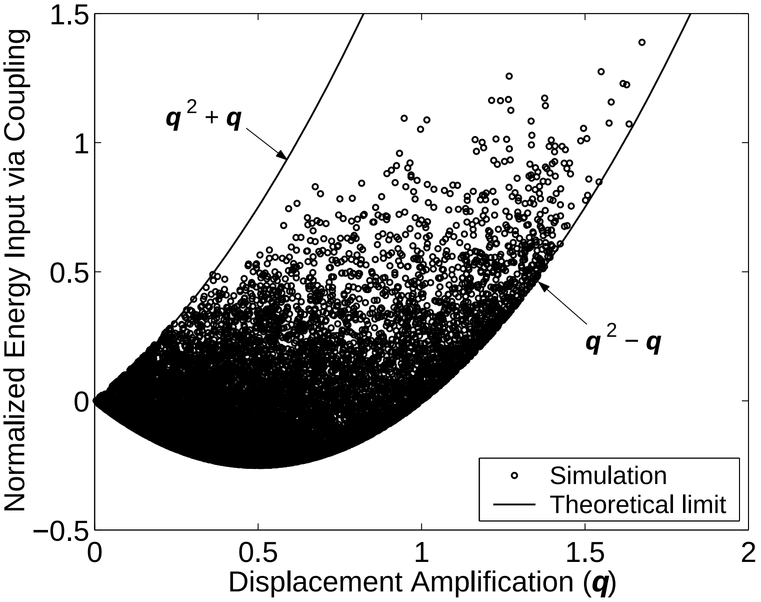

Figure 4.2: Energy input through coupling to a blade versus displacement amplification obtained from 1,000 mistuned systems with a single DOF per sector.

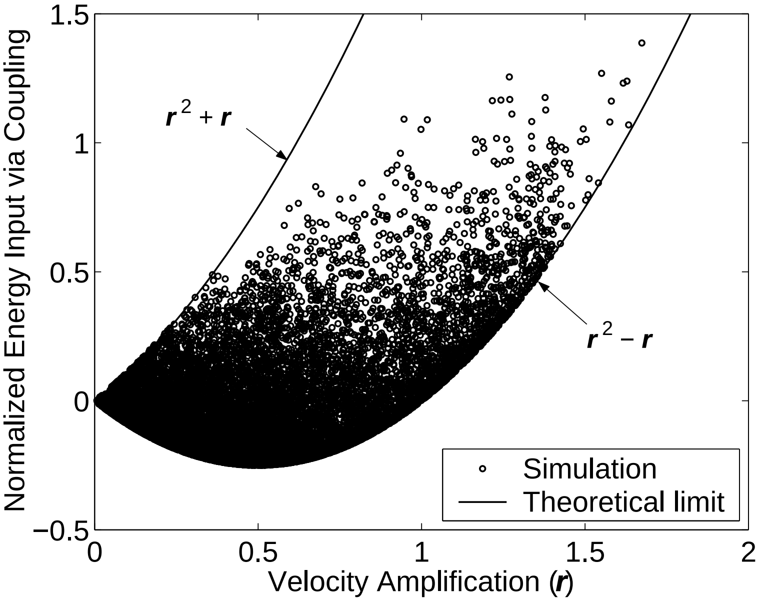

Figure 4.3: Energy input through coupling to a blade versus velocity amplification obtained from 1,000 mistuned systems with a single DOF per sector.

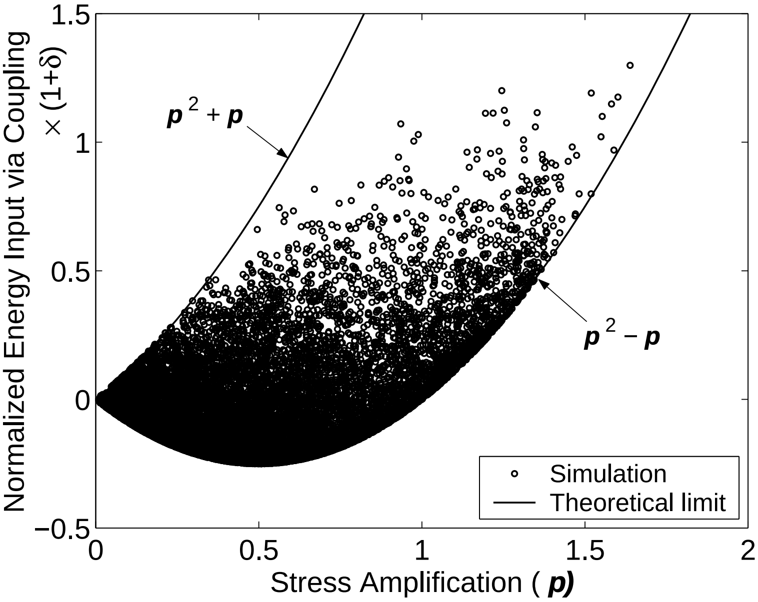

Figure 4.4: Energy input through coupling to a blade versus stress amplification obtained from 1,000 mistuned systems with a single DOF per sector.

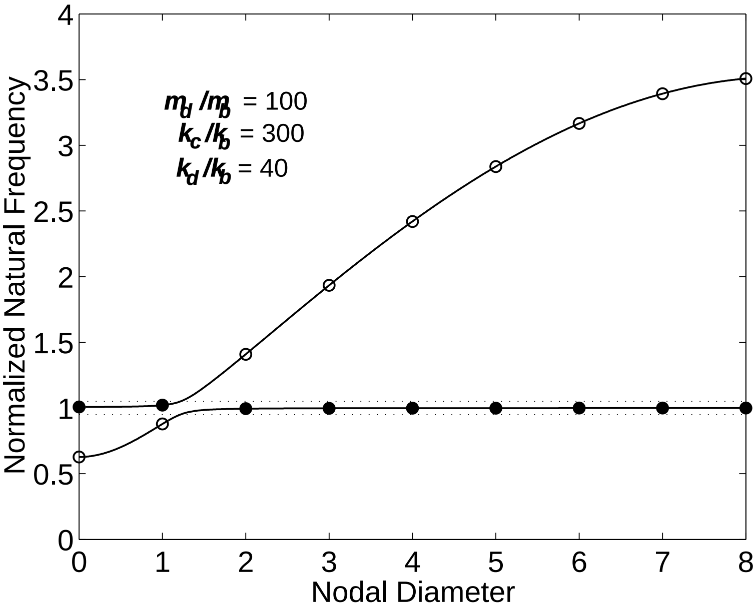

Figure 4.5: Normalized natural frequencies of a tuned 2-DOF-per-sector lumped parameter model.

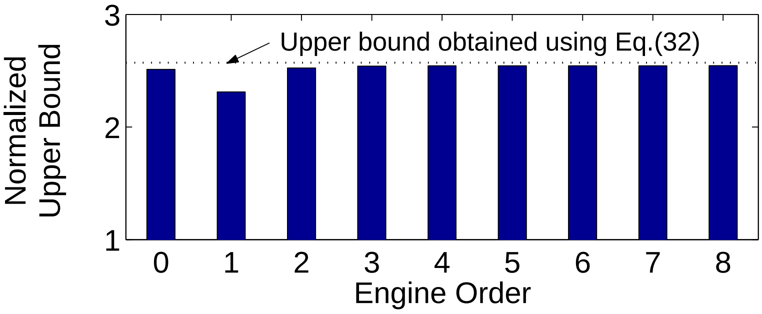

(a) 17 modes in a narrow frequency range included

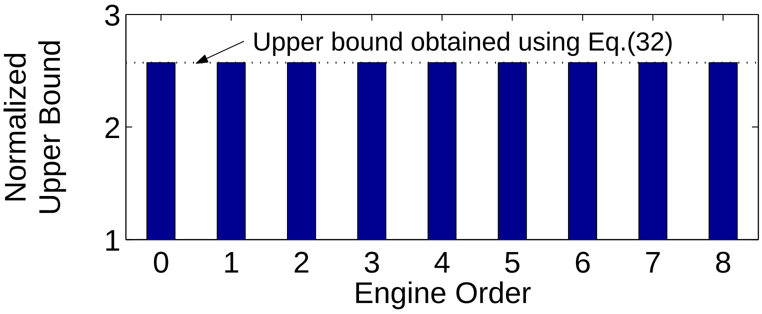

(b) All the modes included

Figure 4.6: Normalized upper bounds of mistuned-system response.

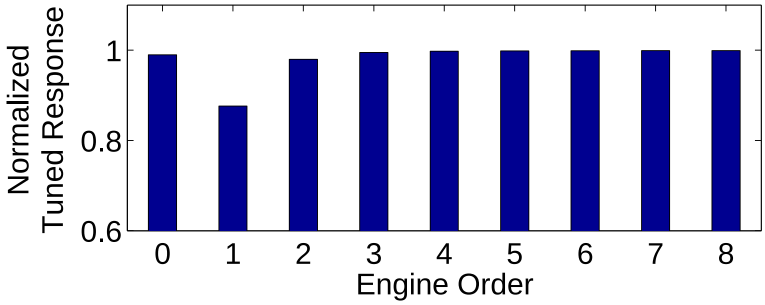

(a) Normalized tuned-system forced response at resonant frequencies

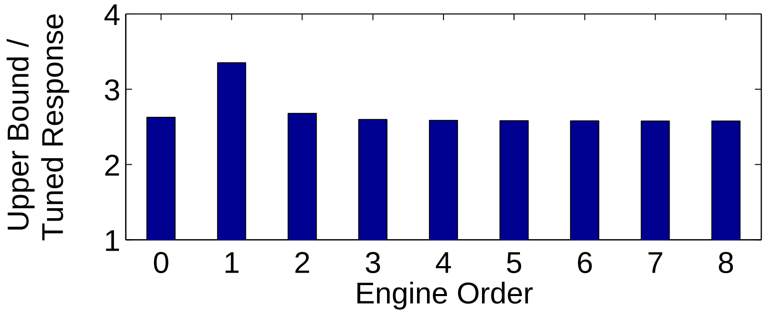

(b) Ratios of upper bounds to tuned-system responses

Figure 4.7: Ratios of upper bounds to tuned-system responses when 17 modes are used.

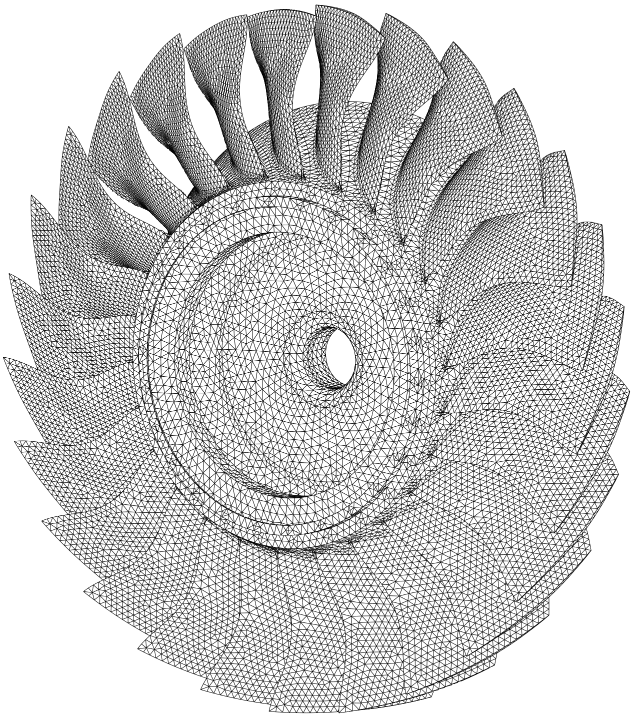

Figure 4.8: Finite element mesh of an advanced bladed disk.

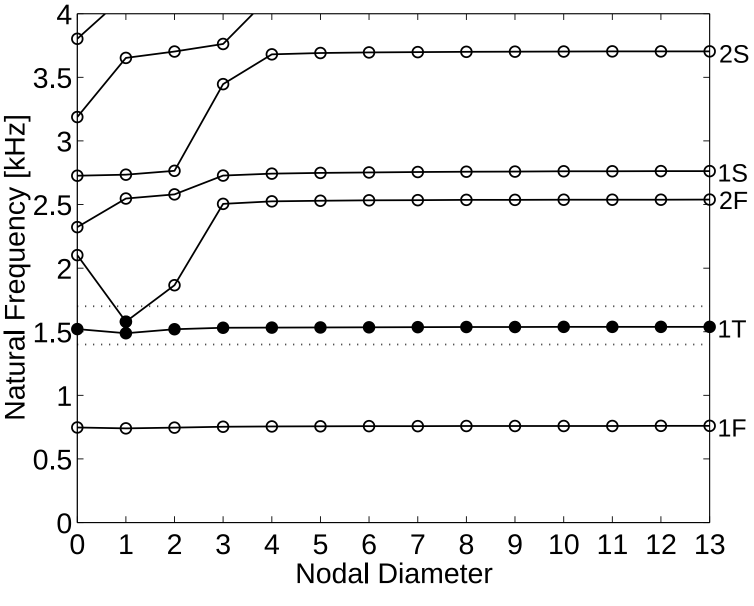

Figure 4.9: Natural frequencies of an advanced bladed disk.

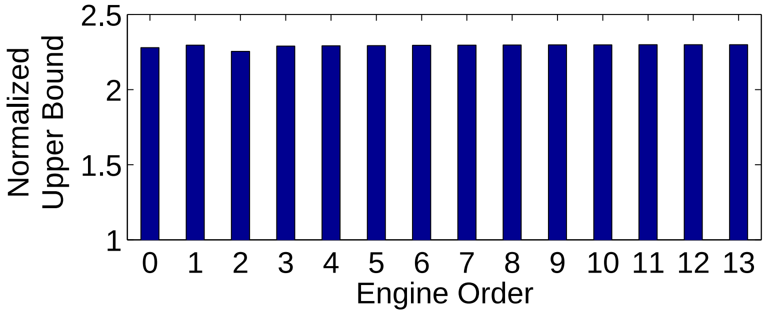

(a) Normalized upper bounds

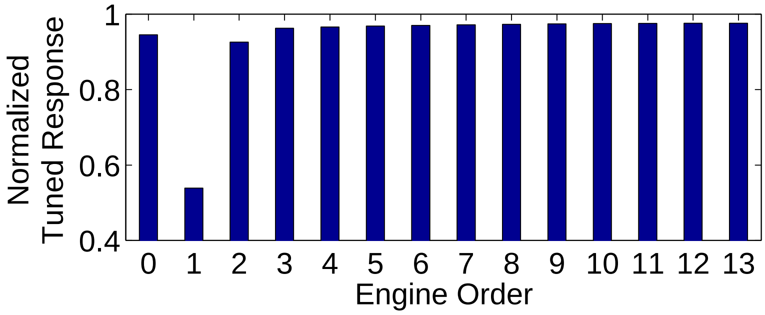

(b) Normalized tuned-system forced response at resonant frequencies

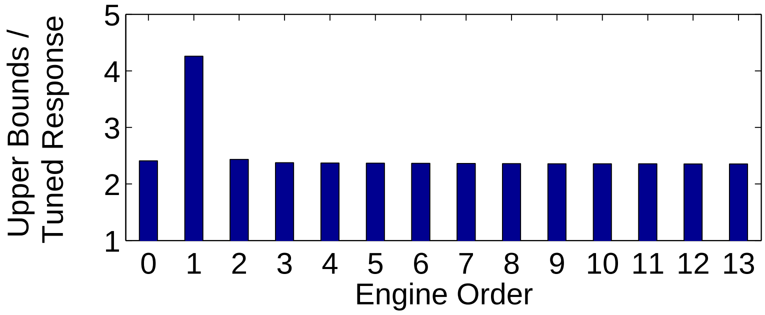

(c) Ratios of upper bounds to tuned-system responses

Figure 4.10: Upper bounds, tuned-system responses, and their ratios for an advanced bladed disk.

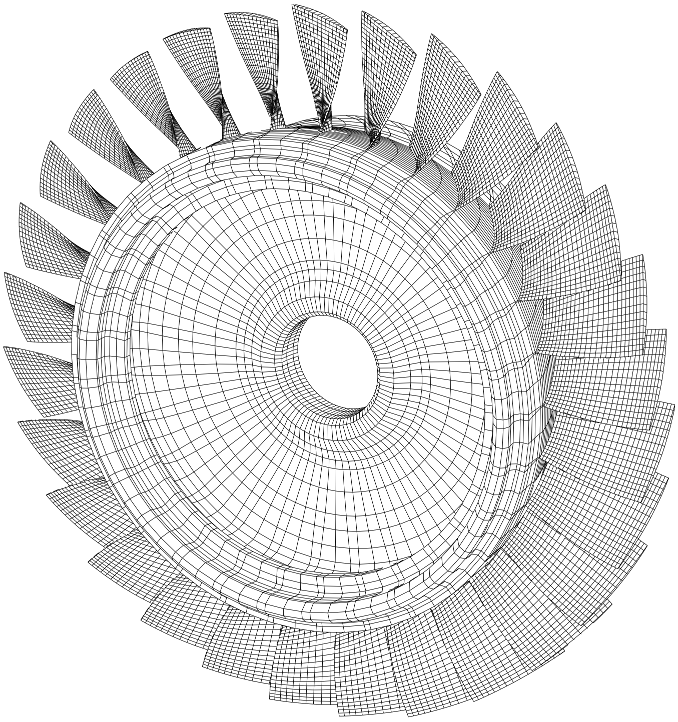

Figure 4.11: Finite element mesh for an industrial rotor.

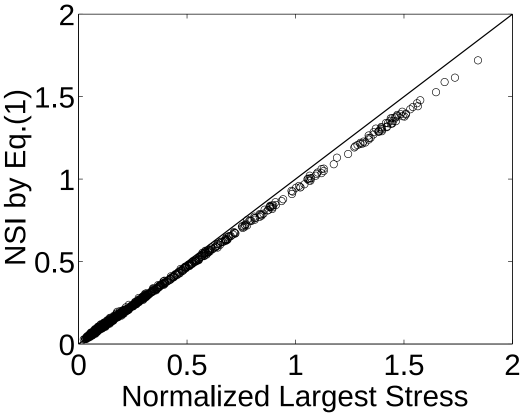

(a) Using Euclidean norm

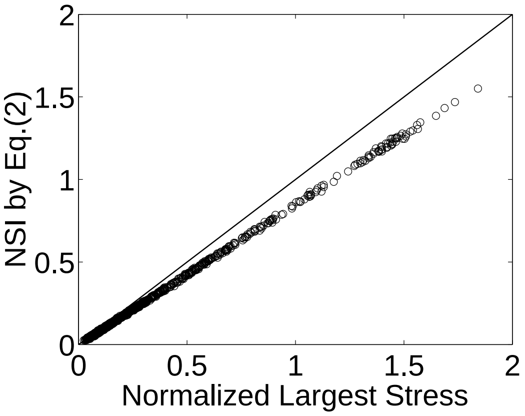

(b) Using modal displacement

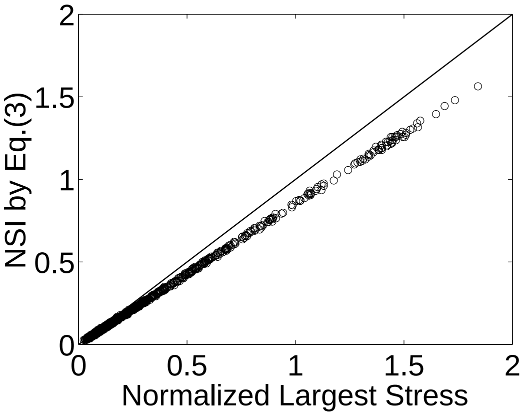

(c) Using strain energy

Figure 4.12: PERFORMANCE OF NORMALIZED STRESS INDICATORS IN THE 2ND FLEXURAL MODE REGION.

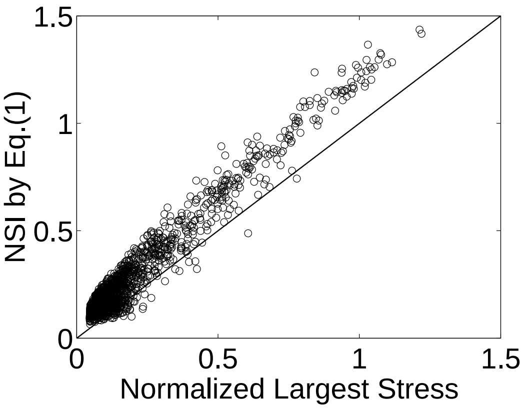

(a) Using Euclidean norm

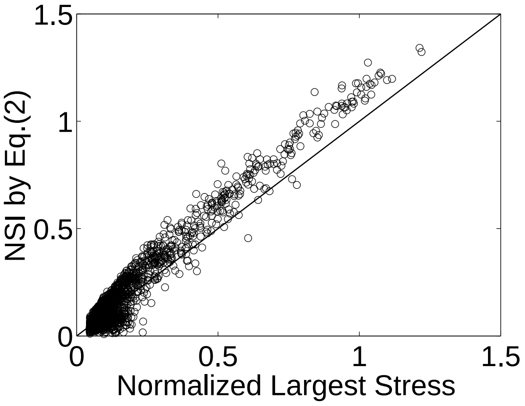

(b) Using modal displacement

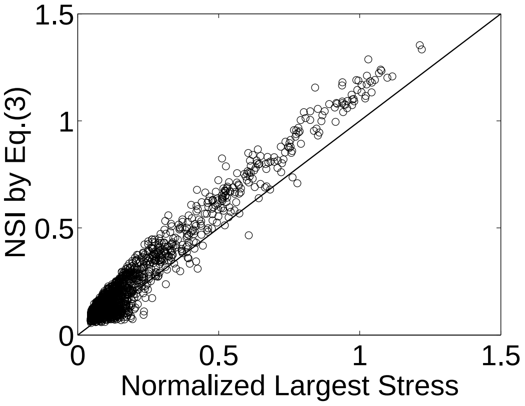

(c) Using strain energy

Figure 4.13: PERFORMANCE OF NORMALIZED STRESS INDICATORS IN THE 3RD FLEXURAL MODE REGION.

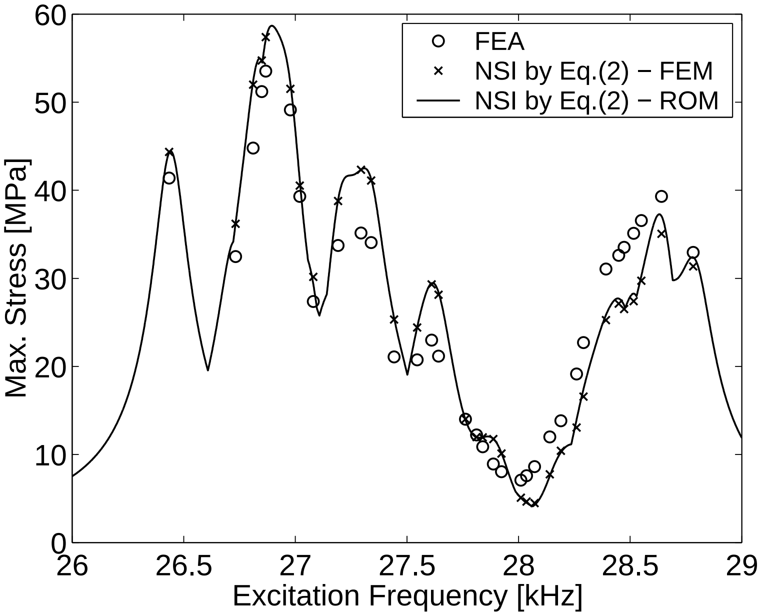

Figure 4.14: Mistuned forced response in 26–29 kHz, where the 7th cantilevered-blade mode is dominant.

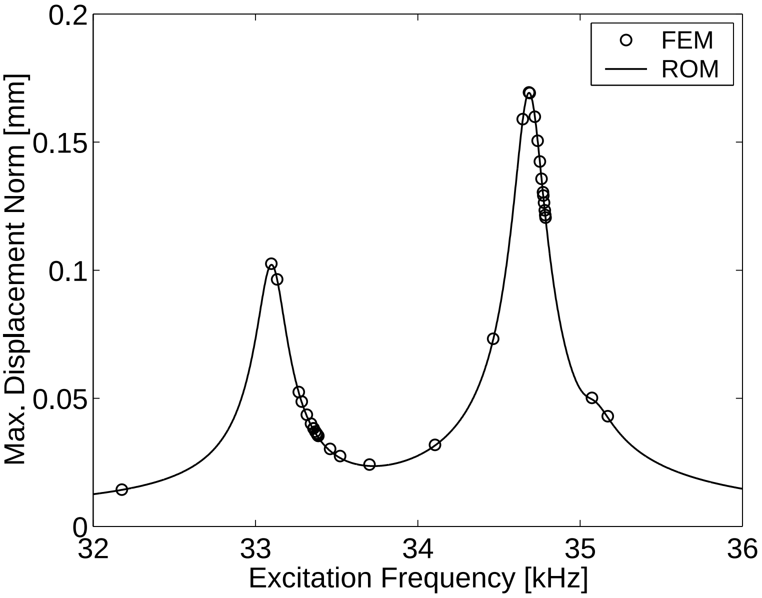

(a) Euclidean displacement norm

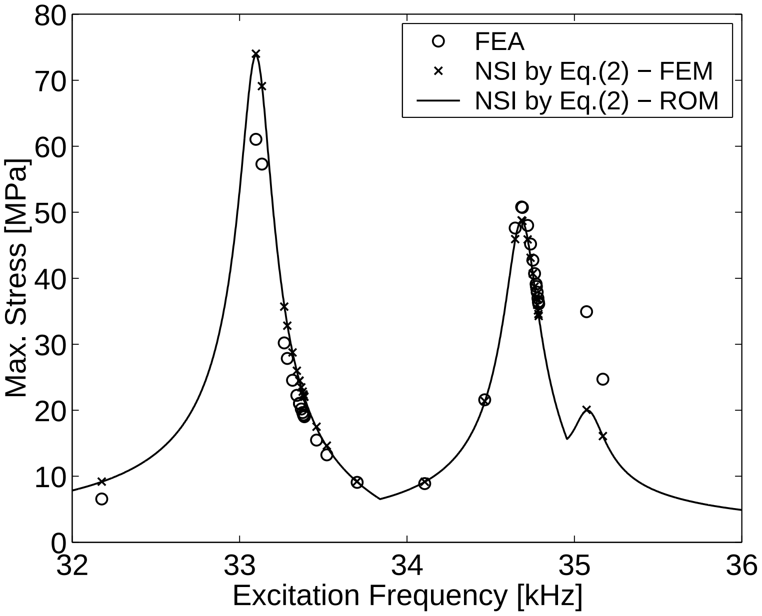

(b) Von Mises Stress

Figure 4.15: Tuned forced response in 32–36 kHz, where the 8th and 9th cantilevered-blade modes are dominant.

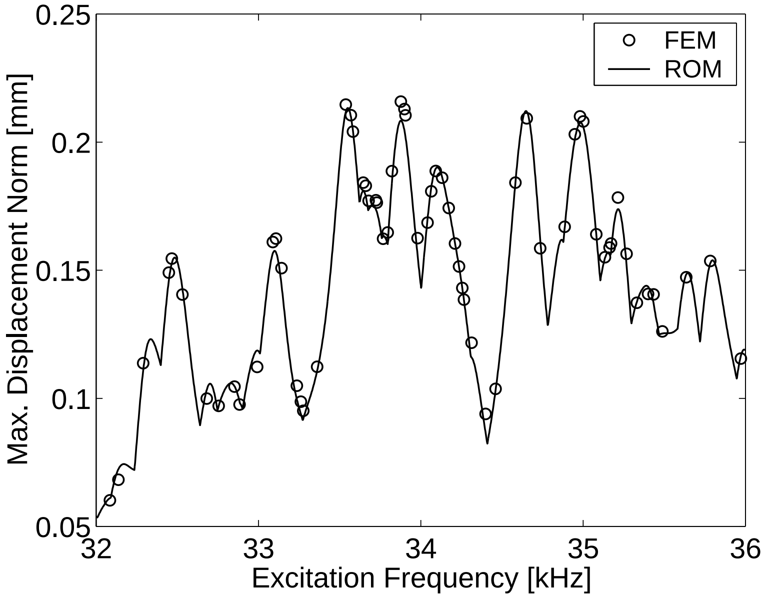

(a) Euclidean displacement norm

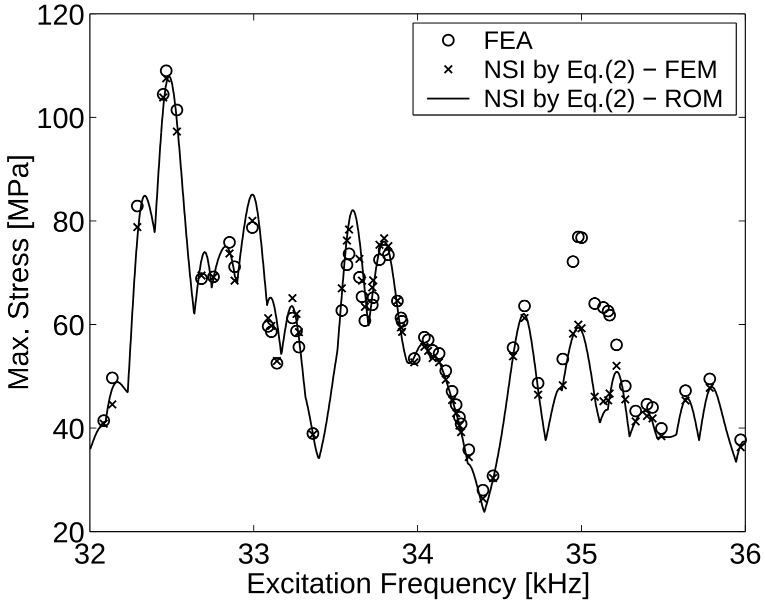

(b) Von Mises Stress

Figure 4.16: Mistuned forced response in 32–36 kHz, where the 8th and 9th cantilevered-blade modes are dominant.

Table 4.1: Examples of mistuning patterns resulting in displacement amplification larger than $(1+\sqrt{N_b})/2$

Damping	Blade mistuning pattern			Displacement amplification
Structural	-0.0520	-0.0224	-0.0226	1.4211
Viscous	-0.0520	-0.0221	-0.0223	1.3928

CHAPTER V

Intentional Mistuning Design Space Reduction Based on Vibration Energy Flow in Bladed Disks

Intentional mistuning is the deliberate incorporation of blade-to-blade parameter variations in the nominal design of a bladed disk. Previous studies have shown that this is a promising strategy for mitigating the damaging effects of unintended, random mistuning. In this paper, the mechanisms of intentional mistuning are studied by investigating the relation between blade response and vibration energy flow in lumped parameter models. Based on key observations from the energy flow analysis, a few design guidelines are proposed that drastically reduce the design space for intentional mistuning patterns. Thus, an optimization may be performed on the reduced design space or skipped altogether, yielding dramatic reductions in computational costs. The guidelines are validated by extensive Monte Carlo simulations for the lumped parameter models as well as for a finite-element-based reduced-order model of an industrial rotor. It is shown that the reduced design space includes optimal or near-optimal intentional mistuning patterns.

5.1 Introduction

Due to manufacturing tolerances, in-operation wear, and other causes, bladed disks always have small, random blade-to-blade variations, called mistuning. While mistuning is beneficial in terms of aerodynamic stability [63, 64], it can lead to a significant increase in the maximum blade vibration relative to the ideal, tuned case [2–5, 7]. The increases in blade vibration amplitudes and stresses due to mistuning are a cause of great concern for the turbine engine community.

One approach to mitigating the damaging effects of mistuning is to move away from a perfectly tuned design. It has been reported that maximum blade forced response levels can be decreased by intentionally introducing some mistuning into the nominal design [8, 29, 35–37]. That is, using two or more designs of blades with nominally different natural frequencies can make the bladed disk system more robust with respect to random mistuning. The effectiveness of this intentional mistuning strategy depends largely on the selected pattern of blade property variation. In order to select the intentional mistuning pattern, one could perform a design optimization. However, in order to optimize intentional mistuning, the increase in blade forced response due to random mistuning needs to be evaluated for each iteration of the intentionally mistuned design. Therefore, the computational cost becomes prohibitive for a large number of possible intentional mistuning patterns. There has been some recent work on determining the pattern of intentional mistuning using optimization algorithms [38]. However, because of the cost, only limited information was used without evaluating the maximum blade forced response.

In addition, there have been several previous studies on using optimization methods to find the worst or best overall mistuning patterns in terms of aeroelastic stability [65–68] or forced response amplification [56, 57, 59, 69]. There have also been a few studies on finding an optimal blade arrangement when a set of mistuned blades are given [70, 71]. The worst mistuning pattern is useful for finding the maximum blade forced response. However, the best mistuning pattern may not actually represent an optimal or near-optimal design, because the actual response may be greatly affected by the additional, random mistuning that will inevitably occur in the manufacturing process, during the assembly, or during engine operation. In fact, Crawley and Hall [67] showed that the performance of the optimal pattern was very sensitive to small changes in the mistuning values. Furthermore, for integrally bladed disks from which blades cannot be separated, blades cannot be rearranged.

The goal of this study is not to perform a true design optimization, but rather to develop a simple approach for identifying a relatively small number of promising patterns of intentional mistuning that are expected to include a near-optimal design. First, the influence of intentional mistuning on the vibration energy flow in a bladed disk system is investigated. An underlying physical mechanism of intentional mistuning is presented using the relation between the energy flow in bladed disks and the stress amplification in blades. Then, based on key observations from the energy flow analysis, some guidelines for selecting effective intentional mistuning patterns are proposed and tested.

This paper is organized as follows. In section 5.2, the energy input to a blade through coupling and the energy flow between sectors are formulated and investigated for lumped parameter models. Three guidelines for intentional mistuning design space reduction are proposed in section 5.3. In section 5.4, these guidelines are validated with lumped parameter models, and several promising configurations of intentional mistuning are tested for an industrial rotor. The conclusions from this study are summarized in section 5.5.

5.2 Energy Flow in Lumped Parameter Models

Many researchers have studied bladed disks using lumped parameter models or simple analytical models [2–4, 7, 8, 10, 12, 36, 38, 65, 66, 70]. In this study, two lumped parameter models are considered. The first model, shown in Fig. 5.1(a), has only a blade DOF for each sector, with tuned mass m_b and tuned stiffness k_b. Each blade DOF is directly coupled to neighboring blades by springs of stiffness k_c. The second model, shown in Fig. 5.1(b), has a blade DOF and a disk DOF for each sector. For this model, the coupling springs connect the disk DOF. Thus, for the 1-DOF-per-sector model, energy flow occurs only between neighboring blades, but for the 2-DOF-per-sector model, energy in a blade can flow to any blade through disk.

In these models, every mass and stiffness can be defined using a ratio with respect to a blade mass m_b and stiffness k_b. Frequencies and stresses can be also non-dimensionalized by a tuned-cantilevered-blade natural frequency and its stress at its resonant frequency. Thereby, in this study, all the results are obtained in non-dimensionalized form. For the forced response, engine order excitations are applied, and only steady-state responses are considered. Structural damping is assumed, and the structural damping ratio is denoted by γ.

Mistuned models are generated by adding stiffness variations to nominal blade stiffnesses. The ith mistuned stiffness is expressed as

$$k_{b,i} = k_b(1 + \delta_i), \tag{5.1}$$

where δ_i is the ith mistuning value to be given randomly or intentionally.

5.2.1 Energy Input to a Blade Through Coupling

In the 1-DOF-per-sector lumped parameter model, the average energy dissipated in blade i over a period of oscillation is

$$E_i^d = \frac{1}{2}\mathrm{Re}\left(j\gamma k_b(1+\delta_i)x_i v_i^*\right) = \frac{1}{2}\gamma k_b(1+\delta_i)\omega|x_i|^2, \tag{5.2}$$

where j is $\sqrt{-1}$, ω is the excitation frequency, x_i is the displacement of the ith blade, and v_i^* is the complex conjugate of the ith-blade velocity. There are two energy sources to balance this energy loss: the energy input by external forcing, and the energy input through the coupling springs. The average energy input to blade i by external forcing is

$$E_i^f = \frac{1}{2}\mathrm{Re}\left(f_i v_i^*\right) = \frac{1}{2}\omega F |x_i| \sin(\Delta\theta), \tag{5.3}$$

where f_i is the external force applied to the ith blade, F is the amplitude of the external force, and $\Delta\theta$ is the phase of f_i subtracted by the phase of x_i. Because engine order excitation is assumed, the forces applied to the blades have the same amplitude, but different phases.

Using Eqs. (5.2) and (5.3), the average energy input to blade i through coupling can be written as

$$E_i^c = E_i^d - E_i^f = \frac{\omega}{2}\left(\gamma k_b(1+\delta_i)|x_i|^2 - F|x_i|\sin(\Delta\theta)\right). \tag{5.4}$$

Therefore, the energy input through coupling is bounded for a given amplitude of displacement as follows:

$$\frac{\omega}{2}\left(\gamma k_b(1+\delta_i)|x_i|^2 - F|x_i|\right) \le E_i^c \le \frac{\omega}{2}\left(\gamma k_b(1+\delta_i)|x_i|^2 + F|x_i|\right). \tag{5.5}$$

Now, in order to relate the stress level of a blade to the energy input through coupling, a stress amplification factor is defined as follows:

$$p_i = \frac{k_b(1+\delta_i)|x_i|}{k_b|x_{cb}|} = \frac{(1+\delta_i)|x_i|}{|x_{cb}|}, \tag{5.6}$$

where x_{cb} is the displacement of a tuned cantilevered blade at its resonant frequency. That is, p_i indicates the ratio of the stress of a mistuned blade to the maximum stress of a tuned cantilevered blade. Since structural damping is used, the resonant frequency is the natural frequency, and the cantilevered blade response is written as

$$|x_{cb}| = \frac{F}{\gamma k_b}, \quad \text{or} \quad F = \gamma k_b |x_{cb}|. \tag{5.7}$$

Inserting Eqs. (5.6) and (5.7) into Eq. (5.5), and normalizing E_i^c with $(\omega/2)\left(\gamma k_b |x_{cb}|^2\right)$, the following relation is obtained:

$$p_i^2 - p_i \le (1+\delta_i)\bar{E}_i^c \le p_i^2 + p_i, \tag{5.8}$$

where $\bar{E}_i^c$ is the normalized energy input to a blade through coupling. The derived relation in Eq. (5.8) shows that the stress amplification of a blade is limited by the energy input through coupling. Similar relations can be derived for different kinds of damping and for the 2-DOF-per-sector model [72]. The relation for a 1-DOF-per-sector model approximately holds for a 2-DOF-per-sector model, because the energy input to a sector can be approximated as the energy input to a blade when the motion is dominated by blades.

These bounds of the energy input are verified using Monte Carlo simulations of mistuned 1-DOF-per-sector and 2-DOF-per-sector models. In the tuned 1-DOF-per-sector model, k_c/k_b is set to be 0.01, which is the value that was used for a weakly coupled system by Wei and Pierre [10]. For the tuned 2-DOF-per-sector model, the parameter values are based on those identified for an industrial rotor [73]. (The finite element model of the industrial rotor will be considered in section 5.4). The parameters were modified slightly to have a frequency veering region at 1 nodal diameter for a 12-blade system. The non-dimensionalized parameters are $m_d/m_b = 500.0$, $k_c/k_b = 2050.0$, and $k_d/k_b = 45.5$. The natural frequencies of the resulting 2-DOF-per-sector tuned system are plotted in Fig. 5.2. The curves connecting points at integer nodal diameters were obtained by applying a method that treats the interblade phase angle as a continuous variable [39]. A structural damping ratio of 0.002 was used for both models. Mistuning values were sampled from uniformly distributed random numbers to obtain 1,000 mistuning patterns. The standard deviations of the random mistuning values were chosen to be 0.012 for 1-DOF-per-sector model and 0.006 for 2-DOF-per-sector model, because the systems show large increases in blade forced response for these mistuning levels.

For the 1-DOF-per-sector model, engine order 3 excitation was used. For the 2-DOF-per-sector model, engine order 1 excitation was used, which corresponds to the veering region at 1 nodal diameter. In each simulation, the resonant frequency with the maximum blade response was found using a golden section search method. At that frequency, the response results for all 12 blades were recorded. So, these simulations yielded 12,000 blade response results for each model, as depicted in Fig. 5.3. For the 2-DOF-per-sector model, the energy input to sectors (not blades) was obtained. Most of the Monte Carlo simulation results appear between the two theoretical limit curves, $p^2 - p$ and $p^2 + p$. For the 2-DOF-per-sector model results, some points are just outside the lower limit. In Fig. 5.3, it is observed that large stress amplification is accompanied by large normalized energy input through coupling. Note that a negative value of normalized energy input indicates a net energy drain to other blades.

For these Monte Carlo simulations, the energy input through coupling is also shown as a function of the difference between excitation frequency and blade natural frequency, $|\omega - \omega_i|$, in Fig. 5.4. The frequency differences were normalized by the tuned-cantilevered-blade natural frequency, ω_{cb}. As can be seen, the level of the energy input through coupling decreases beyond a certain level of the frequency difference. This trend is in good agreement with the findings of Griffin and Hoosac [8]. They observed that the blades most likely to exhibit the largest vibrations were those that had blade-alone (cantilevered-blade) frequencies nearly equal to the tuned system resonant frequency, and that the highest responses occur at frequencies near the tuned system resonant frequency. This means that a blade has a small stress amplification when an excitation frequency is sufficiently separated from the blade natural frequency.

Now, the energy input through coupling into each blade in an intentionally mistuned design is considered. Here, a “square wave” pattern of intentional mistuning with amplitude of 0.1, as shown in Fig. 5.5, is used for the lumped parameter models. Because this pattern consists of alternating groups of two higher-frequency blades and two lower-frequency blades, it is called a 2H2L square wave pattern. The reason for choosing this pattern will be explained in sections 5.3 and 5.4.

Figures 5.6 and 5.7 show the results from Monte Carlo simulations performed in the same way as for the nominally tuned designs. In Fig. 5.6, it can be observed that the level of the energy input through coupling as well as the level of stress amplification is decreased, which means that the intentional mistuning pattern works well. In Fig. 5.7, the results appear in two groups. One group is located at the smaller frequency difference region, and the other at the larger frequency difference region. The separation of these two groups is caused by the level of intentional mistuning being larger than that of random mistuning. The energy input to or drain from the blades in the group at the larger frequency difference region is very small. This verifies again that the energy input through coupling decreases as the frequency difference increases. Furthermore, the energy input available to a blade showing the maximum forced response is reduced due to this small energy drain from those blades at the larger frequency difference region.

5.2.2 Energy Flow Between Sectors Through Coupling

From the investigation of the energy input to a blade through coupling, it was seen that the possible energy source is reduced by intentional mistuning. Here, the propagation of energy is investigated. The energy flow between two neighboring sectors is formulated using stress amplification factors for a 1-DOF-per-sector model. The energy flow from blade $i-1$ to blade i through coupling is written as

$$\begin{aligned} E^c_{i-1,i} &= \frac{1}{2}\mathrm{Re}\left((1+j\gamma)k_c(x_{i-1}-x_i)v_i^*\right) \\ &= \frac{1}{2}\omega k_c\left[|x_{i-1}||x_i|\left(\gamma\cos(\Delta\phi_{i-1,i})+\sin(\Delta\phi_{i-1,i})\right)-\gamma|x_i|^2\right], \end{aligned} \tag{5.9}$$

where $\Delta\phi_{i-1,i}$ is the phase of x_{i-1} subtracted by the phase of x_i. Inserting Eqs. (5.6) and (5.7) into the above equation, and normalizing $E^c_{i-1,i}$ with $(\omega/2)\left(\gamma k_b|x_{\mathrm{cb}}|^2\right)$ again, the following equation is obtained:

$$\bar{E}^c_{i-1,i} = \frac{k_c}{k_b}\left[\left(\frac{p_{i-1}}{1+\delta_{i-1}}\right)\left(\frac{p_i}{1+\delta_i}\right)\left(\cos(\Delta\phi_{i-1,i}) + \frac{1}{\gamma}\sin(\Delta\phi_{i-1,i})\right) - \left(\frac{p_i}{1+\delta_i}\right)^2\right], \tag{5.10}$$

where $\bar{E}^c_{i-1,i}$ is the normalized energy flow from blade $i-1$ to blade i. Since the structural damping γ is usually much smaller than 1, $\bar{E}^c_{i-1,i}$ is dominated by the sine term unless $\sin(\Delta\phi_{i-1,i})$ is negligibly small. Therefore, $\bar{E}^c_{i-1,i}$ may be decreased by decreasing k_c/k_b, p_{i-1}, or p_i; by increasing γ; or by making $\Delta\phi_{i-1,i}$ close to 0 or π.

Now, suppose that mistuning is added to a system so that the natural frequencies of the $i-1$th and ith blades are separated sufficiently, and that the excitation frequency is around the natural frequency of the ith blade. Then, the $i-1$th blade will vibrate with a very small amplitude, and the available level of $\bar{E}^c_{i-1,i}$ may be reduced because of small p_{i-1}. If the natural frequencies of both blades are sufficiently far from the excitation frequency, both p_{i-1} and p_i will be small and $\bar{E}^c_{i-1,i}$ may be further reduced.

For a 2-DOF-per-sector model, an equation similar to Eq. (5.10) is written as follows:

$$\bar{E}^c_{i-1,i} = \frac{k_c/k_b}{(k_d/k_b)^2}\left[p^d_{i-1}p^d_i\left(\cos(\Delta\phi^d_{i-1,i}) + \frac{1}{\gamma}\sin(\Delta\phi^d_{i-1,i})\right) - p^{d^2}_i\right], \tag{5.11}$$

where p^d_i is $(k_d|x^d_i|)/(k_b|x_{cb}|)$, x^d_i is the displacement of the ith disk sector, and $\Delta\phi^d_{i-1,i}$ is the phase of x^d_{i-1} subtracted by the phase of x^d_i. As can be seen, the energy flow depends on disk displacements. Therefore, even if the displacement of the $i-1$th and ith blades are small, the energy flow between the sectors may not be reduced.

From the results of the Monte Carlo simulations for intentionally mistuned systems in the previous section, the plots of the energy flow from sector $i-1$ to sector i versus the difference between excitation frequency and the natural frequency of blade i were obtained as shown in Fig. 5.8. The results appear in two groups, as in Fig. 5.7. It is seen that the level of the energy flow in 1-DOF-per-sector models is small for the blades at the large frequency difference region. However, this trend is not observed in the results for 2-DOF-per-sector models, which means that the vibration energy propagation in 2-DOF-per-sector models may not be affected by intentional mistuning. Also, since the net energy input to a blade at the larger frequency difference region is very small (see Fig. 5.6(b)), it can be concluded that most of the amount of energy flow from sector $i-1$ just passes to sector $i+1$.

5.3 Intentional Mistuning in Nominal Designs

In this section, the design of intentional mistuning patterns is considered in terms of vibration energy source and propagation. Intentional mistuning is introduced into an originally tuned bladed disk design by using multiple blade designs, or blade types, where each blade type has a different blade-alone natural frequency. In this study, the natural frequency differences between blade types, the number of blade types, and the arrangement of blades of different types are considered as the design parameters for intentional mistuning. The first parameter is associated with the amplitude of intentional mistuning, while the second and third are associated with the pattern of intentional mistuning.

5.3.1 Amplitude of Intentional Mistuning

The effects of varying intentional mistuning amplitude are considered by examining stress amplification factors for lumped parameter models with the 2H2L square wave pattern of intentional mistuning shown in Fig. 5.5. To begin, the 99th percentile stress amplification factor is estimated for various standard deviations of random mistuning. In order to estimate the 99th percentile value efficiently, a Weibull distribution fit [29, 39] is applied to the largest blade stress amplification factors obtained from Monte Carlo simulations of mistuned bladed disks. By using a Weibull distribution fit, the number of simulations needed for an accurate prediction of the 99th percentile value can be reduced by orders of magnitude. In this case, 100 simulations were run for each sampled standard deviation value from 0 to 0.03, with a step size of 0.003. The same random mistuning patterns were used for each set of 100 simulations as were used in section 5.2, with the pattern being scaled according to the sampled standard deviation value.

Figure 5.9 shows the 99th percentile stress amplification factors for the 1-DOF-per-sector model for various amplitudes of intentional mistuning. From each curve, the maximum value was taken, which is referred to as the maximum stress amplification.

In Fig. 5.10, the maximum stress amplification is shown as a function of the amplitude of intentional mistuning for both lumped parameter models. The overall trend is that, as the amplitude of intentional mistuning increases, the maximum stress amplification decreases, but the slope becomes less steep. That is, the maximum stress amplification shows slow improvement after a certain level of the natural frequency difference between the two blade types. This trend can be expected from the results in Fig. 5.7. For the remainder of this study, the amplitude of intentional mistuning will be set to 0.1, and only the selection of the pattern of intentional mistuning will be investigated.

5.3.2 Pattern of Intentional Mistuning

For the pattern of intentional mistuning, a key parameter is the number of blade types to be used. As the number of blade types increases, the number of blades with the same nominal natural frequency decreases. This can be interpreted as an advantage. However, if the number of blade types increases but their natural frequencies are distributed in a fixed frequency range, the difference between blade types will decrease, and the advantage will disappear. Also, as the number of blade types increases, the design space increases rapidly. Therefore, using only a few blade types may be desirable.

Once the number of blade types is chosen, the arrangement of blades around the circumference of the disk needs to be designed. One may use an optimization algorithm to find the best intentional mistuning pattern. However, as the number of available configurations becomes very large, the computational cost will become prohibitive. Here, three guidelines are proposed to reduce the design space such that very effective (though not necessarily optimal) configurations can be found in the reduced design space.

First, it is proposed that an equal or nearly equal number of blades should be assigned to each blade type. If the number of blades of a certain type increases, the source of the energy input to a blade through coupling is likely to increase when the excitation frequency is around the natural frequency of those blades.

Second, it is proposed that the blades of each type should be distributed so that the mistuning pattern is “balanced” about the bladed disk. If blades of the same type or similar types are concentrated to one side, the reduction of the energy flow due to small blade response may be small.

Third, it is proposed that an equal or nearly equal number of blades should be assigned to each group of consecutive blades of the same type. If the size of one group of a certain type is larger than the others, the level of the energy flow in this group might be larger when the excitation frequency is around the natural frequency of those blades.

The second and third guidelines are valid only when the energy flow between sectors is dependent on the displacements of blades. As mentioned in section 5.2, the energy flow in a 2-DOF-per-sector model is dependent on the disk displacements. In that case, the second and third guidelines may not be effective. However, if blade displacement levels are completely independent of disk displacement levels, these guidelines will not have a negative effect.

The above three guidelines are satisfied by a few notable classes of intentional mistuning patterns. For example, when two blade types are used, a square wave pattern, such as a 1H1L or 2H2L, satisfies the guidelines very well. For three blade types, the guidelines are satisfied by sawtooth or staircase patterns, such as 1H1M1L or 2H2M2L, where “M” denotes a medium-frequency blade type. More importantly, these guidelines collectively provide a dramatic reduction in the design space for selecting an intentional mistuning pattern. In the next section, the effectiveness of patterns that lie within this design space will be evaluated numerically.

5.4 Numerical Validation

5.4.1 Lumped Parameter Models

Here, reducing the design space for intentional mistuning patterns by following the proposed guidelines is demonstrated, and the effect of the guidelines are validated using lumped parameter models with 12 blades or 15 blades.

Consider the case in which only two blade types are used. After eliminating any patterns that are redundant because they are just rotated versions of another pattern, the number of unique patterns is 350 for the 12-blade system and 2,190 for the 15-blade system.

For a 12-blade system, the first guideline is met when both the numbers of lower-frequency blades and higher-frequency blades are chosen to be 6. For a 15-blade system, one of the numbers can be 7 or 8 with the other being 8 or 7, and here the number of lower-frequency blades is chosen to be 8. Then, the number of the unique patterns that satisfy the first guideline becomes 80 for a 12-blade system, and 429 for a 15-blade system.

Now, the second guideline is applied. In order to select balanced patterns, the deviation of the “center” of the intentional mistuning pattern is used, which is defined as

$$\epsilon = \sqrt{\left(\sum_{i=1}^{N} \delta_i^{int} \cos\left(\frac{2\pi i}{N}\right)\right)^2 + \left(\sum_{i=1}^{N} \delta_i^{int} \sin\left(\frac{2\pi i}{N}\right)\right)^2}, \tag{5.12}$$

where N is the total number of blades, and δ_i^{int} is the ith intentional mistuning value. A low deviation from the center indicates that a pattern is well balanced about the disk.

From the patterns filtered by the first guideline, the best 10% patterns are selected. Then, 8 patterns for a 12-blade system remain, and 43 patterns for a 15-blade system.

In order to apply the third guideline, the standard deviation of the blade group size is evaluated. A low standard deviation means that each group of blades contains a similar number of blades. The best 10% patterns can be selected again from the patterns filtered by the first and second guidelines. However, some patterns have the same standard deviation values so that more than 10% of the patterns are selected. Finally, 3 patterns for a 12-blade system are obtained, and 8 patterns for a 15-blade system. In this manner, the design space for intentional mistuning patterns can be significantly reduced. The 3 patterns for a 12-blade system are square wave patterns: 1H1L, 2H2L, and 3H3L. Also, the 8 patterns for a 15-blade system are similar to square wave patterns. Note that an exact square wave pattern cannot be made for a system with an odd number of blades.

To validate the performance of the filtered patterns, all the available intentional mistuning patterns with two blade types were evaluated. The 12-blade lumped parameter models discussed in section 5.2 were used again. Also, a 15-blade 1-DOF-per-sector model, with the same model parameters as those of the 12-blade model, was tested. For each pattern, 100 simulations were run at each sampled standard deviation value of random mistuning, and the maximum stress amplification factor was determined in the same way as in the previous section. Engine order 3 excitation was applied to the 1-DOF-per-sector models, and engine order 1 excitation to the 2-DOF-per-sector model.

The simulation results are shown in Fig. 5.11, where each data point corresponds to a unique pattern. For each test case, three plots are depicted. First, the plot of the maximum stress amplification values of all the available patterns versus the number of lower-frequency blades is shown. Next, a plot for the patterns filtered by the first guideline is shown with the x-axis being the deviation of the center of intentional mistuning (see

Eq. (5.12)). Third, the plot for the patterns filtered by the first and second guidelines is shown with x-axis being the standard deviation of the blade group size.

It can be seen that the proposed three guidelines are very effective for the 1-DOF-per-sector models. For the 1-DOF-per-sector models, the optimal patterns are found in small numbers of the filtered patterns. However, for the 2-DOF-per-sector model, only the first guideline works well. This is because the energy propagation in a 2-DOF-per-sector model as shown in Fig. 5.1(b) depends on disk displacements that may not be affected by blade displacements. Still, since any adverse effect is not seen, the second and third guidelines may be used. Moreover, the intersection of the three guidelines defines a dramatically reduced design space that includes a near-optimal design. The stress amplification for the 1H1L pattern (1.530), which meets all three guidelines, is close to that of the best design (1.456).

The three guidelines were derived from the investigation of vibration energy flow in bladed disks, regardless of the engine order of excitation. Therefore, the reduced design space can be used for any engine order of excitation. For the 1-DOF-per-sector model with 12 blades subject to engine order 3 excitation, the optimal pattern is a 2H2L square wave pattern. In fact, this pattern is optimal for other engine orders of excitation, except 0 and 6. Figure 5.12 shows the maximum stress amplification values of the optimal and the 2H2L patterns. It can be seen that, even for engine orders 0 and 6, the performance of the 2H2L pattern is very close to the optimal one.

Now, more than two blade types are considered in an intentionally mistuned design. As can be seen in Fig. 5.10, the decreasing rate of the maximum stress amplification for the 2-DOF-per-sector model levels off significantly around the amplitude of 0.025. Therefore, it might be better to have more than two blade types if the available range of intentional mistuning is -0.1 to 0.1. For the case of more than two blade types, all the possible configurations are not simulated because of the computational costs associated with the large design space. Instead, only a few configurations satisfying the three design guidelines are tested. Figure 5.13 shows the tested sawtooth patterns with three, four, six, and twelve blade types, and the maximum stress amplification results are depicted in Fig. 5.14. For the entire engine orders of excitation, the maximum stress amplification values of the tested configurations are significantly lower than those of the nominal design. Also, for engine order 1 excitation, the tested configurations show better performance than any two-blade-type configuration, with the three-blade-type configuration yielding the best results.

5.4.2 Finite-Element-Based Reduced-Order Model

So far, the proposed guidelines have been validated using lumped parameter models. Now, the intentional mistuning design guidelines are used for a finite element model of an industrial bladed disk with 29 blades, which is depicted in Fig. 5.15. The rotor model is clamped at the rims located at the outer edges of the disk, which is a rough approximation of boundary conditions due to neighboring stages. The finite element model is constructed with standard linear brick elements (eight-noded solids), and it has 126,846 DOF. Figure 5.16 displays the free vibration natural frequencies of the tuned bladed disk versus the number of nodal diameters. The blade-dominated mode families are labeled on the right-hand side of the horizontal lines in Fig. 5.16, where F denotes a flexural bending mode, and T a torsion mode. A unit force normal to the blade surface is applied to the node at the center of each blade tip line, and engine order 2 excitation is considered in the range 12–18 kHz, which includes the 2T/2F blade-dominated mode family with a veering region near 2 nodal diameters. The used structural damping ratio is 0.006. Mistuning is implemented by varying the Young's modulus of each blade:

$$Y_i = Y_0(1 + \delta_i), \tag{5.13}$$

where Y_i is the Young's modulus of the ith blade, and Y_0 is the original Young's modulus for a tuned blade. Because simulations employing the full finite element model would be quite expensive even for a small number of selected patterns of intentional mistuning, the component mode mistuning technique [44] was used to generate a reduced-order model with 33 DOF by selecting the 33 system modes around 15 kHz.

For lumped parameter models, blade stress amplification can be easily calculated. However, for a reduced-order model, it is difficult to calculate the stress state in all the elements. Recently, the authors developed an approximate measure of the maximum stress in a blade, called the normalized stress indicator (NSI), which is defined as follows [72]:

$$\text{NSI} = \sqrt{\frac{(1+\delta)U_m}{U_{cb}}}, \tag{5.14}$$

where U_m is the peak strain energy of a mistuned blade during a period of oscillation, U_{cb} is the peak strain energy of a tuned cantilevered blade at its resonant frequency corresponding to the 2T/2F mode, and δ is the Young's modulus mistuning value. This indicator provides an estimate of the amplification of the largest Von Mises stress in a blade due to mistuning.

The amplitude of intentional mistuning is set to 0.1, and 100 random mistuning patterns are used in the same way as for the lumped parameter models. As with the stress amplification in previous sections, the maximum normalized stress indicator is taken to be the peak 99th percentile value for each intentional mistuning configuration. Since the number of blades is 29, the design space is too huge to evaluate all the available patterns even if only two blade types are used. Therefore, a small number of patterns that meet three guidelines well were tested. The tested intentional mistuning patterns and their maximum NSI values are shown in Fig. 5.17. Since the number of blades in this bladed disk is a prime number, each blade type cannot be assigned to exactly the same number of blades. However, the closest approximations to several square wave, sawtooth, and staircase patterns were used. The maximum NSI of the original system without intentional mistuning is 2.474, which indicates the maximum stress level is 147.4% higher than that of a tuned, cantilevered blade. With intentional mistuning, the maximum blade forced response is reduced for all the tested patterns. The best of these designs has a maximum NSI of 1.864.

5.5 Conclusions

The energy flow in lumped parameter models of bladed disks was investigated to provide a deeper understanding of the effects of intentional mistuning on the vibration response, as well as to explore design guidelines for intentional mistuning. It was found that a blade showing large forced response is fed a large amount of vibration energy through coupling springs, and that blade response becomes smaller when the difference between the excitation frequency and the blade-alone natural frequency becomes larger. Also, it was observed that the energy flow between sectors becomes smaller with the increase of the frequency difference when the amount of the energy flow depends on blade displacements. Based on these findings, the following three design guidelines for intentional mistuning were proposed:

1. Assign an equal number of blades to each blade type used in the design
2. Distribute the blades of each type so that they are “well balanced” about the disk
3. Arrange the blades of each type into groups of equal sizes

Classes of designs that satisfy all three rules include simple intentional mistuning patterns with repeated wave forms, such as square wave, sawtooth, and staircase patterns.

The guidelines were validated by performing extensive Monte Carlo simulations of lumped parameter models for all the intentional mistuning patterns that can be constructed with two blade types. It was found that the first guideline is strongly correlated with a reduction in worst-case blade stress. The second and third guidelines showed weaker correlation with blade stress reduction for a 2-DOF-per-sector lumped parameter model where vibration energy propagate only through disk, but neither rule had an adverse effect. Furthermore, these guidelines collectively defined a drastically reduced design space that included optimal or near-optimal intentional mistuning patterns. Also, it is expected that all three guidelines will work for a system with direct coupling between blades, such as bladed disks with shrouds.

The effectiveness of the approach was also evaluated for lumped parameter models with three or more blade types, as well for a finite-element-based reduced-order model of an industrial rotor. For the reduced-order model, simulations were run for ten intentional mistuning configurations satisfying the three guidelines. All of the tested intentional mistuning configurations resulted in significantly reduced stress levels compared to the original design. Overall, it was found that this approach provides a simple way to find effective designs without requiring a costly optimization process.

5.6 Figures

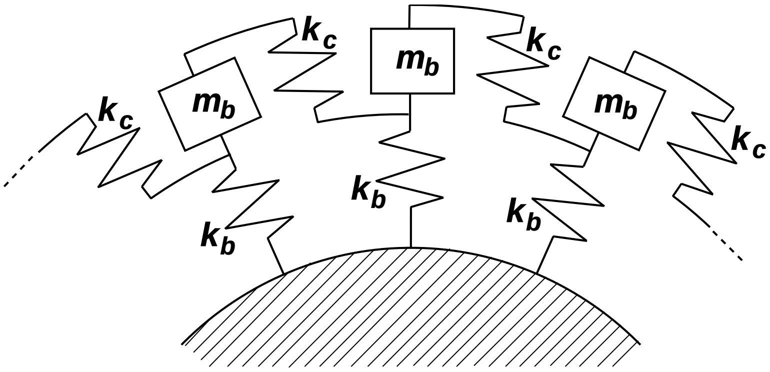

(a) 1-DOF-per-sector model

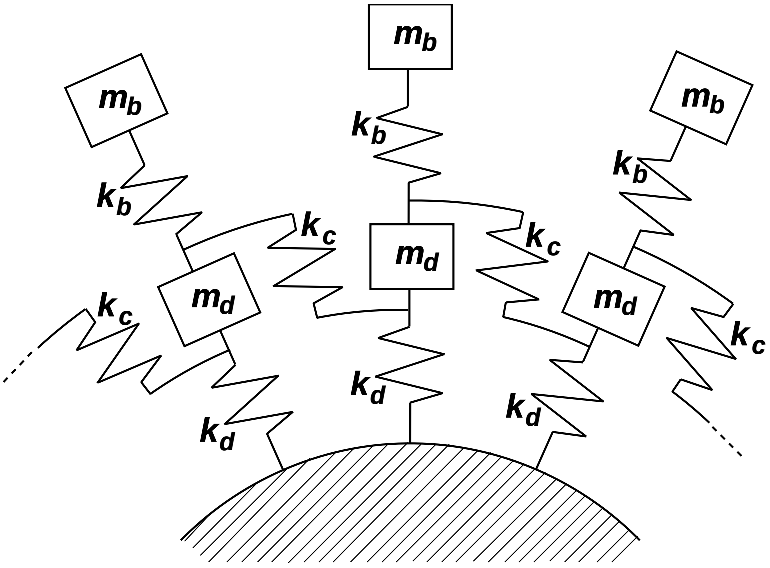

(b) 2-DOF-per-sector model

Figure 5.1: Lumped parameter models

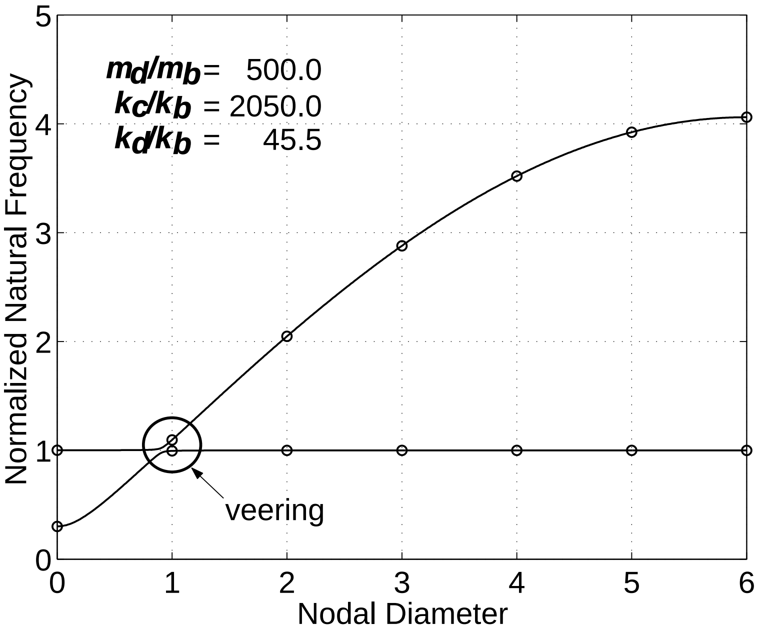

Figure 5.2: Natural frequencies of the tuned 2-DOF-per-sector model

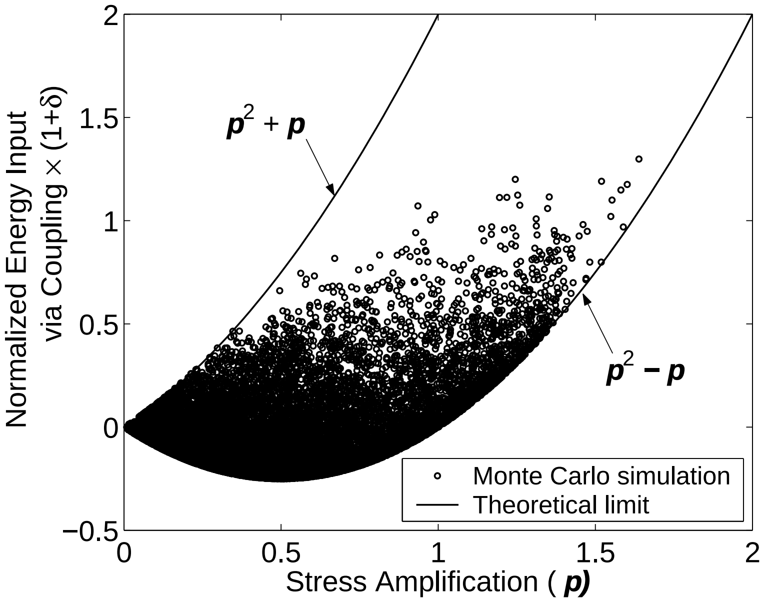

(a) Nominally tuned 1-DOF-per-sector models

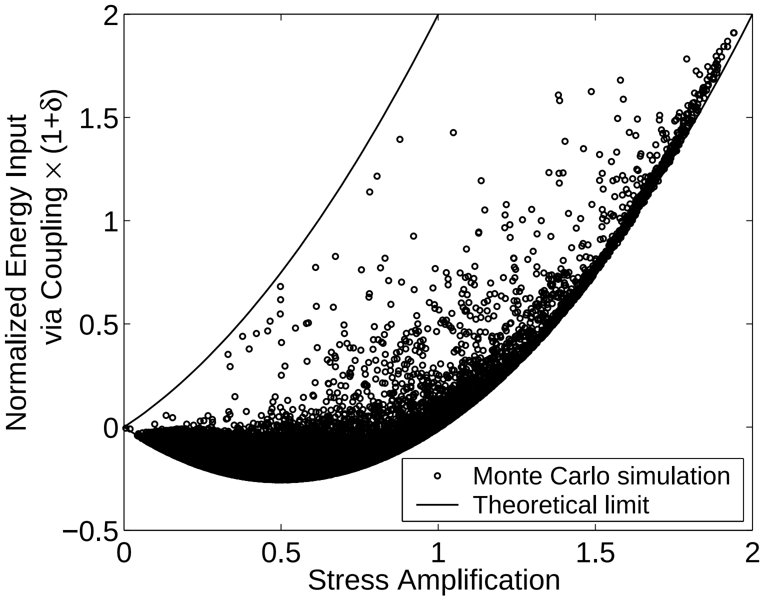

(b) Nominally tuned 2-DOF-per-sector models

Figure 5.3: Energy input through coupling to a sector versus stress amplification obtained from 1,000 monte carlo simulations of nominally tuned systems

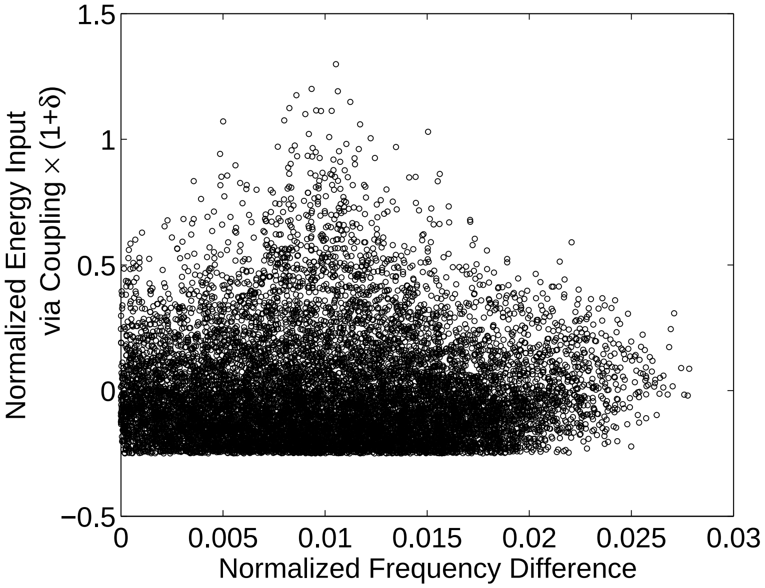

(a) Nominally tuned 1-DOF-per-sector models

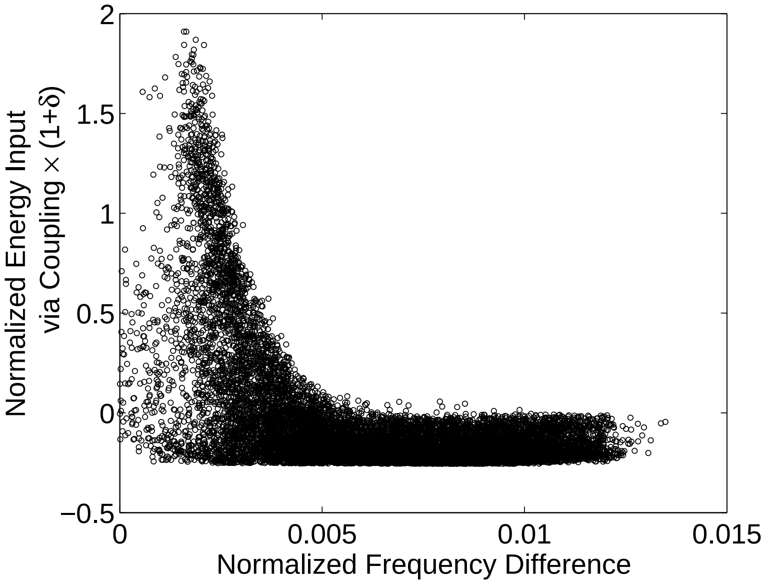

(b) Nominally tuned 2-DOF-per-sector models

Figure 5.4: Energy input through coupling to a sector versus frequency difference obtained from 1,000 monte carlo simulations of nominally tuned systems

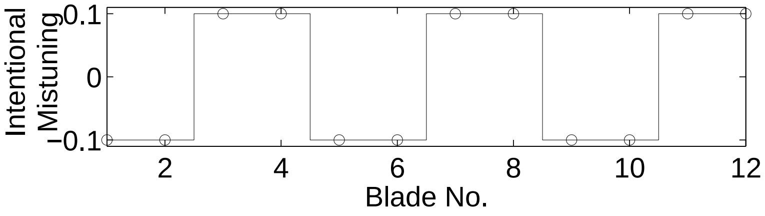

Figure 5.5: 2H2L Square wave pattern of intentional mistuning

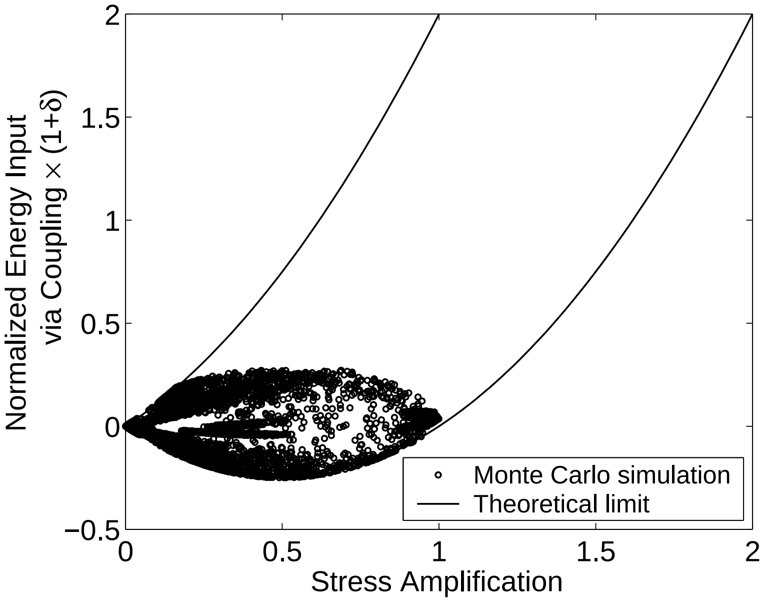

(a) Intentionally mistuned 1-DOF-per-sector models

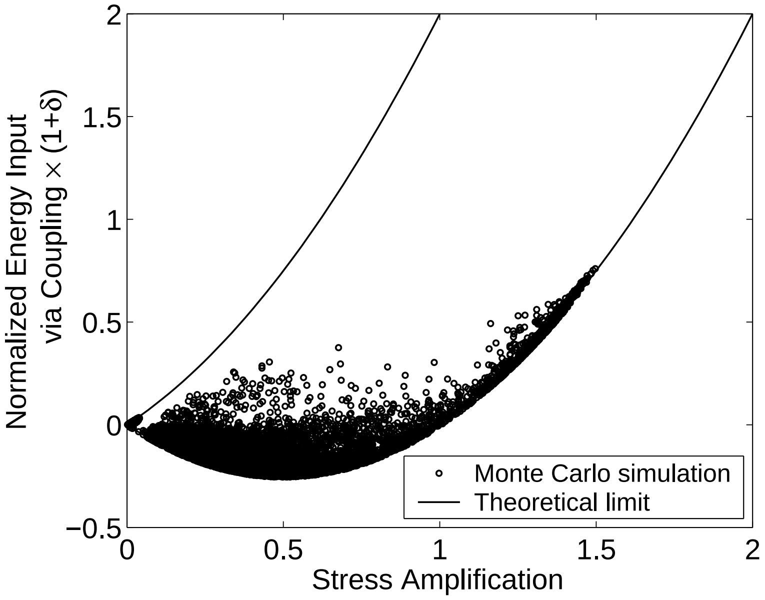

(b) Intentionally mistuned 2-DOF-per-sector models

Figure 5.6: Energy input through coupling to a sector versus stress amplification obtained from 1,000 monte carlo simulations of intentionally mistuned systems

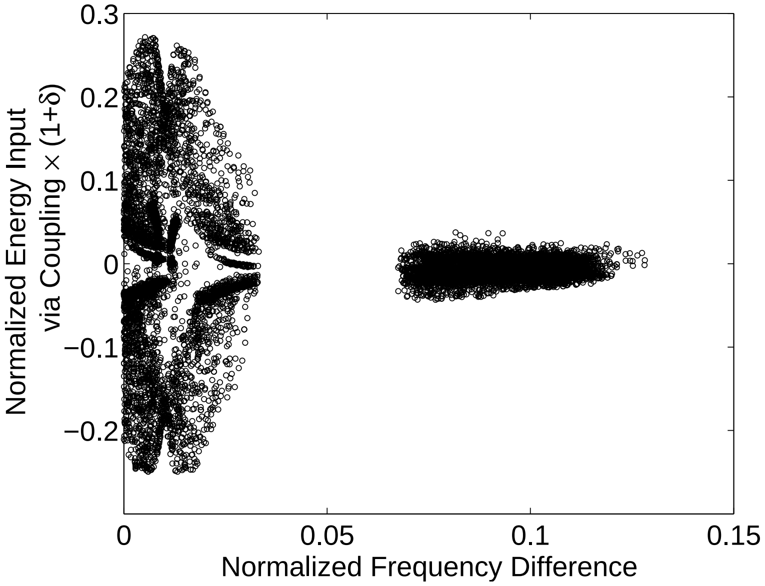

(a) Intentionally mistuned 1-DOF-per-sector models

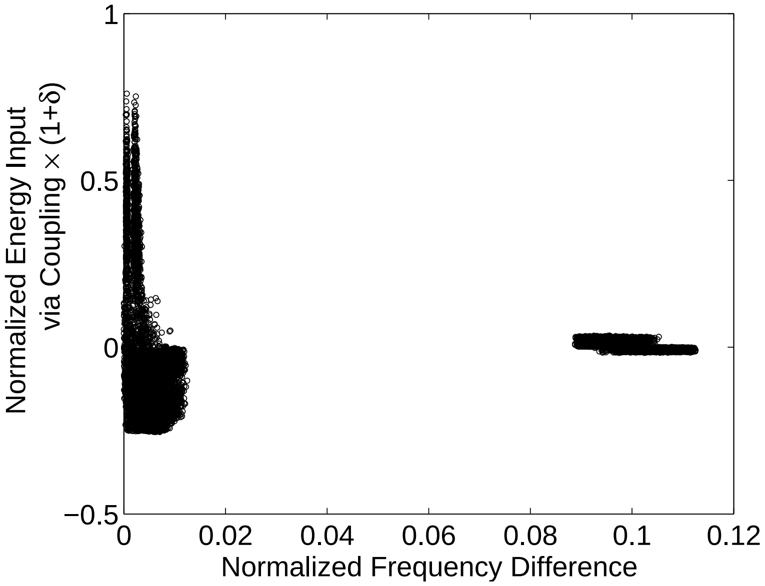

(b) Intentionally mistuned 2-DOF-per-sector models

Figure 5.7: Energy input through coupling to a sector versus frequency difference obtained from 1,000 monte carlo simulations of intentionally mistuned systems

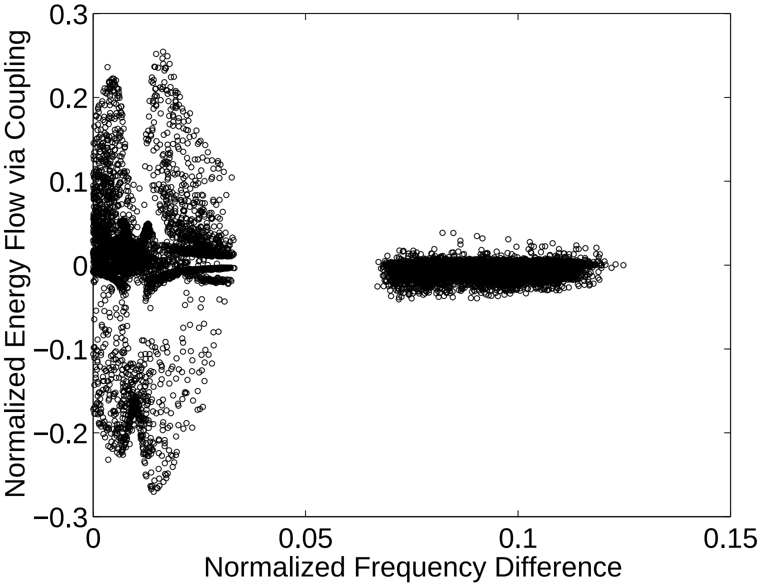

(a) Intentionally mistuned 1-DOF-per-sector models

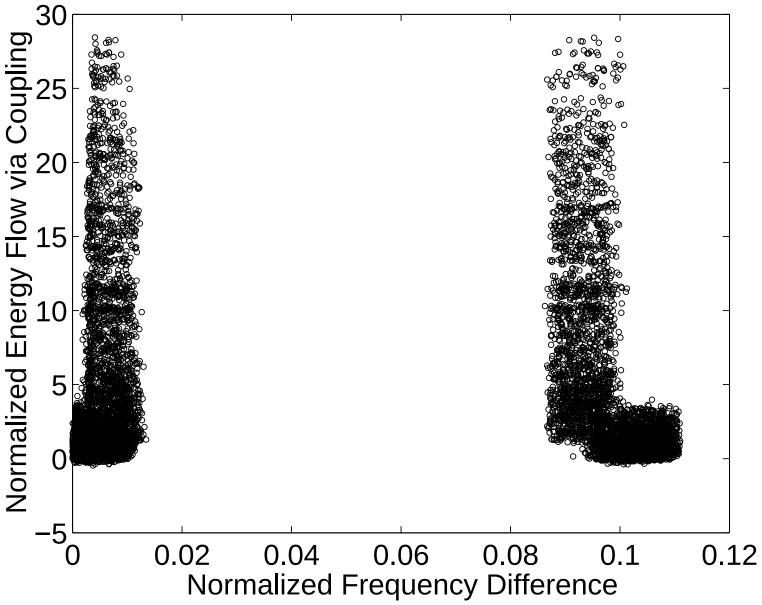

(b) Intentionally mistuned 2-DOF-per-sector models

Figure 5.8: Energy flow through coupling between sectors versus frequency difference obtained from 1,000 monte carlo simulations of intentionally mistuned systems

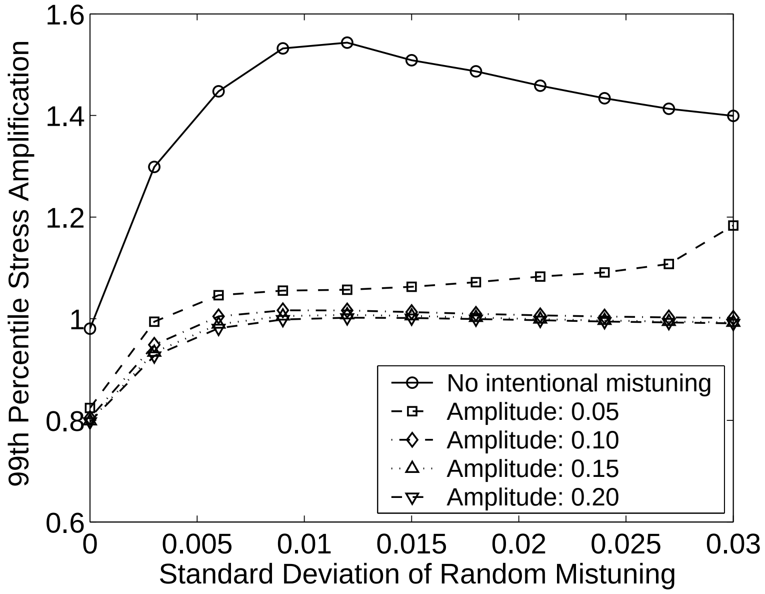

Figure 5.9: 99th percentile stress amplification factors for the intentionally mistuned 1-DOF-per-sector model

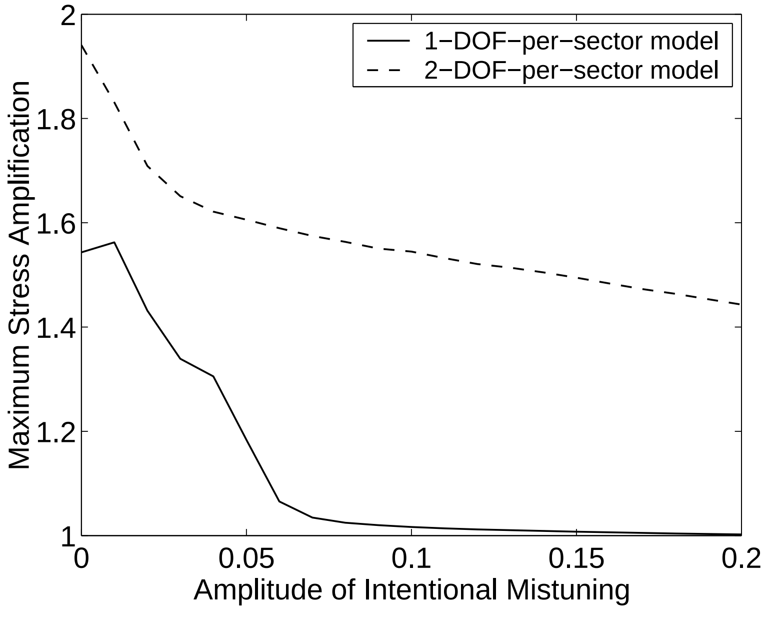

Figure 5.10: Effect of the amplitude of the 2H2L square wave intentional mistuning pattern

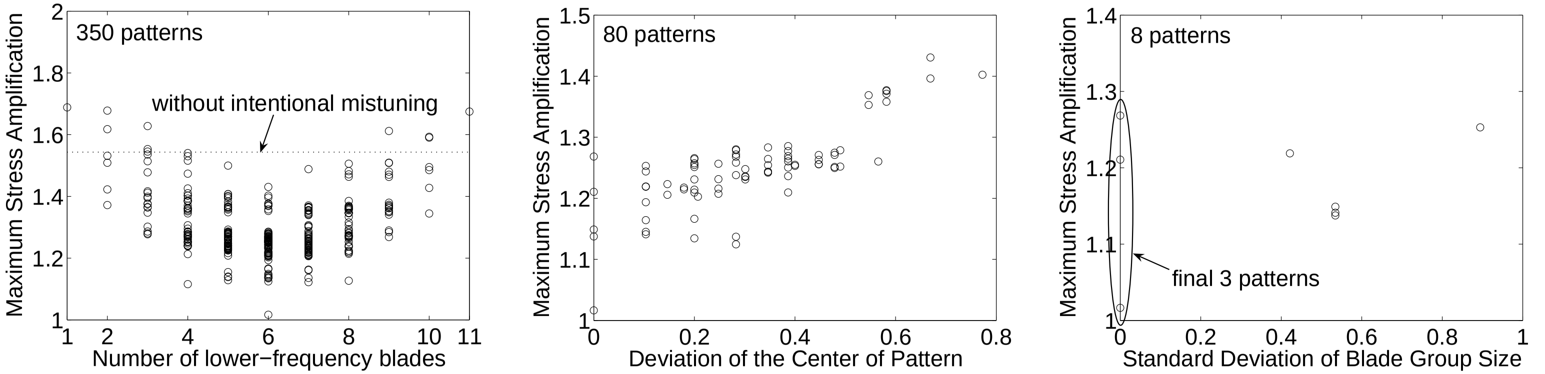

(a) 12-blade 1-DOF-per-sector model subject to engine order 3 excitation

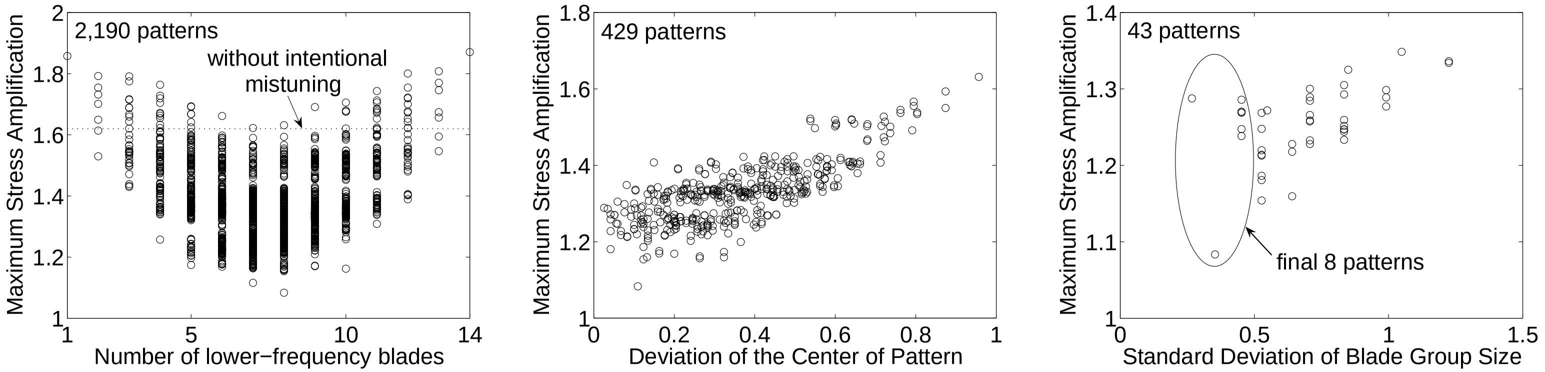

(b) 15-blade 1-DOF-per-sector model subject to engine order 3 excitation

Figure 5.11: Reduction of the design space for intentional mistuning patterns by three guidelines

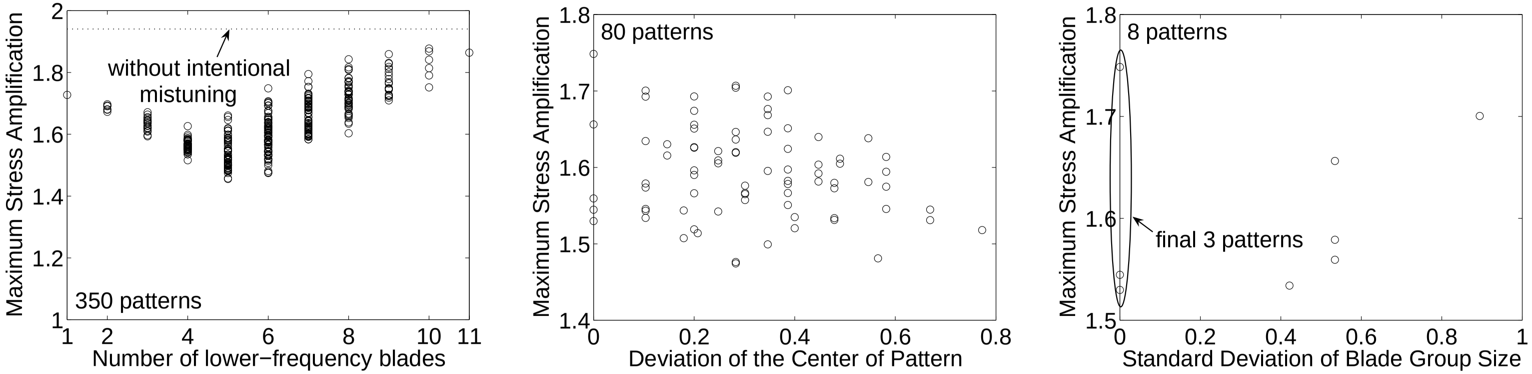

(c) 12-blade 2-DOF-per-sector model subject to engine order 1 excitation

Figure 5.11: (Continued) Reduction of the design space for intentional mistuning patterns by three guidelines

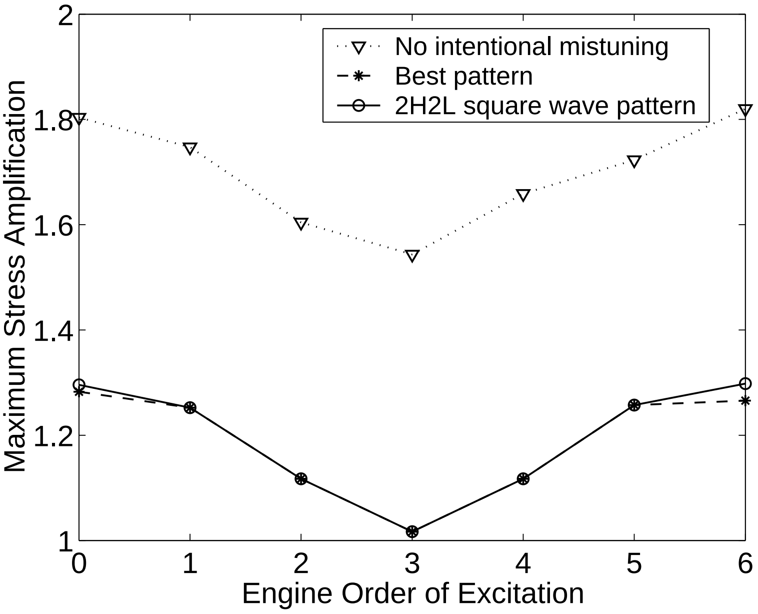

Figure 5.12: Maximum stress amplification for the best of all patterns and the best square wave pattern for different engine orders of excitation

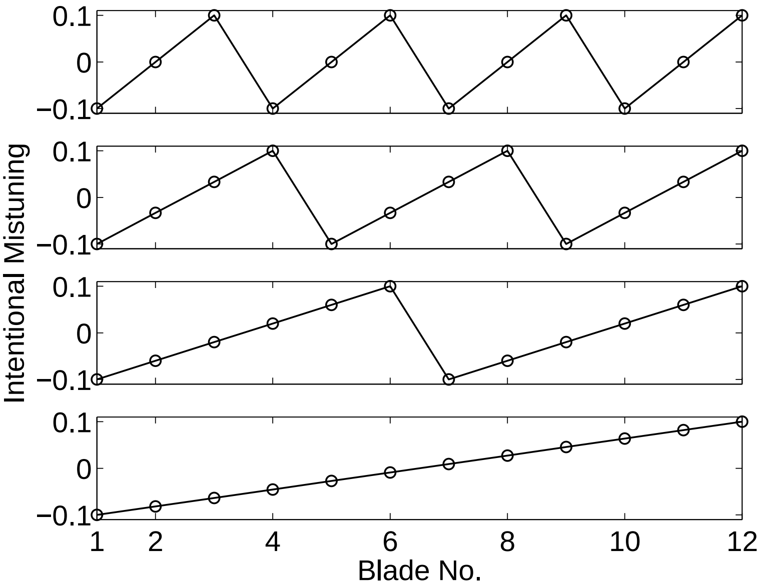

Figure 5.13: Sawtooth patterns of intentional mistuning with more than two blade types

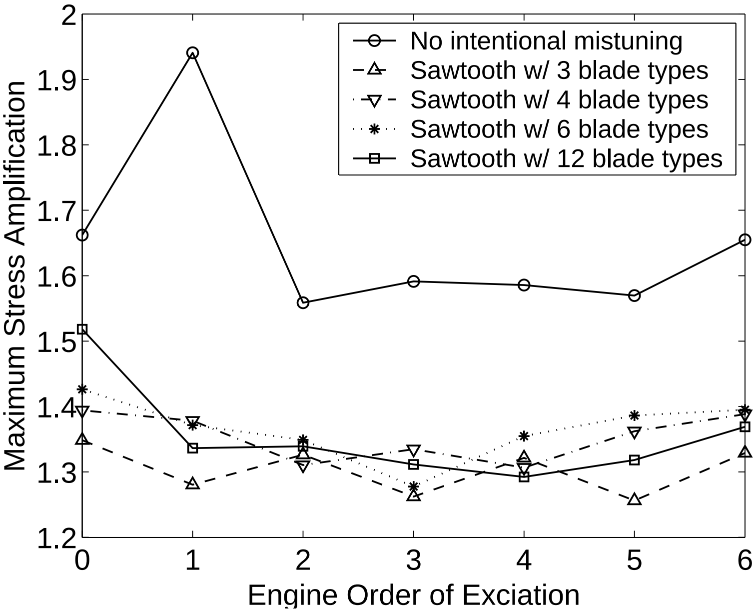

Figure 5.14: Maximum stress amplification for the 2-DOF-per-sector model with sawtooth patterns of intentional mistuning

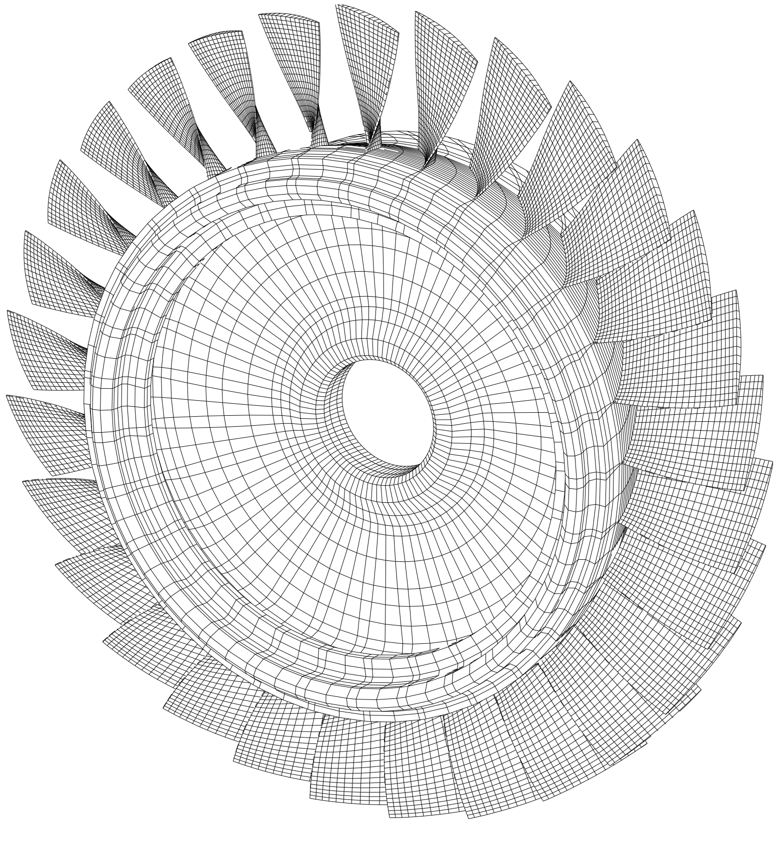

Figure 5.15: Finite element mesh for an industrial rotor

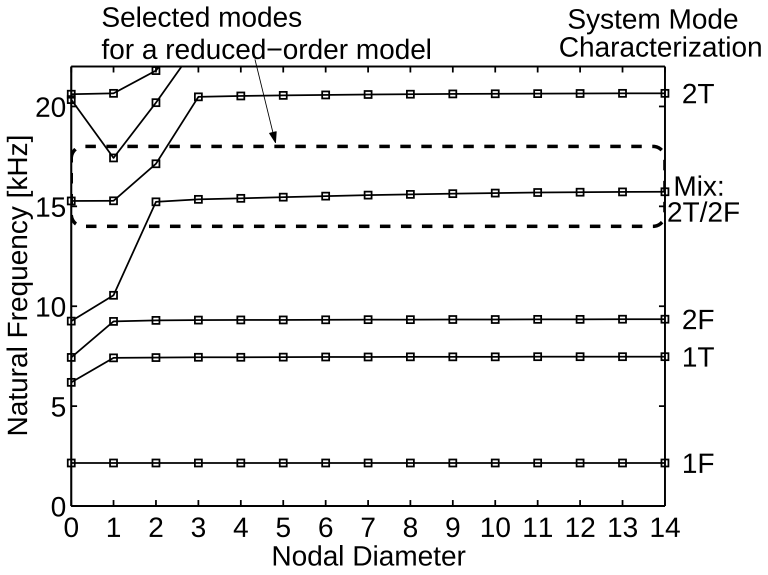

Figure 5.16: Natural frequencies obtained from the tuned finite element model

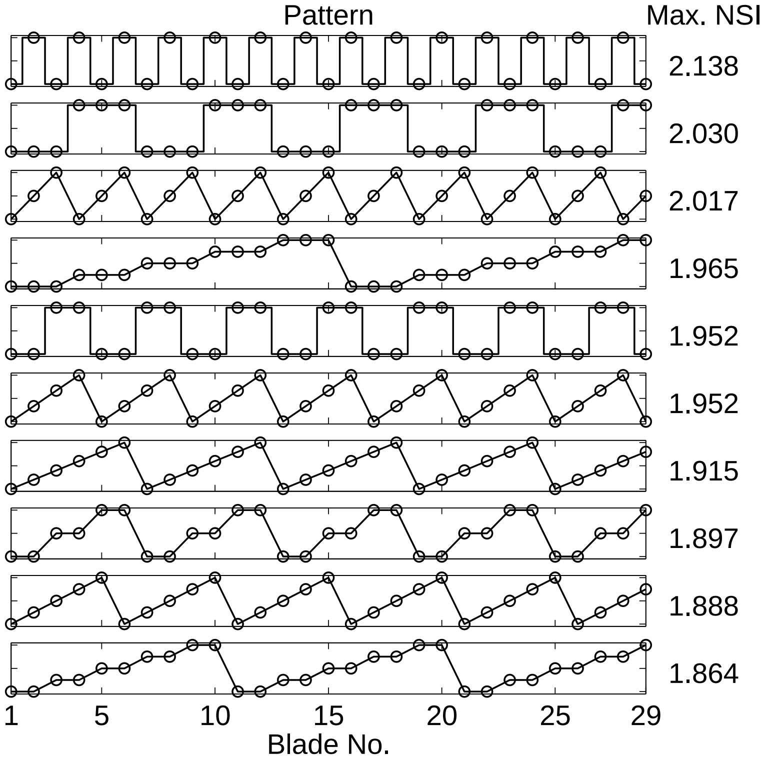

Figure 5.17: Maximum normalized stress indicators for various intentional mistuning patterns tested for the industrial rotor

CHAPTER VI

Vibration Modeling of Bladed Disks Subject to Geometric Mistuning and Design Changes

A new reduced-order modeling technique is presented for bladed disks that feature large, geometric deviations from a nominal design. Various finite-element-based reduced-order models (ROMs) have been proposed in the literature for bladed disks with small blade-to-blade differences, called mistuning. Many of these techniques rely on the fact that mistuned-system normal modes can be effectively represented using a linear combination of the normal modes of the nominal cyclic (tuned) system. However, when the mistuning or geometric deviation is large, the number of tuned-system normal modes required to describe the mistuned-system normal modes increases dramatically. In this work, a method for large mistuning is formulated by employing a mode-acceleration method with static mode compensation. By accounting for the effects of mistuning as though they were produced by external forces, a set of basis vectors is established using a combination of tuned-system normal modes compensated by static modes. The obtained basis vectors approximately span the space of the mistuned-system modes without requiring a much more expensive modal analysis of the mistuned system, and they provide much better convergence than tuned-system normal modes. Furthermore, in order to extend the method to higher frequency ranges, quasi-static modes, in which inertia effects are included, are employed in place of static modes in the mode-acceleration formulation. Validations are performed for an industrial compressor stage, and it is found that ROMs based on the new technique are extremely compact, yet they accurately capture the vibration response of bladed disks subject to geometric mistuning or design changes.

6.1 Introduction

For many years, researchers have investigated the vibration behavior of bladed disks, and most studies have been focused on the effect of small, random blade-to-blade discrepancies (mistuning). Not only is mistuning unavoidable, but the vibration response of a mistuned bladed disk can be considerably different from that of a tuned bladed disk. Although it originates from various sources, mistuning has generally been treated as a small deviation of blade mass, stiffness, or natural frequency from the nominal value in a simplified bladed disk model (a lumped parameter model or a reduced-order model) [2–4, 7–10, 12, 15, 18, 19, 21, 23, 44, 74]. However, in reality mistuning is not necessarily small. Large, geometric variations (e.g., cracking or fracture of a blade due to fatigue or foreign object damage) can also change dramatically the dynamic behavior of a bladed disk, but these large-mistuning cases have rarely been studied.

When a lumped parameter model is employed, the system response can be easily obtained, even for large mistuning. However, the number of degrees of freedom (DOF) is so small that the characteristics of an actual bladed disk may not be captured properly, especially when geometric mistuning is large. A finite element model (FEM) can predict the response of actual bladed disks realistically, regardless of the amount of mistuning [13]. However, an FEM is usually computationally expensive, especially when Monte Carlo simulations are required for statistical analysis of the mistuned response. Therefore, developing a reduced-order model (ROM) of a small size is of great importance to bladed disk research.

Several FEM-based ROMs have been reported in recent years [15, 18, 19, 21, 23, 44]. However, most of these models are based on the assumption that mistuning is small. Two recently developed methods [23, 44] are notable for generating highly compact ROMs that feature excellent accuracy relative to the parent FEM. These models use a basis of tuned-system normal modes to capture mistuned-system normal modes. However, as mistuning becomes large, the required number of tuned-system normal modes increases dramatically, and in some cases a model gives poor results regardless of the number of retained modes.

In 1987, Gu and Tongue [75] showed that modal convergence can be accelerated by using forced modes in addition to free vibration modes. A forced mode (or static mode) is a shape that is induced in the structure by a given external force vector. In the work of Gu and Tongue, external forces were applied to a beam by springs that were included as additional stiffness elements. The concept of a forced mode can be extended to a mistuned system in an analogous manner, for instance by considering mistuning as additional stiffnesses. In 1995, Cai *et al*. [76] considered the effect of mistuning as that of external forces in a lumped-parameter model, obtained a frequency equation in closed form, and solved it. In a recent study by the authors [44], a reduced-order model based on a component mode synthesis (CMS) technique was proposed for large mistuning. In this modeling method, tuned-system normal modes (free vibration modes) and tuned-system attachment modes (forced modes) are employed, and the ROMs show good accuracy and fast convergence with increasing number of tuned-system normal modes. However, the model size is still greater than that generated by a small-mistuning method, because one attachment-mode DOF is retained for each physical DOF in the FEM where geometric mistuning is present.

In this work, a non-CMS method for large mistuning is formulated by employing a mode-acceleration method with static mode compensation. The tuned-system normal modes are compensated by static modes that account for the effects of mistuning as though they were produced by external forces. Thus, a new set of basis vectors is established for the mistuned system. The obtained basis vectors approximately span the space of the mistuned-system modes without requiring a much more expensive modal analysis of the mistuned system, and they provide much faster convergence than the original tuned-system normal modes. Furthermore, in order to extend the method to higher frequency ranges, quasi-static modes [77, 78], in which inertia effects are included, are employed in place of static modes in the mode-acceleration formulation.

In addition to modeling systems with large mistuning, the presented method can also be used in the design process. Usually, when a change is made to a geometric design parameter, the new FEM must be analyzed in order to determine the effects of the design change on the system vibration response. However, if the changes to the mass and stiffness matrices due to the design change are known, then the new modeling technique can be used to construct an updated ROM for the revised design without requiring an additional finite element analysis of the vibration response. In this manner, the process of evaluating geometric design changes can be expedited.

This paper is organized as follows. The authors' previous approach for large mistuning is briefly reviewed in section 6.2. In section 6.3, the new modeling technique is formulated starting from the original mode-acceleration formulation, and it is refined using the modified mode-acceleration formulation with quasi-static modes. Then, an industrial bladed disk with a rogue blade whose geometry deviates severely from the nominal blade design is examined as a case study in section 6.4. The newly developed method is validated using the parent FEM, and its performance is compared with previous methods for large and small mistuning. Two additional cases are examined in sections 6.5 and 6.6, as further applications of the new modeling technique: a bladed disk with a fractured blade, and a bladed disk subject to geometric design changes in the disk. Finally, conclusions are summarized in section 6.7.

6.2 Background: Reduced-Order Modeling by CMS

In this section, a general reduced-order model for large mistuning, which was developed previously by the authors [44], is briefly reviewed. A mistuned bladed disk is divided into a tuned bladed disk ($\mathbf{M}^S, \mathbf{K}^S$) and mistuning components ($\mathbf{M}^\delta, \mathbf{K}^\delta$) that represent the difference between the mistuned and tuned mass and stiffness matrices. The mistuned system model is constructed using a hybrid-interface CMS technique: the tuned system is treated as a free-interface component, and the mistuning components are treated as fixed-interface components. Because the mistuning components are not physically separate from the tuned system, all DOF in the mistuning components are interface DOF. Thus, both tuned-system attachment modes ($\boldsymbol{\Psi}^S$) and a truncated set of normal modes ($\boldsymbol{\Phi}^S$) are used to describe the displacements of the tuned system, but only constraint modes ($\boldsymbol{\Psi}^\delta = \mathbf{I}$) are used for the mistuning components. The synthesized mass and stiffness matrices ($\boldsymbol{\mu}^{syn}, \boldsymbol{\kappa}^{syn}$) of a mistuned system are assembled by enforcing displacement compatibility at the interface DOF:

$$\begin{aligned}\boldsymbol{\mu}^{syn} &= \begin{bmatrix} \mathbf{I} + \boldsymbol{\Phi}_\Gamma^{S^T} \mathbf{M}^\delta \boldsymbol{\Phi}_\Gamma^S & \boldsymbol{\Phi}^{S^T} \mathbf{M}^S \boldsymbol{\Psi}^S + \boldsymbol{\Phi}_\Gamma^{S^T} \mathbf{M}^\delta \boldsymbol{\Psi}_\Gamma^S \\ \boldsymbol{\Psi}^{S^T} \mathbf{M}^S \boldsymbol{\Phi}^S + \boldsymbol{\Psi}_\Gamma^{S^T} \mathbf{M}^\delta \boldsymbol{\Phi}_\Gamma^S & \boldsymbol{\Psi}^{S^T} \mathbf{M}^S \boldsymbol{\Psi}^S + \boldsymbol{\Psi}_\Gamma^{S^T} \mathbf{M}^\delta \boldsymbol{\Psi}_\Gamma^S \end{bmatrix} \\ &= \begin{bmatrix} \mathbf{I} + \boldsymbol{\Phi}_\Gamma^{S^T} \mathbf{M}^\delta \boldsymbol{\Phi}_\Gamma^S & \boldsymbol{\Lambda}^{S^{-1}} \boldsymbol{\Phi}_\Gamma^{S^T} + \boldsymbol{\Phi}_\Gamma^{S^T} \mathbf{M}^\delta \boldsymbol{\Psi}_\Gamma^S \\ \boldsymbol{\Phi}_\Gamma^S \boldsymbol{\Lambda}^{S^{-1}} + \boldsymbol{\Psi}_\Gamma^{S^T} \mathbf{M}^\delta \boldsymbol{\Phi}_\Gamma^S & \boldsymbol{\Psi}^{S^T} \mathbf{M}^S \boldsymbol{\Psi}^S + \boldsymbol{\Psi}_\Gamma^{S^T} \mathbf{M}^\delta \boldsymbol{\Psi}_\Gamma^S \end{bmatrix}\end{aligned} \tag{6.1a}$$

$$\begin{aligned}\boldsymbol{\kappa}^{syn} &= \begin{bmatrix} \mathbf{\Lambda}^S + \mathbf{\Phi}_\Gamma^{S^T}\mathbf{K}^\delta\mathbf{\Phi}_\Gamma^S & \mathbf{\Phi}^{S^T}\mathbf{K}^S\mathbf{\Psi}^S + \mathbf{\Phi}_\Gamma^{S^T}\mathbf{K}^\delta\mathbf{\Psi}_\Gamma^S \\ \mathbf{\Psi}^{S^T}\mathbf{K}^S\mathbf{\Phi}^S + \mathbf{\Psi}_\Gamma^{S^T}\mathbf{K}^\delta\mathbf{\Phi}_\Gamma^S & \mathbf{\Psi}_\Gamma^S + \mathbf{\Psi}_\Gamma^{S^T}\mathbf{K}^\delta\mathbf{\Psi}_\Gamma^S \end{bmatrix} \\ &= \begin{bmatrix} \mathbf{\Lambda}^S + \mathbf{\Phi}_\Gamma^{S^T}\mathbf{K}^\delta\mathbf{\Phi}_\Gamma^S & \mathbf{\Phi}_\Gamma^{S^T} + \mathbf{\Phi}_\Gamma^{S^T}\mathbf{K}^\delta\mathbf{\Psi}_\Gamma^S \\ \mathbf{\Phi}_\Gamma^S + \mathbf{\Psi}_\Gamma^{S^T}\mathbf{K}^\delta\mathbf{\Phi}_\Gamma^S & \mathbf{\Psi}_\Gamma^S + \mathbf{\Psi}_\Gamma^{S^T}\mathbf{K}^\delta\mathbf{\Psi}_\Gamma^S \end{bmatrix}, \end{aligned} \tag{6.1b}$$

where Γ denotes the interface DOF where mistuning exists.

Eq. (6.1) shows that a mistuned system can be described with the normal modes and attachment modes of the tuned system. Since a tuned bladed disk features cyclic symmetry, normal modes and attachment modes can be obtained using only the FEM of a single sector. However, when attachment modes are involved in the CMS formulation, matrix ill-conditioning and numerical instability may occur. This is due to the fact that the displacement values of attachment modes are much smaller than those of normal modes, and also because attachment modes and normal modes may not be clearly independent. The former problem can be overcome by performing a secondary modal analysis on the attachment mode partition of the synthesized mass and stiffness matrices. In order to reduce the effect of the latter problem, the number of retained normal modes must be decreased. However, in this case, the accuracy of the ROM also decreases. To compensate for this loss of accuracy, more attachment modes can be included in the ROM. Of course, including more attachment modes leads a larger model size. In fact, in the authors' previous work [44], the size of the ROM for large mistuning using this approach was much larger than the typical size of a small-mistuning ROM. Therefore, a new, more efficient method is introduced in the next section.

6.3 New Modeling Technique Using Static Mode Compensation

In this section, a new modeling technique for a mistuned system is formulated using the mode-acceleration method. In the derivation, the effect of large mistuning is converted to that of equivalent external forces.

6.3.1 Static Mode Compensation

The mode-acceleration method is usually used to improve the accuracy of forced response predictions by including a static mode ($\mathbf{K}^{-1}\mathbf{f}$) [41]. The formulation for an undamped system is as follows:

$$\mathbf{x} = \mathbf{K}^{-1}\mathbf{f} + \sum_i \left(\frac{\omega^2}{\omega_i^2} \right) \boldsymbol{\phi}_i \eta_i, \tag{6.2}$$

or

$$\mathbf{x} - \mathbf{K}^{-1}\mathbf{f} = \sum_i \left(\frac{\omega^2}{\omega_i^2} \right) \boldsymbol{\phi}_i \eta_i, \tag{6.3}$$

where $\mathbf{x}$ is the displacement vector, $\mathbf{f}$ is the external force vector, ω is the excitation frequency, ω_i is the natural frequency of the ith mode, $\boldsymbol{\phi}_i$ is the ith normal mode, and η_i is the ith modal amplitude that is used in the mode-displacement method. In Eq. (6.3), $\mathbf{x} - \mathbf{K}^{-1}\mathbf{f}$ is expressed as a linear combination of normal modes. Note that, in this combination, lower normal modes will dominate due to the coefficients, ω^2/ω_i^2, if the external forces excite every mode evenly. That is, $\mathbf{x} - \mathbf{K}^{-1}\mathbf{f}$ can be described with a small set of normal modes. Now, suppose that the normal modes are unknown, but a set of vectors of the form $\mathbf{x} - \mathbf{K}^{-1}\mathbf{f}$ are known in a lower frequency range. Then, reversely, lower normal modes can be obtained accurately by employing the set of $\mathbf{x} - \mathbf{K}^{-1}\mathbf{f}$ vectors as a basis, unless $\mathbf{f}$ excites higher modes much more than lower modes.

This concept can be applied to a mistuned system when the tuned-system normal modes are known. Consider a forced response case in which a mistuned system is vibrating at the natural frequency of a tuned-system mode and the motion of the mistuned system is exactly the same as that of the tuned-system mode. Then, Eq. (6.3) can be rewritten as:

$$\boldsymbol{\phi}_j^S - \mathbf{K}^{m-1}\mathbf{f}_j = \sum_i \left(\frac{\omega_j^{S2}}{\omega_i^{m2}} \right) \boldsymbol{\phi}_i^m \eta_{ij}, \tag{6.4}$$

where the external forces required to enforce this motion are

$$\mathbf{f}_j = \left[-\omega_j^{S2}\mathbf{M}^m + \mathbf{K}^m \right] \boldsymbol{\phi}_j^S = \left\{ \begin{array}{c} \mathbf{0} \\ \left[-\omega_j^{S2}\mathbf{M}^\delta + \mathbf{K}^\delta \right] \boldsymbol{\phi}_{\Gamma,j}^S \end{array} \right\}, \tag{6.5}$$

$\mathbf{M}^m$ and $\mathbf{K}^m$ are the mass and stiffness matrices of a mistuned system, ω_j^S and $\boldsymbol{\phi}_j^S$ are the jth natural frequency and mode shape of the tuned system, ω_i^m and $\boldsymbol{\phi}_i^m$ are the ith natural frequency and mode shape of the mistuned system, and η_{ij} is the modal participation factor of the ith mistuned-system normal mode for the jth tuned-system normal mode. The advantage of using tuned-system modes is that they are readily available, because an analysis of a bladed disk usually starts with computing tuned modes that can be obtained from the cyclic symmetry analysis of the FEM of a single sector. Another advantage is that non-zero forcing terms appear only at the DOF where mistuning exists, as indicated by the partitioning of the right-hand side of Eq. (6.5).

$\mathbf{K}^{m-1}\mathbf{f}_j$ is the static mode of the mistuned system. However, it is also possible to obtain the static mode from the FEM of the tuned system by using the following relation:

$$\mathbf{K}^{m-1}\mathbf{f}_j = \mathbf{K}^{S^{-1}}(\mathbf{I} + \bar{\mathbf{K}}^\delta\, \mathbf{K}^{S^{-1}})^{-1}\mathbf{f}_j = \mathbf{K}^{S^{-1}}\mathbf{g}_j, \tag{6.6}$$

where

$$\mathbf{g}_j = (\mathbf{I} + \bar{\mathbf{K}}^\delta\, \mathbf{K}^{S^{-1}})^{-1}\mathbf{f}_j = \left\{ \begin{array}{c} \mathbf{0} \\ \left(\mathbf{I} + \mathbf{K}^\delta\, \boldsymbol{\Psi}_\Gamma^S \right)^{-1} \mathbf{f}_{\Gamma,j} \end{array} \right\}, \tag{6.7}$$

$\mathbf{K}^S$ denotes the stiffness matrix of the tuned system, $\bar{\mathbf{K}}^\delta$ denotes a matrix of the same size as that of $\mathbf{K}^S$, which consists of $\mathbf{K}^\delta$ and zero terms, and $\boldsymbol{\Psi}^S$ is a set of tuned-system attachment modes. That is, the static deflection of the mistuned system induced by the forces $\mathbf{f}_j$ is the static deflection of the tuned system induced by the forces $\mathbf{g}_j$. Here, since

$\mathbf{f}_j$ has non-zero terms for only the DOF where mistuning exists, so does $\mathbf{g}_j$. Computing static modes of a mistuned system by using a tuned system is especially useful for bladed disks, because any static deflection of a tuned bladed disk can be calculated using only the FEM of a single sector.

Static modes can be obtained by directly applying the forces, $\mathbf{f}_j$ or $\mathbf{g}_j$, or they can be computed as a linear combination of tuned-system attachment modes with the coefficients being the corresponding forces. That is,

$$\mathbf{K}^{m-1}\mathbf{f}_j = \mathbf{K}^{S^{-1}}\mathbf{g}_j = \boldsymbol{\Psi}^S\mathbf{g}_{\Gamma,j}. \tag{6.8}$$

If many mistuned systems need to be analyzed, the latter method is more efficient, because the obtained attachment modes can be used for any $\mathbf{K}^\delta$. However, if the number of mistuning DOF is so large that the computation of $\boldsymbol{\Psi}^S$ and $\mathbf{g}_{\Gamma,j}$ is costly, then one should consider computing $\mathbf{K}^{m-1}\mathbf{f}_j$ or $\mathbf{K}^{S^{-1}}\mathbf{g}_j$ directly.

Now, a truncated set of tuned-system normal modes compensated by static modes, $\boldsymbol{\phi}_j^S - \boldsymbol{\Psi}^S\mathbf{g}_{\Gamma,j}$, may be used as an alternative basis that approximately spans the space of the lower mistuned-system normal modes. The reduced mass and stiffness matrices are:

$$\begin{aligned}
\boldsymbol{\mu}^{syn} &= \left(\boldsymbol{\Phi}^S - \boldsymbol{\Psi}^S\mathbf{G}_\Gamma\right)^T \left(\mathbf{M}^S + \mathbf{M}^\delta\right) \left(\boldsymbol{\Phi}^S - \boldsymbol{\Psi}^S\mathbf{G}_\Gamma\right) \\
&= \mathbf{I} + \boldsymbol{\Phi}_\Gamma^{S^T}\mathbf{M}^\delta\boldsymbol{\Phi}_\Gamma^S - \left(\boldsymbol{\Lambda}^{S^{-1}}\boldsymbol{\Phi}_\Gamma^{S^T} + \boldsymbol{\Phi}_\Gamma^{S^T}\mathbf{M}^\delta\boldsymbol{\Psi}_\Gamma^S\right)\mathbf{G}_\Gamma \\
&\quad - \mathbf{G}_\Gamma^T\left(\boldsymbol{\Phi}_\Gamma^S\boldsymbol{\Lambda}^{S^{-1}} + \boldsymbol{\Psi}_\Gamma^{S^T}\mathbf{M}^\delta\boldsymbol{\Phi}_\Gamma^S\right) + \mathbf{G}_\Gamma^T\left(\boldsymbol{\Psi}^{S^T}\mathbf{M}^S\boldsymbol{\Psi}^S + \boldsymbol{\Psi}_\Gamma^{S^T}\mathbf{M}^\delta\boldsymbol{\Psi}_\Gamma^S\right)\mathbf{G}_\Gamma
\end{aligned} \tag{6.9a}$$

$$\begin{aligned}
\boldsymbol{\kappa}^{syn} &= \left(\boldsymbol{\Phi}^S - \boldsymbol{\Psi}^S\mathbf{G}_\Gamma\right)^T \left(\mathbf{K}^S + \mathbf{K}^\delta\right) \left(\boldsymbol{\Phi}^S - \boldsymbol{\Psi}^S\mathbf{G}_\Gamma\right) \\
&= \boldsymbol{\Lambda}^S + \boldsymbol{\Phi}_\Gamma^{S^T}\mathbf{K}^\delta\boldsymbol{\Phi}_\Gamma^S - \left(\boldsymbol{\Phi}_\Gamma^{S^T} + \boldsymbol{\Phi}_\Gamma^{S^T}\mathbf{K}^\delta\boldsymbol{\Psi}_\Gamma^S\right)\mathbf{G}_\Gamma \\
&\quad - \mathbf{G}_\Gamma^T\left(\boldsymbol{\Phi}_\Gamma^S + \boldsymbol{\Psi}_\Gamma^{S^T}\mathbf{K}^\delta\boldsymbol{\Phi}_\Gamma^S\right) + \mathbf{G}_\Gamma^T\left(\boldsymbol{\Psi}_\Gamma^S + \boldsymbol{\Psi}_\Gamma^{S^T}\mathbf{K}^\delta\boldsymbol{\Psi}_\Gamma^S\right)\mathbf{G}_\Gamma,
\end{aligned} \tag{6.9b}$$

where the matrix $\mathbf{G}_\Gamma$ is a set of the vectors $\mathbf{g}_{\Gamma,j}$. The size of these reduced matrices is $N \times N$, where N is the number of tuned-system normal modes in a truncated set.

As mentioned above, the accuracy will be determined by $(\omega_j^{S^2}/\omega_i^2)\eta_{ij}$. If the value of $(\omega_j^{S^2}/\omega_i^2)\eta_{ij}$ for the ith mode is relatively small compared to those for other modes, then the ith mode obtained by this method will be less accurate. That is, mistuned-system normal modes in a high frequency range may be inaccurate because the value of $\omega_j^{S^2}/\omega_i^2$ is smaller for a high mode than for a low mode.

6.3.2 Quasi-Static Mode Compensation

In order to obtain an improved representation in a higher frequency range, the formulation of the mode-acceleration method in Eq. (6.2) is modified. First, the equations of motion of an undamped system are written as follows:

$$\left[-\omega^2\mathbf{M}+\mathbf{K}\right]\mathbf{x}=\left[-\left(\omega^2-\omega_c^2\right)\mathbf{M}+\left(\mathbf{K}-\omega_c^2\mathbf{M}\right)\right]\mathbf{x}=\mathbf{f}, \tag{6.10}$$

where ω_c is a pre-determined frequency, which is the centering frequency used in the quasi-static mode compensation method introduced by Shyu *et al.* [77, 78] to improve CMS models in higher frequency ranges. As can be seen in Eq. (6.10), inertial effects corresponding to a centering frequency are transfered to the stiffness term. Thereby, the motion of the original system, $\mathbf{M}$ and $\mathbf{K}$, at a frequency of ω becomes the same as the motion of an equivalent system, $\mathbf{M}$ and $\mathbf{K}-\omega_c^2\mathbf{M}$, at a frequency of $\sqrt{\omega^2-\omega_c^2}$. The equivalent system has the same mode shapes as those of the original system. However, its eigenvalues are shifted by $-\omega_c^2$ from the original values. Note that the original system can be considered as a special case in which the centering frequency is zero.

Applying the mode-acceleration method to this equivalent system, $\mathbf{x}$ becomes

$$\begin{aligned}\mathbf{x}&=\left(\mathbf{K}-\omega_c^2\mathbf{M}\right)^{-1}\mathbf{f}+\left(\mathbf{K}-\omega_c^2\mathbf{M}\right)^{-1}\left(\omega^2-\omega_c^2\right)\mathbf{M}\mathbf{x}\\&=\left(\mathbf{K}-\omega_c^2\mathbf{M}\right)^{-1}\mathbf{f}+\sum_i\left(\frac{\omega^2-\omega_c^2}{\omega_i^2-\omega_c^2}\right)\boldsymbol{\phi}_i\eta_i.\end{aligned} \tag{6.11}$$

where $\left(\mathbf{K}-\omega_c^2\mathbf{M}\right)^{-1}\mathbf{f}$ are quasi-static modes [77, 78]. Now, as can be seen in Eq. (6.11), the coefficient of $\boldsymbol{\phi}_i$ is $[(\omega^2-\omega_c^2)/(\omega_i^2-\omega_c^2)]\eta_i$. Therefore, if ω_i is close to ω_c, the coefficient of the ith mode can have a larger value than the other modes. Therefore, $\mathbf{x} - \left(\mathbf{K} - \omega_c^2\mathbf{M}\right)^{-1}\mathbf{f}$ can be described by a small number of mistuned modes around the centering frequency.

Following the same procedure as that for static mode compensation using the original mode-acceleration formulation, the quasi-static modes of a mistuned system can be computed from the tuned system as follows:

$$\left(\mathbf{K}^m - \omega_c^2\mathbf{M}^m\right)^{-1}\mathbf{f}_j = \boldsymbol{\Psi}^{S,Q}\mathbf{g}^Q_{\mathit{\Gamma},j}, \tag{6.12}$$

where $\mathbf{g}^Q_{\mathit{\Gamma},j}$ contains the forces that need to be applied to the equivalent tuned system, and is written as

$$\mathbf{g}^Q_{\mathit{\Gamma},j} = \left[\mathbf{I} + \left(\mathbf{K}^\delta - \omega_c^2\mathbf{M}^\delta\right)\boldsymbol{\Psi}^{S,Q}\right]\mathbf{f}_{\mathit{\Gamma},j}$$

and $\boldsymbol{\Psi}^{S,Q}$ is a set of quasi-static attachment modes computed from the stiffness matrix of the equivalent tuned system, $\mathbf{K}^S - \omega_c^2\mathbf{M}^S$. Now, the reduced mass and stiffness matrices are

$$\begin{aligned}
\boldsymbol{\mu}^{syn} &= \left(\boldsymbol{\Phi}^S - \boldsymbol{\Psi}^{S,Q}\mathbf{G}^Q_{\mathit{\Gamma}}\right)^T\left(\mathbf{M}^S + \mathbf{M}^\delta\right)\left(\boldsymbol{\Phi}^S - \boldsymbol{\Psi}^{S,Q}\mathbf{G}^Q_{\mathit{\Gamma}}\right)\\
&= \mathbf{I} + \boldsymbol{\Phi}^{S^T}_{\mathit{\Gamma}}\mathbf{M}^\delta\boldsymbol{\Phi}^S_{\mathit{\Gamma}} - \left[(\boldsymbol{\Lambda}^S - \omega_c^2\mathbf{I})^{-1}\boldsymbol{\Phi}^{S^T}_{\mathit{\Gamma}} + \boldsymbol{\Phi}^{S^T}_{\mathit{\Gamma}}\mathbf{M}^\delta\boldsymbol{\Psi}^{S,Q}_{\mathit{\Gamma}}\right]\mathbf{G}^Q_{\mathit{\Gamma}}\\
&\quad - \mathbf{G}^{Q^T}_{\mathit{\Gamma}}\left[\boldsymbol{\Phi}^S_{\mathit{\Gamma}}(\boldsymbol{\Lambda}^S - \omega_c^2\mathbf{I})^{-1} + \boldsymbol{\Psi}^{S,Q^T}_{\mathit{\Gamma}}\mathbf{M}^\delta\boldsymbol{\Phi}^S_{\mathit{\Gamma}}\right]\\
&\quad + \mathbf{G}^{Q^T}_{\mathit{\Gamma}}\left(\boldsymbol{\Psi}^{S,Q^T}\mathbf{M}^S\boldsymbol{\Psi}^{S,Q} + \boldsymbol{\Psi}^{S,Q^T}_{\mathit{\Gamma}}\mathbf{M}^\delta\boldsymbol{\Psi}^{S,Q}_{\mathit{\Gamma}}\right)\mathbf{G}^Q_{\mathit{\Gamma}}
\end{aligned} \tag{6.13a}$$

$$\begin{aligned}
\boldsymbol{\kappa}^{syn} &= \left(\boldsymbol{\Phi}^S - \boldsymbol{\Psi}^{S,Q}\mathbf{G}^Q_{\mathit{\Gamma}}\right)^T\left(\mathbf{K}^S + \mathbf{K}^\delta\right)\left(\boldsymbol{\Phi}^S - \boldsymbol{\Psi}^{S,Q}\mathbf{G}^Q_{\mathit{\Gamma}}\right)\\
&= \boldsymbol{\Lambda}^S + \boldsymbol{\Phi}^{S^T}_{\mathit{\Gamma}}\mathbf{K}^\delta\boldsymbol{\Phi}^S_{\mathit{\Gamma}} - \left[\boldsymbol{\Lambda}^S(\boldsymbol{\Lambda}^S - \omega_c^2\mathbf{I})^{-1}\boldsymbol{\Phi}^{S^T}_{\mathit{\Gamma}} + \boldsymbol{\Phi}^{S^T}_{\mathit{\Gamma}}\mathbf{K}^\delta\boldsymbol{\Psi}^{S,Q}_{\mathit{\Gamma}}\right]\mathbf{G}^Q_{\mathit{\Gamma}}\\
&\quad - \mathbf{G}^{Q^T}_{\mathit{\Gamma}}\left[\boldsymbol{\Phi}^S_{\mathit{\Gamma}}(\boldsymbol{\Lambda}^S - \omega_c^2\mathbf{I})^{-1}\boldsymbol{\Lambda}^S + \boldsymbol{\Psi}^{S,Q^T}_{\mathit{\Gamma}}\mathbf{K}^\delta\boldsymbol{\Phi}^S_{\mathit{\Gamma}}\right]\\
&\quad + \mathbf{G}^{Q^T}_{\mathit{\Gamma}}\left(\boldsymbol{\Psi}^{S,Q}_{\mathit{\Gamma}} + \omega_c^2\boldsymbol{\Psi}^{S,Q^T}\mathbf{M}^S\boldsymbol{\Psi}^{S,Q} + \boldsymbol{\Psi}^{S,Q^T}_{\mathit{\Gamma}}\mathbf{K}^\delta\boldsymbol{\Psi}^{S,Q}_{\mathit{\Gamma}}\right)\mathbf{G}^Q_{\mathit{\Gamma}},
\end{aligned} \tag{6.13b}$$

where $\mathbf{G}^Q_{\mathit{\Gamma}}$ is the set of the $\mathbf{g}^Q_{\Gamma,j}$.

The accuracy of this approach depends primarily on the value of $[(\omega_j^{S^2} - \omega_c^2)/(\omega_i^2 - \omega_c^2)]\eta_{ij}$.

If $\omega_j^S = \omega_c$, then $\boldsymbol{\phi}_j^S - \boldsymbol{\Psi}^{S,Q}\mathbf{g}_{\Gamma,j}^Q$ is a null vector, and the reduced mass and stiffness matrices have a null column and a null row. If $\omega_i = \omega_c$, then the inverse of $\mathbf{K}^m - \omega_c^2\mathbf{M}^m$ does not exist. Thus ω_c should be chosen so that it is not too close to a natural frequency of the tuned or mistuned system.

Note that it is possible to enhance the method presented in this section by introducing an iteration scheme, or to improve the accuracy of the mode-acceleration method by using a higher-order expression. However, in these cases, the external force vectors ($\mathbf{G}$ or $\mathbf{G}^Q$) used for the computation of static modes would be fully populated; thus the entire set of attachment modes would be needed, and the inversion of a matrix of the size of the full system would be required. Thus, the cost of such a scheme would probably be prohibitive.

6.4 Comparison of Methods

In this section, the newly developed static mode compensation (SMC) technique is validated by examining the vibration response of a turbine engine compressor stage with a rogue blade that has a significant geometric distortion relative to the nominal blade design. Also, the performance of the SMC method is compared with three other methods:

1. The CMS method for large mistuning [44], which was reviewed in section 6.2.
2. Classical modal analysis (CMA) for small mistuning. In this model, a subset of tuned-system normal modes are employed [23], and blade mistuning is projected directly onto the system modes.
3. Component mode mistuning (CMM) technique [44] for small mistuning. As in the above model, tuned-system normal modes are used for building a ROM. However, mistuning is projected to tuned-system normal modes by relating the blade motion in the system modes to the tuned cantilevered-blade normal modes. Thereby, the

eigenvalue mistuning of a cantilevered blade is projected onto the system modes.

The second and third techniques listed above are extremely accurate and efficient, relative to finite element analysis, for small-mistuning cases [23, 44].

For the SMC technique and the two small-mistuning methods, the model size is determined by the number of tuned-system normal modes selected. However, the model size for the CMS-based large-mistuning method is much larger, because the number of DOF is the number of tuned-system normal modes plus the number of attachment modes employed. For this study, the tuned-system normal modes and attachment modes were obtained from the single-sector FEM. Also, the static deflections of a tuned system due to external forces were obtained from this FEM. For the test-case rotor, the number of DOF where mistuning is present due to the geometry deviation is 594, and thus 594 attachment modes are used.

6.4.1 Description of the Test-Case Model

The rotor considered in this study is a 29-blade compressor stage of a gas turbine engine that was used in a previous study by the authors [44]. Figure 6.1 shows the finite element mesh, which is constructed with standard linear brick elements (eight-noded solids) and has 126,846 DOF. This figure also shows a tuned blade for the nominal design. For this test case, the effect of having one damaged blade with significant geometric mistuning, or a rogue blade, is investigated. The rogue blade geometry used in this study is shown in Fig. 6.2. The geometry corresponding to the worst-case blade damage is referred to as 100% distortion. By scaling the difference between the nominal and the 100% distortion models, intermediate cases were generated, such as the 10% distortion case shown in Fig. 6.2. The Young’s modulus and mass density values used for the rogue blade were the same as those for the nominal blade. Nevertheless, due to the geometry change, the mass and stiffness matrices were significantly changed around the distorted area, even for the case of 10% distortion.

First, the natural frequencies and mode shapes of the rogue blade were investigated as distortion increases. Figure 6.3(a) shows eigenvalue mistuning versus geometry distortion for the 1st (first flexural mode, FEM natural frequency 2.22 kHz), 5th (second torsion, 20.95 kHz), 8th (third torsion, 33.68 kHz), and 9th (second stripe, 35.11 kHz) modes of a cantilevered blade that is fixed at its root. The eigenvalue mistuning value is defined as the ratio of the eigenvalue deviation to the nominal eigenvalue. The modal assurance criterion (MAC) values between the modes of a nominal blade and a rogue blade are shown in Fig. 6.3(b). Although all the eigenvalue mistuning values are smaller than 0.07, it is seen that the mode shapes are significantly different. The mode shapes of cantilevered tuned and rogue (100% distortion) blades are depicted in Fig. 6.4. As can be seen, the 1st and 5th modes of a tuned and a rogue blades are similar, while the 8th and 9th modes are quite different.

The tuned test-case rotor has many mode groups that can be characterized in terms of dominant blade motion (see Fig. 2 in the paper by Lim *et al.* [44]). Similarly, the modes of the mistuned system can be characterized by blade motion, but not by the number of nodal diameters. In Figs. 6.5 and 6.6, the natural frequencies for the tuned system and for the mistuned system with a rogue blade (100% distortion) are shown for the 1st, 5th, 8th, and 9th blade-dominated mode groups. The blade motion for each system mode is highly correlated with that of a tuned or rogue cantilevered blade. Note that each mode group has one mistuned-system mode whose natural frequency is away from the others: the mode at 2.1405 kHz in the 1st group, at 19.605 kHz in the 5th group, at 32.912 kHz in the 8th group, and at 34.350 kHz in the 9th group. These modes are highly localized about the rogue blade, as shown in Fig. 6.6, and thus it is expected that they will affect the forced response for any engine order of excitation. Therefore, the ability to capture these rogue blade modes is an important consideration for assessing the performance of a test-case ROM.

6.4.2 Free Response Results

Figures 6.7 and 6.8 present the convergence of the ROM natural frequencies to the FEM results for the four different methods: CMS (Component Mode Synthesis, ○), SMC (Static Mode Compensation using the mode-acceleration formulation, ×), CMA (Classical Modal Analysis with mistuning projection, △), and CMM (Component Mode Mistuning, ◇). The rogue-blade-dominated modes mentioned in the previous section had much larger error than the others. Therefore, the maximum frequency errors were used for the convergence study.

Figure 6.7 shows the maximum natural frequency errors for the lowest blade-dominated mode group as the number of tuned-system normal modes increases, for the cases of 10% distortion and 100% distortion. There are 29 mistuned normal modes in the lowest mode group. For the SMC method, static modes are used rather than quasi-static ones, because the modes of interest are the lowest modes. For the 1st cantilevered blade mode, the mode shapes of tuned and rogue blades were almost the same (the MAC value at 100% deviation is 0.9982). However, as can be seen in Fig. 6.7, the results from the CMA method are poor, even for the case of 10% geometry distortion.

Figure 6.8 shows natural frequency errors for the 5th and the 8th–9th blade-dominated mode groups for the case of a rogue blade with 100% deviation. There are 32 normal modes in the 5th mode group, and 66 normal modes in the 8th and 9th mode groups. The 8th and 9th mode groups are so close that they need to be included in a single ROM. The results by the CMA method were omitted because the errors were too large. For the SMC method, the models were obtained using quasi-static modes. The centering frequency was selected as 20 kHz for the 5th mode group, and 34 kHz for the 8th and 9th mode groups. For fair comparison, for the CMS method the models were constructed using quasi-static attachment modes, and the number of normal modes was increased by including both higher and lower modes around the centering frequencies. As shown in Fig. 6.8, the SMC method gives the best results. The CMS method also yields good results but only after many more normal modes are retained. Note that the CMS results shown here are different from those in the authors' previous work [44], because only 594 attachment modes were used in this study instead of 2496 attachment modes in the previous work. The maximum errors for the 8th and 9th mode groups by the CMM method are around 0.4% and are thus very small. However, the ratio of the standard deviation of the natural frequencies to the average natural frequency is 2.3% for the 8th and 9th mode groups. Thus, an error of 0.4% may still not be acceptable.

Figure 6.9 illustrates a tuned-system normal mode, a static mode, a quasi-static mode, and the resulting basis shapes used in the SMC method, all of which are represented for the geometry of the bladed disk with a rogue blade. It can be seen that the basis shapes obtained using a static mode are very different from those using a quasi-static mode. In addition, the motion of the rogue blade for the basis shape obtained by a quasi-static mode is very similar to the 9th cantilevered-blade mode of the rogue blade shown in Fig. 6.4. Therefore, it is clear that using quasi-static modes can significantly improve the convergence of a model in a higher frequency region.

The rogue-blade dominated mode in each mode group was selected for testing the accuracy of mode shape representation. Table 6.1 shows the convergence of the MAC values between the mode shapes of the various ROMs and those of the FEM. For the mode in the 1st mode group, all three methods show good results. For the 5th mode group, the CMM results are worse than the others. For the 8th and 9th mode groups, the mode shapes obtained by the CMM method are completely different from the FEM ones, even though the natural frequency errors seemed acceptable, as shown in Fig. 6.8. This is because the mode shapes of a mistuned system with large mistuning cannot be captured properly using a basis of tuned-system normal modes.

It should be noted that, although the CMS and SMC methods showed a similar degree of accuracy for the free response results, the SMC method yields a much smaller ROM than the CMS method.

6.4.3 Forced Response Results

In the forced response case, the SMC and CMM methods were considered in order to compare the performance of a large-mistuning and a small-mistuning ROM. Due to the distorted geometry of the rogue blade, the aerodynamic external forces may not be the same as for a bladed disk with nominal geometry. However, for validation purposes, pure engine order 2 and 5 excitations were considered, and two frequency regions corresponding to the 5th (19–22 kHz), and the 8th and 9th (32–36 kHz) mode groups were investigated. The applied forces were unit loads normal to the blade surface at the tip of each blade. The degree of distortion for the rogue blade was 100%.

Figures 6.10 and 6.11 show the envelopes of the individual blades' frequency responses calculated from the ROMs and the FEM. Euclidean displacement norms were obtained for every blade, and the largest responding blade was selected at every excitation frequency. Figure 6.10 depicts results for the 5th mode group, for which 99 tuned-system normal modes in the 14–26 kHz range were used. Figure 6.11 is for the 8th and 9th mode groups, and 136 modes were used in the 26–43 kHz range. The results of the SMC method match well those of the FEM, while the results of the CMM method feature large errors for both the 5th and the 8th and 9th mode groups. Note that the biggest differences occur around the natural frequencies of the rogue-blade-dominated modes (19.6 kHz, 32.9 kHz, and 34.3 kHz). This is because the CMM models cannot capture the rogue-blade-dominated modes. Also note that the CMM method yields poor results, even though the MAC value between the 5th cantilevered-blade modes of a tuned and a rogue blade is around 0.9.

Another case was considered with higher MAC values for the tuned and rogue cantilevered-blade modes. The same model and external forcing were used, except that the geometric deviation for the rogue blade was 10%. The excitation frequency range was 32–36 kHz. The MAC value was 0.9922 for the 8th cantilevered-blade mode and 0.9916 for the 9th mode (see Fig 6.3(b)). The forced response results are shown in Fig. 6.12. Although the mode shapes of the cantilevered rogue and tuned blades are much closer than in the case of 100% geometric deviation, there are still significant differences between the FEM and CMM forced response results. This indicates that the performance of the CMM method is very sensitive to geometric mistuning.

6.5 Application to a System With a Fractured Blade

So far, the number of finite element DOF have been assumed to be the same for the tuned and the mistuned systems. However, the SMC method can also handle cases in which some DOF are removed in the mistuned system. As an example, a bladed disk with a fractured blade, which is represented by removing some elements from the blade FEM, is discussed in this section.

The same nominal rotor model as in section 6.4 is considered. The geometry and example mode shapes of the fractured blade cantilevered at its root are depicted in Fig. 6.13. Note that the natural frequency of the 9th mode for the fractured blade is 4.9 kHz higher than its nominal frequency, while others are close to the nominal values (see Fig. 6.4). Although a finer mesh may be required near the fractured area in order to obtain more accurate results, for the purpose of easy comparison the original mesh was maintained (stress concentration is not considered in this study).

Figure 6.14(a) shows the natural frequencies of a bladed disk with the fractured blade in the frequency range 32–36 kHz, where the line at 33.929 kHz represents the natural frequency of a system mode dominated by the 8th fractured-blade mode. Note that there are 65 mistuned-system normal modes in this frequency range, but there are 66 tuned-system normal modes. This is because a system mode dominated by the 9th fractured-blade mode is outside the range.

In order to derive the reduced matrices for the ROM, first the DOF in the bladed disk model are sorted into three groups: the removed DOF due to fracture (denoted by β), the DOF at the boundary between the removed part and the remaining part (denoted by $\mathit{\Gamma}$), and the interior DOF of the remaining part (denoted by α). Note that the mass and stiffness terms corresponding to α remain unchanged, but the terms corresponding to $\mathit{\Gamma}$ change when the β part is removed. Also note that there is no mass or stiffness coupling terms between the α part and the β part. Therefore, the mass and stiffness matrices of the tuned system and the fractured-blade system can be written as follows:

$$\mathbf{M}^S = \begin{bmatrix} \mathbf{M}_{\alpha\alpha} & \mathbf{M}_{\alpha\mathit{\Gamma}} & \mathbf{0} \\ \mathbf{M}_{\mathit{\Gamma}\alpha} & \mathbf{M}_{\mathit{\Gamma}\mathit{\Gamma}} & \mathbf{M}_{\mathit{\Gamma}\beta} \\ \mathbf{0} & \mathbf{M}_{\beta\mathit{\Gamma}} & \mathbf{M}_{\beta\beta} \end{bmatrix}, \qquad \mathbf{K}^S = \begin{bmatrix} \mathbf{K}_{\alpha\alpha} & \mathbf{K}_{\alpha\mathit{\Gamma}} & \mathbf{0} \\ \mathbf{K}_{\mathit{\Gamma}\alpha} & \mathbf{K}_{\mathit{\Gamma}\mathit{\Gamma}} & \mathbf{K}_{\mathit{\Gamma}\beta} \\ \mathbf{0} & \mathbf{K}_{\beta\mathit{\Gamma}} & \mathbf{K}_{\beta\beta} \end{bmatrix}, \tag{6.14}$$

$$\mathbf{M}^m = \begin{bmatrix} \mathbf{M}_{\alpha\alpha} & \mathbf{M}_{\alpha\mathit{\Gamma}} \\ \mathbf{M}_{\mathit{\Gamma}\alpha} & \mathbf{M}_{\mathit{\Gamma}\mathit{\Gamma}} + \mathbf{M}^\delta \end{bmatrix}, \qquad \mathbf{K}^m = \begin{bmatrix} \mathbf{K}_{\alpha\alpha} & \mathbf{K}_{\alpha\mathit{\Gamma}} \\ \mathbf{K}_{\mathit{\Gamma}\alpha} & \mathbf{K}_{\mathit{\Gamma}\mathit{\Gamma}} + \mathbf{K}^\delta \end{bmatrix}, \tag{6.15}$$

Then, the external forces required to produce motions of the fractured bladed disk that are the same as those in the tuned-system modes can be computed as follows:

$$\begin{aligned}\begin{bmatrix}\mathbf{F}_\alpha \\ \mathbf{F}_\mathit{\Gamma}\end{bmatrix} &= \mathbf{K}^m \begin{bmatrix}\mathbf{\Phi}^S_\alpha \\ \mathbf{\Phi}^S_\mathit{\Gamma}\end{bmatrix} - \mathbf{M}^m \begin{bmatrix}\mathbf{\Phi}^S_\alpha \\ \mathbf{\Phi}^S_\mathit{\Gamma}\end{bmatrix} \mathbf{\Lambda}^S \\ &= \begin{bmatrix}\mathbf{0} \\ (\mathbf{K}^\delta \mathbf{\Phi}^S_\mathit{\Gamma} - \mathbf{K}_{\mathit{\Gamma}\beta}\mathbf{\Phi}^S_\beta) - (\mathbf{M}^\delta \mathbf{\Phi}^S_\mathit{\Gamma} - \mathbf{M}_{\mathit{\Gamma}\beta}\mathbf{\Phi}^S_\beta)\mathbf{\Lambda}^S\end{bmatrix}.\end{aligned} \tag{6.16}$$

Note that $\mathbf{M}^m$ and $\mathbf{K}^m$ are multiplied only by the α and $\mathit{\Gamma}$ components of the tuned-system modes, but that the β part appears in the resulting expression.

Now, as mentioned in section 6.3, static (or quasi-static) modes can be computed in two ways: directly applying $\mathbf{F}_\mathit{\Gamma}$ to a mistuned system, or applying equivalent forces ($\mathbf{G}_\mathit{\Gamma}$ or $\mathbf{G}^Q_\mathit{\Gamma}$) to a tuned system. It should be noted that, since a fractured-blade system does not have DOF corresponding to the β part, the β portion of the static modes obtained from a tuned system is not used in calculating the equivalent forces, and that the static modes of a fractured-blade system can be obtained from an original tuned system by applying forces only to the $\mathit{\Gamma}$ part. Thus, using quasi-static modes, $\mathbf{G}^Q_\mathit{\Gamma}$ can be computed from the following equation.

$$\left(\begin{bmatrix}\mathbf{K}_{\alpha\alpha} & \mathbf{K}_{\alpha\mathit{\Gamma}} \\ \mathbf{K}_{\mathit{\Gamma}\alpha} & \mathbf{K}_{\mathit{\Gamma}\mathit{\Gamma}} + \mathbf{K}^\delta\end{bmatrix} - \omega_c^2 \begin{bmatrix}\mathbf{M}_{\alpha\alpha} & \mathbf{M}_{\alpha\mathit{\Gamma}} \\ \mathbf{M}_{\mathit{\Gamma}\alpha} & \mathbf{M}_{\mathit{\Gamma}\mathit{\Gamma}} + \mathbf{M}^\delta\end{bmatrix}\right)^{-1} \begin{bmatrix}\mathbf{0} \\ \mathbf{F}_\mathit{\Gamma}\end{bmatrix} \begin{bmatrix}\mathbf{\Psi}^{S,Q}_\alpha \mathbf{G}_\mathit{\Gamma} \\ \mathbf{\Psi}^{S,Q}_\mathit{\Gamma} \mathbf{G}_\mathit{\Gamma}\end{bmatrix} = \begin{bmatrix}\mathbf{\Psi}^{S,Q}_\alpha \mathbf{G}^Q_\mathit{\Gamma} \\ \mathbf{\Psi}^{S,Q}_\mathit{\Gamma} \mathbf{G}^Q_\mathit{\Gamma}\end{bmatrix}, \tag{6.17}$$

where $\mathbf{\Psi}^{S,Q}$ is a set of quasi-static attachment modes corresponding to the DOF in the $\mathit{\Gamma}$ part. Since

$$\begin{aligned}(\mathbf{K}_{\alpha\alpha} - \omega_c^2 \mathbf{M}_{\alpha\alpha})\mathbf{\Psi}^{S,Q}_\alpha + (\mathbf{K}_{\alpha\mathit{\Gamma}} - \omega_c^2 \mathbf{M}_{\alpha\mathit{\Gamma}})\mathbf{\Psi}^{S,Q}_\mathit{\Gamma} &= \mathbf{0} \\ (\mathbf{K}_{\mathit{\Gamma}\alpha} - \omega_c^2 \mathbf{M}_{\mathit{\Gamma}\alpha})\mathbf{\Psi}^{S,Q}_\alpha + (\mathbf{K}_{\mathit{\Gamma}\mathit{\Gamma}} - \omega_c^2 \mathbf{M}_{\mathit{\Gamma}\mathit{\Gamma}})\mathbf{\Psi}^{S,Q}_\mathit{\Gamma} + (\mathbf{K}_{\mathit{\Gamma}\beta} - \omega_c^2 \mathbf{M}_{\mathit{\Gamma}\beta})\mathbf{\Psi}^{S,Q}_\beta &= \mathbf{I},\end{aligned}$$

the equivalent force $\mathbf{G}^Q_\mathit{\Gamma}$ becomes

$$\mathbf{G}^Q_\mathit{\Gamma} = (\mathbf{I} + (\mathbf{K}^\delta - \omega_c^2 \mathbf{M}^\delta)\mathbf{\Psi}^{S,Q}_\mathit{\Gamma} - (\mathbf{K}_{\mathit{\Gamma}\beta} - \omega_c^2 \mathbf{M}_{\mathit{\Gamma}\beta})\mathbf{\Psi}^{S,Q}_\beta)^{-1}\mathbf{F}_\mathit{\Gamma}. \tag{6.18}$$

Using this derivation for the quasi-static modes, the reduced mass and stiffness matrices can be obtained in the same way as in section 6.3, except that only the mode shape DOF in the α and $\mathit{\Gamma}$ parts are used.

Since the number of DOF in the $\mathit{\Gamma}$ part of the fractured blade is 72, the 72 attachment modes were used to compute the necessary static modes. The centering frequency was chosen as 34 kHz, and 136 tuned-system normal modes were selected in 26–43 kHz. Figure 6.14(b) shows the forced response results obtained by the fractured-blade system ROM and by the FEM. The same unit forces were applied as in section 6.4 and engine order 5 excitation was considered. Since the number of DOF in the fractured blade is smaller than that in the nominal blade, the Euclidean displacement norm for a single node located at each blade tip end was used as the blade response amplitude, and the largest amplitude of any blade was taken at every frequency to provide an envelope. As can be seen, the results of the ROM and the FEM match very well. Note that the peak around 34 kHz is due to the fractured-blade-dominated mode at 33.929 kHz.

6.6 Application to a System Subject to Design Changes

When the design of a bladed disk is modified for a certain purpose, the updated finite element models of the bladed disk (full or single-sector) need to be re-analyzed to determine the effect of the modification. However, by considering the mass and stiffness variations due to the design change as ”cyclic mistuning” terms in the SMC method, the dynamic response of the modified system can be readily obtained without additional finite element analyses. This approach is described below.

The mass and stiffness matrix modifications resulting from the design change in the disk and/or the blades are treated as a ”cyclic mistuning” that is present and identical in all sectors. Note that since the modified bladed disk still features cyclic symmetry, a modified-system mode of harmonic h can be expressed solely by the original-system modes of harmonic h. Therefore, the SMC method can be formulated for a certain harmonic h, thus further reducing the size of the resulting problem. For example, if n blade-dominated mode groups of the original system are selected to construct the SMC model, then the size of the reduced mass and stiffness matrices will be about $n \times n$ for a single harmonic, or $2n \times 2n$ for a double harmonic, instead of $(n \times N_b) \times (n \times N_b)$, where N_b is the number of blades. Of course, in order to obtain the modes for all the harmonics, one should solve about $N_b/2$ problems.

Cyclic symmetry has been used extensively to analyze bladed disks based on single-sector FEM [15, 18, 79–81]. Here the approach of Bladh *et al.* [18], which is based on the real Fourier matrix and a pseudo-block-diagonal matrix, is selected to construct the reduced matrices for the SMC model. These matrices are obtained by projecting the mass and stiffness matrices in physical coordinates onto a basis (here, a selected set of system normal modes compensated by static modes). This projection can be performed for each sector separately using the cyclic symmetry feature. To do this, all the DOF in the FEM need to be arranged sector by sector, and the boundary DOF between two adjacent sectors need to appear redundantly in both sectors. The mass and stiffness matrices can thus be represented in terms of the single-sector matrices, and the modes in physical (cylindrical) coordinates can be represented in terms of the modes in cyclic coordinates and the real Fourier matrix, $\mathbf{F}$, as follows:

$$\mathbf{M}^S = \mathbf{I} \otimes \mathbf{m}^S \tag{6.19a}$$

$$\mathbf{K}^S = \mathbf{I} \otimes \mathbf{k}^S \tag{6.19b}$$

$$\mathbf{\Phi}^S = (\mathbf{F} \otimes \mathbf{I})\widetilde{\mathbf{\Phi}}^S \tag{6.19c}$$

$$\mathbf{\Psi}^{S,Q} = (\mathbf{F} \otimes \mathbf{I})\widetilde{\mathbf{\Psi}}^{S,Q}(\mathbf{F}^T \otimes \mathbf{I}), \tag{6.19d}$$

where $\otimes$ denotes the Kronecker product. Here, $\mathbf{m}^S$ and $\mathbf{k}^S$ are the mass and stiffness matrices of the single-sector model, and $\widetilde{\boldsymbol{\Phi}}^S$ and $\widetilde{\boldsymbol{\Psi}}^{S,Q}$ are pseudo-block-diagonal matrices containing the modes in cyclic coordinates. A pseudo-block-diagonal matrix has $(N_b + 1)/2$ diagonal blocks for N odd, and $N_b/2$ blocks for N even. The column size of a block corresponding to harmonic h depends on the number of selected modes corresponding to that harmonic, and thus the blocks can have different dimension. Also, the row size of a block corresponding to a double harmonic is twice that of a single-harmonic block. Note that $\mathbf{I} \otimes \mathbf{m}^S$ and $\mathbf{I} \otimes \mathbf{k}^S$ are block-diagonal matrices in which each block has the same number of rows and columns.

From Eqs. (6.5) and (6.12), the external forces corresponding to the variation of mass and stiffness matrices ($\mathbf{I} \otimes \mathbf{m}^\delta$ and $\mathbf{I} \otimes \mathbf{k}^\delta$) are represented in cyclic coordinates as:

$$\begin{aligned}
\mathbf{G}_{\Gamma}^{Q} &= \left[\mathbf{I} + \left(\mathbf{I} \otimes (\mathbf{k}^\delta - \omega_c^2 \mathbf{m}^\delta)\right)(\mathbf{F} \otimes \mathbf{I})\widetilde{\boldsymbol{\Psi}}^{S,Q}(\mathbf{F}^T \otimes \mathbf{I})\right]^{-1} \\
&\quad \times \left[(\mathbf{I} \otimes \mathbf{k}^\delta)(\mathbf{F} \otimes \mathbf{I})\widetilde{\boldsymbol{\Phi}}_{\Gamma}^{S} - (\mathbf{I} \otimes \mathbf{m}^\delta)(\mathbf{F} \otimes \mathbf{I})\widetilde{\boldsymbol{\Phi}}_{\Gamma}^{S}\boldsymbol{\Lambda}^S\right] \\
&= (\mathbf{F} \otimes \mathbf{I})\left[\mathbf{I} + \left(\mathbf{I} \otimes (\mathbf{k}^\delta - \omega_c^2 \mathbf{m}^\delta)\right)\widetilde{\boldsymbol{\Psi}}^{S,Q}\right]^{-1}\left[(\mathbf{I} \otimes \mathbf{k}^\delta)\widetilde{\boldsymbol{\Phi}}_{\Gamma}^{S} - (\mathbf{I} \otimes \mathbf{m}^\delta)\widetilde{\boldsymbol{\Phi}}_{\Gamma}^{S}\boldsymbol{\Lambda}^S\right] \\
&= (\mathbf{F} \otimes \mathbf{I})\widetilde{\mathbf{P}}_{\Gamma},
\end{aligned} \tag{6.20}$$

where

$$\widetilde{\mathbf{P}}_{\Gamma} = \left[\mathbf{I} + \left(\mathbf{I} \otimes (\mathbf{k}^\delta - \omega_c^2 \mathbf{m}^\delta)\right)\widetilde{\boldsymbol{\Psi}}^{S,Q}\right]^{-1}\left[(\mathbf{I} \otimes \mathbf{k}^\delta)\widetilde{\boldsymbol{\Phi}}_{\Gamma}^{S} - (\mathbf{I} \otimes \mathbf{m}^\delta)\widetilde{\boldsymbol{\Phi}}_{\Gamma}^{S}\boldsymbol{\Lambda}^S\right].$$

Here, $\widetilde{\mathbf{P}}$ is a pseudo-block-diagonal matrix representing the external force matrix in cyclic coordinates.

Now, replacing the matrices in Eq. (6.13) with the above matrices defined in cyclic coordinates, the following reduced matrices are obtained.

$$\begin{aligned}\boldsymbol{\mu}^{syn} &= \mathbf{I} + {\widetilde{\boldsymbol{\Phi}}_{\mathit{\Gamma}}^{S}}^{T}(\mathbf{I}\otimes\mathbf{m}^{\delta})\widetilde{\boldsymbol{\Phi}}_{\mathit{\Gamma}}^{S} - \left[(\boldsymbol{\Lambda}^{S}-\omega_c^2\mathbf{I})^{-1}{\widetilde{\boldsymbol{\Phi}}_{\mathit{\Gamma}}^{S}}^{T} + {\widetilde{\boldsymbol{\Phi}}_{\mathit{\Gamma}}^{S}}^{T}(\mathbf{I}\otimes\mathbf{m}^{\delta})\widetilde{\boldsymbol{\Psi}}_{\mathit{\Gamma}}^{S,Q}\right]\widetilde{\mathbf{P}}_{\mathit{\Gamma}} \\ &\quad - \widetilde{\mathbf{P}}_{\mathit{\Gamma}}^{T}\left[\widetilde{\boldsymbol{\Phi}}_{\mathit{\Gamma}}^{S}(\boldsymbol{\Lambda}^{S}-\omega_c^2\mathbf{I})^{-1} + {\widetilde{\boldsymbol{\Psi}}_{\mathit{\Gamma}}^{S,Q}}^{T}(\mathbf{I}\otimes\mathbf{m}^{\delta})\widetilde{\boldsymbol{\Phi}}_{\mathit{\Gamma}}^{S}\right] \\ &\quad + \widetilde{\mathbf{P}}_{\mathit{\Gamma}}^{T}\left({\widetilde{\boldsymbol{\Psi}}^{S,Q}}^{T}(\mathbf{I}\otimes\mathbf{m}^{S})\widetilde{\boldsymbol{\Psi}}^{S,Q} + {\widetilde{\boldsymbol{\Psi}}_{\mathit{\Gamma}}^{S,Q}}^{T}(\mathbf{I}\otimes\mathbf{m}^{\delta})\widetilde{\boldsymbol{\Psi}}_{\mathit{\Gamma}}^{S,Q}\right)\widetilde{\mathbf{P}}_{\mathit{\Gamma}}\end{aligned} \tag{6.21a}$$

$$\begin{aligned}\boldsymbol{\kappa}^{syn} &= \boldsymbol{\Lambda}^{S} + {\widetilde{\boldsymbol{\Phi}}_{\mathit{\Gamma}}^{S}}^{T}(\mathbf{I}\otimes\mathbf{k}^{\delta})\widetilde{\boldsymbol{\Phi}}_{\mathit{\Gamma}}^{S} - \left[\boldsymbol{\Lambda}^{S}(\boldsymbol{\Lambda}^{S}-\omega_c^2\mathbf{I})^{-1}{\widetilde{\boldsymbol{\Phi}}_{\mathit{\Gamma}}^{S}}^{T} + {\widetilde{\boldsymbol{\Phi}}_{\mathit{\Gamma}}^{S}}^{T}(\mathbf{I}\otimes\mathbf{k}^{\delta})\widetilde{\boldsymbol{\Psi}}_{\mathit{\Gamma}}^{S,Q}\right]\widetilde{\mathbf{P}}_{\mathit{\Gamma}} \\ &\quad - \widetilde{\mathbf{P}}_{\mathit{\Gamma}}^{T}\left[\widetilde{\boldsymbol{\Phi}}_{\mathit{\Gamma}}^{S}(\boldsymbol{\Lambda}^{S}-\omega_c^2\mathbf{I})^{-1}\boldsymbol{\Lambda}^{S} + {\widetilde{\boldsymbol{\Psi}}_{\mathit{\Gamma}}^{S,Q}}^{T}(\mathbf{I}\otimes\mathbf{k}^{\delta})\widetilde{\boldsymbol{\Phi}}_{\mathit{\Gamma}}^{S}\right] \\ &\quad + \widetilde{\mathbf{P}}_{\mathit{\Gamma}}^{T}\left(\widetilde{\boldsymbol{\Psi}}_{\mathit{\Gamma}}^{S,Q} + \omega_c^2{\widetilde{\boldsymbol{\Psi}}^{S,Q}}^{T}(\mathbf{I}\otimes\mathbf{m}^{S})\widetilde{\boldsymbol{\Psi}}^{S,Q} + {\widetilde{\boldsymbol{\Psi}}_{\mathit{\Gamma}}^{S,Q}}^{T}(\mathbf{I}\otimes\mathbf{k}^{\delta})\widetilde{\boldsymbol{\Psi}}_{\mathit{\Gamma}}^{S,Q}\right)\widetilde{\mathbf{P}}_{\mathit{\Gamma}}.\end{aligned} \tag{6.21b}$$

Note that $\boldsymbol{\mu}^{syn}$ and $\boldsymbol{\kappa}^{syn}$ are square pseudo-block-diagonal matrices whose sizes are determined by the number of original-system normal modes selected. Therefore, each block in these matrices can be handled separately according to harmonic number, as follows:

$$\begin{aligned}\widetilde{\boldsymbol{\mu}}_h^{syn} &= \mathbf{I}_h + {\widetilde{\boldsymbol{\Phi}}_{\mathit{\Gamma},h}^{S}}^{T}(\mathbf{I}_h\otimes\mathbf{m}^{\delta})\widetilde{\boldsymbol{\Phi}}_{\mathit{\Gamma},h}^{S} \\ &\quad - \left[(\boldsymbol{\Lambda}_h^{S}-\omega_c^2\mathbf{I}_h)^{-1}{\widetilde{\boldsymbol{\Phi}}_{\mathit{\Gamma},h}^{S}}^{T} + {\widetilde{\boldsymbol{\Phi}}_{\mathit{\Gamma},h}^{S}}^{T}(\mathbf{I}_h\otimes\mathbf{m}^{\delta})\widetilde{\boldsymbol{\Psi}}_{\mathit{\Gamma},h}^{S,Q}\right]\widetilde{\mathbf{P}}_{\mathit{\Gamma},h} \\ &\quad - \widetilde{\mathbf{P}}_{\mathit{\Gamma},h}^{T}\left[\widetilde{\boldsymbol{\Phi}}_{\mathit{\Gamma},h}^{S}(\boldsymbol{\Lambda}_h^{S}-\omega_c^2\mathbf{I}_h)^{-1} + {\widetilde{\boldsymbol{\Psi}}_{\mathit{\Gamma},h}^{S,Q}}^{T}(\mathbf{I}_h\otimes\mathbf{m}^{\delta})\widetilde{\boldsymbol{\Phi}}_{\mathit{\Gamma},h}^{S}\right] \\ &\quad + \widetilde{\mathbf{P}}_{\mathit{\Gamma},h}^{T}\left({\widetilde{\boldsymbol{\Psi}}_h^{\mathrm{S,Q}}}^{T}(\mathbf{I}_h\otimes\mathbf{m}^{S})\widetilde{\boldsymbol{\Psi}}_h^{S,Q} + {\widetilde{\boldsymbol{\Psi}}_{\mathit{\Gamma},h}^{S,Q}}^{T}(\mathbf{I}_h\otimes\mathbf{m}^{\delta})\widetilde{\boldsymbol{\Psi}}_{\mathit{\Gamma},h}^{S,Q}\right)\widetilde{\mathbf{P}}_{\mathit{\Gamma},h}\end{aligned} \tag{6.22a}$$

$$\begin{aligned}\widetilde{\boldsymbol{\kappa}}_h^{syn} &= \boldsymbol{\Lambda}_h^{S} + {\widetilde{\boldsymbol{\Phi}}_{\mathit{\Gamma},h}^{S}}^{T}(\mathbf{I}_h\otimes\mathbf{k}^{\delta})\widetilde{\boldsymbol{\Phi}}_{\mathit{\Gamma},h}^{S} \\ &\quad - \left[\boldsymbol{\Lambda}_h^{S}(\boldsymbol{\Lambda}_h^{S}-\omega_c^2\mathbf{I}_h)^{-1}{\widetilde{\boldsymbol{\Phi}}_{\mathit{\Gamma},h}^{S}}^{T} + {\widetilde{\boldsymbol{\Phi}}_{\mathit{\Gamma},h}^{S}}^{T}(\mathbf{I}_h\otimes\mathbf{k}^{\delta})\widetilde{\boldsymbol{\Psi}}_{\mathit{\Gamma},h}^{S,Q}\right]\widetilde{\mathbf{P}}_{\mathit{\Gamma},h} \\ &\quad - \widetilde{\mathbf{P}}_{\mathit{\Gamma},h}^{T}\left[\widetilde{\boldsymbol{\Phi}}_{\mathit{\Gamma},h}^{S}(\boldsymbol{\Lambda}_h^{S}-\omega_c^2\mathbf{I}_h)^{-1}\boldsymbol{\Lambda}_h^{S} + {\widetilde{\boldsymbol{\Psi}}_{\mathit{\Gamma},h}^{S,Q}}^{T}(\mathbf{I}_h\otimes\mathbf{k}^{\delta})\widetilde{\boldsymbol{\Phi}}_{\mathit{\Gamma},h}^{S}\right] \\ &\quad + \widetilde{\mathbf{P}}_{\mathit{\Gamma},h}^{T}\left(\widetilde{\boldsymbol{\Psi}}_{\mathit{\Gamma},h}^{S,Q} + \omega_c^2{\widetilde{\boldsymbol{\Psi}}_h^{S,Q}}^{T}(\mathbf{I}_h\otimes\mathbf{m}^{S})\widetilde{\boldsymbol{\Psi}}_h^{S,Q} + {\widetilde{\boldsymbol{\Psi}}_{\mathit{\Gamma},h}^{S,Q}}^{T}(\mathbf{I}_h\otimes\mathbf{k}^{\delta})\widetilde{\boldsymbol{\Psi}}_{\mathit{\Gamma},h}^{S,Q}\right)\widetilde{\mathbf{P}}_{\mathit{\Gamma},h},\end{aligned} \tag{6.22b}$$

where the subscript h denotes a harmonic number, and $\mathbf{I}_h$ is an identity matrix. Note that $\mathbf{I}_h$, $\widetilde{\boldsymbol{\mu}}_h^{syn}$ and $\widetilde{\boldsymbol{\kappa}}_h^{syn}$ are square matrices whose size is determined by the number of selected normal modes corresponding to harmonic h. Therefore, the amount of computation for a sector design change is smaller than for the case of a single mistuned blade.

As an application of this method, a case in which the thickness of the rim of the disk is changed is discussed. The same nominal rotor model as in the previous sections was used. As shown in Fig. 6.15, the thickness of the rim on one side of the rotor was varied by stretching some elements in the radial direction. The stretching ratio, r, defined as the ratio of the radial coordinate of a modified node to that of an original node, ranged from 0.980 for a thick rim to 1.015 for a thin rim, by increments of 0.001. Therefore, 36 different designs were obtained. Rim thickness change can be expected to affect the disk-dominated modes, and therefore the characteristics of the attendant natural frequency veerings, thus potentially causing significant changes in mistuned forced response levels [39, 82, 83].

The 34 modes in the range 26–30 kHz were examined as the thickness of the rim was varied. In order to build a ROM, 34 normal modes of the original system are selected. For quasi-static modes, 27 kHz was chosen as the centering frequency. Thus, two-DOF models were obtained for harmonics 0, 1, and 4–14; and four-DOF models were obtained for harmonics 2 and 3. The maximum error of the natural frequencies by the ROM relative to the FEM ones was obtained for each stretching ratio, and plotted in Fig. 6.16. For $r = 1$, the error is zero, because there is no design modification. As can be seen, the error increases as the amount of stretch increases. However, the error level is so small that it can be concluded that the SMC method produced an accurate ROM.

The rotor natural frequencies are depicted in Fig. 6.17 for the 36 possible rim thicknesses. As expected, the natural frequencies decrease with the rim thickness. The frequencies of blade-dominated modes, which are located at harmonics 1 and 4–14, do not change much, and the change in rim thickness affects mostly the disk-dominated modes. Figure 6.17 also shows the variation of a harmonic-0 mode shape. As the rim becomes thinner, the mode shape features less blade motion and more disk motion.

This case study indicates that the SMC reduced-order modeling approach can be used to evaluate the effects of geometric design changes. If a design is changed just once, then a finite element re-analysis may be more efficient, as computing the normal modes may be cheaper than computing static modes and building a ROM. However, if the modification of a certain geometric region needs to be repeated for a design sensitivity analysis or a design optimization procedure, then the SMC method will provide greatly improved computational efficiency.

6.7 Conclusions

A new reduced-order modeling technique has been developed for bladed disks with large, geometric mistuning by utilizing the mode-acceleration method. In this approach, the static modes used in the mode-acceleration method are calculated by converting the effect of mistuning to that of equivalent external forces. In order to improve convergence and accuracy in a higher frequency range, the original formulation has been extended through the introduction of quasi-static modes. The new techniques allow for the generation of large-mistuning reduced-order models whose size is comparable to those obtained with previously-developed methods for small mistuning.

The new method was compared with three other reduced-order modeling techniques for a test-case model that had a rogue blade whose geometry was severely distorted. The reduced-order model obtained by a component mode synthesis technique reported earlier by the authors [44] gave good accuracy. However, the model size was much larger than for the other methods. The small-mistuning model based on classical modal analysis could not capture mistuned-system normal modes, even when the geometry deviation was small. Another small-mistuning model based on the component mode mistuning method could capture the response of the mistuned system, but only when the change in the mode shapes of the cantilevered rogue blade was negligible. As the amount of mode-shape change increased, the error of the CMM model increased, especially in the estimation of the rogue-blade-dominated modes. This indicates that, even when the mode shape of a blade differs only slightly from that of the nominal blade, a small-mistuning model is not able to predict the behavior of the bladed disk. In contrast, the results obtained by the newly developed technique showed excellent agreement with the FEM results, regardless of the amount of mode-shape change due to mistuning.

To demonstrate the power of the new large-mistuning approach, two other applications were examined, namely a bladed disk with a fractured blade and a bladed disk subject to a geometric design change. The case of a fractured blade, which was represented by removing some elements from the finite element model near the blade tip, showed that the new technique can be used even in the extreme case of a blade with missing material. Furthermore, it was demonstrated that the new method holds great promise for the efficient evaluation of the effects of geometric design changes in the disk and blades on bladed disk response. Although the case study was performed only on bladed disks, the new method is applicable to any system subject to a large change in the mass and stiffness matrices.

6.8 Figures and Tables

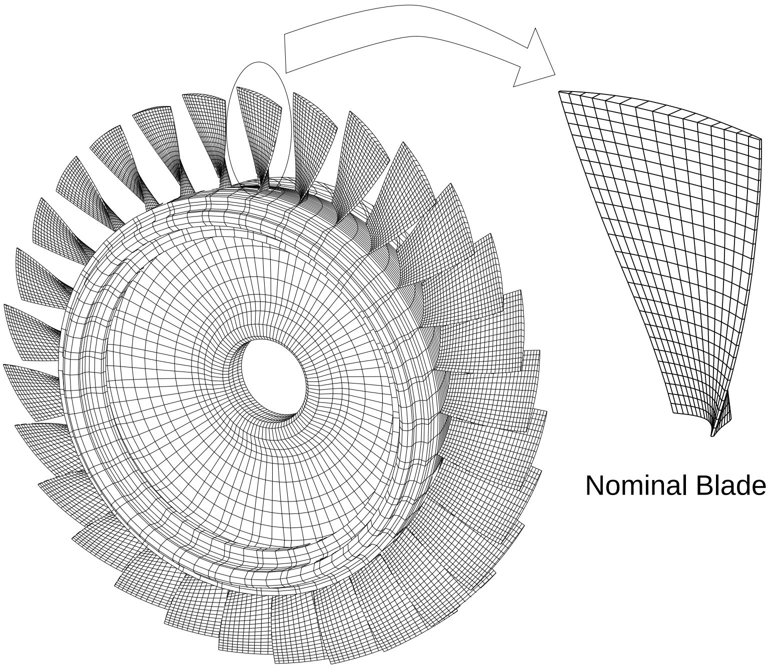

Figure 6.1: Finite element mesh of the test case rotor

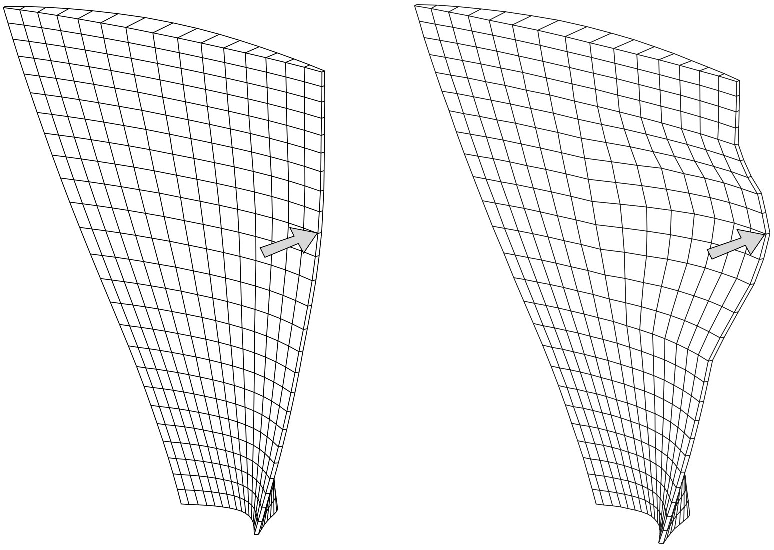

10% Distortion 100% Distortion

Figure 6.2: Rogue blade geometry

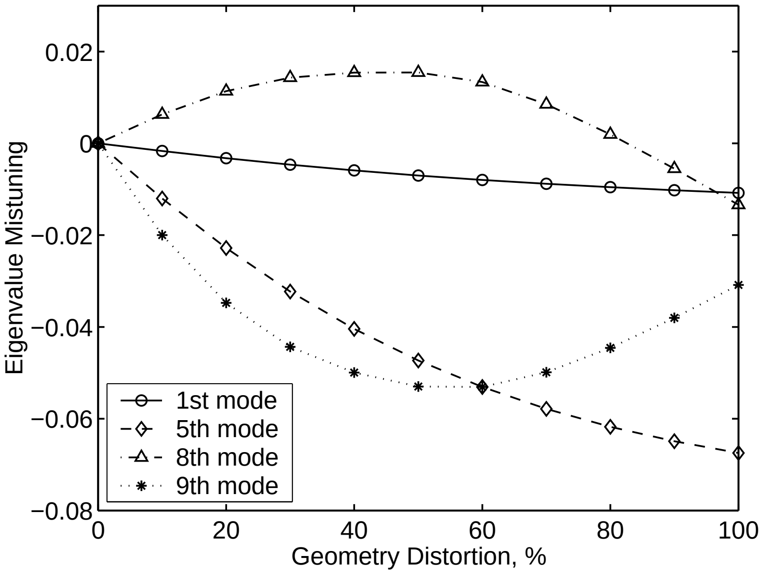

(a) Eigenvalue mistuning of a cantilevered rogue blade

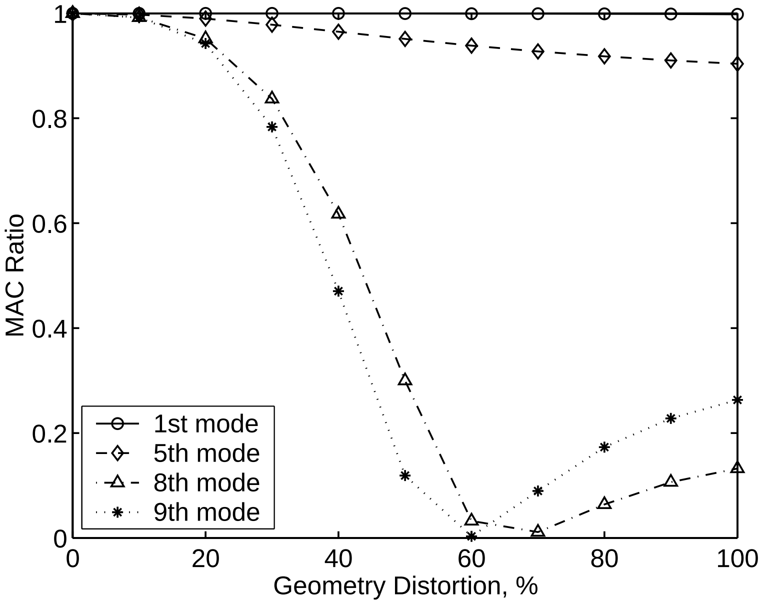

(b) MAC values between cantilevered tuned and rogue blades

Figure 6.3: Effect of increasing rogue blade geometry distortion on free response

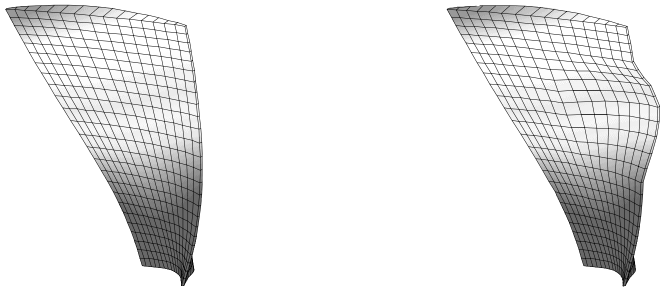

1st tuned mode (2221.6 Hz) 1st rogue mode (2209.6 Hz)

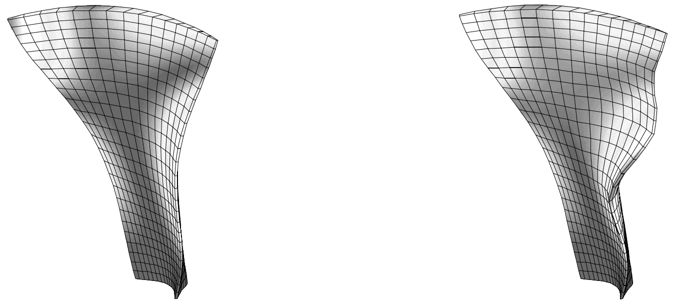

5th tuned mode (20954.2 Hz) 5th rogue mode (20235.1 Hz)

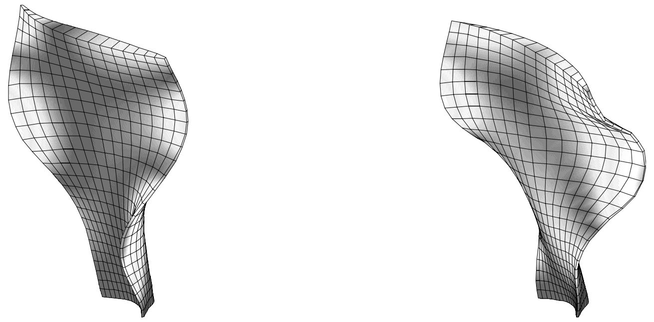

8th tuned mode (33679.5 Hz) 8th rogue mode (33453.4 Hz)

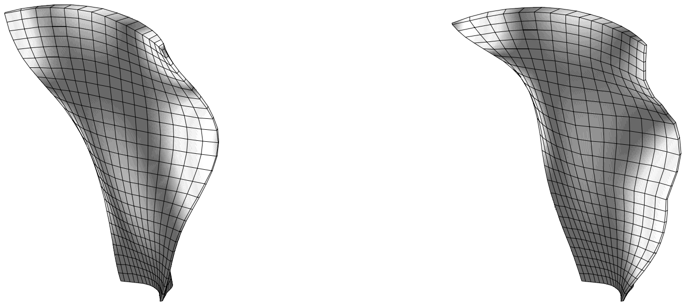

9th tuned mode (35108.4 Hz) 9th rogue mode (34562.6 Hz)

Figure 6.4: Mode shapes of a tuned blade and a rogue blade (100% distortion)

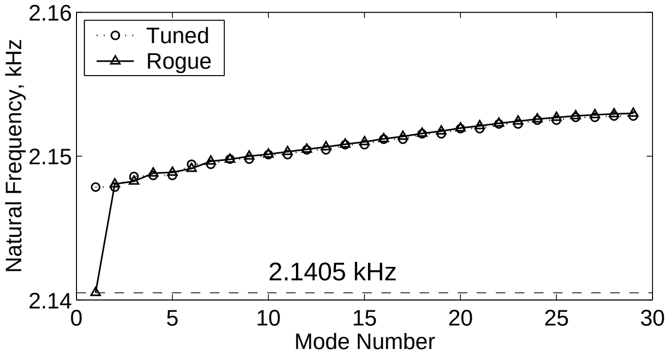

(a) 1st mode group

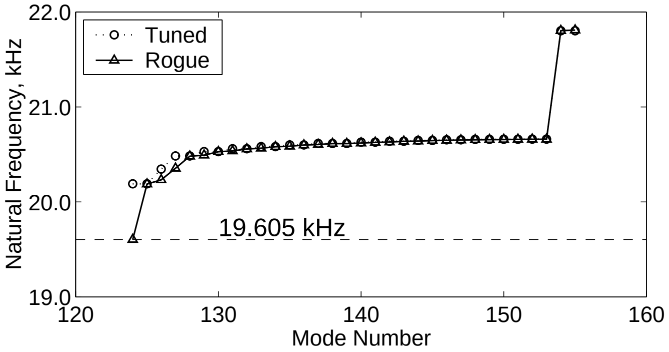

(b) 5th mode group

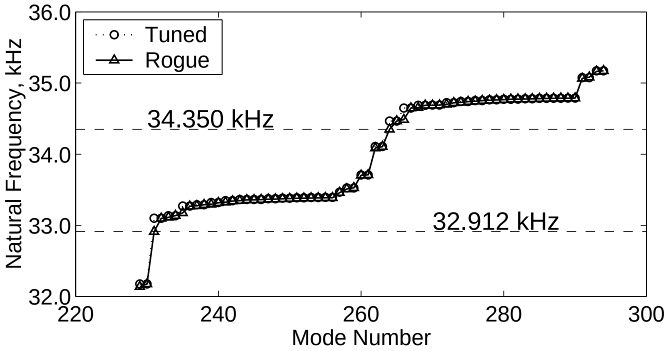

(c) 8th and 9th mode groups

Figure 6.5: Natural frequencies a bladed disk with a rogue blade (100% distortion)

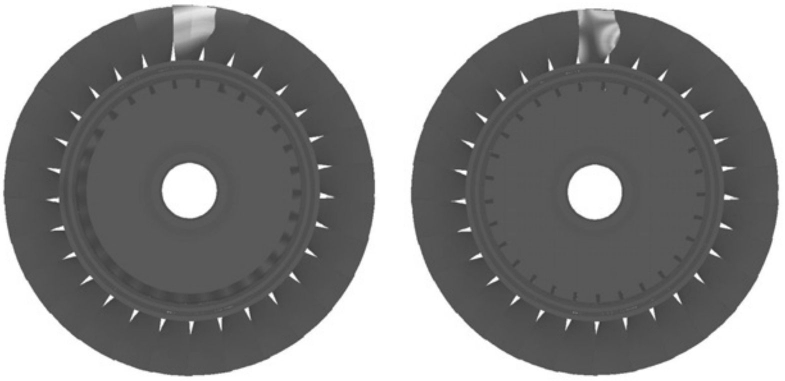

(a) 2.1405 kHz (b) 19.605 kHz

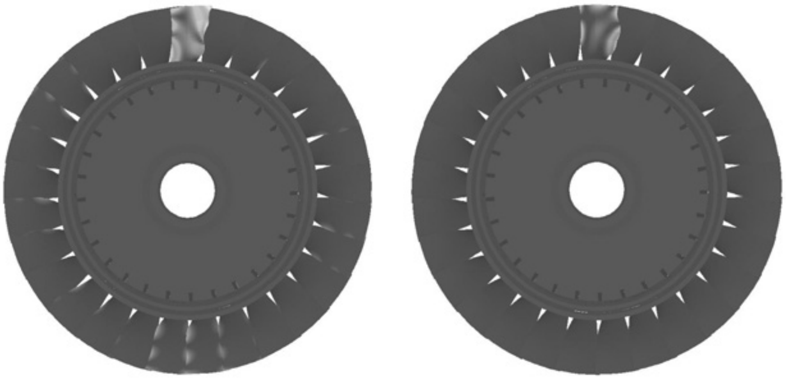

(c) 32.912 kHz (d) 34.350 kHz

Figure 6.6: Rogue-blade-dominated system modes for the case of 100% distortion

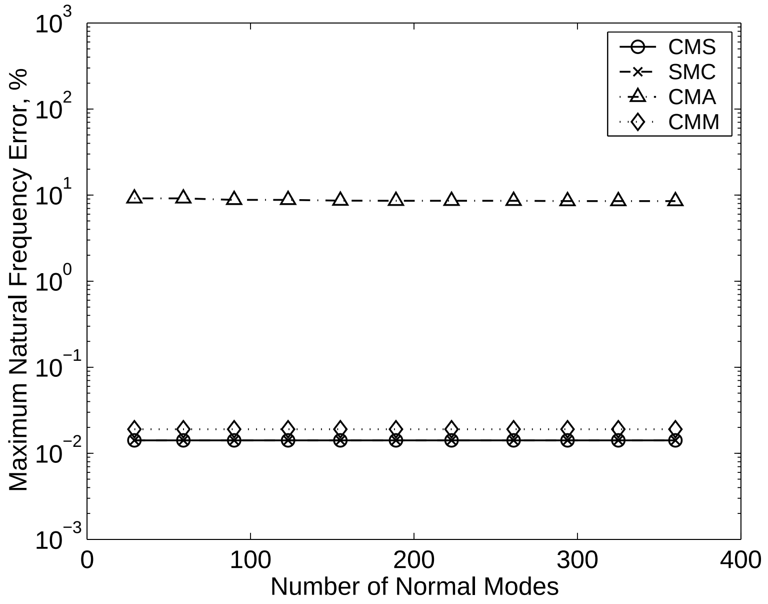

(a) 10% distortion

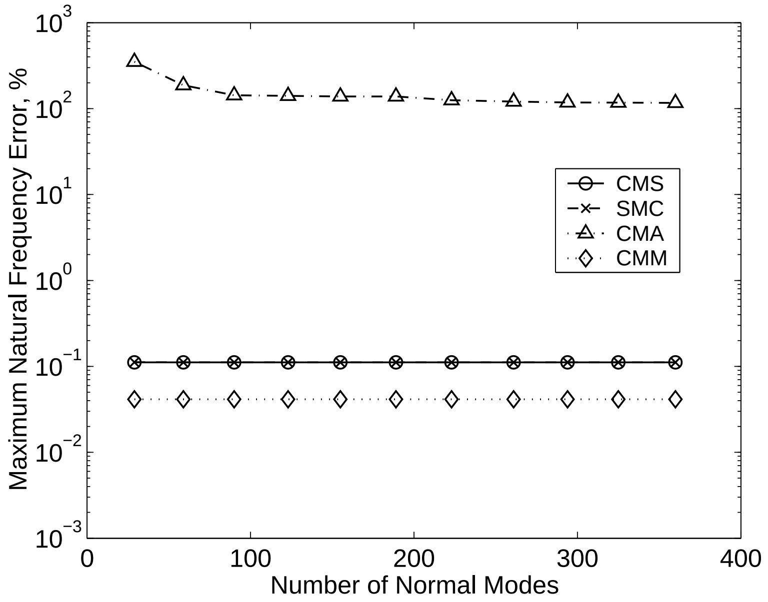

(b) 100% distortion

Figure 6.7: Convergence of natural frequency errors for the 1st blade-dominated mode group

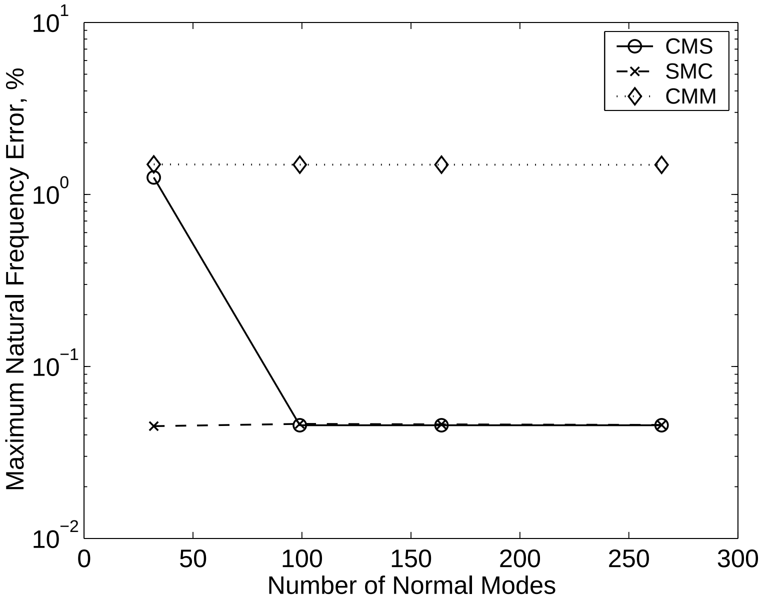

(a) 5th mode group

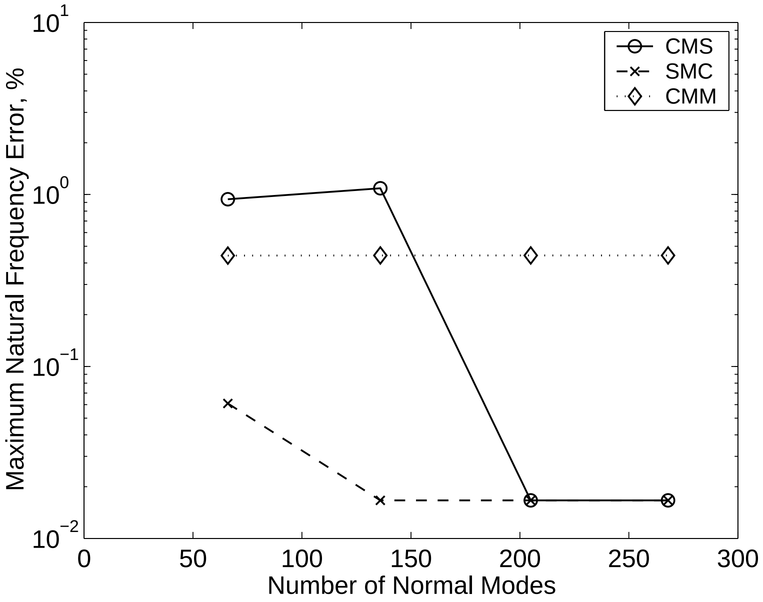

(b) 8th and 9th mode groups

Figure 6.8: Convergence of natural frequency errors for the case of 100% geometry distortion

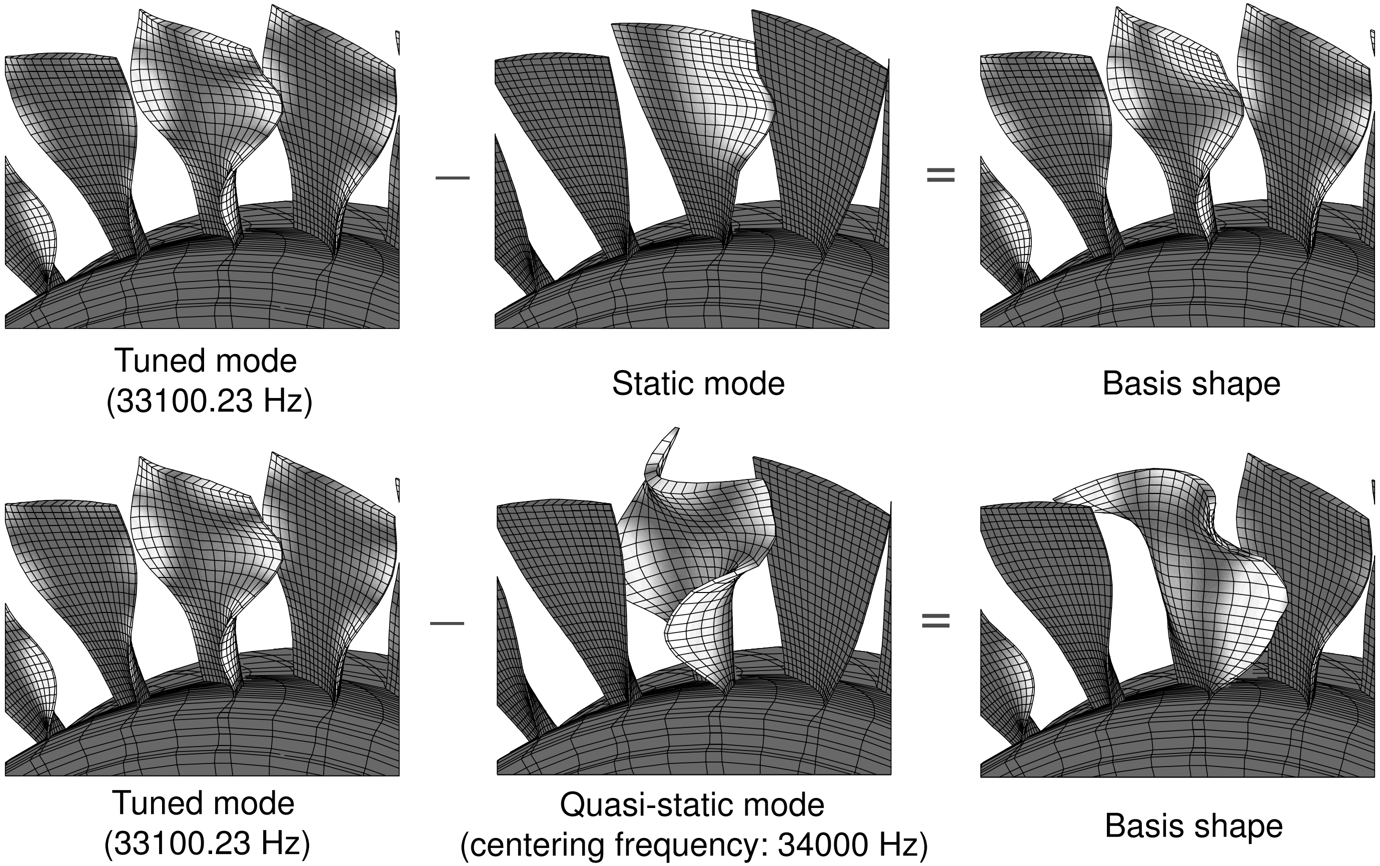

Tuned mode
(33100.23 Hz)

Static mode

Basis shape

Tuned mode
(33100.23 Hz)

Quasi-static mode
(centering frequency: 34000 Hz)

Basis shape

Figure 6.9: Basis shapes obtained by a static mode and by a quasi-static mode

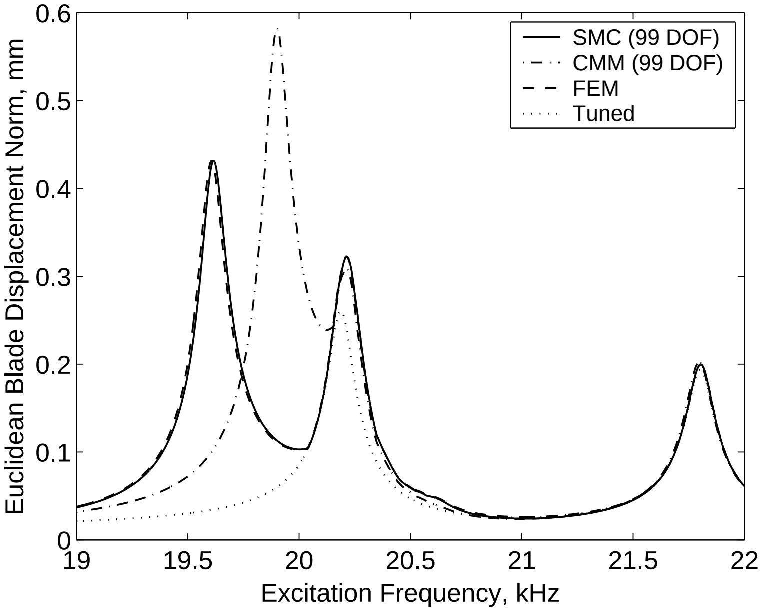

(a) Engine order 2 excitation

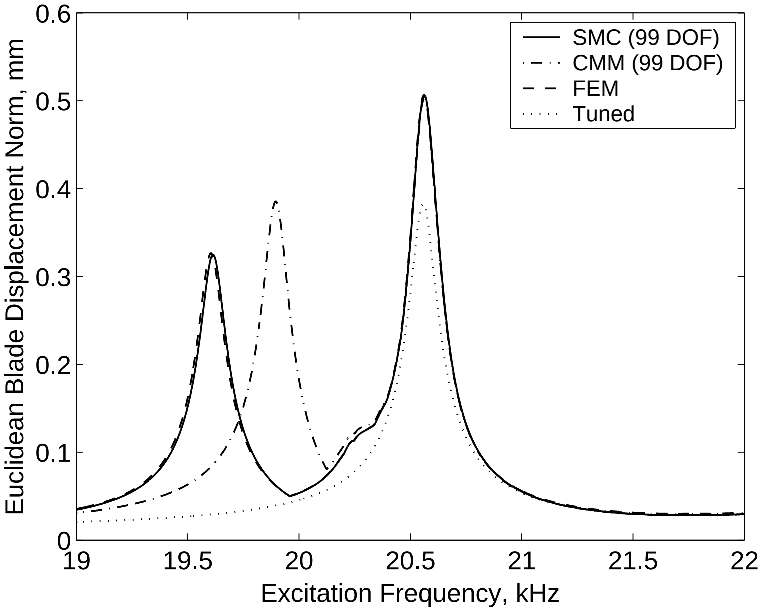

(b) Engine order 5 excitation

Figure 6.10: Forced response in the range 19–21 kHz for 100% geometry distortion

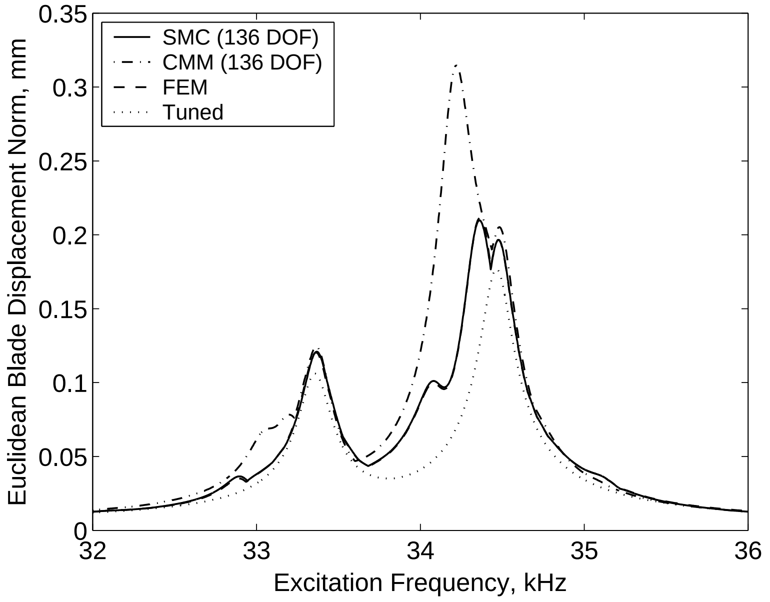

(a) Engine order 2 excitation

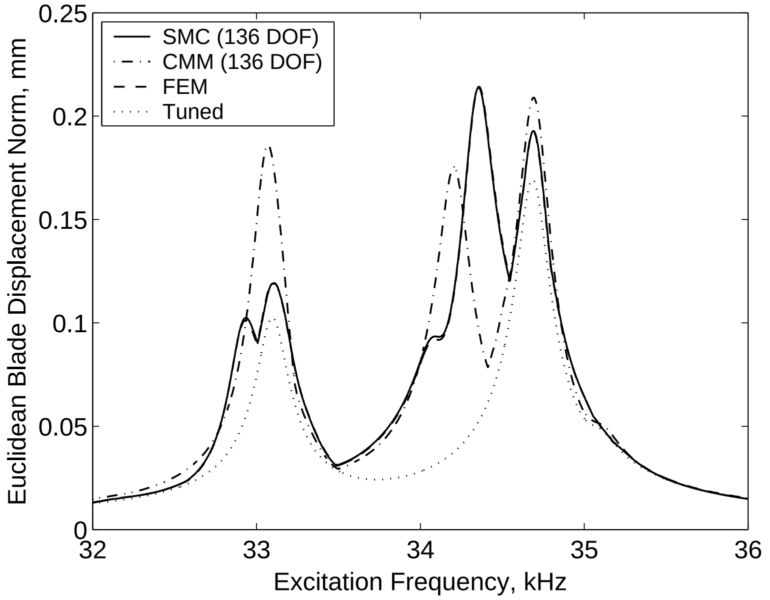

(b) Engine order 5 excitation

Figure 6.11: Forced response in the range 32–36 kHz for 100% geometry distortion

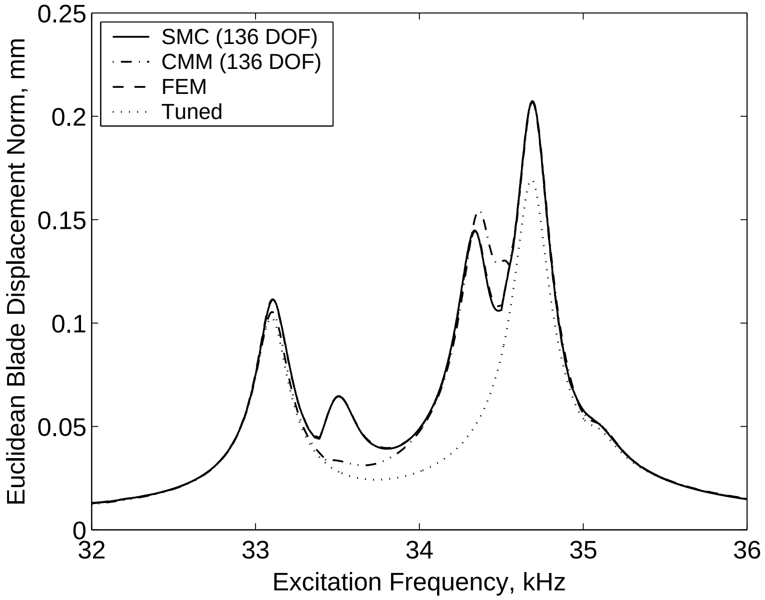

Figure 6.12: Forced response to engine order 5 excitation in the range 32–36 kHz for 10% geometry distortion

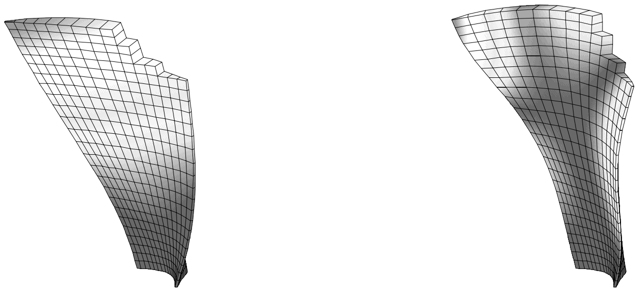

1st mode

(2318.9 Hz)

5th mode

(21357.3 Hz)

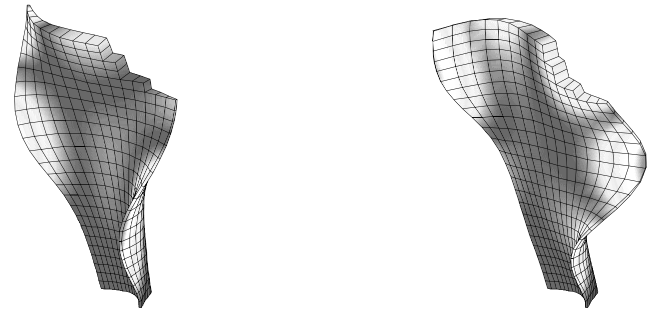

8th mode

(34141.5 Hz)

9th mode

(39973.9 Hz)

Figure 6.13: Mode shapes of a fractured blade

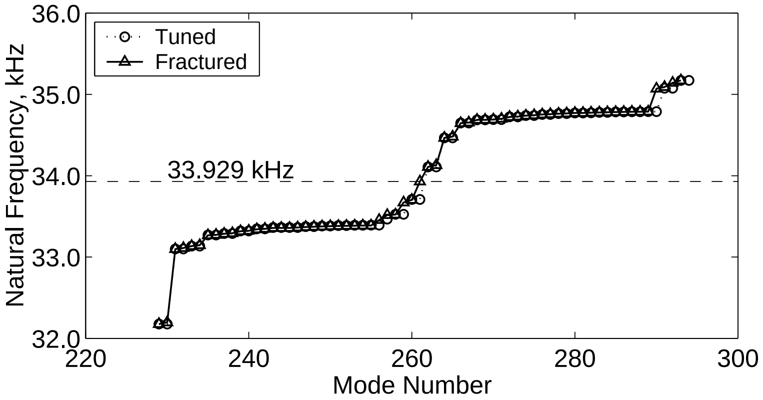

(a) Natural frequencies

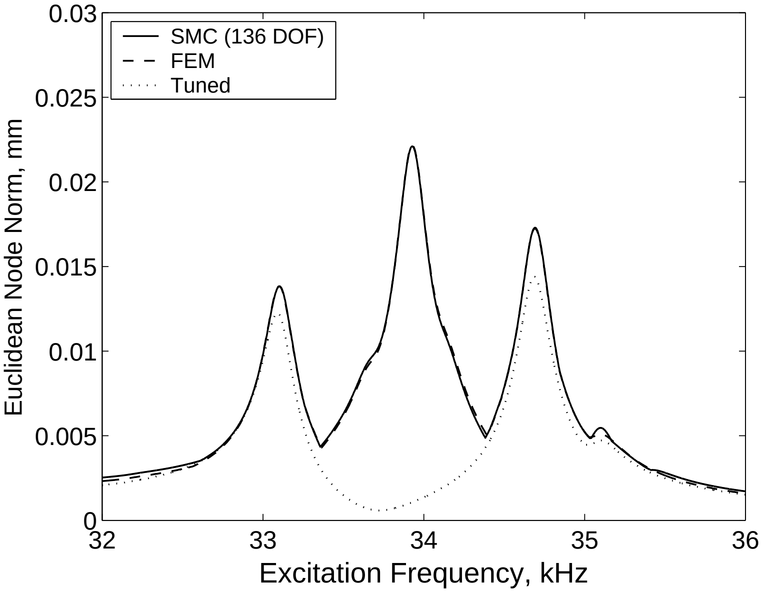

(b) Forced response

Figure 6.14: Free and forced response results for a bladed disk with a fractured blade

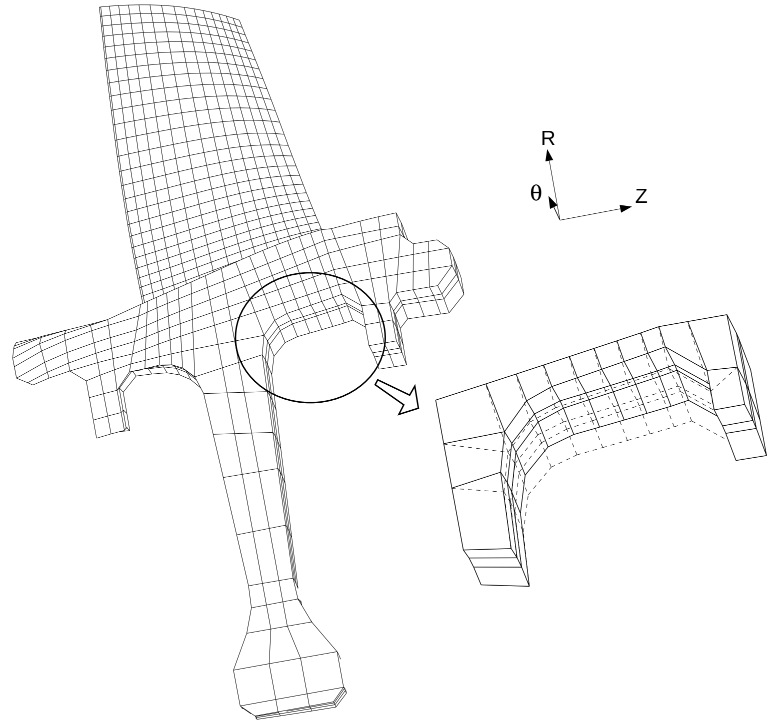

Figure 6.15: Stretch of rim in radial direction

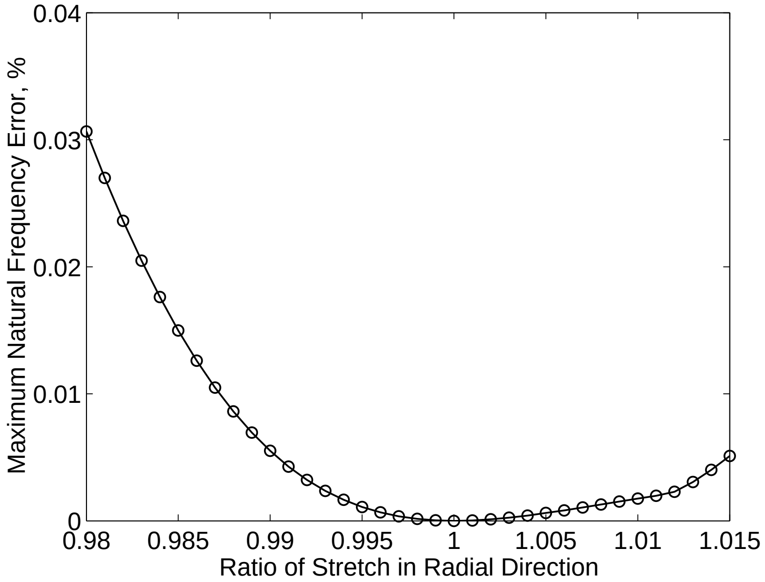

Figure 6.16: Natural frequency error versus rim thickness

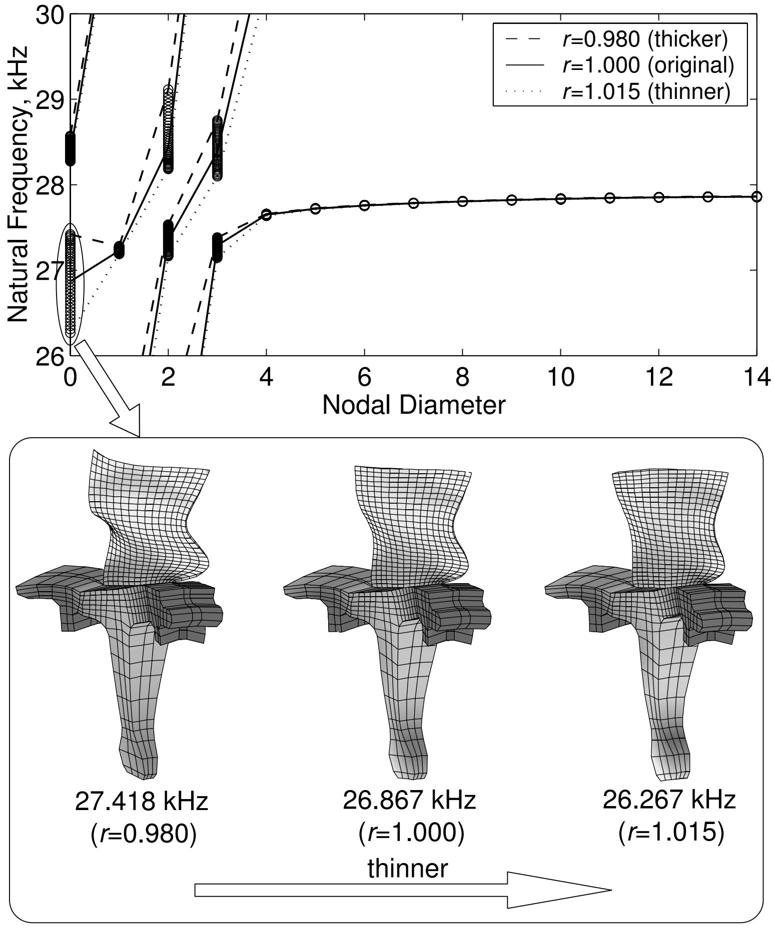

Figure 6.17: Variation of natural frequencies and mode shapes in terms of disk rim thickness

Table 6.1: Convergence of MAC values for the rogue-blade-dominated modes calculated with various ROMs, using the FEM modes as reference.

Mode group	No. of normal modes selected	MAC value (CMS)	MAC value (SMC)	MAC value (CMM)
1st group	29	0.996140	0.996114	0.998239
	59	0.996141	0.996131	0.998237
	90	0.996141	0.996138	0.998237
	123	0.996141	0.996138	0.998237
5th group	32	0.999975	0.999636	0.930084
	99	0.999992	0.999974	0.921637
	164	0.999993	0.999987	0.921462
	265	0.999994	0.999992	0.921296
8th group	66	0.974233	0.994455	0.000723
	136	0.993267	0.999569	0.000688
	205	0.999217	0.999828	0.000685
	268	0.999980	0.999889	0.000680
9th group	66	0.999893	0.999854	0.355521
	136	0.999946	0.999943	0.356131
	205	0.999958	0.999945	0.356410
	268	0.999957	0.999951	0.356573

CHAPTER VII

Conclusions

7.1 Dissertation Contributions

The main contributions of this dissertation are summarized as follows:

- In chapter II, a general reduced-order vibration modeling framework for mistuned bladed disks was developed. Also, from the general formulation, a compact reduced-order model (ROM) for the case of small blade mistuning was derived, which is called a component mode mistuning model. In the component mode mistuning method, mistuning projection is performed using the modal participation factors of cantilevered-blade component modes. Thereby, mistuning in physical coordinates is efficiently and accurately implemented in a ROM, and the size of the model is only on the order of the number of blades. The development of this small and accurate ROM allows cheaper and faster statistical investigations of bladed disks.
- Based on the developed component mode mistuning modeling technique, a method for the identification of blade mistuning was developed in chapter III. In order to compensate for the difference between an actual bladed disk and its finite element model, a "cyclic modeling error" term was introduced. By identifying both cyclic modeling error and blade mistuning, the accuracy of the identification results is

significantly improved. That is, by incorporating a model updating procedure, the identification method becomes robust with respect to the errors in modeling parameters.

- In chapter IV, the upper bound of blade forced response was investigated. A generalized expression was derived so that a specific upper bound can be calculated for any bladed disk model, even for a finite element model. Also, indicators for estimating the largest stress in a blade were proposed. Blade displacement is typically used as a measure of blade response, but stress is more important in terms of design safety. The proposed stress indicators can be used to approximate the level of blade stress directly from ROM displacement results, even for cases in which the trend for the stress level is different from that for blade displacement level.

- In chapter V, the underlying physical mechanism by which intentional mistuning leads to vibration reduction was investigated in terms of vibration energy flow in bladed disks. Based on key observations from the energy flow analysis, three guidelines were proposed to significantly reduce the design space for intentional mistuning patterns so that an optimal or near-optimal intentional mistuning pattern may be found efficiently.

- In chapter VI, a new reduced-order modeling technique was developed for a system subject to large, geometric mistuning or design changes. When large deviations are present, it is usually hard to capture the motion of a system using the modes of the original system. That is, the convergence is very slow. The developed technique provides very fast convergence in capturing the motion of a system with large deviations.

7.2 Future Research

Based on the work reported in this dissertation, some ideas for future research are proposed as follows:

- In chapter III, a mistuning identification method was presented, but it was validated only for a single blade-dominated mode family. However, there exist cases in which more than one mode family can interact due to mistuning. Further validation for these cases will distinguish the method from other previous methods.

- Usually, engine order excitations or single-blade excitations are used in experiments on bladed disks, and masses are added to the blades in order to implement mistuning. However, if the phase and magnitude of the forcing applied to each blade can be controlled independently, the response of the original system with any additional mistuning can be experimentally simulated by applying non-engine-order excitations. That is, without the cumbersome procedure of adding masses, the response of many mistuned systems can be obtained using only one bladed disk. Using this "virtual mistuning" approach, experimental Monte Carlo simulations may be performed.

- The reduced-order modeling technique developed in chapter VI is not limited only to the cases of bladed disks. It can be applied to general structural vibration problems. For example, the following three areas are worth exploring with the developed technique:

    1. Design optimization (or possibly topology optimization). The developed technique can handle for the case of large structural property changes, even for the case in which some finite elements are removed. Therefore, a design optimiza-

tion process associated with improving vibration response can be expedited with this technique.

2. Component mode synthesis. Some ROMs for large and complex structures can be still large. When the structural properties of a component is significantly changed for a certain reason, a small part of the reduced mass and stiffness matrices may be also changed greatly. By applying the developed technique for the modified reduced mass and stiffness matrices, more efficient vibration analysis may be achieved.
3. Aerodynamic effects on structures. When aerodynamic forces are added, the motion of a structure may be considerably different from the structure-alone motion. Suppose a situation in which the motion of the structure subject to aerodynamic forces is the same as that of a structure-alone mode at the corresponding structure-alone natural frequency. Then, an analogy between a system with large mistuning and a system subject to aerodynamic forces can be found.

- Finally, the reduced-order modeling method for large mistuning developed in chapter VI should be combined with a small-mistuning technique such as the component mode mistuning method presented in chapter II. Key applications of such a combined technique include the assessment of vibration response for a system that suffers blade damage, and the optimization of bladed disk designs for reduced stress and increased safety. Thus, it would provide a comprehensive vibration analysis and design tool for bladed disks that would help enable the development of more robust and reliable turbine engines.

APPENDIX

APPENDIX A

Modal Participation Factors of Cantilevered-Blade Normal Modes

Since a tuned bladed disk features cyclic symmetry, a system mode can be represented by a mode of a single sector in cyclic coordinates and its harmonic number. Therefore, once the modal participation factors for the blade portion of a cyclic single-sector mode are obtained, all the factors for the corresponding full system mode in physical coordinates can be easily computed.

Tuned-system normal modes can be obtained from a single-sector finite element model as

$$\mathbf{\Phi}^S = (\mathbf{F} \otimes \mathbf{I}) \underset{h=0,\ldots,H}{\tilde{\mathbf{B}}\mathbf{diag}} \left[\tilde{\mathbf{\Phi}}_h^S \right], \tag{A.1}$$

where $\underset{h=0,\ldots,H}{\tilde{\mathbf{B}}\mathbf{diag}} [\cdot]$ denotes a pseudo-block-diagonal matrix, in which block sizes can be different, and $\tilde{\mathbf{\Phi}}_h^S$ is a real cyclic normal mode set corresponding to harmonic h. H is $(N-1)/2$ if N is odd, or $N/2$ if N is even. In this manner, the blade portion of the tuned-system modes in physical coordinates is expressed as follows:

$$\mathbf{\Phi}_\Gamma^S = (\mathbf{F} \otimes \mathbf{I}) \underset{h=0,\ldots,H}{\tilde{\mathbf{B}}\mathbf{diag}} \left[\tilde{\mathbf{\Phi}}_{\Gamma,h}^S \right] \tag{A.2}$$

Next, $\tilde{\mathbf{\Phi}}^S_{\Gamma,h}$ is described by cantilevered-blade component modes.

$$\tilde{\mathbf{\Phi}}^S_{\Gamma,h} = \begin{bmatrix} \tilde{\mathbf{\Phi}}^S_{i,h} \\ \tilde{\mathbf{\Phi}}^S_{b,h} \end{bmatrix} = \begin{cases} \begin{bmatrix} \mathbf{\Phi}^B_o & \mathbf{\Psi}^{B,m}_o \\ \mathbf{0} & \mathbf{I} \end{bmatrix} \begin{bmatrix} \tilde{\mathbf{q}}^m_{\phi,h} \\ \tilde{\mathbf{q}}^m_{\psi,h} \end{bmatrix}, \\ \text{or} \\ \begin{bmatrix} \mathbf{\Phi}^B_o & \mathbf{\Psi}^{B,k}_o \\ \mathbf{0} & \mathbf{I} \end{bmatrix} \begin{bmatrix} \tilde{\mathbf{q}}^k_{\phi,h} \\ \tilde{\mathbf{q}}^k_{\psi,h} \end{bmatrix}, \end{cases} \tag{A.3}$$

where $\tilde{\mathbf{q}}^m_{\phi,h}$, $\tilde{\mathbf{q}}^m_{\psi,h}$, $\tilde{\mathbf{q}}^k_{\phi,h}$, and $\tilde{\mathbf{q}}^k_{\psi,h}$ are the participation factors of the cantilevered-blade and boundary modes in the blade portion of the cyclic tuned-system modes of harmonic h. From Eq. (A.3), it is obvious that

$$\tilde{\mathbf{q}}^m_{\psi,h} = \tilde{\mathbf{q}}^k_{\psi,h} = \tilde{\mathbf{\Phi}}^S_{b,h}. \tag{A.4}$$

Before calculating the modal participation factors of the cantilevered-blade modes, it should be noted that the normal modes and the boundary modes of a cantilevered blade are orthogonal with respect to nominal mass and stiffness matrices. This is proved using Eq. (2.8),

$$\begin{aligned} &\begin{bmatrix} \mathbf{\Phi}^B_o \\ \mathbf{0} \end{bmatrix}^T \begin{bmatrix} \mathbf{M}^B_{ii,o} & \mathbf{M}^B_{ib,o} \\ {\mathbf{M}^B_{ib,o}}^T & \mathbf{M}^B_{bb,o} \end{bmatrix} \begin{bmatrix} \mathbf{\Psi}^{B,m}_o \\ \mathbf{I} \end{bmatrix} \\ &= \begin{bmatrix} \mathbf{\Phi}^B_o \\ \mathbf{0} \end{bmatrix}^T \begin{bmatrix} \mathbf{M}^B_{ii,o}\mathbf{\Psi}^{B,m}_o + \mathbf{M}^B_{ib,o} \\ {\mathbf{M}^B_{ib,o}}^T\mathbf{\Psi}^{B,m}_o + \mathbf{M}^B_{bb,o} \end{bmatrix} \\ &= \begin{bmatrix} \mathbf{\Phi}^B_o \\ \mathbf{0} \end{bmatrix}^T \begin{bmatrix} \mathbf{0} \\ {\mathbf{M}^B_{ib,o}}^T\mathbf{\Psi}^{B,m}_o + \mathbf{M}^B_{bb,o} \end{bmatrix} = 0 \end{aligned} \tag{A.5a}$$

$$\begin{aligned}
&\begin{bmatrix} \mathbf{\Phi}_o^B \\ \mathbf{0} \end{bmatrix}^T \begin{bmatrix} \mathbf{K}_{ii,o}^B & \mathbf{K}_{ib,o}^B \\ {\mathbf{K}_{ib,o}^B}^T & \mathbf{K}_{bb,o}^B \end{bmatrix} \begin{bmatrix} \mathbf{\Psi}_o^{B,k} \\ \mathbf{I} \end{bmatrix} \\
&= \begin{bmatrix} \mathbf{\Phi}_o^B \\ \mathbf{0} \end{bmatrix}^T \begin{bmatrix} \mathbf{K}_{ii,o}^B \mathbf{\Psi}_o^{B,k} + \mathbf{K}_{ib,o}^B \\ {\mathbf{K}_{ib,o}^B}^T \mathbf{\Psi}_o^{B,k} + \mathbf{K}_{bb,o}^B \end{bmatrix} \\
&= \begin{bmatrix} \mathbf{\Phi}^B \\ \mathbf{0} \end{bmatrix}^T \begin{bmatrix} \mathbf{0} \\ {\mathbf{K}_{ib,o}^B}^T \mathbf{\Psi}_o^{B,k} + \mathbf{K}_{bb,o}^B \end{bmatrix} = \mathbf{0}
\end{aligned} \tag{A.5b}$$

Using these orthogonality conditions, $\tilde{\mathbf{q}}_{\phi,h}^m$ and $\tilde{\mathbf{q}}_{\phi,h}^k$ can be obtained from Eq. (A.3) as follows:

$$\begin{aligned}
\begin{bmatrix} \mathbf{\Phi}_o^B \\ \mathbf{0} \end{bmatrix}^T \mathbf{M}_o^B \tilde{\mathbf{\Phi}}_{\Gamma,h}^S &= \begin{bmatrix} \mathbf{\Phi}_o^B \\ \mathbf{0} \end{bmatrix}^T \mathbf{M}_o^B \begin{bmatrix} \mathbf{\Phi}_o^B & \mathbf{\Psi}_o^{B,m} \\ \mathbf{0} & \mathbf{I} \end{bmatrix} \begin{bmatrix} \tilde{\mathbf{q}}_{\phi,h}^m \\ \tilde{\mathbf{q}}_{\psi,h}^m \end{bmatrix} \\
&= \begin{bmatrix} \mathbf{I} & \mathbf{0} \end{bmatrix} \begin{bmatrix} \tilde{\mathbf{q}}_{\phi,h}^m \\ \tilde{\mathbf{q}}_{\psi,h}^m \end{bmatrix} = \tilde{\mathbf{q}}_{\phi,h}^m
\end{aligned} \tag{A.6a}$$

$$\begin{aligned}
\begin{bmatrix} \mathbf{\Phi}_o^B \\ \mathbf{0} \end{bmatrix}^T \mathbf{K}_o^B \tilde{\mathbf{\Phi}}_{\Gamma,h}^S &= \begin{bmatrix} \mathbf{\Phi}_o^B \\ \mathbf{0} \end{bmatrix}^T \mathbf{K}_o^B \begin{bmatrix} \mathbf{\Phi}_o^B & \mathbf{\Psi}_o^{B,k} \\ \mathbf{0} & \mathbf{I} \end{bmatrix} \begin{bmatrix} \tilde{\mathbf{q}}_{\phi,h}^k \\ \tilde{\mathbf{q}}_{\psi,h}^k \end{bmatrix} \\
&= \begin{bmatrix} \mathbf{\Lambda}_o^B & \mathbf{0} \end{bmatrix} \begin{bmatrix} \tilde{\mathbf{q}}_{\phi,h}^k \\ \tilde{\mathbf{q}}_{\psi,h}^k \end{bmatrix} = \mathbf{\Lambda}_o^B \tilde{\mathbf{q}}_{\phi,h}^k
\end{aligned} \tag{A.6b}$$

Once $\tilde{\mathbf{q}}_{\phi,h}^m$ and $\tilde{\mathbf{q}}_{\phi,h}^k$ are obtained, $\mathbf{q}_{\phi,n}^m$ and $\mathbf{q}_{\phi,n}^k$ are expressed using the real Fourier matrix, **F**, and the Kronecker product in the same manner as in Eq. (A.1) and (A.2). That is,

$$\begin{bmatrix} \vdots \\ \mathbf{q}^{m}_{\phi,n} \\ \vdots \end{bmatrix} = \left(\mathbf{F} \otimes \mathbf{I}\right) \tilde{\mathbf{B}}\underset{h=0,\ldots,H}{\mathbf{diag}} \left[\tilde{\mathbf{q}}^{m}_{\phi,h}\right] \tag{A.7a}$$

$$\begin{bmatrix} \vdots \\ \mathbf{q}^{k}_{\phi,n} \\ \vdots \end{bmatrix} = \left(\mathbf{F} \otimes \mathbf{I}\right) \tilde{\mathbf{B}}\underset{h=0,\ldots,H}{\mathbf{diag}} \left[\tilde{\mathbf{q}}^{k}_{\phi,h}\right] \tag{A.7b}$$

BIBLIOGRAPHY

BIBLIOGRAPHY

[1] S. A. Tobias and R. N. Arnold. The Influence of Dynamical Imperfection on the Vibration of Rotating Disks. *Proceedings of the Institution of Mechanical Engineers*, 171:669–690, 1957.

[2] D. S. Whitehead. Effect of Mistuning on the Vibration of Turbomachine Blades Induced by Wakes. *Journal Mechanical Engineering Science*, 8(1):15–21, 1966.

[3] J. T. Wagner. Coupling of Turbomachine Blade Vibrations Through the Rotor. *ASME Journal of Engineering for Power*, 89(4):502–512, 1967.

[4] R. C. F. Dye and T. A. Henry. Vibration Amplitudes of Compressor Blades Resulting From Scatter in Blade Natural Frequencies. *ASME Journal of Engineering for Power*, 91(3):182–188, 1969.

[5] D. J. Ewins. The Effects of Detuning Upon the Forced Vibrations of Bladed Disks. *Journal of Sound and Vibration*, 9(1):65–79, 1969.

[6] D. J. Ewins. A Study of Resonance Coincidence in Bladed Discs. *Journal Mechanical Engineering Science*, 12(5):305–312, 1970.

[7] L. E. El-Bayoumy and A. V. Srinivasan. Influence of Mistuning on Rotor-Blade Vibrations. *AIAA Journal*, 13(4):460–464, 1975.

[8] J. H. Griffin and T. M. Hoosac. Model Development and Statistical Investigation of Turbine Blade Mistuning. *ASME Journal of Vibration, Acoustics, Stress, and Reliability in Design*, 106:204–210, 1984.

[9] C.-C. Lin and M. P. Mignolet. An Adaptive Perturbation Scheme for the Analysis of Mistuned Bladed Disks. *ASME Journal of Engineering for Gas Turbines and Power*, 119(1):153–160, 1997.

[10] S. T. Wei and C. Pierre. Localization Phenomena in Mistuned Assemblies with Cyclic Symmetry, Part I: Free Vibrations. *ASME Journal of Vibration, Acoustics, Stress, and Reliability in Design*, 110(4):429–438, 1988.

[11] S. T. Wei and C. Pierre. Localization Phenomena in Mistuned Assemblies with Cyclic Symmetry, Part II: Forced Vibrations. *ASME Journal of Vibration, Acoustics, Stress, and Reliability in Design*, 110(4):439–449, 1988.

[12] G. S. Óttarsson and C. Pierre. On the Effects of Interblade Coupling on the Statistics of Maximum Forced Response Amplitudes in Mistuned Bladed Disks. In AIAA Paper 95-1494, *Proceedings of the 36th AIAA/ASME/ASCE/AHS Structures, Structural Dynamics, and Materials Conference,* New Orleans, Louisiana, number 5, pages 3070–3078. AIAA, New York, NY, 1995.

[13] H. Irretier. Spectral Analysis of Mistuned Bladed Disk Assemblies by Component Mode Synthesis. In *Vibrations of Bladed Disk Assemblies, Proceedings of the ASME 9th Biennial Conference on Mechanical Vibration and Noise,* Dearborn, Michigan, pages 115–125. ASME, New York, 1983.

[14] Z.-C. Zheng and F.-R. Wang. Dynamic Analysis of Blade Groups Using Component Mode Synthesis. In *Vibrations of Blades and Bladed Disk Assemblies, Proceedings of the ASME 10th Biennial Conference on Mechanical Vibration and Noise,* Cincinnati, Ohio, pages 97–103, 1985.

[15] M. P. Castanier, G. Óttarsson, and C. Pierre. A Reduced-Order Modeling Technique for Mistuned Bladed Disks. *Journal of Vibration and Acoustics*, 119(3):439–447, 1997.

[16] M. J. Kruse and C. Pierre. Forced Response of Mistuned Bladed Disks Using Reduced-Order Modeling. In *Proceedings of the 37th AIAA/ASME Structures, Structural Dynamics, and Materials Conference,* Salt Lake City, Utah, volume 4, pages 1938–1950. AIAA, New York, 1996.

[17] M. J. Kruse and C. Pierre. Dynamic Response of an Industrial Turbomachinery Rotor. In *Proceedings of the 32nd AIAA/ASME/SAE/ASEE Joint Propulsion Conference and Exhibit,* Lake Buena Vista, Florida, 1996.

[18] R. Bladh, M. P. Castanier, and C. Pierre. Reduced Order Modeling and Vibration Analysis of Mistuned Bladed Disk Assemblies with Shrouds. *ASME Journal of Engineering for Gas Turbines and Power,* 121(3):515–522, 1999.

[19] R. Bladh, M. P. Castanier, and C. Pierre. Component-Mode-Based Reduced Order Modeling Techniques for Mistuned Bladed Disks—Part I: Theoretical Models. *ASME Journal of Engineering for Gas Turbines and Power*, 123(1):89–99, 2001.

[20] R. Bladh, M. P. Castanier, and C. Pierre. Component-Mode-Based Reduced Order Modeling Techniques for Mistuned Bladed Disks—Part II: Application. *ASME Journal of Engineering for Gas Turbines and Power,* 123(1):100–108, 2001.

[21] F. Moyroud, T. Fransson, and G. Jacquet-Richardet. A comparison of two finite element reduction techniques for mistuned bladed disks. *Journal of Engineering for Gas Turbines and Power,* 124(4):942–952, 2002.

[22] M.-T. Yang and J. H. Griffin. A Reduced Order Approach for the Vibration of Mistuned Bladed Disk Assemblies. *ASME Journal of Engineering for Gas Turbines and Power*, 119:161–167, 1997.

[23] M.-T. Yang and J. H. Griffin. A Reduced Order Model of Mistuning Using a Subset of Nominal System Modes. *ASME Journal of Engineering for Gas Turbines and Power*, 123:893–900, 2001.

[24] D. S. Whitehead. Research Note: Effect of Mistuning on Forced Vibration of Blades with Mechanical Coupling. *Journal Mechanical Engineering Science,* 18(6):306–307, 1976.

[25] D. S. Whitehead. The Maximum Factor by Which Forced Vibration of Blades Can Increase Due to Mistuning. *ASME Journal of Engineering for Gas Turbines and Power,* 120(1):115–119, 1998.

[26] J. A. Kenyon and J. H. Griffin. Forced Response of Turbine Engine Bladed Disks and Sensitivity to Harmonic Mistuning. *ASME Journal of Engineering for Gas Turbines and Power,* 125(1):113–120, 2003.

[27] J. A. Kenyon, J. H. Griffin, and D. M. Feiner. Maximum Bladed Disk Forced Response From Distortion of a Structural Mode. *ASME Journal of Turbomachinery,* 125(2):352–363, 2003.

[28] A. J. Rivas-Guerra and M. P. Mignolet. Maximum Amplification of Blade Response due to Mistuning: Localization and Mode Shape Aspects of the Worst Disks. *ASME Journal of Turbomachinery,* 125(3):442–454, 2003.

[29] M. P. Castanier and C. Pierre. Consideration on the Benefits of Intentional Blade Mistuning for the Forced Response of Turbomachinery Rotors. In *Proceedings of The 1997 International Mechanical Engineering Congress and Exposition: The Winter Annual Meeting of the ASME,* Dallas, Texas, pages 419–425, 1997.

[30] J. Judge, C. Pierre, and S. L. Ceccio. Experimental Validation of Mistuning Identification Techniques and Vibration Predictions in Bladed Disks. In *Proceedings of the 2001 CEAS/AAIA/AIAE International Forum on Aeroelasticity and Structural Dynamics,* Madrid, Spain, volume 2, pages 89–98, 2001.

[31] J. Judge, C. Pierre, and S. L. Ceccio. Mistuning Identification in Bladed Disks. In *Proceedings of the International Conference on Structural Dynamics Modeling,* Madeira Island, Portugal, 2002.

[32] D. M. Feiner and J. H. Griffin. Mistuning Identification of Bladed Disks Using a Fundamental Mistuning Model - Part I: Theory. *ASME Journal of Turbomachinery,* 126(1):150–158, 2004.

[33] D. M. Feiner and J. H. Griffin. Mistuning Identification of Bladed Disks Using a Fundamental Mistuning Model - Part II: Application. *ASME Journal of Turbomachinery*, 126(1):159–165, 2004.

[34] D. J. Ewins. Further Studies of Bladed Disc Vibration: Effects of Packeting. In *Proceedings of the Second International Conference on Vibrations in Rotating Machinery,* Cambridge, UK, pages 97–102, 1980.

[35] M. P. Castanier and C. Pierre. Investigation of the Combined Effects of Intentional and Random Mistuning on the Forced Response of Bladed Disks. In AIAA Paper 98-3720, 1998.

[36] M. P. Castanier and C. Pierre. Using Intentional Mistuning in the Design of Turbomachinery Rotors. *AIAA Journal*, 40(10):2077–2086, 2002.

[37] M. E. Brewer, M. P. Castanier, and C. Pierre. Effects of Harmonic Intentional Mistuning on the Free Response of Bladed Disks. In ASME Paper DETC99/VIB-8012, 1999.

[38] B.-K. Choi, J. Lentz, A. J. Rivas-Guerra, and M. P. Mignolet. Optimization of Intentional Mistuning Patterns for the Reduction of the Forced Response Effects of Unintentional Mistuning: Formulation and Assessment. *ASME Journal of Engineering for Gas Turbines and Power*, 125(1):131–140, 2003.

[39] R. Bladh, M. P. Castanier, C. Pierre, and M. J. Kruse. Dynamic Response Predictions for a Mistuned Industrial Turbomachinery Rotor Using Reduced Order Modeling. *ASME Journal of Engineering for Gas Turbines and Power*, 124(2):311–324, 2002.

[40] E. P. Petrov, K. Y. Sanliturk, and D. J. Ewins. A New Method for Dynamic Analysis of Mistuned Bladed Disks Based on the Exact Relationship Between Tuned and Mistuned Systems. *ASME Journal of Engineering for Gas Turbines and Power*, 124:586–597, 2002.

[41] R. R. Craig. *"Structural Dynamics, An Introduction to Computer Methods"*. Wiley, New York, 1981.

[42] M.-T. Yang and J. H. Griffin. A Normalized Modal Eigenvalue Approach for Resolving Modal Interaction. *ASME Journal of Engineering for Gas Turbines and Power*, 119:647–650, 1997.

[43] C. Pierre and D. V. Murthy. Aeroelastic Modal Characteristics of Mistuned Blade Assemblies: Mode Localization and Loss of Eigenstructure. *AIAA Journal*, 30(10):2483–2496, 1992.

[44] S. Lim, R. Bladh, M. P. Castanier, and C. Pierre. A Compact, Generalized Component Mode Mistuning Representation for Modeling Bladed Disk Vibration. In AIAA Paper 2003-1545, *Proceedings of the 44th AIAA/ASME/ASCE/AHS Structures, Structural Dynamics, and Materials Conference*, volume 2, pages 1359–1380. AIAA, 2003.

[45] D. M. Feiner and J. H. Griffin. A Fundamental Model of Mistuning for a Single Family of Modes. *ASME Journal of Turbomachinery*, 124(4):597–605, 2002.

[46] M. P. Mignolet, A. J. Rivas-Guerra, and J. P. Delor. Identification of Mistuning Characteristics of Bladed Disks From Free Response Data - Part I. *ASME Journal of Engineering for Gas Turbine and Power*, 123(2):395–403, 2001.

[47] A. J. Rivas-Guerra, M. P. Mignolet, and J. P. Delor. Identification of Mistuning Characteristics of Bladed Disks From Free Response Data - Part II. *ASME Journal of Engineering for Gas Turbine and Power*, 123(2):404–411, 2001.

[48] M. P. Mignolet and C.-C. Lin. Identification of Structural Parameters in Mistuned Bladed Disks. *ASME Journal of Vibration and Acoustics,* 119(3):428–438, 1997.

[49] F. Pichot, F. Thouverez, L. Jezequel, and E. Seinturier. Mistuning Parameters Identification of a Bladed Disk. *Key Engineering Materials - Damage Assesment of Structures - DAMAS 2001*, 204–205:123–132, 2001.

[50] D. M. Feiner, J. H. Griffin, K. W. Jones, J. A. Kenyon, O. Mehmed, and A. P. Kurkov. System Identification of Mistuned Bladed Disks from Traveling Wave Response Measurements. In *Proceedings of ASME 2003 Design Engineering Technical Conferences and Computers and Information in Engeineering Conference,* Chicago, Illinois, 2003.

[51] J. Judge. *Experimental Investigations of the Effects of Mistuning on Bladed Disk Dynamics*. PhD thesis, The University of Michigan, Ann Arbor, 2002.

[52] K. W. Jones and C. J. Cross. Traveling Wave Excitation System for Bladed Disks. *Journal of Propulsion and Power*, 19(1):135–141, 2003.

[53] J. Judge, S. L. Ceccio, and C. Pierre. Traveling-wave Excitation and Optical Measurement Techniques for Non-contacting Investigation of Bladed Disk Dynamics. *Shock and Vibration Digest*, 35(3):183–190, 2003.

[54] R. Bladh. *Efficient Predictions of the Vibratory Response of Mistuned Bladed Disks by Resuced Order Modeling*. PhD thesis, The University of Michigan, Ann Arbor, 2001.

[55] J. C. MacBain and P. W. Whaley. Maximum Resonant Response of Mistuned Bladed Disks. *ASME Journal of Vibration, Acoustics, Stress, and Reliability in Design*, 106:218–223, 1984.

[56] E. P. Petrov, R. Vitali, and R. T. Haftka. Optimization of Mistuned Bladed Diskcs Using Gradient-based Response Surface Approximations. In AIAA Paper 2000-1552, *Proceedings of the 41th AIAA/ASME/ASCE/AHS/ASC Structures, Structural Dynamics, and Materials Conference,* Atlanta, Georgia, volume 1, pages 1129–1139. AIAA, Reston, VA, 2000.

[57] E. P. Petrov and D. J. Ewins. Analysis of the worst mistuning patterns in bladed disk assemblies. *ASME Journal of Turbomachinery*, 125(4):623–631, 2003.

[58] A. Sinha. Computation of the Maximum Amplitude of a Mistuned Bladed Disk Assembly via Infinity Norm. In *Proceedings of the ASME International Mechanical Engineering Congress and Exposition,* Dallas, Texas, volume AD-55, pages 427–432. ASME, Fairfield, NJ, 1997.

[59] M. Rotea and F. D'Amato. New Tools for Analysis and Optimization of Mistuned Bladed Disks. In AIAA Paper 2002-4081, 2002.

[60] A Sinha. Calculating the Statistics of Forced Response of a Mistuned Bladed Disk Assembly. *AIAA Journal*, 24(11):1797–1801, 1986.

[61] A Sinha and Chen S. A Higher Order Technique to Compute the Statistics of Forced Response of a Mistuned Bladed Disk Assembly. *Journal of Sound and Vibration*, 130(2):207–221, 1989.

[62] J. A. Kenyon and J. H. Griffin. Mistuned Bladed Disk Forced Response with Frequency Veering. In *Proceedings of the 8th National Turbine Engine High Cycle Fatigue Conference*, Monterey, California, 2003.

[63] K. R. V. Kaza and R. C. Kielb. Flutter and Response of a Mistuned Cascade in Incompressible Flow. *AIAA Journal*, 20(8):1120–1127, 1982.

[64] R. C. Kielb and K. R. V. Kaza. Effects of Structural Coupling on Mistuned Cascade Flutter and Response. *ASME Journal of Engineering for Gas Turbines and Power*, 106(1):17–24, 1984.

[65] E. Nissim. Optimization of Cascade Blade Mistuning, Part I: Equations of Motion and Basic Inherent Properties. *AIAA Journal*, 23(8):1213–1222, 1985.

[66] E. Nissim and Haftka R. T. Optimization of Cascade Blade Mistuning, Part II: Global Optimum and Numerical Optimization. *AIAA Journal*, 23(9):1402–1410, 1985.

[67] E. F. Crawley and K. C. Hall. Optimization and Mechanisms of Mistuning in Cascades. *ASME Journal of Engineering for Gas Turbines and Power*, 107(2):418–426, 1985.

[68] B. Shapiro and B.D. Coller. Characterizing Optimal Mistuning by Symmetry Arguments: A General Framework Applied to a Dynamic Flutter Model. In *Proceedings of the IEEE Conference on Control Applications*, pages 901–906. IEEE, New York, NY, 1997.

[69] A. Sinha. Computation of the Maximum Amplitude of a Mistuned Bladed Disk Assembly via Infinity Norm. In *Analysis and Design Issues for Modern Aerospace Vehicles*, pages 427–432. ASME, New York, NY, 1997.

[70] H. Yiu and D. J. Ewins. Dependence on Blade Arrangements of Mistuned Bladed Disc of the Optimal and Critical Resonant Responses. In *Proceedings of the 6th International Symposium on Transport Phenomena and Dynamics of Rotating Machinery,* Honolulu, Hawaii, volume 1, pages 237–251. Pacific Center of Thermal-Fluids Engineering, Kihei, HI, 1996.

[71] E. P. Petrov and D. J. Ewins. Search for the Best Blade Arrangement in a Mistuned Bladed Disc Assembly. In *Proceedings of the 7th National Turbine Engine High Cycle Fatigue Conference,* Palm Beach Garden, Florida, 2002.

[72] S. Lim, M. P. Castanier, and C. Pierre. Predicting Mistuned Blade Amplitude Bounds and Stress Increases from Energy Formulations. In *Proceedings of the 9th National Turbine Engine High Cycle Fatigue Conference,* Pinehurst, North Carolina, 2004.

[73] S. Baik, M. P. Castanier, and C. Pierre. Mistuning Sensitivity Prediction of Bladed Disks Using Eigenvalue Curve Veerings. In *Proceedings of the 9th National Turbine Engine High Cycle Fatigue Conference,* Pinehurst, North Carolina, 2004.

[74] D. J. Ewins and Z. S. Han. Resonant Vibration Levels of a Mistuned Bladed Disk. *ASME Journal of Vibration, Acoustics, Stress, and Reliability in Design*, 106(2):211–217, 1984.

[75] Keqin Gu and Benson H. Tongue. Method to improve the modal convergence for structures with external forcing. *ASME Journal of Applied Mechanics,* 54(4):904–909, 1987.

[76] C. W. Cai, Y. K. Cheung, and H. C. Chan. Mode Localization Phenomena in Nearly Periodic Systems. *ASME Journal of Applied Mechanics*, 62(1):141–149, 1995.

[77] W.-H. Shyu, Z.-D. Ma, and G. M. Hulbert. A New Component Mode Synthesis Method: Quasi-Static Mode Compensation. *Finite Elements in Analysis and Design*, 24:271–281, 1997.

[78] W.-H. Shyu, Jianmin Gu, G. M. Hulbert, and Z.-D. Ma. On the use of multiple quasi-static mode compensation sets for component mode synthesis of complex structures. *Finite Elements in Analysis and Design*, 35:119–140, 2000.

[79] J. A. Joseph. Cyclic Symmetry in MSC/NASTRAN. In *MSC/NASTRAN Application Manual,* chapter 3.2, pages 10–24. The MacNeal-Schwendler Corporation, 1981.

[80] V. Elchuri, G. C. C. Smith, and A. M. Gallo. NASTRAN Forced Vibration Analysis of Rotating Cyclic Structures. *ASME Journal of Vibration, Acoustics, Stress, and Reliability in Design*, 106:224–234, 1984.

[81] D. Hitchings and M. Singh. Cyclic Symmetry Through Constraint Equations with Application to the Analysis of Steam Turbines. In *Bladed Disk Assemblies, Proceedings of the ASME 11th Biennial Conference on Mechanical Vibration and Noise,* Boston, Massachusetts, pages 113–119, 1987.

[82] C. Pierre. Mode Localization and Eigenvalue Loci Veering Phenomena in Disordered Structures. *Journal of Sound and Vibration*, 126(3):485–502, 1988.

[83] R. Bladh, M. P. Castanier, and C. Pierre. Effects of Multistage Coupling and Disk Flexibility on Mistuned Bladed Disk Dynamics. *ASME Journal of Engineering for Gas Turbines and Power*, 125(1):121–130, 2003.

ABSTRACT

DYNAMIC ANALYSIS AND DESIGN STRATEGIES FOR MISTUNED BLADED DISKS

by

Sang-Ho Lim

Co-Chairs: Christophe Pierre and Matthew P. Castanier

Bladed disks are used in many important engineering applications, including turbine engine rotors. Typically, each disk-blade sector in a bladed disk is assumed to be identical, and the bladed disk is analyzed based on a single sector model. However, due to manufacturing tolerances, operational wear, and other unavoidable factors, an actual bladed disk always has discrepancies among individual sectors, called mistuning. Even small mistuning can alter dramatically the vibration response of a bladed disk compared to the ideal, tuned system. In particular, the vibration energy may be concentrated in a few blades, leading to increased stress levels and fatigue problems. Moreover, since mistuning destroys cyclic symmetry, the whole assembly model must be analyzed, which is computationally expensive.

In this work, a new reduced-order vibration modeling technique for mistuned bladed disks is presented. This is called the component mode mistuning (CMM) method, and it allows for easy implementation of mistuning and yields more efficient and accurate reduced-order models (ROMs) compared to previous methods. Based on the CMM method, a mistuning identification technique is also developed. In order to account for the difference between an actual bladed disk and the finite element model, the concept of "cyclic modeling error" is introduced in the CMM formulation, and a model updating procedure is implemented to compensate for this error. As a result, the identification method becomes more accurate and robust. In addition, because the increase in maximum blade response due to mistuning is used for design safety evaluation, two methods for calculating the upper bound of this response amplification are presented. Then, as a design strategy for significantly reducing the worst-case amplification, the use of intentional mistuning in a nominal design is investigated. Based on key observations from an analysis of vibration energy flow in bladed disks, some guidelines are proposed for reducing the design space for intentional mistuning patterns, so that an optimal or near-optimal pattern can be found without requiring an expensive optimization process. Finally, a novel reduced-order modeling technique is presented for a system subject to large, geometric mistuning or design changes. A ROM constructed by this new technique shows fast convergence and excellent accuracy in capturing the motion of a system featuring large deviations from the original design, which cannot be handled with existing small-mistuning ROMs.